EVA KOZIC

ULTRASONIC METHODS FOR MATERIAL AND FAILURE CHARACTERIZATION

MONTANUNIVERSITÄT LEOBEN

ULTRASONIC METHODS FOR MATERIAL AND FAILURE CHARACTERIZATION

MAG. RER. NAT. EVA KOZIC

May 2018

SUPERVISOR:
This thesis was supervised by Priv.-Doz. Dipl.-Ing. Dr.mont. **Roland Brunner**
(Montanuniversität Leoben; Materials Center Leoben, Leoben, Austria).

Materials Center Leoben Forschung GmbH
Department for Microelectronics
Roseggerstrasse 12
A-8700 Leoben

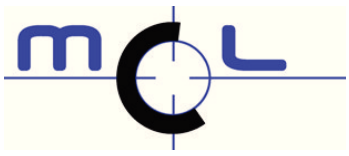

in cooperation with
Mag. Dr.rer.nat. **Robert Nuster** and
Ao.Univ.-Prof. Mag. Dr.rer.nat.**Günther Paltauf**
Karl-Franzens University of Graz
Institute of Physics
Universitätsplatz 5
A-8010 Graz

AFFIDAVIT

I declare in lieu of oath, that I wrote this thesis and performed the associated research by my self, using only literature cited in this document.

Leoben, May 2018

Eva Kozic

To my family and Darjan.

You must let what happens happen. Everything must be equal in your eyes, good and evil, beautiful and ugly, foolish and wise.

— Michael Ende

ACKNOWLEDGMENTS

This thesis was conducted in the years between 2014 and 2018 during my occupation at the **Materials Center Leoben (MCL)** Forschung GmbH. I greatfully acknowledge the funding by the Projects **eRamp** and **Metro4 3D**.

I express my gratitude towards my supervisor **Roland Brunner** for the possibility to work as his PhD student, his support and advice as well as towards the **MCL** for providing a friendly work environment.

Furthermore, I would like to thank our cooperation partners at the **University of Graz**. I want to especially mention the open doors of **Günther Paltauf** and **Heinz Krenn**. In the same sense, I am particularly indebted to **Robert Nuster**. I am very grateful for his excellent support and that he always found time despite his very busy schedule and shared a lot of his experience in most valuable discussions.

My sincere thanks also goes to our projectpartners for supplying high class samples. I am especially thankful to **R. Zelsacher, M. Ehmann, F. Schrank and J. Siegert** in this regard.

I want to express my gratitude towards my colleague **René Hammer**, who was willing to spend a lot of his time discussing physics and ultrasound. My deepest gratitude goes to my lab partner **Jördis Rosc** for many valuable discussions and training concerning measurements with the acoustic microscope. I also thank my colleague **Thomas Vorauer** for proofreading my thesis and valuable comments.

Furthermore, I have the privilege to gratefully acknowledge all of my friends. They have supported me, cheered me up in times of desperation and ensured the necessary level of work-live-balance which keeps a PhD student from getting crazy. I am particularly thankful to **Andrea Janics**, **Matthias Puhr**, **Robert and Miriam Wimmer-Teubenbacher**, **Mirjam Holzer**, **Eva Gögele**, **Irene Rieder** and **Sanja Damjanovic**.

I am very grateful to my family for their support throughout the course of my life and education. The trust and caring of my parents - **Johann and Maria** - as well as their appreciated advice were and will always be most valuable to me. In the same sense, I thank my brother **Hannes** and my sisters **Alexandra** and **Katharina**.

Foremost, I am grateful to my husband **Darjan**, for his constant support and strength. His advice, encouragement, belief and affection were the cornerstones for the successful conclusion of this thesis.

ABSTRACT

Current trends in micro- and nano-electronics are More-than-Moore (MtM) technologies, enabling functions similar to the five human senses, all integrated in a single electronic device. This ongoing trend of increased functionality and miniaturization leads to increased complexity and failure risk of MtM components. Consequently, the realization of MtM technologies demands advanced failure and material characterization, where methods showing at-line or in-line potential are most beneficial.

The material- and failure characterization in metallic and polymer coatings as well as in layered systems is of high relevance due to their vast applications. However, many state of the art methods are destructive (*e.g.* focused ion beam milling) or at least require the direct loading of the analysed sample for material characterization (*e.g.* the determination of the Young's modulus by nanoindentation). Concerning failure characterization, the challenges include the localization of the defect on and within the sample and the distinction between various failure modes. Moreover, the defects in MtM devices often show extensions down to the nm regime. In addition, the applied technique must be time- and cost efficient.

In this thesis, the two ultrasonic methods *laser induced ultrasound (LUS)* and *scanning acoustic microscopy (SAM)* are used for material and failure characterization of MtM relevant devices. The LUS and the SAM methods are tested regarding their potentials concerning (1) the determination of elastic properties of thin film systems and (2) the detection of defects in MtM relevant components. A special focus lies on the potential for at-line or in-line inspection of the ultrasonic methods. Moreover, the SAM evaluations are supported by *elastodynamic finite integration technique (EFIT)* simulations.

The LUS method is used for the material characterization of metallic and polymer thin films for MtM technologies. In addition, the step-wise characterization of multi-layered systems via LUS is discussed. The possibility to distinguish different deposited metallic coatings via LUS measurements is analysed and the sensitivity of surface acoustic waves to light exposure of polymer coatings is demonstrated. For these LUS analyses, surface acoustic waves (SAWs) are excited on the sample by short laser pulses and detected using a second continuous wave laser. In layered systems, the SAW phase velocity can depend on the frequency. This dispersion relation (obtained from the LUS measurement) can also be calculated. By fitting the theoretical dispersion to the experimentally evaluated curve, material properties can be extracted from the SAW propagation. Alternatively, the SAW velocity can be used directly for material monitoring.

The SAM analysis of delaminated printed circuit boards (PCBs) is presented in this work. Although the acoustic failure analysis is complicated by the multi-layered build up of the PCBs, an "indirect failure detection" was successfully applied. Moreover, the detection of subsurface cracks with extensions below the lateral and axial resolution limit of the SAM in through silicon vias (TSVs) – highly relevant MtM components – is

carried out. The focus lies on the automatized failure detection via pattern recognition algorithms on the one hand and on the excitation of additional wave modes for failure detection on the other hand. The advantages of the low frequency excitation of additional wave modes - in contrast to high frequency SAM measurements - are discussed in detail. Moreover, SAM is used for material characterization, performing V(z) analyses, and the results are compared to the LUS outcome. Furthermore, the sound propagation during SAM measurements is simulated using EFIT.

The results presented in this work are corroborated via variety of other state of the art characterization techniques (*e.g.* high resolution X-Ray computed tomography, scanning electron microscopy and nanoindentation) and are published in [33–39].

ZUSAMMENFASSUNG

Einen aktuellen Trend in der Mikro- und Nanoelektronik stellen More-than-Moore (MtM) Technologien dar. Diese ermöglichen eine integrierte Funktionsvielfalt von elektronischen Komponenten - ähnlich den fünf menschlichen Sinnen. Der andauernde Trend der zunehmenden Funktionalität und Miniaturisierung von MtM Bauteilen erhöht deren Komplexität, was zu einer steigenden Fehleranfälligkeit führt. Aus diesem Grund bedarf die Realisierung von MtM Technologien der Weiterentwicklung von Fehler- und Materialcharakterisierungstechniken, wobei Methoden, die direkt in oder an der Produktionslinie geführt werden können, natürlich vorteilhaft sind.

Die Material- und Fehlercharakterisierung von metallischen oder polymeren Beschichtungen sowie von Vielschichtsystemen hat große Bedeutung aufgrund ihrer vielfältigen Anwendungen. Viele Charakterisierungsmethoden sind jedoch zerstörend oder erfordern zumindest die direkte Belastung der analysierten Probe. In Bezug auf die Fehlercharakterisierung liegen die Herausforderungen zum einen in der Lokalisierung des Fehlers auf und innerhalb der Probe, zum anderen muss eine Differenzierung verschiedener Fehlermoden gemacht werden können. Des Weiteren zeigen Defekte in MtM Bauteilen oft sehr kleine Ausdehnungen im Nanometer-Bereich. Darüber hinaus sollte die angewandte Methode zeit- und kosteneffizient sein.

In dieser Arbeit werden die zwei Ultraschall Methoden *Laser induzierter Ultraschall (LUS)* und *Rasterultraschallmikroskopie (scanning acoustic microscopy, SAM)* für die Material- und Fehlercharakterisierung von MtM relevanten Bauteilen herangezogen. Die LUS und die SAM Methode werden in Bezug auf (1) die Bestimmung von elastischen Parametern von Dünnschichtsystemen und (2) die Detektion von Defekten in MtM Komponenten getestet. Im Vordergrund steht das Potenzial, die Methoden direkt an oder in der Produktionslinie einzusetzen. Darüber hinaus werden die SAM Messungen von *Elastodynamic Finite Integration Technique (EFIT)* Simulationen unterstützt.

Die LUS Methode wird in dieser Arbeit zur Materialcharakterisierung von metallischen und polymeren Schichten für MtM Technologien verwendet. Zusätzlich wird die schrittweise Charakterisierung von Vielschichtsystemen via LUS diskutiert. Die Möglichkeit zwischen verschieden abgeschiedenen metallischen Schichten mittels LUS zu

unterscheiden und die Sensitivität von Oberflächenwellen auf die Belichtungsdauer von Polymerschichten werden demonstriert. Für die LUS Analysen werden Oberflächenwellen auf der Probe durch kurze Laserpulse induziert und mit einem zweiten, kontinuierlichen Laser detektiert. In Schichtsystemen kann die Phasengeschwindigkeit der Oberflächenwelle von der Frequenz abhängen. Die aus dem Experiment ermittelte Dispersionskurve kann auch berechnet werden. Durch das Anpassen der theoretischen Dispersion an die experimentell ermittelte Kurve können Materialeigenschaften bestimmt werden. Alternativ kann die Oberflächenwellengeschwindigkeit auch direkt zur Materialkontrolle herangezogen werden.

SAM wird in dieser Arbeit für die Detektion von delaminierten Schichten in Leiterplatten (printed circuit boards, PCBs) verwendet. Obwohl der Vielschichtaufbau des PCBs die akustische Analyse erschwert, konnte eine „indirekte Fehlerdetektion“ erfolgreich angewandt werden. Des Weiteren wird die Detektion von Rissen unterhalb der Probenoberfläche mit Ausdehnungen kleiner als die laterale und axiale Auflösung des SAMs in Silizium Durchkontaktierungen – sogenannten "through silicon vias (TSVs)", hoch relevante MtM Komponenten – präsentiert. Der Fokus liegt hier zum einen auf der automatisierten Bilderkennung, zum anderen werden zusätzliche Wellenmoden zur Fehlerdetektion angeregt. Die Vorteile der niederfrequenten Anregung von zusätzlichen Wellenmoden im Gegensatz zu hochfrequenten SAM Untersuchungen werden im Detail diskutiert. Zusätzlich wird SAM in dieser Arbeit zur Materialcharakterisierung – mittels der sogenannten V(z) Analyse – verwendet und die Ergebnisse werden mit LUS Resultaten verglichen. Darüber hinaus werden EFIT Simulationen der Schallausbreitung während SAM Messungen durchgeführt.

Die LUS und SAM Ergebnisse dieser Arbeit werden von einer Vielfalt anderer Highend-Methoden, wie etwa hochauflösender Röngencomputertomographie, Rasterelektronenmikroskopie und Nano-Indentierung, bekräftigt und sind publiziert in [33–39].

PUBLICATIONS

Parts of the work presented in this thesis were already investigated and published in research papers or conference proceedings. In the following, the concerning publications are listed:

[1] E. Grünwald, R. Nuster, R. Treml, D. Kiener, G. Paltauf, and R. Brunner. "Young's Modulus and Poisson's Ratio Characterization of Tungsten Thin Films Via Laser Ultrasound." In: *Materials Today: Proceedings* 2.8 (2015). nanoFIS 2014 - Functional Integrated nanoSystems, pp. 4289 –4294. ISSN: 2214-7853. DOI: http://dx.doi.org/10.1016/j.matpr.2015.09.015.

[2] E. Grünwald, R. Hammer, J. Rosc, G.A. Maier, M. Bärnthaler, M.J. Cordill, S. Brand, R. Nuster, T. Krivec, and R. Brunner. "Advanced 3D failure characterization in multi-layered PCBs." In: *NDT & E International* 84 (2016), pp. 99 –107. ISSN: 0963-8695. DOI: http://dx.doi.org/10.1016/j.ndteint.2016.08.003.

[3] E. Grünwald, J. Rosc, R. Hammer, P. Czurratis, M. Koch, J. Kraft, F. Schrank, and R. Brunner. "Automatized failure analysis of tungsten coated TSVs via scanning acoustic microscopy." In: *Microelectronics Reliability* 64 (2016). Proceedings of the 27th European Symposium on Reliability of Electron Devices, Failure Physics and Analysis, pp. 370 –374. ISSN: 0026-2714. DOI: http://dx.doi.org/10.1016/j.microrel.2016.07.075.

[4] E. Grünwald, R. Nuster, R. Hammer, H. Aßmann, R. Brunner, and G. Paltauf. "Characterization of polyimid-multi-layer thin films combining laser ultrasonic measurements and numerical evaluations." In: *2016 17th International Conference on Thermal, Mechanical and Multi-Physics Simulation and Experiments in Microelectronics and Microsystems, EuroSimE 2016*. 2016. ISBN: 9781509021062. DOI: DOI:10.1109/EuroSimE.2016.7463353.

[5] E. Grünwald, R. Hammer, J. Rosc, B. Sartory, and R. Brunner. "Accretion Detection via Scanning Acoustic Microscopy in Microelectronic Components - Considering Symmetry Breaking Effects." In: *Microscopy and Microanalysis* 23.S1 (2017), 14661467. DOI: 10.1017/S1431927617007991.

[6] E. Grünwald, R. Nuster, G. Paltauf, T. Maier, R. Wimmer-Teubenbacher, R. Treml, D. Kiener, V. Leitgeb, A. Köck, and R. Brunner. "Laser Ultrasonic Thin Film Characterization of Si-Cu-Al-Cu Multi-Layered Stacks." In: *Materials Today: Proceedings*. Vol. 4. 7. 2017, pp. 7122–7127. DOI: 10.1016/j.matpr.2017.08.006.

[7] E. Grünwald, R. Hammer, R. Nuster, P. Wieser, M. Hinderer, I. Wiesler, R. Zelsacher, M. Ehmann, and R. Brunner. "Simulation of Acoustic Wave Propagation in Aluminium Coatings for Material Characterization." In: *Coatings* 7.12 (2017), p. 230. ISSN: 2079-6412. DOI: 10.3390/coatings7120230.

[8] E. Kozic, J. Rosc, B. Sartory, J. Siegert, F. Schrank, and R. Brunner. "Novel Approach for Acoustic Microscopy Enabling nm-Sized Failure Detection in Open TSVs." In: *TBA* (2018).

[9] E. Kozic, R. Nuster, V. Razumovskiy, J. Zechner, B. Sartory, H. Katz, U. Kleb, R. Zelsacher, M. Ehmann, and R. Brunner. “TBA.” In: *TBA* (2018).

[10] E. Kozic, J. Rosc, B. Sartory, J. Siegert, F. Schrank, and R. Brunner. “Wave Mode Enhanced Failure Detection via Scanning Acoustic Microscopy.” In: *TBA* (2018).

CONTENTS

LIST OF FIGURES

LIST OF TABLES

Part I

INTRODUCTION

This thesis was written in the framework of the projects **eRamp** (Excellence in Speed and Reliability for More Than Moore Technologies, ENIAC, FP7 research (No.:621270) and FFG (No.:843740) program) and **Metro4 3D** (Metrology for future 3D-technologies, EU, H2020 (P. No.: 688225) program).

The project **eRamp** aimed for the strengthening of Europe's market position in automotive industries, electronics industries and leading know how for "More than Moore" (MtM) based technologies. One goal of the project eRamp was the "material and failure characterization for MtM devices" with focus on rapid learning.
The project **Metro4 3D** concerns advanced metrology techniques for MtM technologies with focus on 3D integration of devices. One part of Metro4 3D concerns metrology via scanning acoustic microscopy with focus on advanced simulations of ultrasonic sound propagation.

In this work, the two ultrasonic methods **scanning acoustic microscopy (SAM)** and **laser induced ultrasound (LUS)** are used in order to

(1) determine **sound wave propagation related properties** of bulk materials and thin films relevant for application in MtM devices, and
(2) **detect and analyse failure modes** in micro-electronic relevant components for MtM technologies.

With respect to (1) and (2), the potential of **LUS** and **SAM** for at- line or inline inspection - enhancing the possibility of **rapid learning** for **MtM technologies** - are considered. Furthermore, the SAM evaluations are supported by **simulation of sound propagation**. It is stressed that the obtained results are also of relevance for *e.g.* automotive industries or biological applications.

The introduction is structured as follows: The preamble defines "More Than Moore" technologies, summarising the challenges in their realization and emphasizes the need for advanced material and failure characterization in this context. After a short paragraph about ultrasound, short historical overviews of ultrasound, LUS and SAM are given, followed by the state of the art concerning LUS and SAM. Finally, the research goals of this thesis are discussed in detail and the contents of this work are outlined.

1 PREAMBLE

1.1 MORE THAN MOORE TECHNOLOGIES

Moore's law [101] is phrased in [151] as: "The number of transistors on a microprocessor chip will double every two years or so – which has generally meant that the chip's performance will, too" (Waldrop, 2016, p.1). The semi-conductor industry released a road map for manufacturers and suppliers in order to stay in step with Moore's law – More Moore strategy [151]. More than More (MtM) technologies refer to silicon based or silicon derived technologies that do not simply scale with Moore's law. [166] From the application side of view, MtM will enable functions similar to human senses of seeing, hearing, smelling, touching and mobility all integrated in one system [166]. MtM technolgies successfully emerged in the middle of the previous decade [6]. In addition, researchers have targeted the 3rd dimension to continue the trend of increased integration density and functionality [118]. Accoring to [167], the realization of MtM technologies results in:

- **increased complexity**,
- **decreased design margins**,
- **increased chances and consequences of failures**,
- **decreased product development time**,
- **decreased qualification times**,
- **increased gap between technology advance and development of fundamental knowledge** and
- **increased difficulties to meet quality, robustness and reliability requirements**.

Consequently, the need for advanced material and failure characterization with potential for at-line or in-line analysis at wafer level is steadily increasing while MtM technologies are developed.

1.2 ULTRASOUND

The term „ultrasound" refers to vibratory waves in gases, liquids and solids at frequencies above the average human hearing range [24]. For a young, healthy human adult the hearing range extends from ~ 20Hz to ~ 20kHz, see *e.g.* [139].
According to [24], the field of ultrasonics concerns (1) the basic science of energy-matter interaction, (2) the technology necessary for the generation and detection of ultrasound and (3) an increasingly range of applications, important in almost every field of engineering, in many fields of science and in medicine [24]. Unsurprisingly, more than 200 000

entries of ultrasonics literature can be found [24].

An important differentiation must be made between high and low intensity ultrasound. High intensity ultrasound - on the one hand - is used in order to produce an effect on a medium, *e.g.* in medical therapy. Low intensity ultrasound - on the other hand - is applied with the intention to transmit energy through a medium without causing any change in the medium [24].

This thesis deals with ultrasonic methods for material and failure characterization; therefore only low intensity ultrasound is considered in this work.

1.2.1 *Short History of Ultrasound*

An overview about the historical aspects concerning ultrasound can be found in *e.g.* [32] or [24]. The scientific interest in acoustics dates presumably back to Pythagoras (sixth century B.C.) and Aristotle (fourth century B.C) [32]. In 1638, Galileo published the observation that pitch is associated with vibration [24]. Boyle demonstrated in 1662, that sound needs a material medium to propagate [24]. In 1681, Hooke (known for Hooke's law) proposed a toothed wheel as first ultrasonic generator [32]. According to [24], a variety of well known scientists contributed to the field of acoustics - including Saveur, Taylor, Newton, d'Alembert, Lagrange and Fourier - in the 17th and 18th century. In the 19th century, the speed of sound in water was successfully determined by Colladen and Sturm at Lake Geneva [32] and the Savant Wheel (used to achieve frequencies up to 24kHz) and the Galton Whistle (to test the audible limits in men and animals) were presented [32]. In 1877, Lord Rayleigh published **„The theory of sound"** [83], a milestone in the development of the science of acoustics [24]. The Curie brothers discovered piezoelectricity in 1880 [20]. Also in 1880, Bell reported **„On the production and reproduction of sound by light"** [11], nowadays referred to as „the photoacoustic effect".

It is generally recognized, that ultrasonics was "born" in 1917, with the invention of the sonar for submarine detection [32], for this reason, Langevin is sometimes referred to as "father of ultrasonics" [143]. According to [32], Sokolov proposed the use of ultrasound for flaw detection, he also proposed an acoustic microscope in 1935 [140]. The first **scanning acoustic microscope (SAM)** was developed in 1974 by Lemons and Quate [78]. In the 1970s and 1980s, lasers have been considered as non-contact alternative to piezoelectric transducers in the generation and detection of ultrasonic waves, often refered to as **laser ultrasound (LUS)** [135].

1.3 LASER INDUCED ULTRASOUND: FROM HISTORICAL OVERVIEW TO CURRENT WORK

In the following, a short overview of previous published research in the field of material characterization via LUS is given.

1.3.1 *LUS - Brief historical overview*

Since 1880, when Bell published „On the production and reproduction of sound by light“ [11] - where the principle of light induced sound waves is introduced – many researchers contributed to todays standard of laser ultrasonic techniques [135]. In the following, some exemplary, important works are summarised.
Already in 1885, surface acoustic waves (SAWs) were discovered by Lord Rayleigh [83]. Nearly a century later, according to [135], in the 1960s and 1970s, pioneering work concerning the LUS techniques was published, *e.g.* [76, 88] and more systematic studies were carried out in the late 1970s and 1980s, *e.g.* [54]. In 1990, Scruby and Drain authored a book on laser ultrasonics [135] and in 1992 Neubrand and Hess reported on „Laser generation and detection of surface acoustic waves: elastic properties of surface layers“ [103]. The thickness and sound velocity measurement in thin transparent films by picosecond acoustics were performed by Wright in 1992 [158] and in 1993 Davis et al. published „Laser-generated ultrasound: its properties, mechanisms and multifarious applications“ [21]. The heating of multi-layer metals by femtosecond lasers was considered in [114], followed by a variety of literature entries by Schneider et al. [128],[129],[130],[131]. Metallic multilayers were studied via picosecond ultrasound in [107].

In recent years, the laser ultrasonic material characterization has further thrived, and a variety of substrates, thin film on substrate systems and free standing films, down to the nm regime have been characterized by LUS.

1.3.2 *LUS - State of the art*

The mechanical characterization of ultra-thin films of 5–30nm thickness was tested in 2000 by Schneider et al. [132]. The investigation of nonlinear mixing of SAWs was described in [52], where a decrease in sensitivity to background non linearity and increase in spatial sensitivity to acoustic non linearity induced by material micro structure was studied. The anisotropic elastic properties of a thin film were determined in [51]. The probing of carrier diffusion in gallium arsenide via picosecond pulses was described in [159]. A review about the use of SAWs in material science was given by Hess in 2002 [47]. Brillouin Scattering, laser-generated SAWs and acoustic microscopy were conisdered in [25]. How these methods obtain elastic properties and other information such as film thickness and density and examples for applications were given in [25]. In [29], a laser ultrasonic system was presented for the real-time cure monitoring of a graphite-epoxy composite. Narrow band ultrasonic waves (laser-generated) were used in order to characterize free standing thin films with nm thickness by Hernandez, Murray and Krishnaswamy [46]. In 2004, Monchalin published “Laser-ultrasonics: from the laboratory to industry” [100]. Real-time metallurgical transformations were monitored via LUS in [71], the technique is appropriate for online industrial material characterization [71]. [150] reported on the „determination of material properties using guided waves“ and [136] described „numerical simulation of laser-generated ultrasonic waves in layered plates.“ In [166], laser induced SAWs and line-focus acoustic microscopy were used in order to characterize Cr- and W-doped dimamond-like carbon coatings. The results were compared to nanoindentation, where good agreement was found. In [53], the SAW propagation across the boundary between two single crystals was analysed. In 2007,

[84] studied the attenuation of lamb waves for purposes of material characterization and condition monitoring. In [89], the excitation and detection of high-frequency SAWs and longitudinal waves enabled the determination of Young's modulus and Poisson's ratio for a film with submicron thickness. Asphaltic concrete was analysed via SAWs in the frequency range from $40 - 100\mathrm{MHz}$. The phase velocity and the amplitude attenuation were measured and their sensitivity to local compositional structural variations was considered in [55]. In [79], sub-picosecond laser pulses were focused onto a nano-patterned thin film sample, generating SAWs and longitudinal waves. This technique can be extended in order to determine the Young's modulus and the Poisson ratio of films showing sub-10nm thickness [79]. [93] reported on „High-frequency guided ultrasonic waves for hidden defect detection in multi-layered aircraft structures". In [61] the density and the elastic constants of a SiO_2 film were determined by a laser ultrasonic method. Also in 2015, Matsuda et al. published „an introduction to picosecond laser ultrasonics" [94].

In conclusion, the recent laser ultrasonic research considered mainly:

- the characterization of (anisotropic) elastic constants, densities and thicknesses of thin films, down to the nm regime,
- the applicability of the LUS method in industry and
- numerical simulation of sound wave propagation in layered samples.

In contrast, the following points were not in focus of state of the art LUS research:

- the analysis of the error caused by the fitting routine in order to give a confidence interval for *e.g.* the obtained elastic constants,
- the comparison of *e.g.* the elastic constants obtained from density functional theory calculations to the results achieved by the LUS method,
- test the possibility to step-wise characterize multiple layers by a numerically solvable model,
- try to distinguish different deposition procedures via laser induced SAWs and
- test the sensitivity of SAWs on the light dosage a sample has been exposed to.

1.4 SCANNING ACOUSTIC MICROSCOPY: FROM HISTORICAL OVERVIEW TO CURRENT WORK

1.4.1 *SAM - Brief historical overview*

After Sokolov proposed flaw detection via ultrasound and an acoustic microscope in the early 1930s [140], Lemons and Quate developed a SAM with $10\mu\mathrm{m}$ resolution in 1974 [78]. In the 1970s, numbers of articles concerning SAM have been published. In 1978, Atalar proposed an angular-spectrum approach for the material signature obtained by SAM measurements, also called $V(z)$ curves, (see also Section 10.1) [7]. Johnston et al. used the SAM to resolve small objects separated by 0.5 – 0.7 µm in the context of sub-cellular

imaging [57]. A review on SAM was given by Quates et al. in 1979 [116]. In the 1980s, extensive scientific literature in the context of SAM was published, possibly due to the fact that since then acoustic microscopes were produced by companies in Germany, Japan, France and in the USA. In 1981, Sheppard and Wilson considered „Effects of high angles of convergence on $V(z)$ in the scanning acoustic microscope“ [137]. Living cells were observed by SAM in vitro in 1981 [48]. In 1983, a review about SAM, especially about the $V(z)$ response, was published by Wickramasinghe [156]. In 1984, the characterization of bulk materials and thin layers via SAM is described in [157] and the characterization of living cells via SAM was performed by Issouckis [56] in 1985. The penetration depth a SAM can achieve was analysed by Atalar in 1985 [8]. A further review about the many applications of SAM was given by Hoppe and Bereiter-Hahn in 1985 [50]. In 1991, the elastic properties of cells were measured by $V(z)$ curves, evaluated using the simplex algorithm [72]. Yu proposed the inversion of $V(z)$ data in order to determine material properties of layered samples [163]. The properties of cancer tissues – gastritic cancer – were obtained via SAM in [125]. In the publication by Khuri-Yakub, the SAM operating principle was explained and various applications were presented, including: integrated circuits, composite materials, metrology and biological applications [58]. In 1993, Lee considered $V(z)$ curves obtained with a line-focus lens on layered anisotropic materials [77]. The determination of elastic properties of individual living human cells via SAM was discussed in [16]. In 1994, Marrow et al. proposed the in-situ SAM characterization of crack bridging in fine-grained polycrystalline alumina [90]. The $V(z)$ curve properties obtained by the SAM analysis of a spherical micro-particle were analysed in [91]. In 1995, Hasegawa et al. published results concerning the measurement of elastic properties of osteoporotic bone [44]. The measurement of elastic constants of materials with high acoustic velocities via a line-focus transducer was discussed in [148].

1.4.2 *SAM - State of the art*

In 2001, Cook reported on the detection of surface-breaking cracks via SAWs [18]. Subsurface structure and bulk investigations were carried out for an aluminium casting via SAM in [86]. In 2003, Every and Deschamps published results on the surface wave velocities on an anisotropic solid when analysed via a point focus lens $V(z)$ measurement [26]. Also in 2003, a finite element model for the detection of near surface discontinuities via SAWs was proposed in [165]. The mechanical properties of glass-ionomer cement was studied in [22] via SAM. In [60], the calibration-free crack sizing of surface-breaking cracks was discussed by using anti-plane shear waves. In 2007, Schenkl et al. presented a multiphoton acoustic microscope for the in-vivo observation of living cells, where GHz ultrasound was generated [127]. In [92], the sizing of surface cracks was discussed and in [81], the sizing of partially closed cracks – also surface-breaking – with SAWs was presented. Longo et. al discussed the sizing of surface-breaking cracks via SAWs that were detected by a laser doppler vibrometer [82]. Through the evaluation of tissue elasticity, structural characteristics of disease were observed in [97]. In 2013, Laugier et al. considered the „Quantitative Scanning Acoustic Microscopy of Bone“ [75]. It was found in [102], that the SAM can be used for the determination of the margin of squamous cell carcinoma. In 2014, the depth of surface cracks was evaluated by Her et. al [45]. Concerning metrology via SAM, the applicability of GHz scanning acoustic microscopy for some 3D integration technologies was considered in 2014, see [12]. SAM was also

established in order to disciminate cancer cells [98]. Aterial stiffness was measured by SAM in [2]. In 2017, Vien et. al presented the experimental and computational analysis of the scattering of SAWs at a crack on a racecourse shaped hole [149]. Recently, GHz SAM was applied to the characterization of bulk voids in Cu-Sn micro-connects, see [122].

On the one hand, the recent investigations carried out via SAM consider mainly:

- Material characterization using $V(z)$ curves, ranging from layered samples to cells.
- Biological or medical evaluations via SAM, including images of bone, tissue and cells.
- Failure analysis, predominantly in the microelectronics field, where the SAM GHz regime is targeted in particular.
- Detection and characterization - mostly sizing - of surface-breaking cracks in bulk samples, often in combination with simulations.

On the other hand, the following points received relatively little attention in state of the art SAM research:

- The difficulties in the standard SAM analysis of printed circuit boards (PCBs).
- The possibility to detect cracks below the lateral and axial resolution limit of SAM in MtM relevant components:
  - it is known that surface-breaking cracks with openings smaller than the resolution limit can be detected via SAM exploiting interference effects;
  - test this principle for cracks that do not break the sample surface and are not in bulk material but in MtM relevant components;
  - these cracks might lie perpendicular or parallel to the sample surface;
  - test the possibility to detect cracks in combination with other failure modes, *e.g.* delamination.
- The simulation of the SAM analyses for
  - physical insight into mechanisms which may allow for the detection of defects below the resolution limits;
  - the production of a simulated A-scan (see Chapter 10) equivalent and compare it to measurements;
  - the SAM $V(z)$ measurement and comparison to SAM and LUS results;
  - the consideration of *e.g.* changing geometries, elastic properties, etc.

2 RESEARCH GOALS

As already stated, the two ultrasonic methods **SAM** and **LUS** are used in this work in order to

(1) determine **sound wave propagation related properties** of bulk materials in addition to metal based and polymer thin films relevant for application in MtM microelectronics, and

(2) **detect and analyse various failure modes** in micro-electronic relevant components for MtM technologies.

In this work, the LUS measurements and evaluations are exclusively applied to material characterization. Failure detection and characterization via LUS are not considered, although the LUS method is also fit for these tasks in principle. In contrast, the SAM method is mainly used for the detection and analysis of various failure modes in MtM relevant components. In addition, the $V(z)$ SAM measurement is performed for the case of an aluminium bulk sample and an aluminium coating. In this case, the SAM outcome is compared to the LUS evaluations. The SAM results are supported by acoustic sound propagation simulations.

2.1 RESEARCH GOALS - MATERIAL CHARACTERIZATION

Metal-based thin films are used in electronic devices as conducting lines and interconnects, as barrier layers and as metallization layers. Due to their widespread use in different areas of microelectronics, knowledge about the elastic properties of metal based thin films is crucial in order to develop advanced understanding of the mechanics concerning microelectronics. However, many state of the art methods for the determination of mechanical properties are destructive or require the direct loading of the sample (*e.g.* nanoindentation). Ultrasonic methods provide the possibility for non-destructive or even non-contact measurements, showing high potential for rapid at-line or in-line inspection. In this work the following goals were considered:

- The characterization of thin film systems on Si-substrate suitable for MtM technologies is carried out (*e.g.* aluminium, copper, tungsten and alloys, polyimid thin films);
- the error in the obtained elastic constants caused by the fitting routine is evaluated, *e.g.* via a statistical approach;
- the obtained results are compared to nanoindentation results and to density functional theory calculations;

- the thin film characterization is tested in the characterization of multiple layers on a substrate;
- for the multiple-layer characterization, the theoretical model, *e.g.* Tiersten [145] is extended, according to Rose [121] and the fitting routine is adapted accordingly;
- the possibility to distinguish differently deposited tungsten thin films is tested via the LUS method;
- the sensitivity of SAWs on the light dosage polyimid samples were exposed to (before the LUS measurements) is tested.

2.2 RESEARCH GOALS - FAILURE CHARACTERIZATION

Moreover, the failure detection and failure analysis of micro-electronic relevant components for MtM technologies is carried out. The reliable, fast and cost efficient detection and analysis of failure modes in microelectronic components is of the same relevance as material characterization of thin films. Also in this case, ultrasonic methods show highly beneficial properties: they provide insight into opaque media, are non-destructive and they allow for defect detection down to the micron regime [122]. Here,

- the SAM analysis of delamination in printed circuit boards is carried out, the difficulties are discussed,
- the possibility to detect surface and subsurface cracks with openings below the lateral and axial resolution limit of SAM are analysed in MtM relevant components for micro-electronic devices in combination with simulation,
- the $V(z)$ measurements of bulk materials and thin film systems are tested and compared to laser ultrasonic evaluation,
- the SAM analyses are supported by acoustic simulations in order to:
  - give insight into mechanisms which might hinder or amplify the SAM potential,
  - visualize the ultrasound propagation,
  - produce a simulated A-scan (see Chapter 10) equivalent,
  - consider influences of changing geometries, elastic properties, etc.
  - give insight into the physical mechanisms allowing for the detection of cracks below the axial and lateral resolution limit of SAM.

With respect to (1) and (2), the LUS and SAM techniques are highly relevant for at-line or in-line inspection, enhancing the possibilities of rapid learning for MtM technologies.

2.3 CONTENTS OF THIS THESIS

In the following, the two major parts of this thesis are presented. Part ii deals with the LUS method and the corresponding results, whereas a summary of the work concerning the SAM method is given in Part iii.

2.3.1 *LUS characterization of thin film systems*

In Chapter 3, the LUS fundamentals are summarised and Chapter 4 gives an overview of the LUS measurement and data analysis. Subsequently, the results obtained with the LUS measurements and evaluations are presented. The LUS characterization of a single layer on silicon substrate is considered in Chapter 5, the determination of elastic properties of a polyimid coating on a layered system is presented in Chapter 6, where also the sensitivity of SAWs to the light exposure of polyimid samples is discussed. In Chapter 7, multi-layered metal films are characterized via the LUS method and in Chapter 8 an AlCu alloy coating is analysed via the LUS technique, where the confidence intervals for the obtained results are given and the outcome is compared to density functional theory calculations and nanoindentation results. The work presented in Chapter 8 is planned to be published in the near future [65]. In Chapter 9, the possibility to distinguish between differently deposited metallic layers is discussed. Part ii deals with the work published in [33, 36, 38] and the paper in preparation [65].

2.3.2 *SAM failure and material characterization*

The SAM results are presented in Part iii. First, the SAM principle is introduced in Chapter 10. Then the results concerning the delamination detection in multi-layered PCBs are discussed in Chapter 11. The SAM analysis of defects in TSVs, focusing on automatized failure detection, is carried out in Chapter 12. Chapter 13 considers the detection of sub-resolution defects in TSVs via SAM measurement and simulation. In Chapter 14, the $V(z)$ SAM measurement of aluminium samples is presented, the outcome is corroborated via LUS measurements. Part iii considers the already published work [34, 35, 37, 39] and the publications in preparation [64, 66].

In addition, Part iv concludes the presented work and an outlook is given. Part v provides a collection of the publications written in the context of this thesis.

Part II

LASER INDUCED ULTRASOUND

The following part deals with the characterization of elastic properties of thin films and thin film systems on silicon substrates via LUS. The fundamentals of LUS are summarised in Chapter 3, the setup is shown in Section 4.1 and the LUS measurement as well as the data evaluation are presented in Section 4.2.2. In Chapter 5, the analysis of a single tungsten layer on a silicon substrate is carried out, summarising the results published in [36]. Chapter 6 considers a polyimide layer on a silicon substrate, where an 800nm intermediate layer is present, rendering the system a two-layer on substrate stack. The polyimide layer was characterized and the results are shown in [38]. In addition, the influence of exposing the polyimide to different light dosages on the SAW propagation is discussed in Chapter 6. In Chapter 7 metallic multi-layered systems are considered, where first tests of the LUS evaluation of a Si-Cu-Al-Cu are presented [33]. Additional material concerning multi-layered thin films on Si substrates is shown in Chapter 7, where good agreement between measurement and theory was found. Chapter 8 discusses the LUS characterization of an aluminium alloy thin film on a silicon substrate compared to two other state of the art methods. Here, a confidence interval for the LUS results is given. Chapter 9 discusses the sensitivity of LUS signals on the deposition procedure in tungsten stack manufacturing.

3

LASER INDUCED ULTRASOUND (LUS) FUNDAMENTALS

3.1 LASER INDUCED ULTRASOUND PRINCIPLE

Nearly 100 years after Bell's observation in 1880 [11], that one can use light to generate sound waves - or transduce absorbed electromagnetic energy into mechanical energy in a material - White demonstrated the generation of acoustic pulses by laser irradiation in 1963 [155].
According to [70], the laser generation of ultrasonic waves is achieved in the following way: The light of a pulsed laser (or an intensity modulated continuous wave (cw) laser) is partially absorbed by a small volume in the material, which causes a rapid local temperature rise and thermal expansion, generating sound waves in the medium that can be subsequently detected via *e.g.* a second cw laser or a piezoelectric element, see the schematic in Figure 1, (l.h.s.). In a solid, a number of ultrasonic wave modes can be gen-

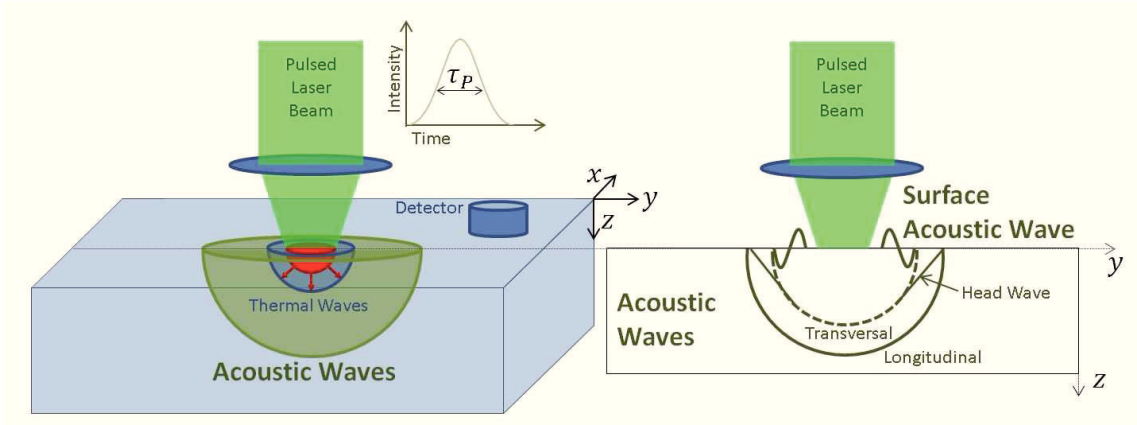

Figure 1: Schematic of laser induced ultrasound principle. Excitation of thermal and sound waves via a pulsed laser in a material (l.h.s.) and a schematic of the acoustical waves excited in the material by the pulsed laser irradiation (r.h.s.).

erated after the laser impinges the material: longitudinal, transverse, surface acoustic (Rayleigh) and head waves, see the schematic in Figure 1, (r.h.s.). The longitudinal wave has the highest sound velocity, typically it is twice as fast as the transverse or shear wave. The Rayleigh waves propagate at about 90% of the shear wave velocity. The head wave is a longitudinal mode consisting of traction and compression and propagates between the shear and the longitudinal wave [5], [17]. Although Rayleigh waves are not the only waves which can propagate on the surface of a sample [15], the terms Rayleigh waves and SAWs are synonymously used in this work.
A distinction can be made concerning two generation mechanisms for ultrasonic waves via laser illumination of a material, see *e.g.* [70], [162] or [4]. If the laser power density is high enough (typical power densities of $> 10^7 W\,cm^{-2}$ for a metal in the near infrared/visible wavelength region) [162], partial ablation of the illuminated target surface and ionization of the ablative material takes place. In this case, the laser induces a

plasma which expands away from the surface with very high pressures. The amplitudes of Rayleigh and compressional waves are increased. Due to the destructive nature of sound excitation in the ablative regime, the generation of acoustic waves via low power densities ($< 10^7 W cm^{-2}$ for a metal in the near infrared/visible wavelength region) [162] is used in non-destructive material characterization. Here, the laser source causes heating and the generation of thermal waves (via heat conduction) and ultrasonic waves (elastic waves), see Figure 1, (l.h.s.). According to [70], the generation of ultrasonic waves in the thermoelastic regime shows the following advantages:

- it is a non-contact method,
- it is non-destructive because no material is ablated,
- it can be used for in situ setups,
- in contrast to *e.g.* SAM, a coupling liquid is not necessary,
- it can be operated on curved surfaces and
- frequency ranges from kHz to GHz are possible.

3.2 SAW GENERATION BY LINE FOCUSED LASER PULSES

According to [162] or [135], the characteristics of laser induced ultrasonic waves in a material depend on the properties of the laser and the material itself. Material related properties are: the optical penetration, the thermal diffusion, the elastic properties and the geometry of the material. Concerning the laser, the pulse width, the shape of the pulse and the focus spot or focus line represent the determining features. Figure 2 shows a schematic of the excitation of a Rayleigh wave on a layered sample via a line-focused laser pulse. The excitation via line-focused laser beams has the advantages of improved signal to noise ratio and almost plane wavefronts (parallel to the line source) [4].

In the following, the line focus excitation of ultrasonic waves in a linear elastic, isotropic material is considered from a theoretical point of view and [4, 162] are reproduced in the three steps (I-III): (I), all important parameters are summarised in Table 1.

(II), the time-dependent hyperbolic thermal diffusion equation represents one of the coupled equations of thermoelasticity. For the temperature T it is given by

$$\nabla^2 T - \frac{1}{\kappa}\frac{\partial T}{\partial t} - \frac{1}{c_l^2}\frac{\partial^2 T}{\partial t^2} = -q/k, \tag{1}$$

where q denotes the heat source due to the laser illumination. In the case of a line-focus excitation q can be considered as

$$q = E(1-R)\frac{e^{-z/\gamma}}{\gamma} f(x)g(t). \tag{2}$$

Here, E is the energy of the laser beam per unit length, γ is the penetration depth, $f(x)$ and $g(t)$ denote the spatial and temporal distributions of the laser pulse (see Figure 2) respectively:

$$f(x) = \frac{1}{\sqrt{(2\pi)}}\frac{2}{\omega} e^{-2x^2/\omega^2}, \tag{3}$$

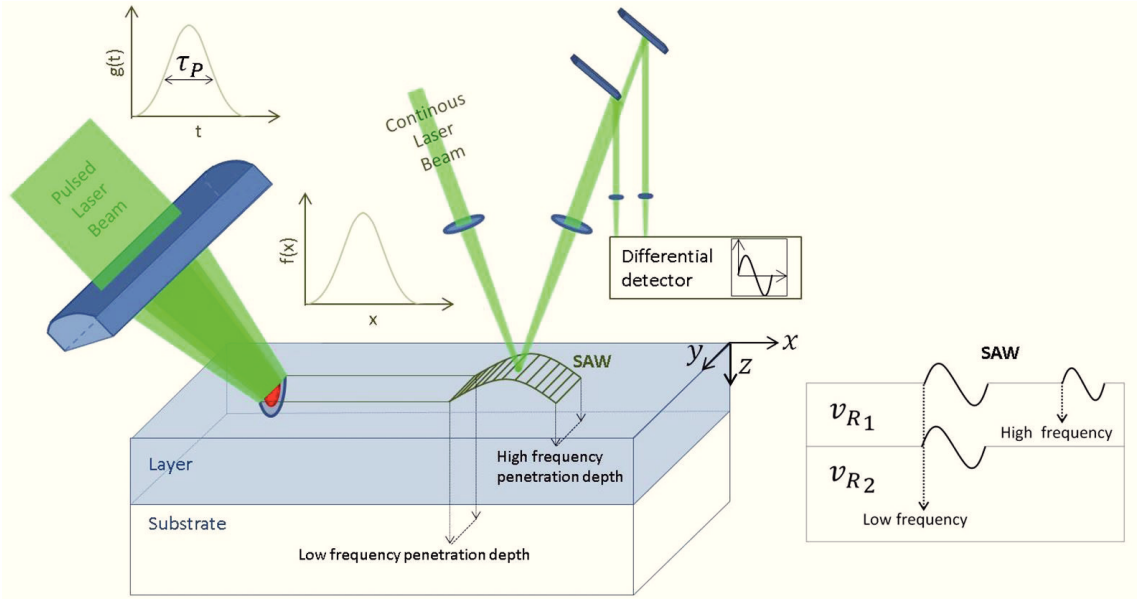

Figure 2: Line focus excitation of broadband surface acoustic waves (SAW) on a layered material via pulsed laser illumination; the SAW is detected via a beam deflection method and the spatial and temporal distributions are sketched (l.h.s.). The higher frequency components of the SAW propagate mainly in the thin film due to their lower penetration depth, whereas the low frequency components travel mainly in the substrate, as depicted on the r.h.s according to [132]. Here, the case of higher layer SAW velocity $v_{R1} > v_{R2}$ is shown.

$$g(t) = \frac{8t^3}{\nu^4} e^{-2t^2/\nu^2}, \tag{4}$$

where ω and ν denote the Gaussian width and the pulse duration of the laser beam.

(III), the second coupled equation of thermoelasticity is given by:

$$\mu\nabla^2\mathbf{u} + (\lambda+\mu)\nabla(\nabla\cdot\mathbf{u}) = \rho\frac{\partial^2\mathbf{u}}{\partial t^2} + \beta\nabla T, \tag{5}$$

where $\mathbf{u}$ denotes the displacement vector. The displacement vector $\mathbf{u}$ can be expressed in terms of the dilatational potential ϕ and the rotational potential ψ

$$\mathbf{u} = \nabla\phi + \nabla\times\psi. \tag{6}$$

The displacement potentials ϕ and ψ fulfill the following wave equations:

$$\nabla^2\phi - \frac{1}{c_1^2}\frac{\partial^2\phi}{\partial t^2} = \frac{\beta}{c_1^2\rho}T, \tag{7}$$

$$\nabla^2\psi - \frac{1}{c_2^2}\frac{\partial^2\psi}{\partial t^2} = 0. \tag{8}$$

SYMBOL	PARAMETER	DESCRIBING/DEPENDS ON
c_1	longitudinal sound velocity	material
c_2	transverse sound velocity	material
ρ	mass density	material
α	linear expansion coefficient	material
κ	thermal diffusivity	material
k	thermal conductivity	material
μ	shear elastic modulus	material
λ	Lamé elastic modulus	material
ν	Poisson ratio	material
β	thermal coupling constant	material
c_P	heat capacity	material
R	reflectivity	material and wavelength
γ	penetration depth	material and wavelength
ω	with of spacial distribution of laser beam	laser beam
ν	width of temporal distribution of laser beam	laser beam
E	energy of laser pulse per unit length	laser beam
Q	laser intensity (power per illuminated area)	laser & focus spot

Table 1: Relevant parameters for laser induced ultrasound in a material.

Here, c_1 and c_2 denote the longitudinal and transverse sound velocities in the material. The stresses σ are related to the displacements by

$$\sigma = \lambda \nabla \cdot \mathbb{1} + \mu(\nabla \mathbf{u} + \mathbf{u}\nabla) - \beta \mathbb{1} \nabla T. \tag{9}$$

Utilizing Equation 1 - Equation 9, the displacements and tractions generated by a line-focus irradiating of a material by a laser beam can be obtained. However, the numerical determination of laser induced ultrasonic waves was not the focus of this work. The solutions can be found in [162] or [4].

In [103] it was stated, that the amplitude of the Rayleigh wave is proportional to the laser intensity Q and the thermal-expansion coefficient α and inversely proportional to the heat capacity c_P per unit volume.

For the experiment, important quantities are the laser intensities Q applied to the sample, the pressure distribution P generated in the material and the local heating ΔT of the sample surface. Concerning the power densities, it has already been mentioned, that the thermoelastic excitations of ultrasonic waves in most metals are achieved by power densities smaller than $10^7 W cm^{-2}$ [162]. The pressure distribution P caused by the laser illumination is given by the thermal stresses $\sigma_{ij}^{thermal}$ and the mechanical stresses σ_{ij}^{mech} generated in the material [111]. $\sigma_{ij}^{thermal}$ and σ_{ij}^{mech} can be found by

the extension of Hooke's law (see also Appendix A), to the so-called Duhamel-Neumann relations for the anisotropic body [104]. They read:

$$\sigma_{ij} = C_{ijkl}\epsilon_{kl} - \beta_{ij}\Delta T. \tag{10}$$

where C_{ijkl} denotes the elastic stiffness tensor, ϵ_{kl} is the strain tensor, $\beta_{ij} = \xi\delta_{ij}$ and $\xi = (3\lambda + 2\mu)\alpha_t$, consisting of the material constants λ and μ (Lamé constants) and the linear thermal expansion coefficient α_t. If the illuminated area A is large in comparison to the optical penetration depth γ and the film thickness d, only the pressure distribution in z-direction, $p(z)$ must be taken into account [111]. In the work presented here, A is typically in the range of $150000\mu m^2$, d is in the order of $1 - 10\mu m$ and the penetration depth γ in the analysed metals (W, Al, Cu) is in the order of $10 - 20nm$ for the applied laser wavelength. Furthermore, in the case of an isotropic material, Equation 10 becomes

$$\sigma_{ij} = 2\mu\epsilon_{ij} + (\lambda\epsilon_{kk} - \xi\Delta T)\delta_{ij}. \tag{11}$$

In this case (isotropic material and pressure distribution only in z-direction), σ_{33} corresponds to the pressure distribution caused by the laser irradiation and is given by

$$\sigma_{33} = (2\mu\epsilon_{33} + \lambda)\epsilon_{33} - (3\lambda + 2\mu)\alpha_t\Delta T. \tag{12}$$

Here, the first term on the r.h.s corresponds to σ_{ij}^{mech} and the second term represents $\sigma_{ij}^{thermal}$. σ_{ij}^{mech} depends on the Lamè constants λ and μ. In addition, $\sigma_{ij}^{thermal}$ depends on the linear thermal expansion coefficient α_t and the temperature rise in the material caused by the laser irradiation and ΔT. In some cases,

$$\tau_p << \tau_{ac} \tag{13}$$

is fulfilled. If Equation 13 holds, the laser pulse duration τ_p is smaller than the acoustic relaxation time τ_{ac}. τ_{ac} is given by the ratio of the minimal extension of the illuminated area (either the penetration depth or the lateral diameter of the illuminate area) and the sound velocity of the material. In this case, the small, heated volume cannot expand, leading to a pressure distribution caused only by $\sigma_{ij}^{thermal}$ (see also [105]). However, according to [104] a typical velocity in metals is $4000m/s$ and (as already mentioned) penetration depths γ can be smaller than $10nm$ for the applied excitation laser wavelength, requiring laser pulses in the picosecond regime that would fulfill Equation 13.

Concerning the temperature distribution in the sample, an estimation for metals can be made via the 1D heat equation [105]. From Figure 3 it can be seen, that the maximal temperature increase is around 180K. The analysed material is aluminium, where the mass density $\rho = 2700kg/m^3$, the specific heat capacity $c_P = 880J/(kgK)$ and the thermal conductivity $\kappa = 240W/(mK)$. The laser pulse energy E_P is 1mJ, the irradiated area $A = 0.15mm^2$, the pulse width is $10ns$. The sample does not heat up globally in this case.

The detection of SAWs in our setup was performed via a beam deflection method, see Figure 2, where the distance between excitation and detection of SAW was in the order of 10mm.

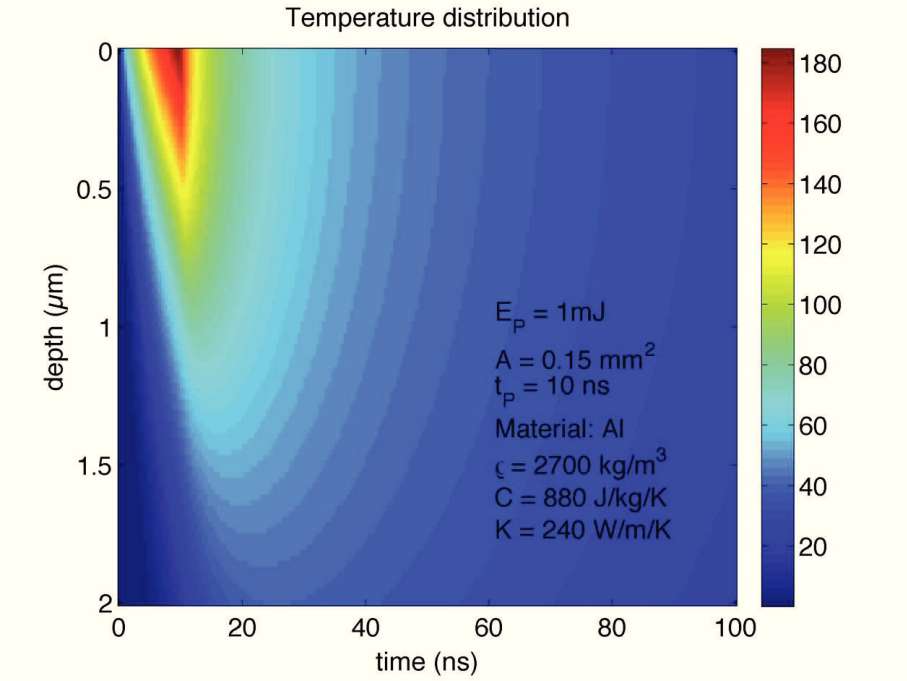

Figure 3: Temperature distribution caused by laser induced ultrasound generation. Theoretical analysis for an aluminium sample, where the pulse energy E_P is 1mJ, the irradiated area $A = 0.15mm^2$, the pulse width is 10ns, the mass density $\rho = 2700kg/m^3$, the specific heat capacity $c_P = 880J/(kgK)$ and the thermal conductivity $\kappa = 240W/(mK)$. The scale bar shows the temperature in K; courtesy of R. Nuster [105].

3.3 SURFACE ACOUSTIC WAVE (SAW) PROPAGATION ON LAYERED SAMPLES

As indicated in Figure 2, the lower frequency components of the broadband SAWs travel mainly in the substrate, whereas higher frequency components propagate in the thin film. If the film and the substrate differ in their sound velocities, the propagation of the SAW becomes dispersive, i.e. the phase velocity of the sound wave depends on frequency, see *e.g.* [103, 129, 145]. Assuming a linear elastic and isotropic material behaviour, the frequency dependent Rayleigh wave velocity $v_R(f)$ can be calculated via a theoretical model, see [145] or [121]. Fitting the theory to the measurement of the dispersion curve $v_R(f)$, a number of material properties can be evaluated. In the following, the determination of material properties in this way is discussed. First, the measurement of $v_R(f)$ is discussed, then the theoretical model and the fitting routine are presented.

4 LUS MEASUREMENT AND DATA EVALUATION

4.1 LUS SETUP

The experimental setup for the LUS measurement was provided by **Robert Nuster** and **Günther Paltauf** at Karl-Franzens University of Graz, Department of Experimental Physics, Graz, Austria (KFU); a similar setup is described in [106].

A schematic of the LUS setup is shown in Figure 4. It is designed to switch between two DPSS (diode pumped solid state) pulsed excitation lasers, see Table 2. The first excitation laser has an approximate pulse width of 10ns, a wavelength of 532nm and a repetition rate of 10Hz. The spectrum of excited SAWs extends to approximately 100MHz in this case. The second excitation laser has also a wavelength of 532nm, but a pulse width of 2ns and was operated at a repetition rate of 20Hz. The shorter pulse length allows for the excitation of SAWs with frequencies up to 500MHz. The chosen excitation laser is focused on the sample surface using a cylindrical lens, see Figure 2. The laser energies are at $1-2$mJ and the focus line has extensions of about 20mm times 7.5µm. The line focus excitation causes plane SAWs to propagate on the sample. The SAWs are detected via an optical beam deflection method, where a continuous wave (CW) laser beam is focused to a point on the sample surface. The detection laser has a wavelength of 532nm. The reflected light from the detection point on the sample is divided into two equivalent parts by placing a sharp edged mirror in the beam path. The two equivalent reflected beams are detected by a balanced photodetector (BPD). SAWs propagating through the detection spot cause deflection and slightly alter the two beams at the balanced photodetector. Therefore, the division ratio of the back reflected light power at the two photodiodes of the BPD is proportional to the slope of the surface displacement caused by the SAWs.

4.2 LUS ANALYSIS: WORK FLOW

Robert Nuster and **Günther Paltauf** (Karl-Franzens University of Graz, Department of Experimental Physics, Graz, Austria) provided support concerning the data evaluation

PURPOSE	TYPE	λ[nm]	τ_P[ns]	REPETITION RATE [Hz]
Excitation 1	pulsed	532	10	10
Excitation 2	pulsed	532	2	20
Detection 2	continous wave	532	-	-

Table 2: Laser specifications, λ denotes the wavelength and τ_P denotes the pulse width.

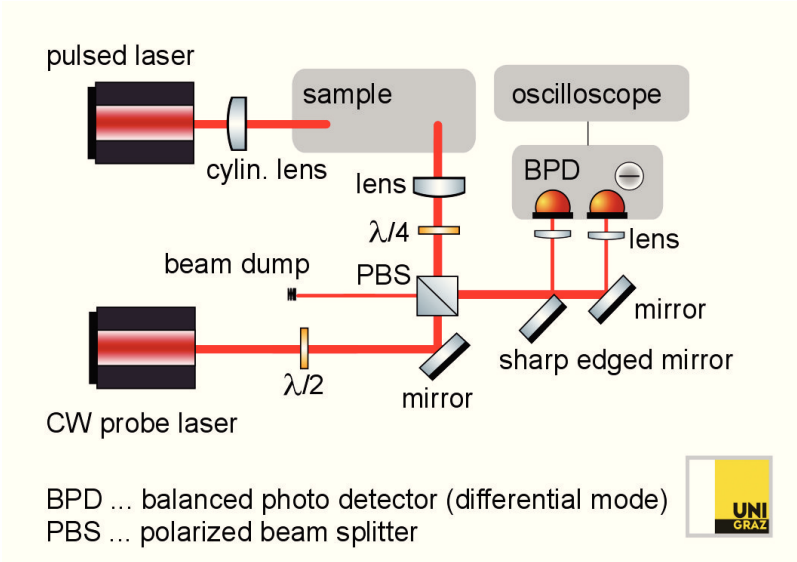

Figure 4: Schematic of LUS setup at KFU.

and interpretation.

In Figure 5, the typical evaluation steps of the LUS analysis are sketched. First, the SAWs are excited and detected and their frequency dependent phase velocity is determined as a second step. Third, the frequency dependent Rayleigh wave velocity is evaluated via a theoretical model. Fitting the theory to the measurement in step 4, parameters of the thin film can be determined. In the following, each step is discussed in detail.

4.2.1 *Measurement*

In step one, the SAWs propagating on the sample are detected at two positions (or excited at two positions and detected at the same spot on the sample). As an example, Figure 6 shows five measurements of laser induced SAWs, excited at five positions on the sample. The excitation position one is approximately 8mm distanced from exciting position five, where position five is closest to the detection point. Therefore, the SAW signal is still quite compact after traveling from the excitation point five to the detection point. In contrast, excitation point one is relatively far away from the detection spot. Here, the higher frequencies lag behind the lower frequencies to a greater extent. In this case, the substrate shows higher Rayleigh wave velocity than the layer.

4.2.2 *Data evaluation*

In step two, the frequency dependent Rayleigh wave velocity $v_R(f)$ is determined via [132]

$$v_R(f) = \frac{|dx|2\pi f}{[\Phi_2(f) - \Phi_1(f)]} \tag{14}$$

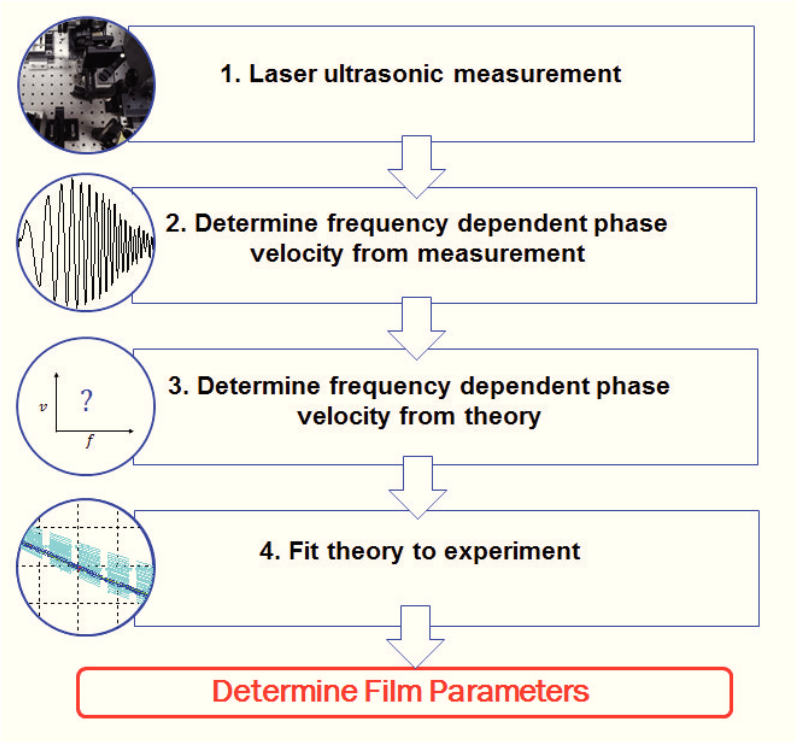

Figure 5: Flow chart showing the extraction of material parameters from LUS measurements and numerical evaluation.

where dx denotes the difference between two propagation paths. Φ_1 denotes the phase of the Fourier transformed first ultrasonic signal and Φ_2 denotes the phase of the Fourier transformed second signal. The error in the derived phase velocity Δv_R is given by [132]

$$\left|\frac{\Delta v_R}{v_R}\right| \leqslant \left|\frac{2\Delta x}{dx}\right| + \left|\frac{2\Delta t\omega}{(\Phi_2 - \Phi_1)}\right|. \tag{15}$$

Δx denotes the accuracy of the translation stage, Δt the sampling rate and ω the circular frequency. With $\Delta x = 10^{-5}\,m$, a sampling rate of $0.2\,ns$ and dx of about $10\,mm$, the error of our measurement is in the range of some m/s. Compared to the analysed sound velocities, this corresponds to a relative error of about 0.1% and error-bars are therefore not always depicted in our graphs.

4.2.3 *Theory of acoustic wave propagation in multi-layered isotropic systems*

In this section, the global matrix formalism and a partial wave ansatz [121] are used in order to determine $v_R(f)$ of SAWs on multi-layered systems. Here, isotropic and linear elastic material behaviour are assumed, see also Appendix A. For the nth layer, the particle displacements u_i and the stress-components σ_{ij} are given by [121]:

$$u_1^{(n)} = \sum_{m=4n-3}^{4n} B_m e^{ik(x_1 + \alpha_m x_3 - c_P t)}, \tag{16}$$

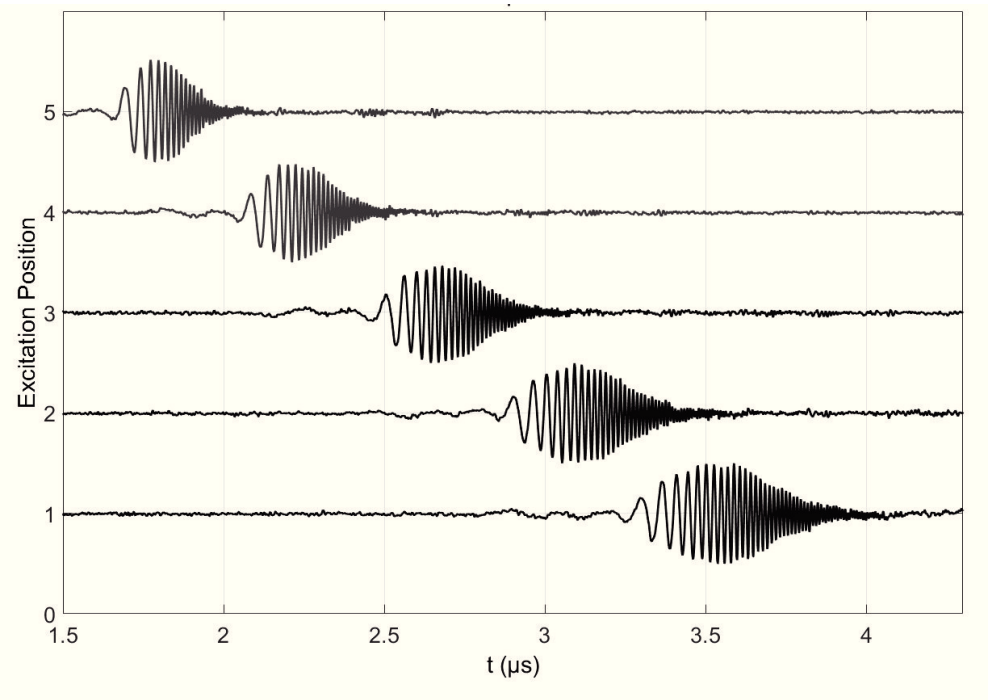

Figure 6: Laser induced surface acoustic waves, excited at five positions with an increment of 2mm.

$$u_3^{(n)} = \sum_{m=4n-3}^{4n} B_m U_{3m} e^{ik(x_1+\alpha_m x_3-c_P t)}, \tag{17}$$

$$\sigma_{33}^{(n)} = \sum_{m=4n-3}^{4n} B_m \left[\lambda^{(n)} + (\lambda^{(n)} + 2\mu^{(n)})\alpha_m U_{3m}\right] (ik) e^{ik(x_1+\alpha_m x_3-c_P t)}, \tag{18}$$

$$\sigma_{31}^{(n)} = \sum_{m=4n-3}^{4n} B_m \left[\alpha_m + U_{3m}\right] \mu^{(n)} (ik) e^{ik(x_1+\alpha_m x_3-c_P t)}. \tag{19}$$

Here, μ and λ denote the Lamé constants and k is the wave number, c_P the phase velocity. The wave vectors U_{in} and the polarizations α_n are eigenvectors and eigenvalues of the Christoffel equation, Equation 36 in Appendix A. The thickness of each layer is denoted $h^{(n)}$, the position of the top surface of each layer can be defined as $H^{(n)} = \sum_{m=1}^{n} h^{(m)}$, see Figure 7. The boundary conditions for the system are:

$$\sigma_{31}^{(1)} = 0 \quad @ \quad x_3 = 0, \tag{20}$$

$$\sigma_{33}^{(1)} = 0 \quad @ \quad x_3 = 0, \tag{21}$$

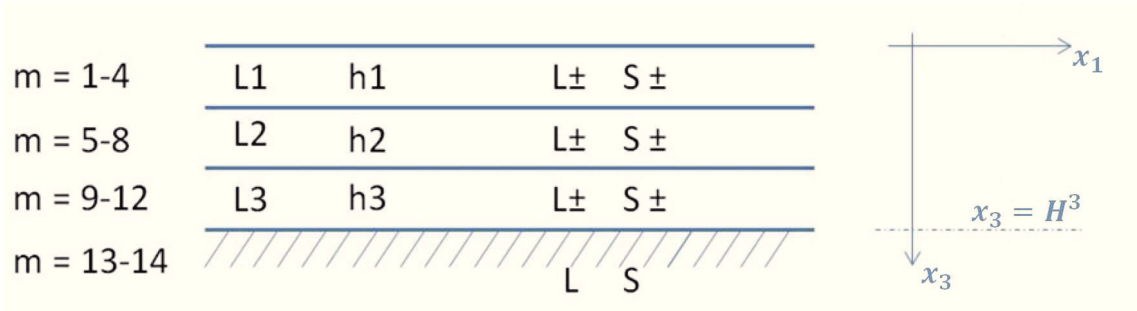

Figure 7: Schematic of three isotropic layers on an isotropic substrate. Longitudinal and transverse wavesare indicated by L and S, where + markes up-going waves and − downgoing waves.

$$u_{31}^{(n)} = u_{31}^{(n-1)} \quad @ \quad x_3 = H^{(n-1)}, \tag{22}$$

$$u_{33}^{(n)} = u_{33}^{(n-1)} \quad @ \quad x_3 = H^{(n-1)}, \tag{23}$$

$$\sigma_{31}^{(n)} = \sigma_{31}^{(n-1)} \quad @ \quad x_3 = H^{(n-1)}, \tag{24}$$

$$\sigma_{33}^{(n)} = \sigma_{33}^{(n-1)} \quad @ \quad x_3 = H^{(n-1)}, \tag{25}$$

yielding four boundary conditions for the four wave modes in the layers and two boundary conditions for the substrate. For 3 isotropic layers on an isotropic substrate, this gives a 14×14 boundary condition matrix $\mathbf{D}$. The frequency dependent phase velocities of the allowed wave modes are found by iterating combinations of k and c_P which give $\mathbf{DB} = 0$.

4.2.4 *Fitting routine*

A least square fitting routine [42, 133] is employed in order to determine the longitudinal and transverse sound velocitiy, v_L and v_T, of the analysed thin film. The theoretical model is evaluated for a variety of different combinations of transverse and longitudinal sound velocities (or equivalently Young's moduli and Poison ratios) and the deviation to the measured curve is evaluated. The combination of v_L and v_T which yields the minimal deviation from the measured curve, provides the film parameters. The density and thickness of the thin film have to be known for this procedure as well as the substrate

characteristics. In the case of an anisotropic substrate, the stiffness tensor of the material and the density have to be known, whereas in the case of an isotropic substrate the Lamé constants and the density are necessary input values. In the case of *e.g.* silicon substrate, isotropy can be assumed if the measurement is performed along a symmetry axis of the substrate, see [132].

5 SINGLE LAYER ON SUBSTRATE CHARACTERIZATION

As a first step towards the laser ultrasonic characterization of thin films and thin film systems, the characterization of a 695nm layer of tungsten on a silicon (100) substrate was carried out and the Young's modulus E and the Poisson ratio ν of the thin tungsten film were determined. The outcome of the analysis was compared to literature values, where agreement was found [33].

5.1 MOTIVATION

As already mentioned earlier, the accurate characterization of thin films plays an important role in many fields of science and industry. Especially in micro- and nanoelectronics, the need for thin films and coatings increases steadily due to ongoing miniaturization processes. In the ongoing efforts to reduce the size of devices, whilst the functionality and package density are steadily increased, tungsten is a material with many beneficial properties, *e.g.* high endurance to increasing current densities [110]. In 3D technologies, *e.g.* tungsten is used as coating material of through silicon vias (TSVs, see also Section 12.1) alternatively to copper fillings [69]. In the analysis of residual stresses in tungsten thin film systems, *e.g.* [63], reliable elastic input values for material simulations are crucial. Additionally, the anisotropic factor of tungsten is close to one [124], justifying the assumption of an isotropic layer made in the data evaluation of the LUS measurements.

5.2 MEASUREMENT AND DATA EVALUATION

5.2.1 *LUS measurement*

The experimental setup is shown in Section 4.1. However, for the analysis of the tungsten thin films, the LUS setup was at that time only equipped with one nanosecond laser system, namely the Nd:YAG laser with a wavelength of 532nm, a pulse length of 10ns and a repetition rate of 10Hz, yielding broad band SAWs on the sample surface with frequencies up to about 100MHz. The SAWs were detected via a beam deflection method according to Section 4.1. Figure 8 shows the two analysed SAW signals. Following Section 4.2.2, the frequency dependent phase velocity was determined via Equation 14 and the error in the measurement was determined according to Equation 15. The error in our measurement is smaller than 3m/s, corresponding to a relative error of about 0.1%.

5.2.2 *Data evaluation*

The analysis of the LUS data was carried out according to Chapter 4. A semi-infinite, linear elastic half space was assumed, see [146]. In Figure 9 a scanning electron microscopy (SEM, see *e.g.* [119]) image of the analysed layer-on substrate system is shown.

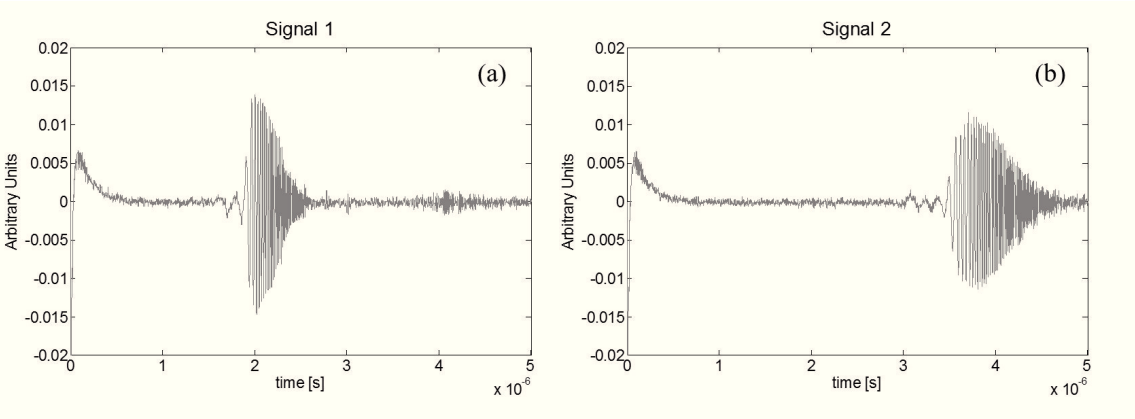

Figure 8: Laser induced SAWs, excited at two different positions on the sample. The two excitation points are distanced by 8mm.

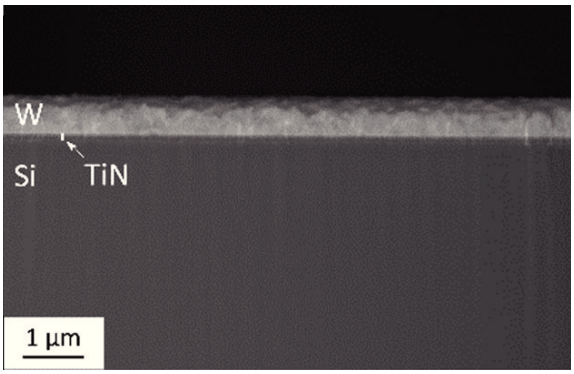

Figure 9: SEM image of the analysed sample: 695nm W on Si with a 20nm TiN adhesion layer.

On the Si substrate, a thin coating of TiN and a 695nm thick tungsten layer are visible. TiN shows good adhesion to tungsten and therefore improves the contact stability and the reliability of the thin film system [154]. However, the thin TiN film of only few nm thickness was neglected in our data evaluation because it did not change the dispersion relation to a measurable extent. For the data evaluation, the longitudinal sound velocity v_L^S and the transverse sound velocity v_T^S of Si, 8432m/s and 5843m/s respectively, were taken as input parameters as well as the density of the substrate ρ^S and the density of the tungsten layer ρ [124], (see Table 3). The thickness of the tungsten layer had to be measured as an input value. This was achieved by using ImageJ [117] evaluation software for the SEM images. The fitted theoretical curve and the experimentally evaluted dispersion relation are shown in Figure 10.

5.2.3 *Results*

The results of our analysis are summarised in Table 4. The obtained values for the Young's modulus and the Poisson ratio agree with the literture values.

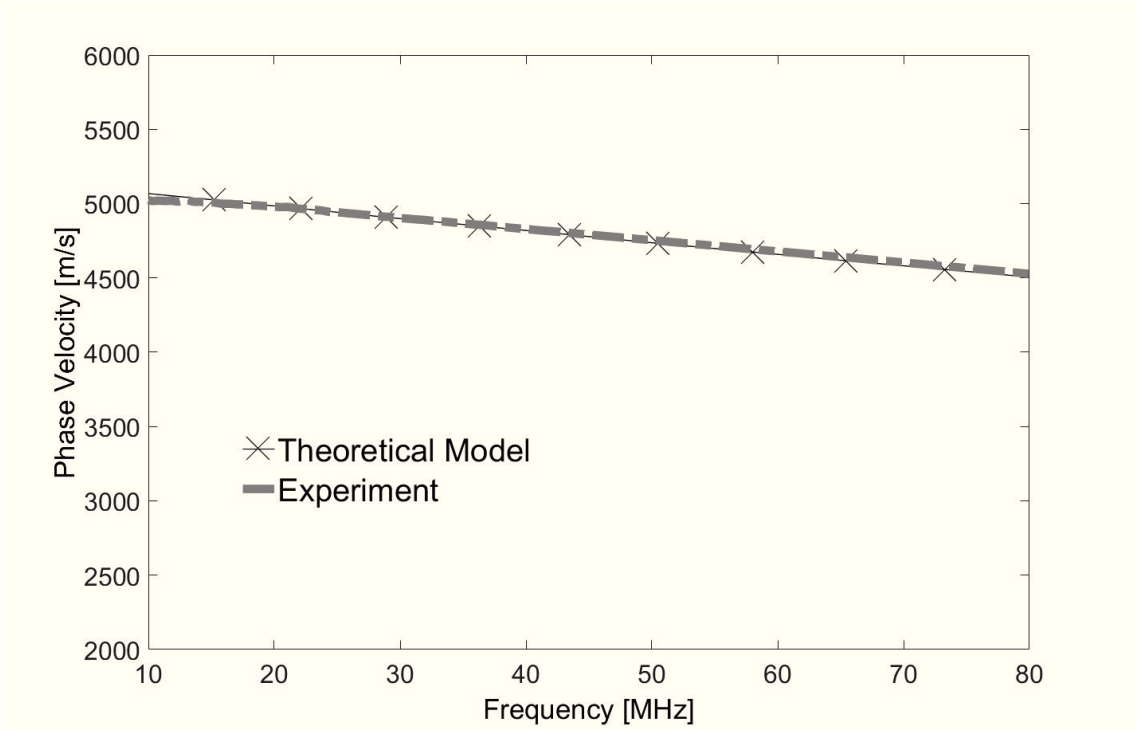

Figure 10: Theoretical model fitted to LUS measurement data (695nm W on Si).

MATERIAL	$v_L\,[m/s]$	$v_T\,[m/s]$	$\rho\,[kg/m^3]$	$d\,[nm]$
Tungsten	Fit	Fit	19250	695
Silicon	8432	5843	2329	-

Table 3: Fitting values and material input parameters for fitting routine of tungsten layer on silicon substrate; v_L denotes the longitudinal sound velocity, v_T denotes the transverse sound velocity, ρ the mass density and d the thickness of the layer; v_L and v_T of the tungsten layer are evaluated in the fitting routine.

5.3 DISCUSSION AND CONCLUSION

In the work reported in [33], the Young's modulus and the Poisson ratio of a single tungsten layer on a silicon substrate were determined via a contact-less LUS measurement (Section 4.1) in combination with a numerically solved theoretical model (Section 4.2.3). The assumption of linear elastic solids and isotropy was made in the analysis. In [33] the thin TiN layer was neglected. This assumption was justified because the TiN layer had a thickness of only 20nm and did not alter the dispersion relation to a measurable extent. However, many state of the art devices in micro- and nanoelectronics rely on thicker intermediate layers. For instance, the case of a 800nm intermediate layer between silicon and polyimide is discussed in Chapter 6, presenting a two-layer on substrate system.

SOURCE	YOUNG'S MODULUS [GPA]	POISSON RATIO
LUS	405	0.28
Literature [43, 123, 144]	380 - 420	0.28 - 0.30

Table 4: Comparison of LUS results to literature values for the 695nm tungsten coating on Si.

6 CHARACTERIZATION OF POLYIMID-MULTI-LAYERED-SYSTEMS

In [36] a stacked system consisting of (1) a Si wafer, (2) 800nm of silicon nitride and (3) 11µm of polyimide is analysed. The Young's modulus and the Poisson's ratio of the polyimide are determined and compared to literature values. The analysis of higher wave modes is discussed. In addition to the results published in [36], LUS measurements of photosensitive polyimide samples exposed to different light dosages are shown in this chapter. It is shown that the SAW propagation is sensitive to the light dosage.

6.1 MOTIVATION

Altough the characterization of single layer thin-film-on-substrate-systems is currently a very important task in a variety of industrial and academic applications, many modern microelectronic devices require the use of multi-layered stacks, rendering the characterization of multi-layered systems equally important. Reference [36] concerns the analysis of a multi-layered system relevant in *e.g.* the realization of microelectronic devices, namely a spin coated polyimide layer of 11µm thickness on 800nm silicon nitride deposited on a (100) silicon substrate.

Polyimides are one of the most heat resistant polymers [80]. They show long term temperature durability in the range of 250 – 350°C [120] and are often referred to as „high performance polymers" for this reason [120]. In addition to their excellent thermal stability, the properties of polyimides can be altered to a remarkable extent by molecular engineering of their functional groups [80, 120, 161]. Some of the beneficial properties of polyimides are listed in [120], *e.g.* light weight, high corrosion resistance, good wear properties, dimensional stability, low flammability, moisture resistance and insulating properties. (The electrical resistivity of undoped polyimide is in the order of $10^{21}\,\mu\Omega\mathrm{cm}$ [96]; compare to *e.g.* copper in Table 7). Due to their many advantageous properties, high performance polyimide films are often used for microelectronic fabrication and packaging, *e.g.* as photoresists [99]. If photosensitive polyimides are applied, the use of photoresists for patterning in the fabrication of electronic devices becomes unnecessary and the number of fabrication steps is reduced [161]. Moreover, photosensitive polyimides are expected to be of great relevance in the manufacturing of photonic devices, enabling the design and control of hyper fine structures [161]. It has also been reported, that the mechanical properties of polyimide degrade, when irradiated with increasing UV light dosage (as a consequence of the high enough energy of the UV photons that can dissociate molecular bonds) in [115]. Regarding the 800nm of silicon nitride between silicon and polyimde, established inorganic materials such as silicon oxide or silicon nitride are used as highly temperature resistant gate insulators, inter layer dielectrics or passivation layers [161].

MATERIAL	$\rho[kg/m^3]$	$v_L[m/s]$	$v_T[m/s]$	$d[\mu m]$
Polyimide	1464	2660	1160	11
SiN	3185	10607	6204	0.8
Si	2329	8432	5843	-

Table 5: Input values for the evaluation of Figure 11: Film thickness d, density ρ, longitudinal and transverse sound velocity v_L and v_T of polyimide [23], SiN [15] and Si [124].

The fabrication attendant characterization methods on wafer level for such high performance polymers are in demand and the contact-less LUS method seems to be a promising candidate in the ongoing characterization efforts.

6.2 MEASUREMENT AND DATA EVALUATION

6.2.1 *Theoretical model of acoustic wave propagation*

The theoretical model for the determination of the dispersion relation of the two-layer on substrate system can be found in Section 4.2.3 and the result is shown in Figure 11. Here, higher wave modes (H_1, H_2, H_3) are present in the frequency range up to 120MHz. The Rayleigh wave starts at the Rayleigh wave velocity of the substrate: 5150m/s [124]. The higher wave modes (H_1, H_2, H_3) start at the cut-off velocity of about 5843m/s, corresponding to the transverse sound velocity of the substrate. The input parameters used for the evaluation of Figure 11 are summarized in Table 5, where ρ denotes mass density and v_L and v_T denote longitudinal and transverse sound velocity.

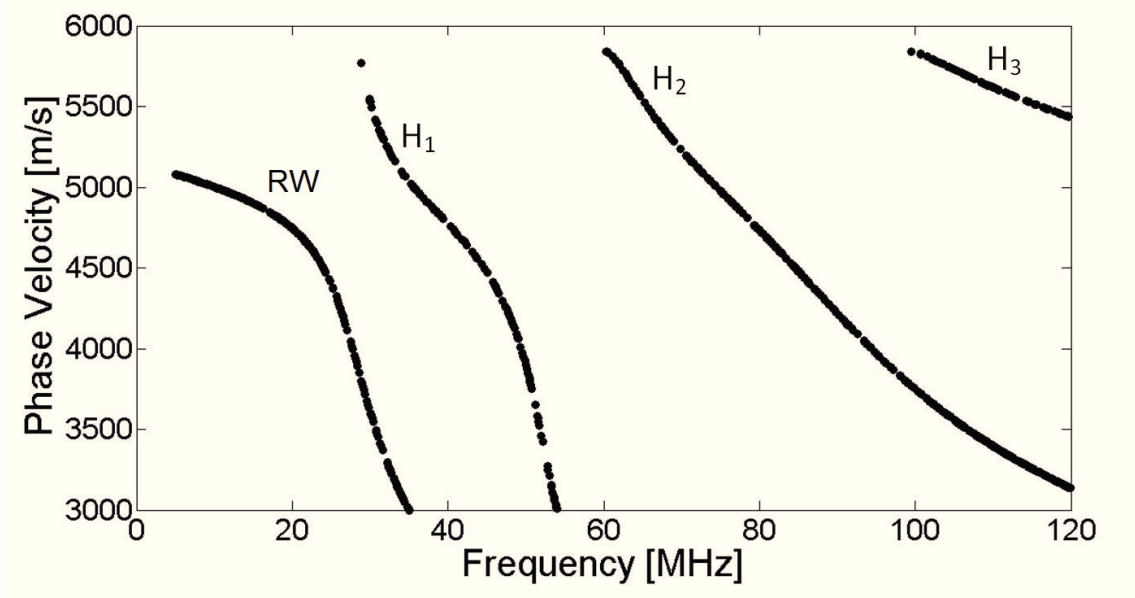

Figure 11: Theoretically evaluated dispersion relation for 11μm polyimide on silicon nitride deposited on silicon (100). *RW* denotes the Rayleigh wave and H_1, H_2 and H_3 denote higher wave modes.

6.2.2 *LUS experiment*

The LUS measurement was performed according to Section 4.1. In the analysis of the polyimide stacks, the 10ns Nd:YAG laser was applied, because as a consequence of the 11µm film thickness, and the covered frequency range of 100MHz additional wave modes are already present in the layer on substrate system, see Figure 11. The SAW propagating on the surface of the sample was detected via the beam deflection method described in Section 4.1. Figure 12 shows the detected SAW signals excited at five positions spaced 2mm apart. The form of the signals is altered, compared to *e.g.* Figure 8, due to higher wave modes present in the sample. The excitation of higher frequencies (by using the excitation laser with the shorter pulse width of 2ns) would lead to even more interacting wave modes.
Since an isotropic substrate was assumed, the measurement was performed along the [110] direction of the silicon (see also [132]) substrate for which the literature values, given in Table 5, can be used as input parameters.

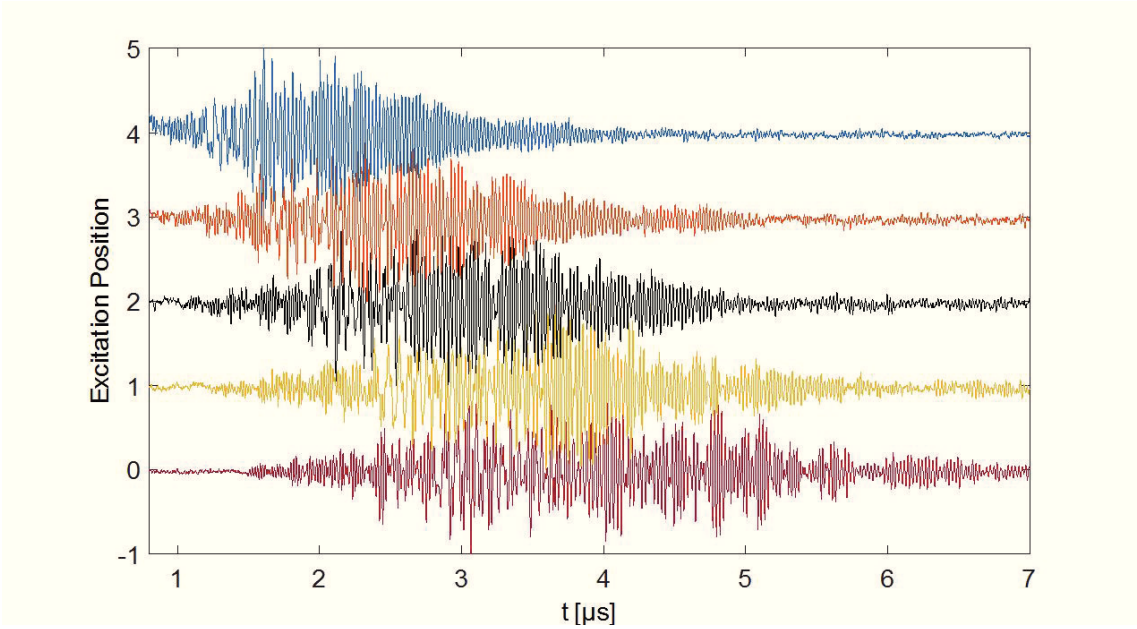

Figure 12: SAWs on polyimide-SiN-Si system, where laser induced signals for five propagation distances are shown. The excitation positions are distanced by 2mm in each case.

6.3 RESULTS

In Figure 13 the result for the experimentally evaluated dispersion relation for the polyimide-SiN-Si system and the fitted theoretical curve are shown. The frequency range for the fitting procedure is approximately up to 27 MHz. In this frequency range only the Rayleigh wave mode (RW) is present, see Figure 11. In the frequency range where more than one wave mode is allowed, the measured phase velocity lies between the two present wave modes, see Figure 11 for comparison. The data evaluation uses the input values summarised for SiN and Si in Table 5. Additionally, the thicknesses of the SiN layer and the polyimide layer serve as input values for the theoretical model. Only

SOURCE	YOUNG'S MODULUS [GPA]	POISSON RATIO
LUS	4.92	0.39
Literature [14, 23, 124]	5.44	0.38

Table 6: Comparison of LUS results to literature values the polyimide coating.

the longitudinal and transversal sound velocity of the polyimide layer are altered in the fitting procedure. The results for the Young's modulus and the Poisson ratio of the polyimide thin film are summarised in Table 6.

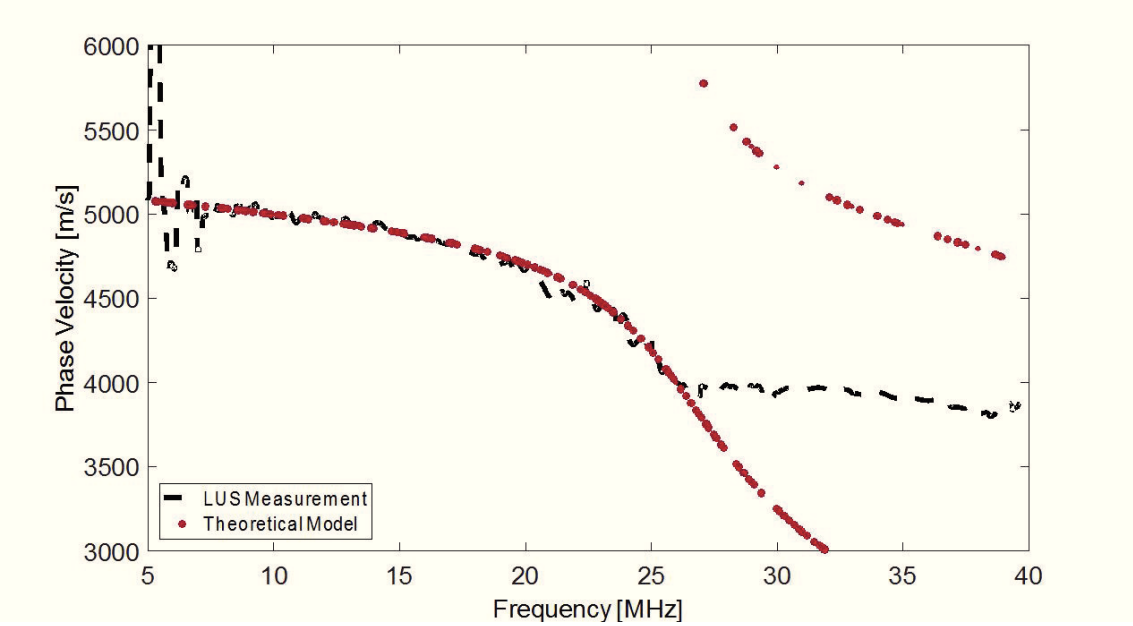

Figure 13: Experimentally obtained dispersion curve with theoretical fit for the polyimide-SiN-Si system.

6.4 DISCUSSION

In Figure 14 the theoretically obtained dispersion relations for the literature values of polyimide are compared to the dispersion relations obtained via the elastic properties evaluated via LUS, see Table 6. Higher wave modes are more influenced by small differences in elastic properties and should therefore be considered in the analysis of polyimide thin film systems in future investigations.

6.5 DIFFERENT LIGHT DOSAGE

In the following, the sensitivity of laser induced SAWs on the exposure of polyimide thin film systems on different light dosages is briefly shown. The samples were exposed to UV light energies of 1000J to 6500J per m^2 before the LUS analysis. The exposure increased from sample 1 to 18. Figure 15 shows exemplarily the dispersion relation for 3 samples exposed to different light dosages. The SAW velocity decreases with increasing

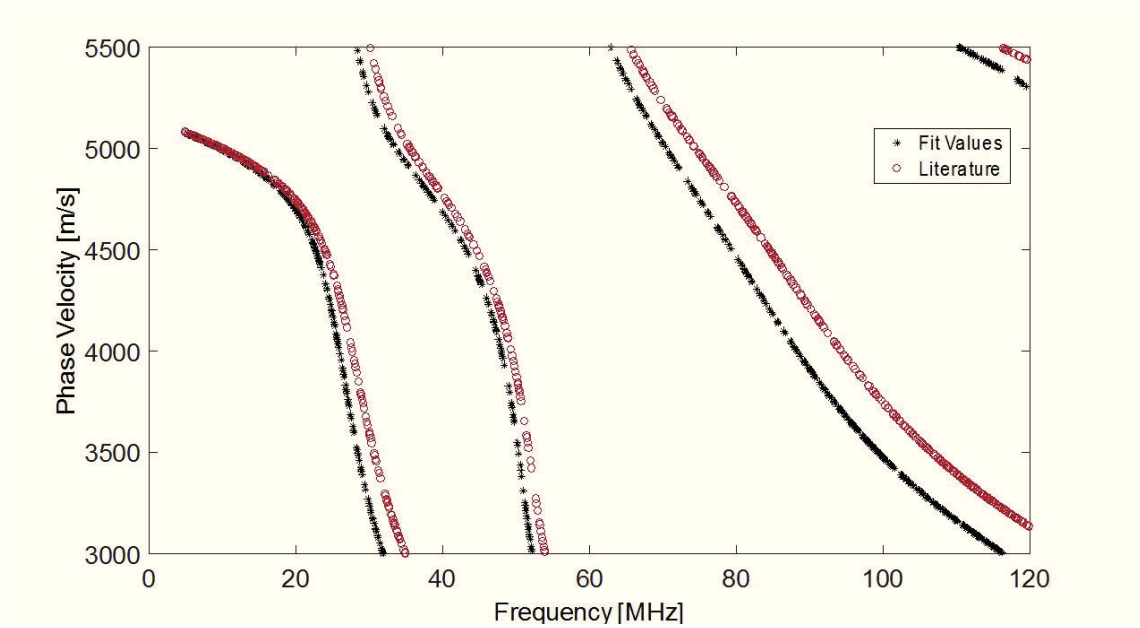

Figure 14: Theoretically evaluated dispersion relations of the PI-SiN-Si-system. The dispersion curves are compared for the case of literature values as input (circles) to the case of dispersion curves obtained with the fitted values (crosses).

light exposure of the polyimide thin film systems. The measurements of dosage 1, 8 and 12 were repeated on 2 days, indicating a certain threshold light dosage at which the SAW velocity is slowed down to a certain extent. However, from dosage 8 to dosage 12, the SAW velocity remains comparable, see Figure 16.

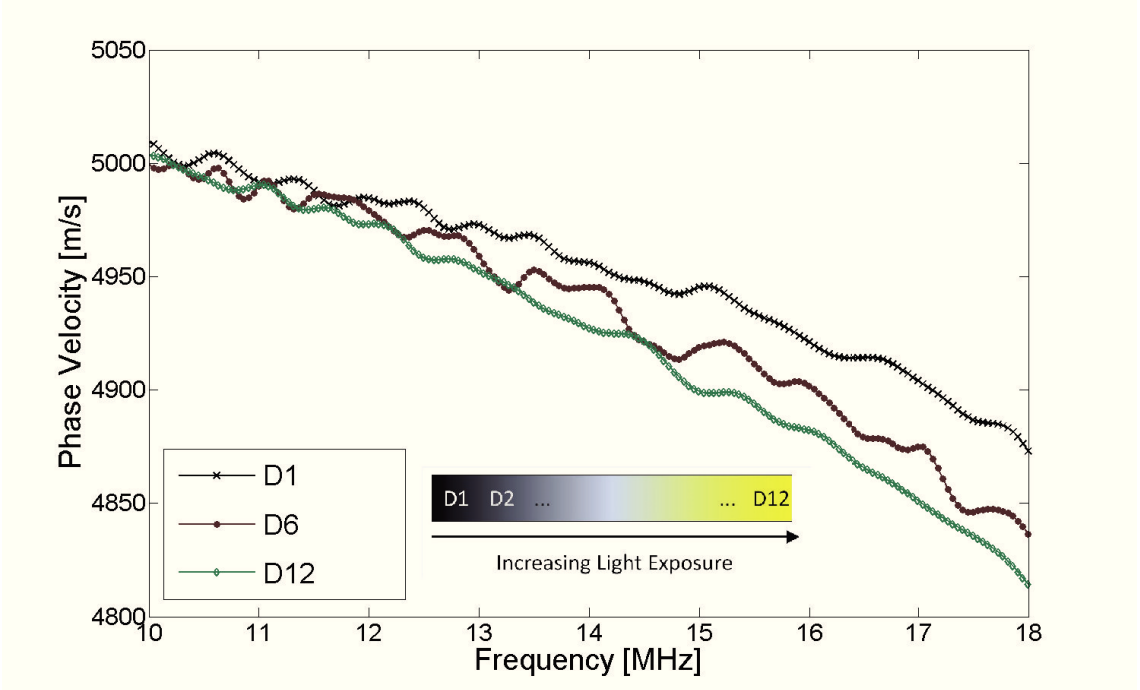

Figure 15: Sensitivity of SAW propagation on light exposure of polyimid sample: Light dosage increases from D1 to D12.

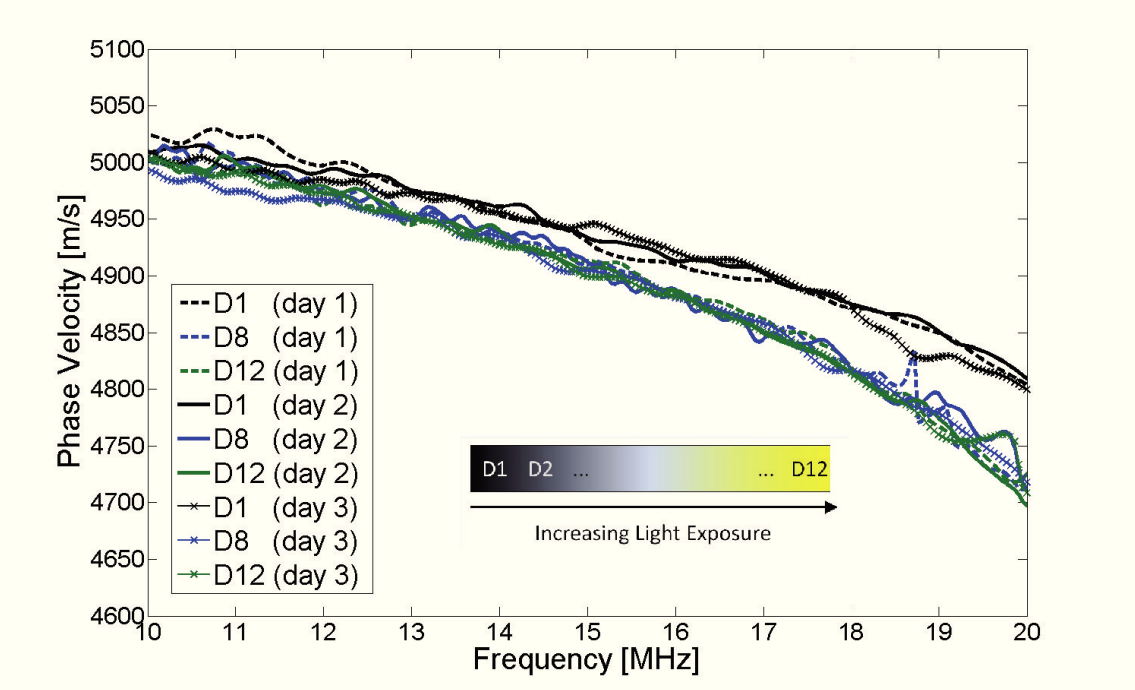

Figure 16: Sensitivity of SAW propagation on light exposure of polyimid samples: repeated measurements on three days. Light dosage increases from D1 to D12. SAW propagation shows higher sound velocity on sample D1 compared to the samples D8 and D12.

6.5.1 *Discussion*

A sensitivity of the SAW propagation to the exposure of polyimide systems to different light dosages was found, see Figure 15 and Figure 16. However, the dispersion relations shown in Figure 15 and Figure 16 are not smooth (the dispersion curves show ripples). This is a consequence of the SAW measurement over multiple lithographic patterns on the polyimide. The fine lattice causes multiple reflections and disturbs the SAW propagation.

6.6 ACKNOWLEDGEMENTS

The polyimide samples were kindly provided by H. Aßmann (Infineon Technologies Dresden GmbH, Dresden, Germany). The LUS measurements were carried out in cooperation with R. Nuster and G. Paltauf (Karl-Franzens University of Graz, Department of Experimental Physics, Graz, Austria).

7

CHARACTERIZATION OF MULTI LAYERED METAL FILMS ON SI

The functionality of MtM microelectronic devices is achieved by the complex combination of metallic, semiconducting and insulating layers, where the careful stack design requires accurate knowledge of the material properties of the thin films. In this context, metallic thin films play a very important role in different steps of fabrication processes and for the functionality of electronic devices. They are used as conducting lines and interconnects.

According to [154], interconnects (as means of transportation of information in a microelectronic circuit) have to fulfill the following requirements:

- low resistivity (high electrical conductivity),
- high thermal conductivity,
- high melting point,
- technology compatibility to the back-end-of-line (see *e.g.* [154]) process.

In Table 7 the advantageous material properties of aluminium and copper concerning their application as interconnects are summarized according to [154]. As smaller interconnect cross-sections increase the risk of electromigration, aluminium alloys are also commonly used as interconnects. The lower resistivity of copper is generally mentioned as advantage, because it improves the RC product, see *e.g.* [154]. Also the high melting point of copper is beneficial for its reliability as interconnect. However, effective diffusion barriers are necessary when copper interconnects are used , because copper readily diffuses into silicon oxide as well as into silicon [154].

In this chapter, two multi-layer sample sets are considered. First, Si-Cu-Al-Cu stacks and secondly four silicon samples with stacks of SiO_2, AlCu, WTi and Cu are characterized via the LUS method. In both cases, the Young's moduli and the Poisson's ratios of the metallic films are determined and compared to literature values.

PHYSICAL PROPERTY	Al	Cu
Specific electrical resistivity $[\mu\Omega cm]$	2.27	1.71
Thermal conductivity $[W/(mK)]$	238	327.7
Melting Point $[K]$	933.5	1358

Table 7: Beneficial material properties of aluminium and copper as interconnects in microelectronics [154].

7.1 CHARACTERIZATION OF Si – Cu – Al – Cu STACKS

This section deals with the step-wise determination of the Young's moduli and Poisson's ratios of Si-Cu-Al-Cu stacks via LUS measurements, because Al and Cu are frequently used as interconnects in microelectronic components.

The non-destructive, step-wise characterization of the Young's moduli and the Poisson's ratios of a Si-Cu-Al-Cu stack was carried out using LUS measurements in combination with a theoretical model, see Appendix A. Fitting the theoretical model to the experimentally evaluated data, only a limited number of parameters can be derived, *e.g.* the longitudinal and transverse sound velocities of one of the layers. In the step-wise approach, (1) a Si-Cu system (see Figure 18) is characterized, (2) a Si-Cu-Al system is evaluated and the gained results are used for the characterization of (3) a Si-Cu-Al-Cu stack. The use of the step-wise approach enables the analysis of the whole Si-Cu-Al-Cu multi-layered stack. All three layers have a thickness of 1 µm and were deposited via the same sputter process. The presented non-contact method shows high potential regarding the non-destructive evaluation of elastic properties of thin films in multi-layered systems, the results are summarised in [38]. The results for the obtained elastic properties are compared to literature values for bulk materials [38].

7.1.1 *Measurement and data evaluation*

The optical setup displayed in Section 4.1 was used, where the pulsed laser with the longer pulse width of about 10ns was operated. A schematic of the set up and an example for LUS induced signals on the analyzed samples is shown in Figure 17. The theoretical model presented in Section 4.2.3 in combination with the fitting routine described in Section 4.2.4. The fitting routine described in Section 4.2.4 was applied for one layer at a time (Figure 19). The input values are summarized in Table 8.

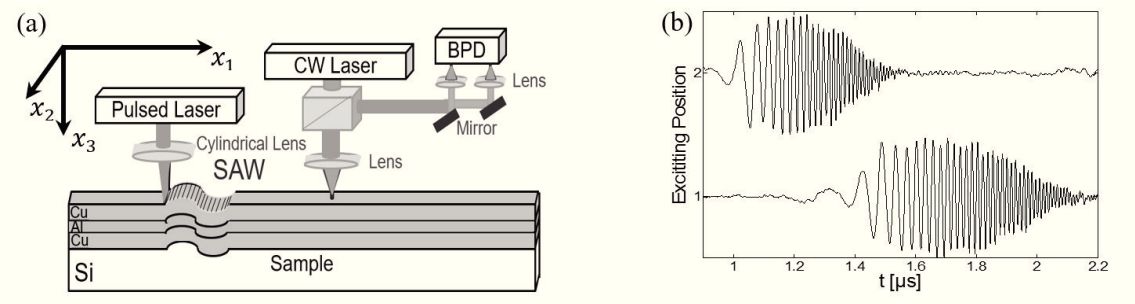

Figure 17: (a) Schematic of the LUS setup and (b) two LUS induced signals on the Si-Cu-Al-Cu stack, measured at two different propagation distances.

7.1.2 *Results*

In Table 9, the LUS results are listed and compared to literature values.

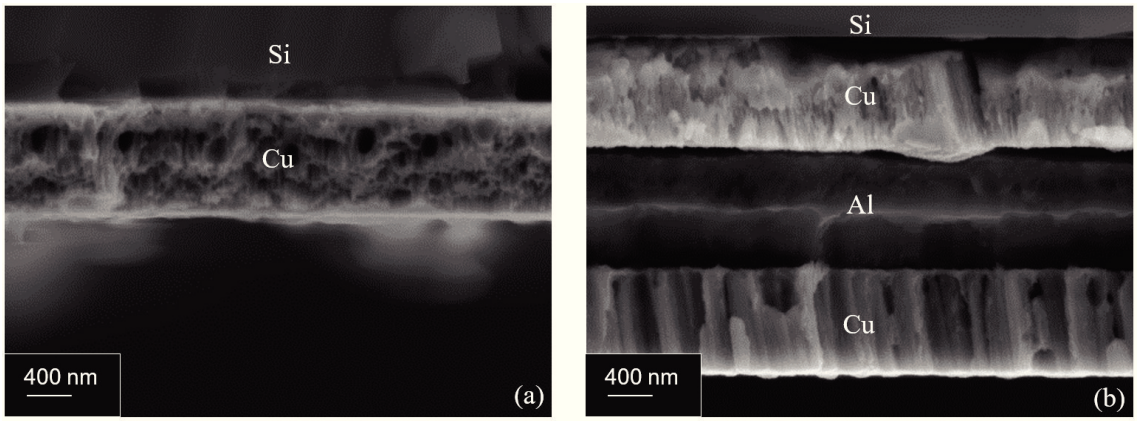

Figure 18: SEM images of two analysed systems (a) Si-Cu and (b) Si-Cu-Al-Cu stack.

MATERIAL	$\rho[kg/m^3]$	$v_L[m/s]$	$v_T[m/s]$	$d[\mu m]$
Cu	8933	Fit	Fit	1
Al	2698	Fit	Fit	1
Si	2329	8432	5843	-

Table 8: Input values for the theoretical evaluation of the Si-Cu-Al-Cu stack, where d denotes the layer thickness, ρ the mass density and v_L and v_T the longitudinal and transverse sound velocity, respectively [15, 124]; v_L and v_T of the Al and Cu layers are evaluated in the fitting routine.

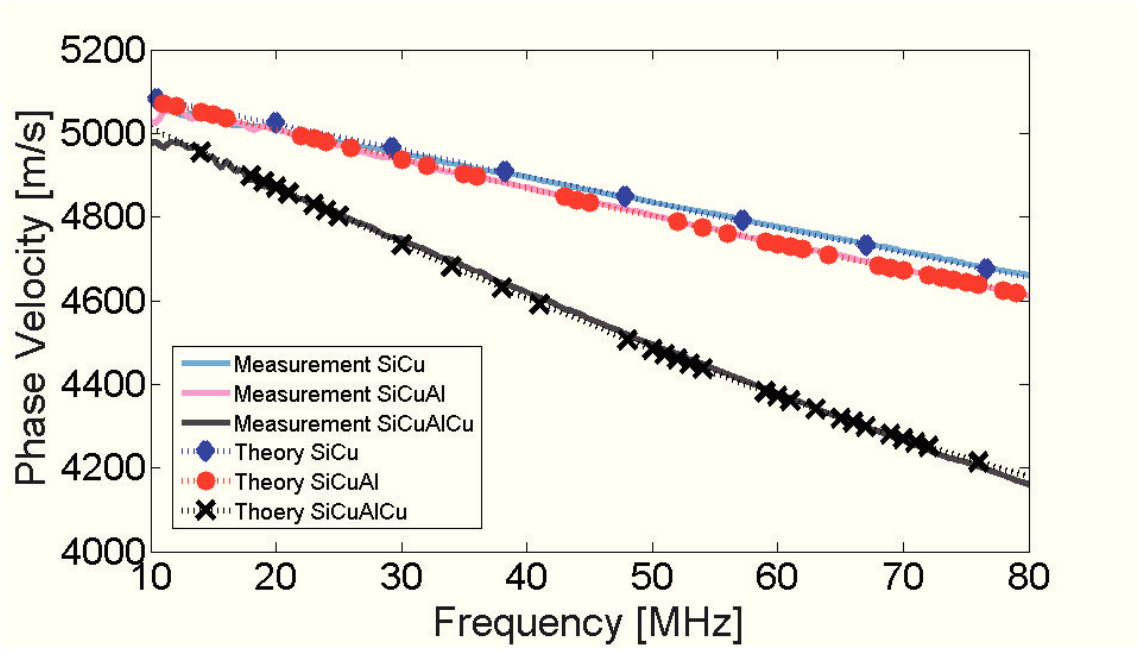

Figure 19: Numerical models fitted to experimental evaluations for Si-Cu, Si-Cu-Al and Si-Cu-Al-Cu.

7.2 LUS MEASUREMENTS OF $Si - SiO_2 - AlCu - WTi - Cu$ STACKS AND THEORETICAL EVALUATIONS

Aluminium and its alloys show many beneficial properties for the realization of MtM technologies, *e.g.* high conductivity and high corrosion resistance. These properties are

LAYER	E [GPA] LUS	ν LUS	E [GPA]	ν
Cu Layer 1	132	0.35	110 - 130	0.33 - 0.36
Al Layer	70	0.33	70	0.33
Cu Layer 2	112	0.35	110 - 130	0.33 - 0.36

Table 9: Comparison of LUS results to literature values [14, 112, 124, 126] for Si-Cu-Al-Cu stack.

SAMPLE	$SiO_2(20nm)$	$AlCu(3200nm)$	$WTi(150nm)$	$Cu(4700nm)$
KP1	x	**x**	o	o
KP3	x	x	x	**x**
KP4	x	x	o	**x**
KP6	x	o	**x**	o

Table 10: Description of multi-layered samples (x $\cdots$ layer deposited, o $\cdots$ layer not deposited).

especially important as the size and costs of microelectronic components decrease, whilst their functionality and packing density is steadily increasing. As already mentioned, Cu is often used in interconnects of electronic devices [154] and SiO_2 as well as WTi are used as barrier layers [31]. The four samples considered in this section are described in Table 10.

7.2.1 *LUS measurements*

The optical setup described in Section 4.1 was used, where the pulsed laser with the shorter pulse width of about 2ns was applied in the case of the samples KP1 and KP6; the laser with the 10ns pulse width was used for the characterization of the samples KP3 and KP4. Exemplarily, the LUS measurement of the sample KP6 is shown in Figure 20.

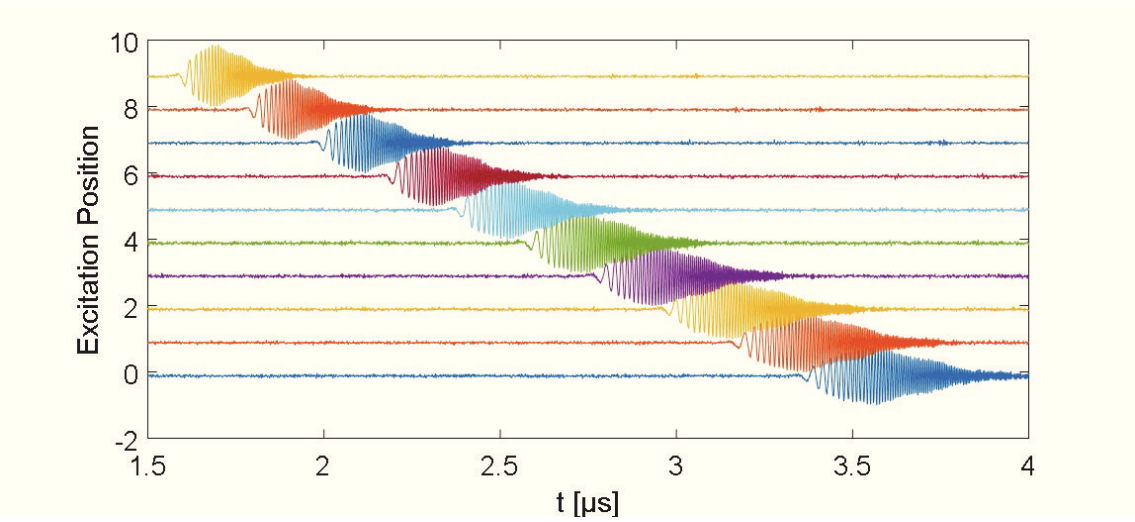

Figure 20: LUS measurement of sample KP6; the excitation positions are distanced by 1mm in each case.

SAMPLE	LAYER	E[GPa] LUS	ν LUS	E[GPa]	ν
KP 1	AlCu	78	0.3	77	0.31
KP 4	Cu	115-135	0.32-0.34	110-130	0.33-0.36
KP 6	WTi	388	0.25	na	na

Table 11: Preliminary LUS results for multi-layered samples compared to literature values for Cu [112, 124, 126] and to measurements for AlCu (Chapter 8).

7.2.2 *Results*

The theoretical model presented in Section 4.2.3 in combination with the fitting routine described in Section 4.2.4 was applied in order to obtain the Young's modulus and the Poisson ratio of the top layers of the samples KP1, KP4 and KP6, see Figure 21. The results are summarised in Table 11.

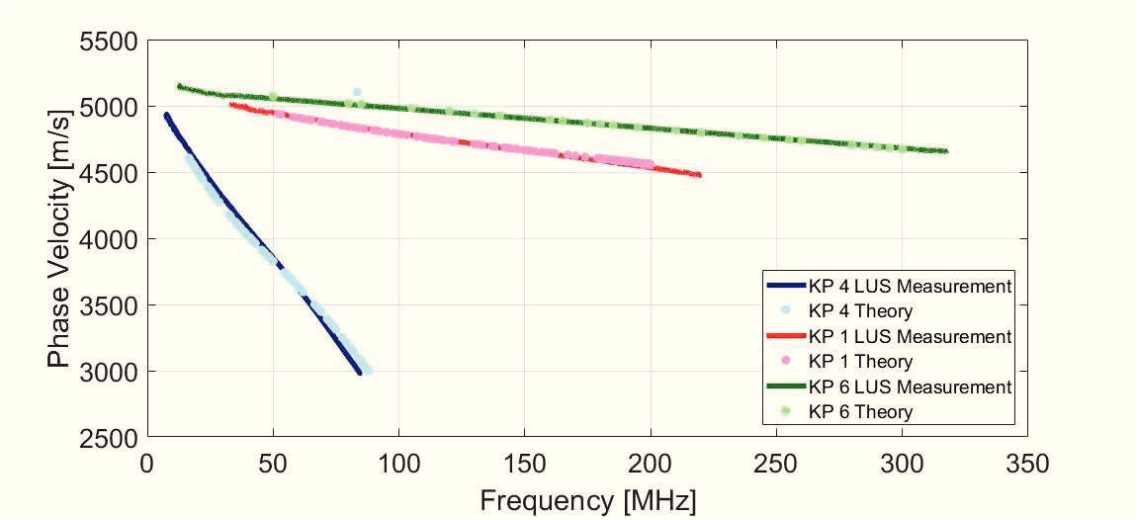

Figure 21: Theoretically evaluated dispersion curves fitted to experimentally evaluated data. The top layer of KP1, KP4 and KP6 are analysed and their Young's modulus E and Poisson ratio ν are determined.

7.3 DISCUSSION AND CONCLUSION

In [38], the results obtained via LUS measurements and numerical evaluations for the Si-Cu-Al-Cu stack are comparable to literature values [14, 112, 124, 126].

The outcome in Table 11 for the Si-SiO_2-AlCu-WTi-Cu system presented in this work gives reasonable values. The Cu values in Table 11 are comparable to literature values [112, 124, 126] and the AlCu result is in agreement with the results presented in Chapter 8. The Young's modulus and the Poisson ratio of the specific tungsten titanium alloy are not to be found in the literature. For this reason, the results from the samples KP1, KP4 and KP6 (in Table 11) were used as input values for the theoretical evaluation (see Appendix A for details) of the dispersion curve corresponding to sample KP3. The dis-

persion curves from the LUS measurement are directly compared to the outcome of the theoretical model in Figure 22, where good agreement is found.

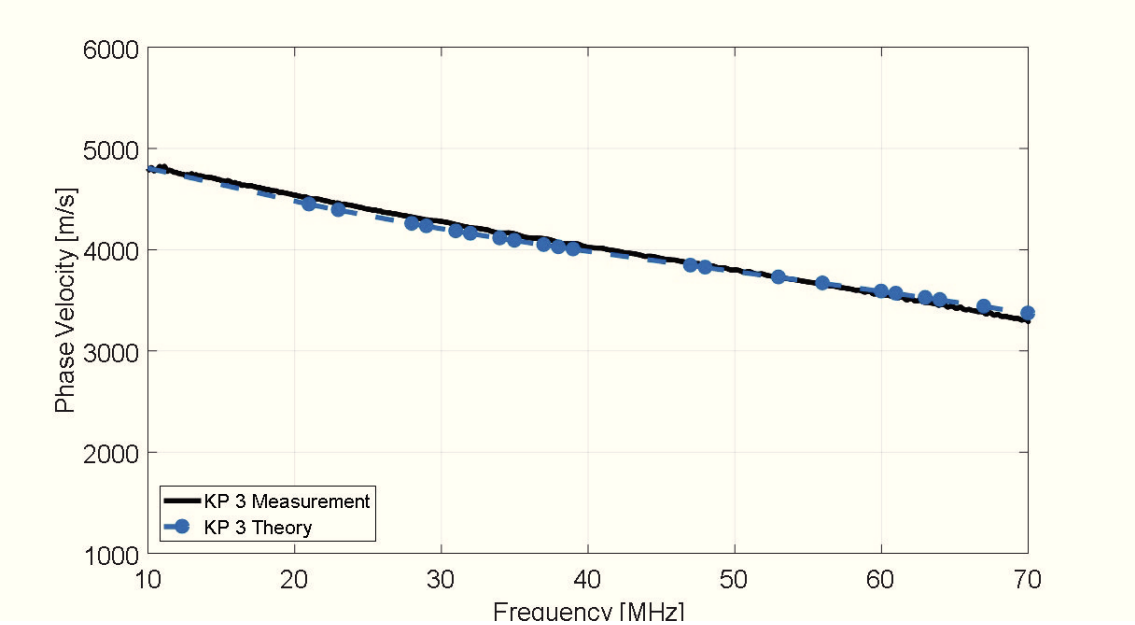

Figure 22: LUS measurement and theoretical evaluation of sample KP3. No fitting procedure was applied, but the results presented in Table 11 were used as input for the theoretical model described in Section A.3.

In the analysis of the metallic multi-layered systems on Si subtrates, no confidence interval for the determined Young's modulus and the Poisson ratio is given. Besides, the outcome in [38] and the results for the Si-SiO_2-AlCu-WTi-Cu stack are not compared to the evaluation of other methods.

In the following section, the characterization of a thin aluminium alloy film on a silicon substrate is carried out by the LUS method. The LUS results are compared to nanoindentation (see *e.g.* [28]) results and density function theory (DFT) calculations (see *e.g.* [138]). Moreover, the confidence intervals of the elastic properties determined via LUS are discussed in Chapter 8, [65].

7.4 ACKNOWLEDGEMENTS

The Si-SiO_2-AlCu-WTi-Cu stacks were kindly provided by R. Zelsacher and M. Ehmann (IFAT, Infineon Technologies Austria AG, Villach, Austria). The LUS measurements were carried with the support of R. Nuster and G. Paltauf (Karl-Franzens University of Graz, Department of Experimental Physics, Graz, Austria).

8

ALUMINIUM-COPPER ALLOY COATINGS ON SILICON SUBSTRATES

In this chapter, the characterization of AlCu layers on silicon substrates is carried out via LUS, where the confidence interval for the obtained Young's moduli and Poisson ratios are given. Secondly, the Young's moduli obtained by LUS are compared to nanoindentation (NI, see *e.g.* [28]) results and density function theory (DFT) calculations (see *e.g.* [138]). The work presented in this chapter is planned to be published in the near future [65].

8.1 MOTIVATION

As mentioned in Chapter 7, aluminium is frequently used as interconnect in microelectronics due to its relatively high electrical conductivity, high thermal conductivity and high melting point (see Table 7). However, electromigration seems to increase as MtM miniaturization efforts take place. This is a consequence of increased current densities [154]. It was observed, that an increase in lifetime can be achieved by alloying aluminium with copper [3]. In general, alloying with trace elements can have the following effects [154]:

- prevent interdiffusion,
- create self passivating layers,
- promote adhesion,
- reduce fatigue effects,
- improve electromigration.

Due to the many beneficial effects of alloying, AlCu alloys are commonly used as interconnects [154] and their non-destructive characterization is highly in demand.

8.2 SAMPLES

The samples analysed in this work are Si (100) wafers with approximately 20nm thermal oxide and AlCu layers of 1µm, 2µm and 5µm thickness. The thin films were fabricated by a physical vapor deposition process and the wafers were cut into 2x4cm^2 plates.

8.2.1 *Thickness measurement by profilometry and by SEM image analysis*

The thickness of the thin films was measured via profilometry in the case of the 2µm and 1µm film thickness. The profilometric measurements were carried out for each 2x4cm^2 plate, in this way, a mean value and a standard deviation for the layer thickness over the whole wafer was determined. The thickness of the 5µm samples was measured with

AlCu[µm]	LATTICE CONSTANT [Å]	DENSITY [$\frac{kg}{m^3}$]
1	66.04	2794
2	66.21	2787
5	66.16	2789

Table 12: XRD measurements of AlCu samples.

the ImageJ software [117] analysis of scanning electron microscopy (SEM, see *e.g.* [154]) images, see Figure 23. The sample cross-section shown in Figure 23 was obtained by ion-slicing, see *e.g.* [160]. The thickness measurements using the imageJ software were carried out at ten positions for each plate, yielding a mean value for the sample thickness and a corresponding standard deviation.

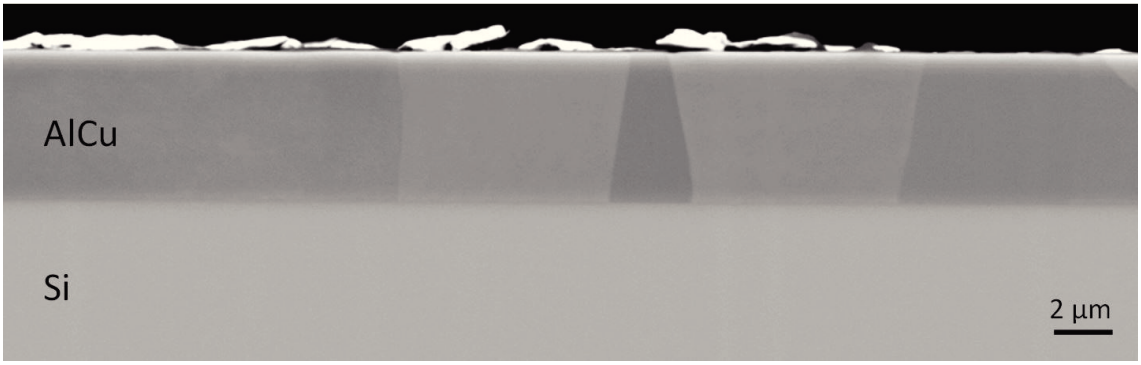

Figure 23: SEM image of the cross-section of the 5µm AlCu layer on Si after ion-slicing.

8.2.2 *Density measurement via XRD*

The lattice constants and the densities of the AlCu layers were determined via XRD measurements (see *e.g.* [152, 154]). The results are summarised in Table 12. The densities serve as input for the LUS evaluations and the DFT calculations. Additionally to the densities, also the lattice constants are required for the DFT calculations of the AlCu stiffness tensor.

8.3 LUS MEASUREMENT AND DATA EVALUATION

The setup described in Section 4.1 was used, where the laser with the shorter pulse duration of 2ns was operated in the cases of the 2µm and 1µm thin films. The laser with a pulse duration of about 10ns was applied in the case of the 5µm coating. The theoretical model for the data evaluation can be found in Section 4.2.3. Fitting the theoretical model to the experimentally evaluated frequency dependent phase velocity (see Section 4.2.2), the elastic modulus E and the Poisson ratio ν of the thin film can be evaluated, see Figure 24. The fitting procedure relies on the input parameters of the substrate. Under the assumption of an isotropic substrate, the longitudinal and transverse sound velocity and the density of silicon (see Table 8 [124]) are needed as input values. The

assumption of isotropy can be applied in the measurement, as long as the measurement is performed along a symmetry axis of the silicon [132]. In our analysis, the measurements were performed along the [110] axis of the silicon substrate. In addition to the substrate parameters, also input parameters of the thin film are required, namely the density (determined by XRD measurements) and the thickness of the film (determined via profilometry and cross-checked via the analysis of SEM – measurements). As a test,

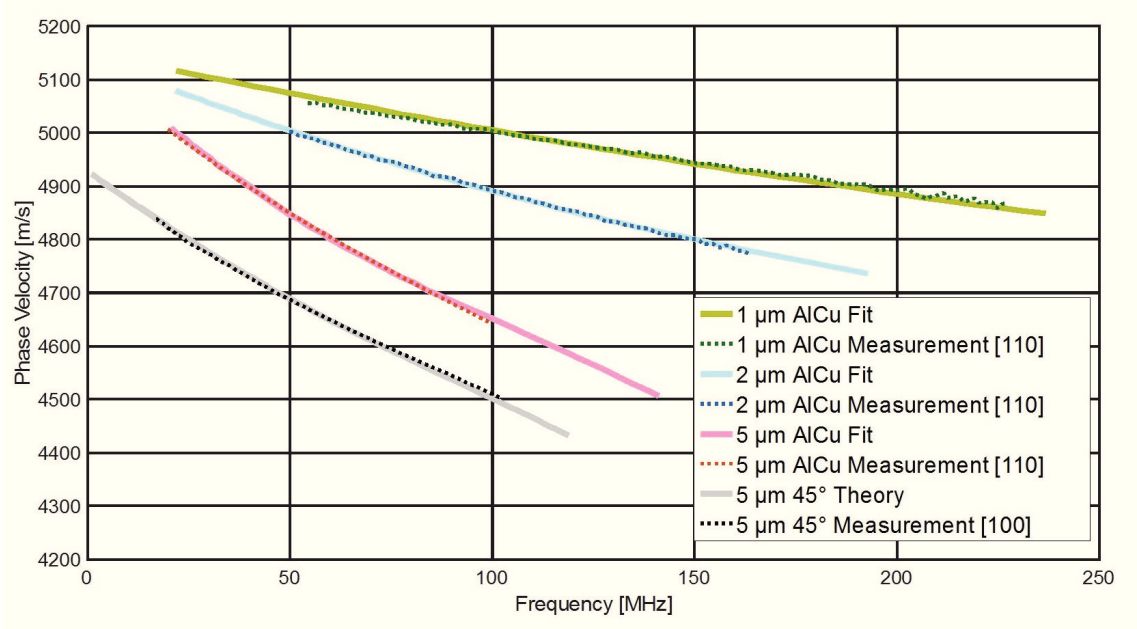

Figure 24: Theoretical models (dotted lines) fitted to experimentally evaluated dispersion curves (solid line) for the case of 1µm, 2µm and 5µm AlCu coatings on silicon substrate in the [110] direction. Measurement (black dots) and theoretical (grey line) evaluation of 5µm AlCu coating along the [100] direction.

the LUS measurement was performed under a 45° rotation of the sample in the case of one sample with 5µm AlCu on Si, performing a measurement in the [100] direction. The theoretical model for acoustic wave propagation in an isotropic layer on an anisotropic substrate with cubic symmetry was used to calculate the frequency dependent phase velocity in this direction [100] (see Appendix A), taking the anisotropy of the Si and the results obtained from the fitting routine for the [110] direction into account. Here, the three elastic constants of the substrate ($c_{11} = 166\text{GPa}, c_{12} = 64\text{GPa}, c_{44} = 80\text{GPa}$ [153]) were used as input parameters. The obtained result for the [100] direction (black gray line in Figure 24) agrees with the measurement (dotted black line in Figure 24). This test corroborates the assumption of isotropic SAW wave propagation, in accordance with the electron backscatter diffraction (EBSD, see e.g. [154]) data shown in Figure 25.

In addition, the problem of multiple solutions (when more than one set of fitting parameters yields the best least square fit) in one fitting process was addressed as follows: every time the standard deviation from the multiple solutions was higher than 1GPa in the case of elastic modulus E and higher than 0.01 in the case of the Poisson ratio ν was counted, which yielded zero cases. This means the multiple solutions are very close to our obtained results and within the confidence interval calculated in the following subsection.

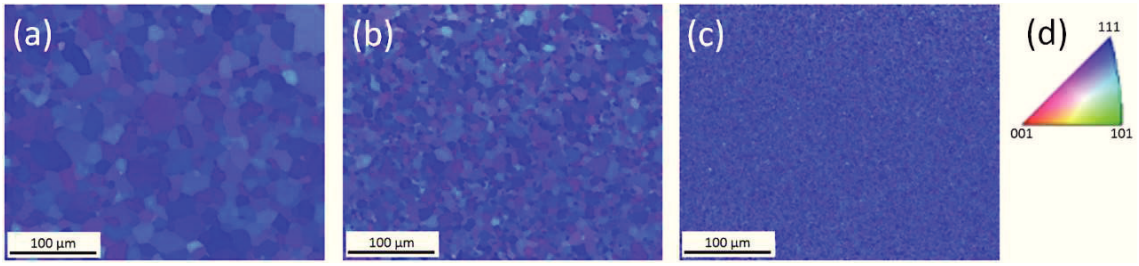

Figure 25: Lateral EBSD analyses of (a) 5µm, (b) 2µm and (c) 1µm AlCu thin films (sample surfaces); the colour code (d) corresponds to the grain orientation.

8.3.1 *Confidence intervals*

For the evaluation of the confidence interval of the LUS results, a statistical error analysis was performed, see *e.g.* [19]. To this purpose, not a single input for each parameter was chosen, but each parameter was given a normal distribution in the range of the error estimated via the measurements. The corresponding distributions of the input parameters are shown in Figure 26, where v_{LS}, v_{TS}, ρ_S, ρ_L and d_L denote the longitudinal sound velocity of the substrate, the transverse sound velocity of the substrate, the mass density of the substrate and the layer and the thickness of the layer, respectively.

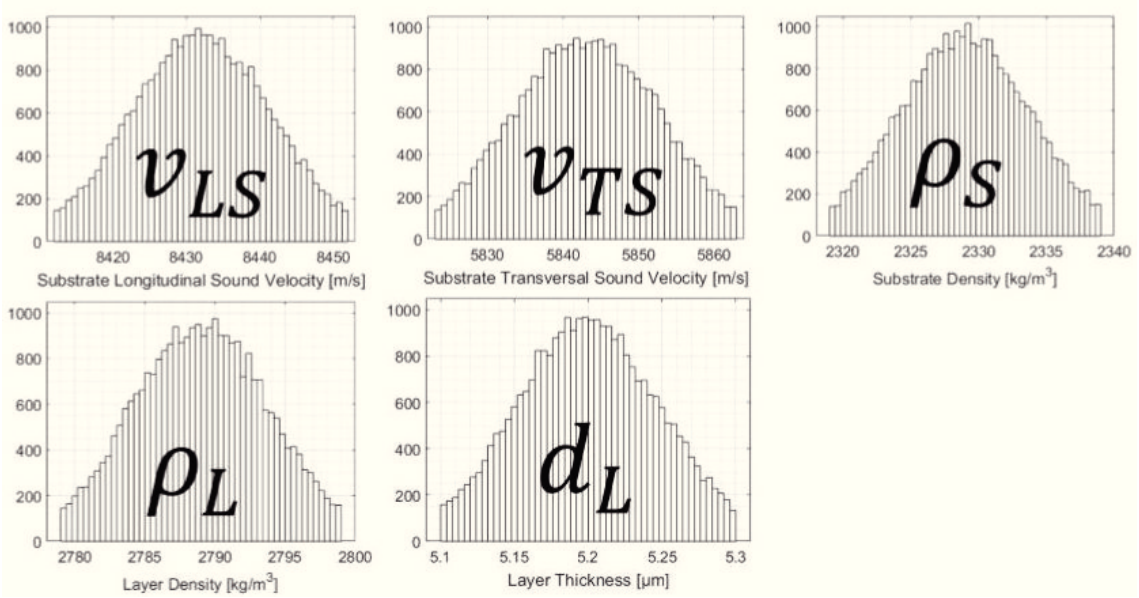

Figure 26: Determination of confidence interval: Gaussian distribution of fitting parameters for the evaluation of the Young's modulus and the Poisson ratio of the aluminium coatings on Si substrates.

The least square fitting procedure was then applied to the measured dispersion curve using the theoretical model for 6000 parameter sets. For each parameter set, the input parameters are chosen randomly from the 5 normal distributions. After the analysis of 6000 parameter sets, the system approximated certain constant mean values for the elastic modulus E and the Poisson ratio ν, see Figure 27. From the evaluation of the

6000 parameter sets, distributions for the elastic modulus E and the Poisson ratio ν are obtained, see Figure 28. Each parameter set corresponds to one iteration step.

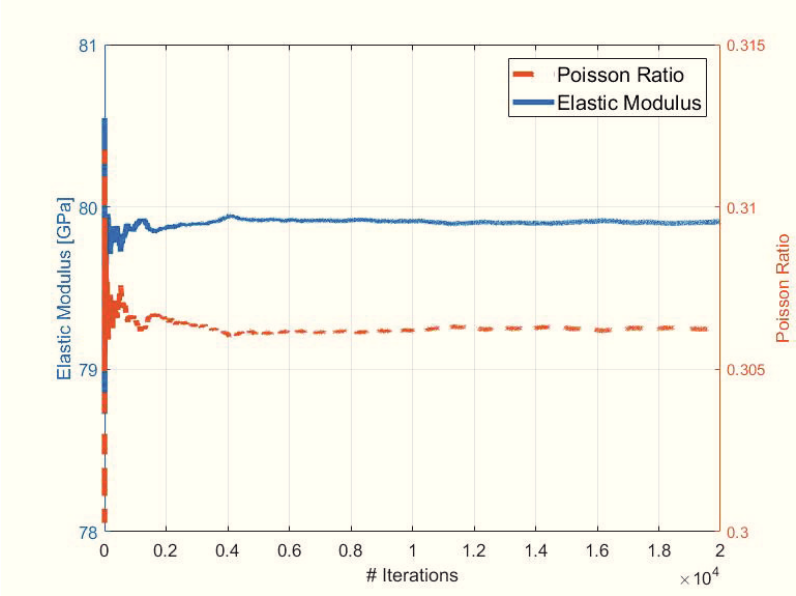

Figure 27: Iteration steps for the evaluation of the mean Young's modulus and the mean Poisson ratio via a statistical error analysis.

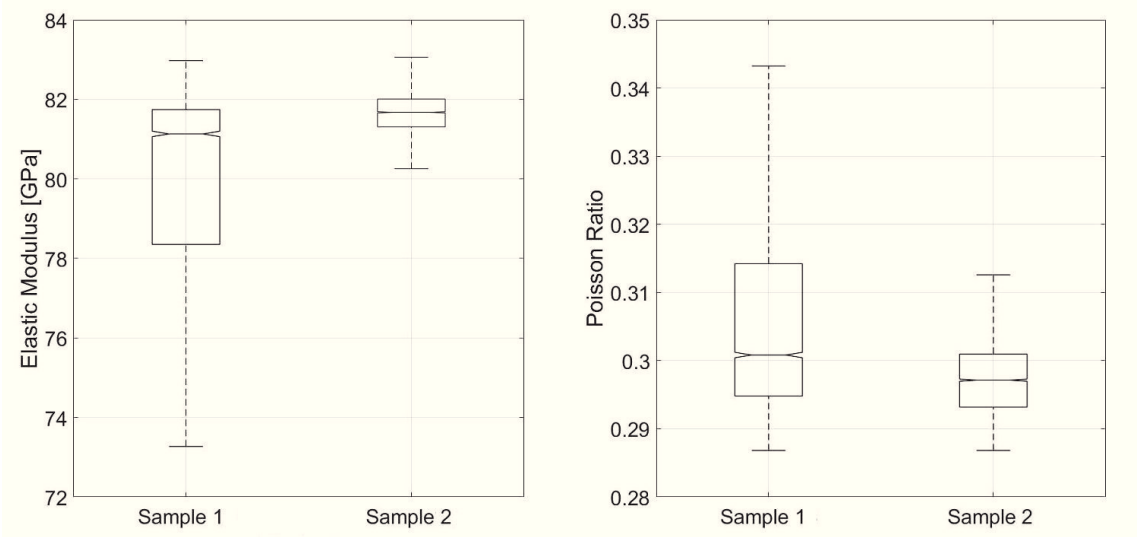

Figure 28: Elastic modulus and the Poisson ratio evaluations for two different samples of 5µm AlCu on Si.

8.4 RESULTS

In Table 13, the results for the AlCu layers of 1µm, 2µm and 5µm thickness are summarised. The distribution for E and ν are skew, therefore they are presented as boxplots in Figure 28 and their median and first quantile (ΔE and Δν) are given. The outcome of the LUS method is compared to NI and DFT data.

METHOD	THICKNESS	$E[GPa]$	$\Delta E[GPa]$	ν	$\Delta\nu$
LUS	5µm	**81**	3	**0.30**	0.02
LUS	5µm	**82**	1	**0.30**	0.01
NI	5µm	**84**	3	**0.30**	–
DFT	5µm	**79**	–	**0.33**	–
LUS	2µm	**78**	4	**0.34**	0.02
NI	2µm	**83**	6	**0.34**	–
DFT	2µm	**79**	–	**0.33**	–
LUS	1µm	**73**	4	**0.36**	0.01
NI	1µm	**78**	7	**0.36**	–
DFT	1µm	**81**	–	**0.33**	–

Table 13: Comparison of the LUS, NI and DFT results for E and ν regarding the AlCu samples, ΔE and $\Delta\nu$ denote the median and first quantile in the case of the LUS measurement.

8.5 DISCUSSION AND SUMMARY

The obtained results, summarised in Table 13, were achieved by three different measurement and evaluation procedures, where good agreement for the Young's modulus was found. The Poisson ratios were achieved via LUS and DFT, the LUS result for the Poisson ratio serving as input for the NI evaluation.

The Young's moduli show a slight tendency to decrease with decreasing film thickness in the LUS and also in the NI results.

According to [154], the texture and grain size corresponds to a homogeneous film in Al interconnects and the grain size is of the order of the film thickness. The texture can be influenced by intermediate layers and deposition parameters. It has been found, that narrow (111) texture improves the interconnect reliability [62]. In the case of AlCu alloys different micro-structures, depending on the heat treatment, can be observed. In the EBSD analysis (Figure 25) a decrease in grain size with decreasing film thickness as well as a predominent (111) texture is shown. The AlCu grain sizes are of the order of the film thickness in the axial direction (one grain over the film thickness, see Figure 23). In the lateral direction (Figure 25), the average grain sizes range from about $1\mu m$ in the case of the $1\mu m$ thin film to about $16\mu m$ in the case of the $5\mu m$ AlCu coating.

It was reported that for very small grains (about $10-100nm$), the Young's modulus can decrease with the grain size [10, 40, 168]. NI results concerning this effect can be found in *e.g.* [40, 168] and a theoretical study is presented in [10].

One advantage of the LUS approach in comparison to NI is the contact-less measurement. Moreover, the LUS method enables fast data evaluation compared to the more advanced DFT calculations, necessary to determine the elastic constants of the AlCu

alloy. Also, the DFT calculations do not take the decreasing grain size into account. The presented results are planned to be published in the near future [65], where a detailed description of the NI and DFT evaluations is planned to be given.

8.6 ACKNOWLEDGEMENTS

The samples were kindly provided by R. Zelsacher and M. Ehmann (IFAT, Infineon Technologies Austria AG, Villach, Austria). The LUS measurements were carried out with the support of R. Nuster and G. Paltauf (Karl-Franzens University of Graz, Department of Experimental Physics, Graz, Austria). The XRD measurements were carried out by M. Wießner (MCL), the EBSD and SEM analyses by B. Sartory (MCL) and W. Costin (MCL), the nanoindentation measurements were performed by J. Zechner (KAI, Kompetenzzentrum Automobil- Industrie-Elektronik, Villach, Austria), the density functional theory calculations were obtained by V. Razumovskiy (MCL). The determination of the confidence interval of the Poisson ratio and the Young's modulus was determined in cooperation with U. Kleb and H. Katz (JR, Joanneum Research, Graz, Austria).

9 TUNGSTEN STACKS DIFFERENT DEPOSITION PROCEDURES

The contact-less nature of the LUS characterization is highly interesting for the at-line or in-line thin film characterization, especially the process-attendant monitoring of thin film deposition procedures during manufacturing is considered most relevant.

In the following, customized tungsten stacks of different deposition procedures and thicknesses were analysed via LUS. In Figure 29, schematics of the analysed samples are shown. Figure 29a shows the silicon substrate, some intermediate layers and tungsten layers of (1) 200nm thickness, (2) 400nm thickness and (3) 600nm thickness. The tungsten layers in Figure 29a were deposited in a single step. In contrast, Figure 29b depicts the scenario, where 200nm of tungsten were applied in each deposition step (see also Table 14). The formation of oxide layers during the step-wise deposition was assumed. In the work reported here, the potential formation of oxide layers during the manufacturing process is tested via LUS measurements and theoretical evaluations. The material and thickness of the intermediate layers are known to the authors but should not be published. The intermediate layers (between silicon and tungsten as well as the assumed oxide layers) were included in the theoretical model for the analysis of the tungsten stacks, see Appendix A.

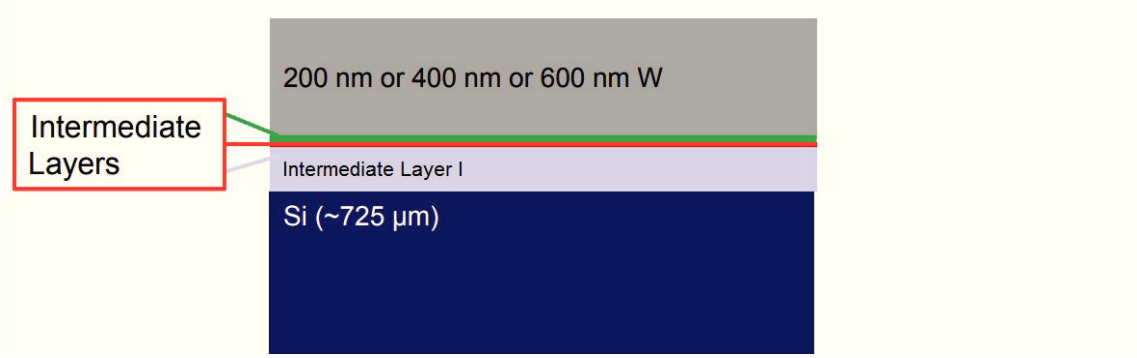

(a) Tungsten deposited in single step.

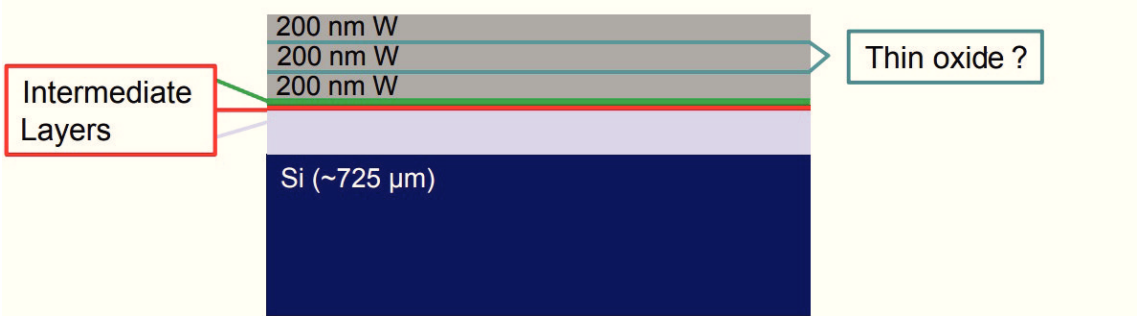

(b) Multiple step deposited tungsten.

Figure 29: Tungsten stacks deposited via different procedures; the formation of thin oxide layers during the step-wise deposition was assumed.

NOMENCLATURE	STEP 1	STEP 2	STEP 3	STEP 4
W12	200nm	-	-	-
W13	200nm	200nm	-	-
W14	200nm	200nm	200nm	-
W15	200nm	200nm	200nm	200nm
W16	400nm	-	-	-
W17	600nm	-	-	-

Table 14: Nomenclature for tungsten stacks deposited via different procedures.

MATERIAL	REFERENCE	v_L [m/s]	v_T [m/s]	ρ [kg/m^3]
Tungsten	[15]	5180	2870	19250
Tungsten Oxide	[15]	4314	2134	18000
Silicon	[124]	8432	5843	2329

Table 15: Material input values for the theoretical evaluations of tungsten layers on silicon substrate; single-step and multi-step deposition procedure, where v_L denotes the longitudinal sound velocity, v_T denotes the transverse sound velocity and ρ the mass density.

9.1 MEASUREMENT AND THEORY

The setup for the LUS measurement is shown in Section 4.1. The Nd:YAG laser with a wavelength of 532nm, a pulse length of 10ns and a repetition rate of 10Hz was used for the excitation of broad band SAWs with frequencies up to about 100MHz. A beam deflection method according to Section 4.1 was used to detect the SAWs. Here, no fitting procedure was carried out. The theoretical model for the evaluation of the frequency dependent SAW velocity for systems with an arbitrary number of isotropic layers (up to nine layers on substrate systems were successfully tested) on a substrate is summarised in Section A.3. The material input parameters can be found in Table 15. The frequency dependent phase velocity was determined according to Equation 14. The error in the determined SAW velocity was determined via Equation 15. Due to shorter distances between the excitation points, the errors in the LUS measurements presented in this section are in the range of ± 5m/s up to ± 20m/s.

9.2 RESULTS

9.2.1 *Influence of intermediate layers - theoretical evaluation*

In Figure 30, the influence of the intermediate layers is evaluated via a theoretical model, see Section 4.2.3. First, the case of no intermediate layers, only a tungsten layer on silicon is plotted (cross), second, "Intermediate Layer 1" (see Figure 29a) is included (stars) and third, all intermediate layers are included (circle). Due to the influence on the phase ve-

locity in the high frequency range, all intermediate layers are included in the theoretical evaluation of the tungsten stacks.

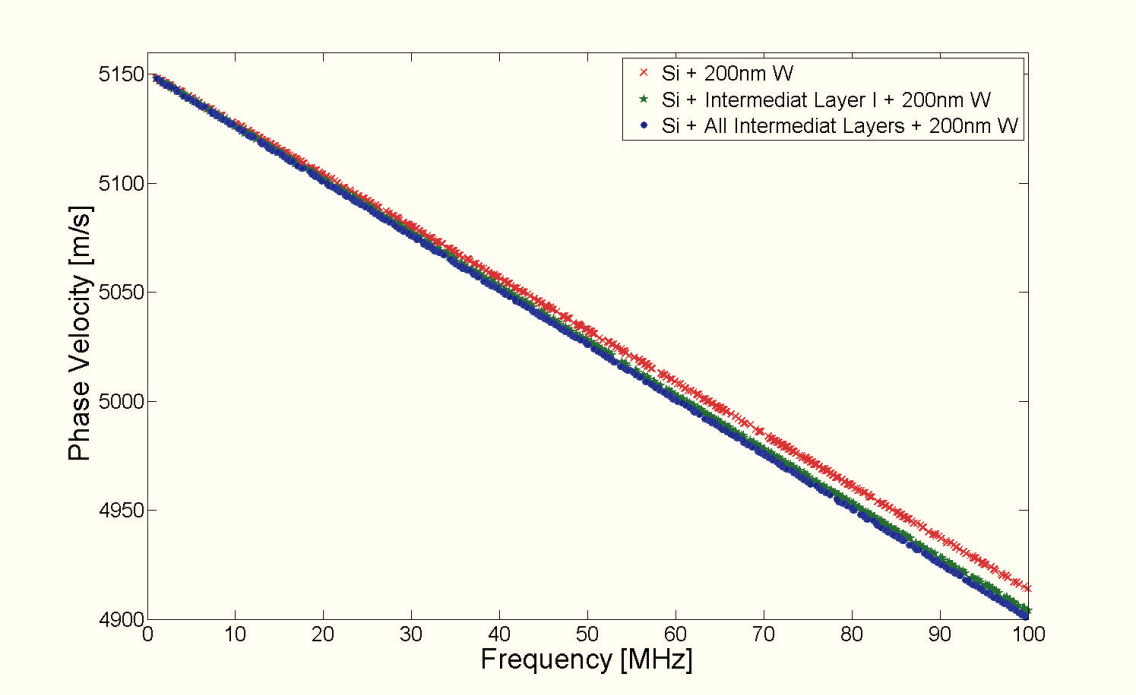

Figure 30: Calculated dispersion curve for a silicon sample coated with tungsten compared to the cases where intermediate layers between tungsten and silicon are present.

9.2.2 *Comparison of single and multiple step procedure - measurement*

The dispersion curves are shown in Figure 31 for the case of single-step deposited tungsten layers and in Figure 32 for the multi-step deposited tungsten according to Figure 29a and Figure 29b, respectively.

With increasing film thickness, the higher frequency part of the SAW propagates in the substrate to lower extent, leading to a stronger decline of the phase velocity with increasing film thickness in Figure 31 and Figure 32.

The comparison of Figure 31 and Figure 32 indicates a change in phase velocity of approximately 50m/s at 100MHz in the case of 400nm tungsten when deposited stepwise in comparison to a single step deposited tungsten layer. In the case of the 600nm tungsten layer, a change of approximately 100m/s in phase velocity at 100MHz can be observed.

9.2.3 *Comparison of single and multiple step procedure - theoretical evaluation*

In Figure 33, the influence of thin oxide layers is considered via a theoretical model, see Section 4.2.3 and Section A.3.

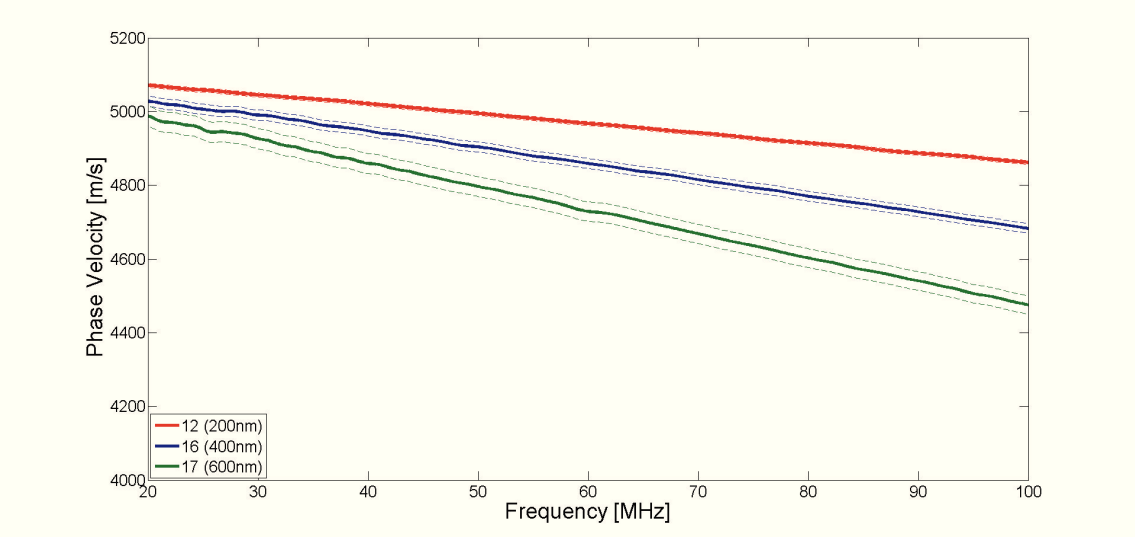

Figure 31: Measured dispersion curves for single step deposited tungsten; the error in the LUS measurements is indicated by broken lines.

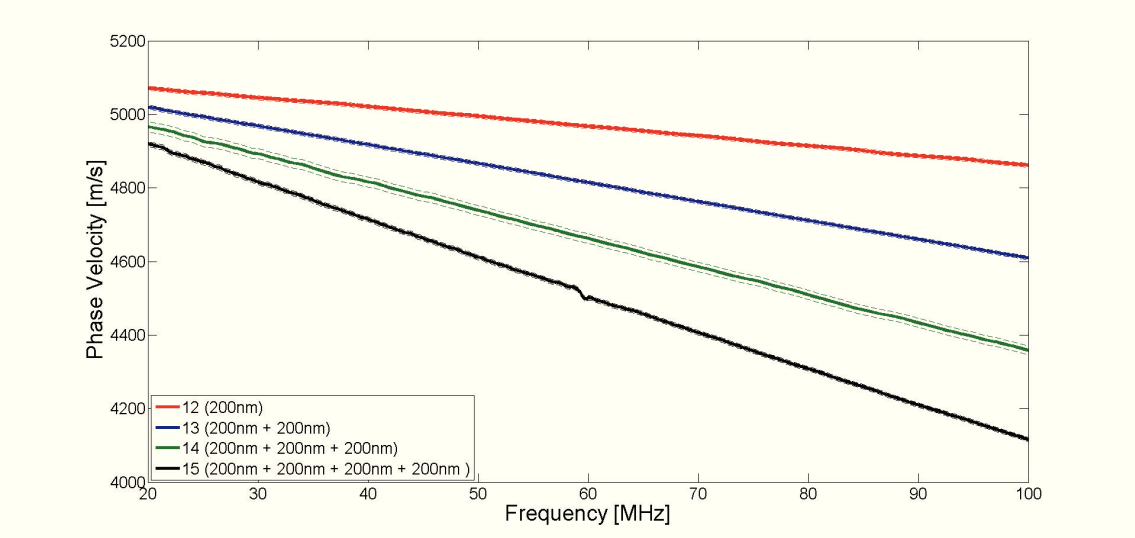

Figure 32: Measured dispersion curves for multiple step deposited tungsten; the error in the LUS measurements is indicated by broken lines.

The inclusion of 10nm tungsten oxide layers changes the phase velocity by approximately 10m/s at 100MHz in the case of a step-wise deposited 400nm tungsten layer (circles), where only one layer of tungsten oxide is present. In the case of a 600nm step-wise deposited tungsten layer (crosses), where two intermediate tungsten oxide layers are present, the phase velocity changes about 20m/s in the high frequency range.

The calculated changes in phase velocity due to intermediate oxide layers of up to 20m/s (shown in Figure 33) are not comparable to the measured changes of up to 100m/s (see Figure 31 and Figure 32).

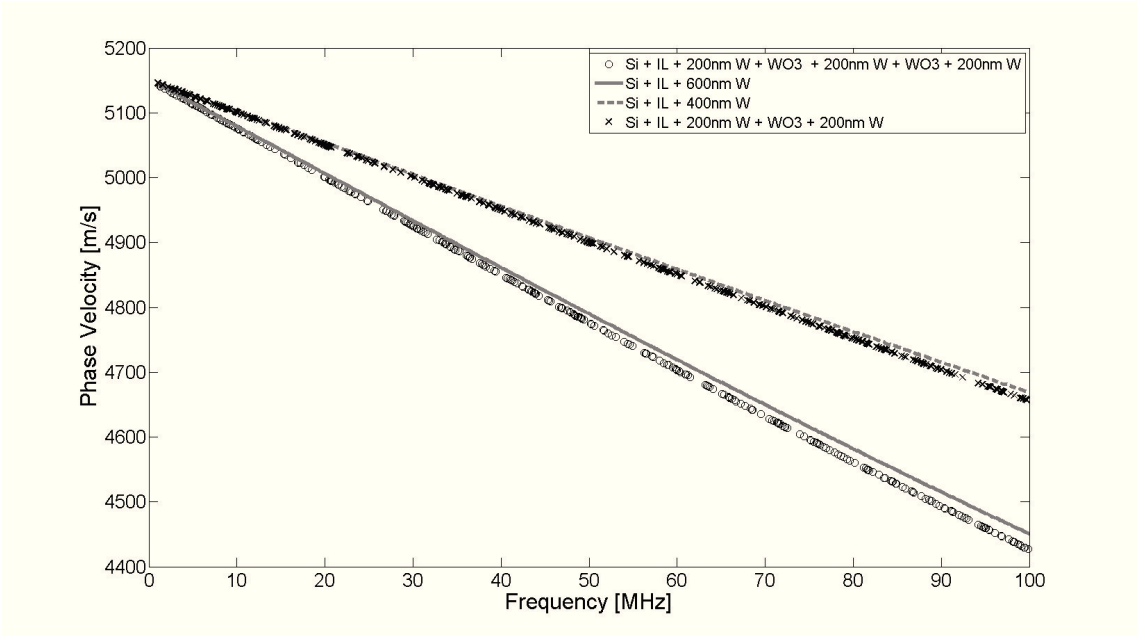

Figure 33: Calculated dispersion curves for tungsten layers on silicon compared to the case where intermediate oxide layers are present.

9.3 DISCUSSION

In this chapter, the analysis of customized tungsten stacks of different deposition procedures via LUS measurements and theoretical models was presented. The sensitivity of the LUS measurements to the different deposition procedures was shown (compare Figure 31 and Figure 32). The change in the phase velocity of the Rayleigh waves exceeds the changes due to intermediate oxide layers predicted by the theoretical model, see Figure 33. The changes might stem from (a) variations in density, (b) stresses or (c) thickness of the deposited layers. Because the change in the sound velocity increased steadily (see Figure 33) with increasing layer thickness, the assumption of a thickness variation in the two deposition processes was made. Follow up SEM measurements of the stacks corroborated the LUS results and the assumption of thickness variations in the deposition processes, see Figure 34 and Figure 35.

In Figure 37, the LUS measurements are compared to the theoretically evaluated dispersion curves for the actual film thicknesses obtained from the SEM images shown in Figure 34 and Figure 35. Here, good agreement is found which corroborates the assumption of a variation in film thickness in the single-step deposition procedure compared to the multiple-step deposition procedure. The findings in this chapter corroborate the theoretical calculated dispersion curves for multi-layered systems. Due to the multi-layered build up, no fitting procedures for the determination of *e.g.* the Young's modulus was performed. Fitting procedures might be possible, when higher wave modes (see also Chapter 6) are considered in the LUS measurements, in the data evaluation and in the fitting routine in future analyses.

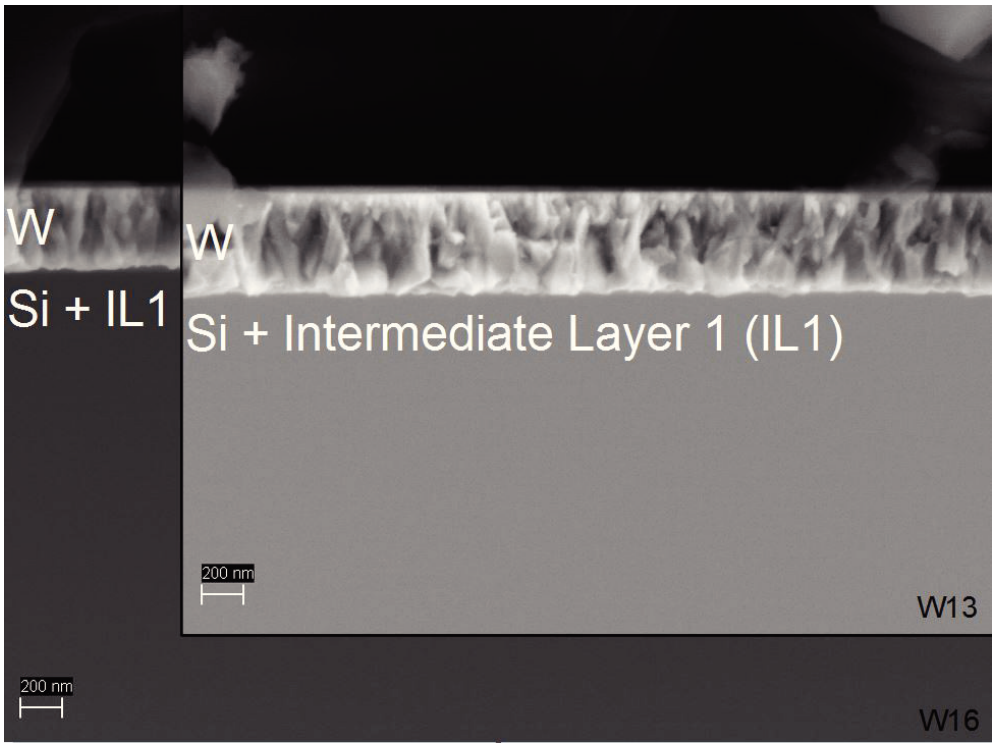

Figure 34: SEM images of single-step deposited tungsten (W16) and step-wise deposited tungsten layer (W13) of roughly 400nm thickness. The film thickness of the W layers deviates in the cases of step-wise and single-step deposition procedure.

9.4 ACKNOWLEDGEMENTS

The customized test samples were kindly provided by J. Siegert and F. Schrank (ams AG, Premstätten, Austria). The LUS measurements were carried out with the support of R. Nuster and G. Paltauf (Karl-Franzens University of Graz, Department of Experimental Physics, Graz, Austria). The SEM images were provided by R. Treml (ESI, Erich Schmid Institute of Material Science, Leoben, Austria).

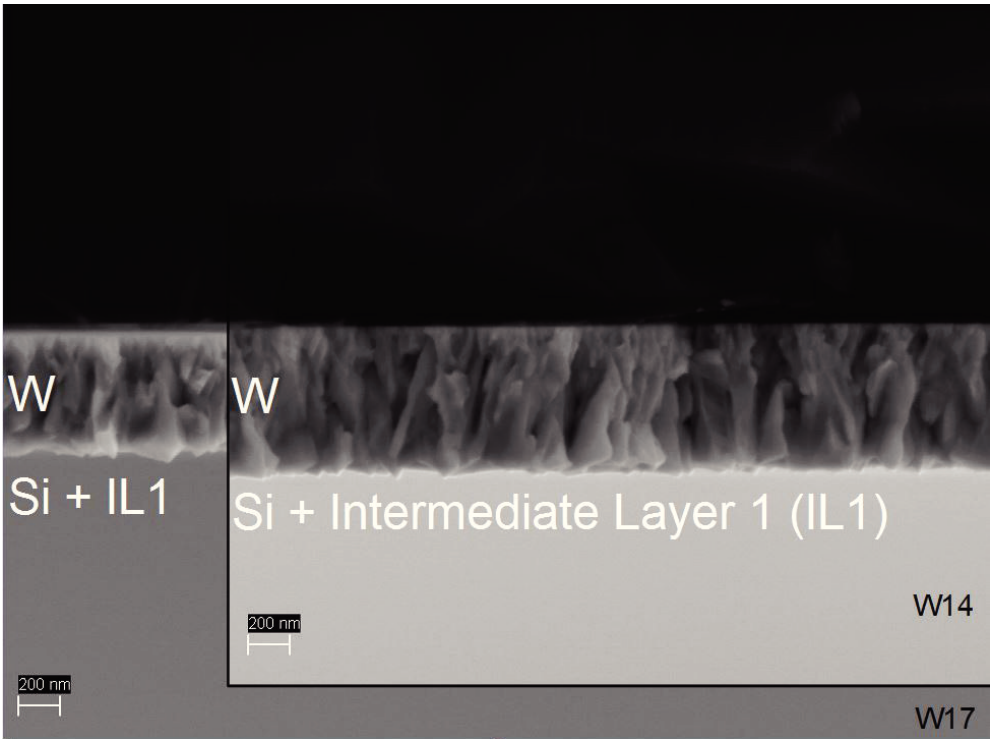

Figure 35: SEM images of single-step deposited tungsten (W17) and step-wise deposited tungsten layer (W14) of roughly 600nm thickness. The film thickness of the W layers deviates in the cases of step-wise and single-step deposition procedure.

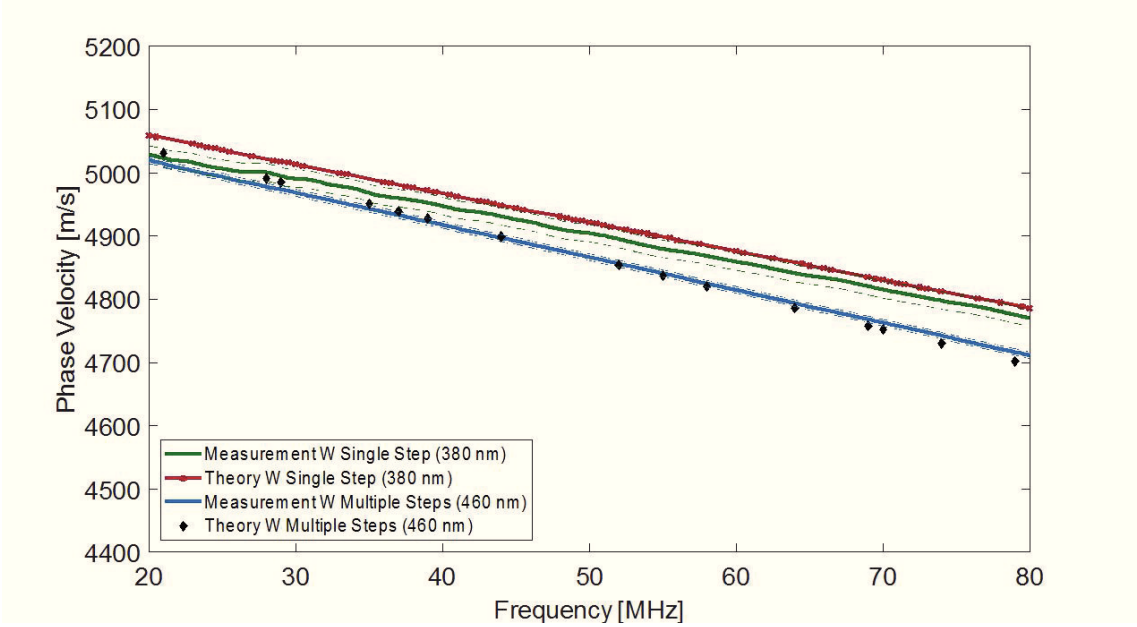

Figure 36: LUS measurements compared to the theoretical evaluated dispersion curves for film thicknesses obtained from the SEM data in the case of the presumed 400nm film thickness; the error in the LUS measurements is indicated by broken lines.

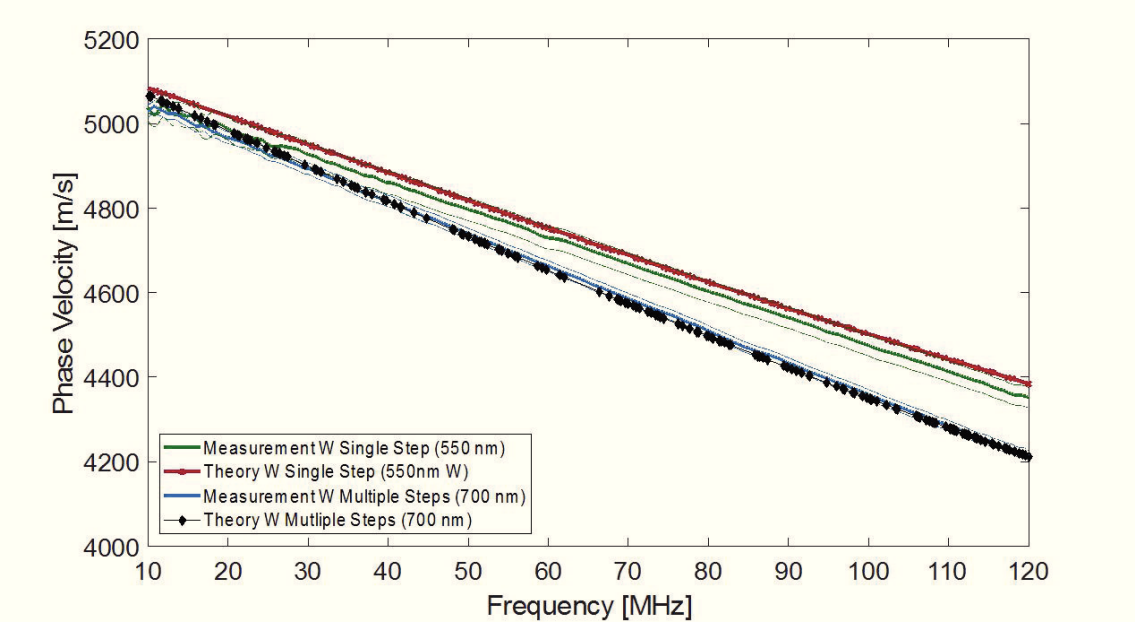

Figure 37: LUS measurements compared to the theoretical evaluated dispersion curves for film thicknesses obtained from the SEM data in the case of the presumed 600nm film thickness; the error in the LUS measurements is indicated by broken lines.

Part III

SCANNING ACOUSTIC MICROSCOPY

This part deals with the failure and material characterization by SAM. In Chapter 10, the SAM principle is introduced and the V(z) measurement as well as the elastodynamic finite integration technique (EFIT) simulation [27, 134] of SAM measurements are briefly discussed. In Chapter 11 the indirect detection of delaminations in PCBs, presented in [34], is reviewed. Chapter 12 and Chapter 13 consider the detection of defects in so-called through silicon vias (TSVs) for 3D integration in MtM technologies. Here, Chapter 12 deals with the automatized failure detection by SAM [35] and first simulations for wave mode enhanced failure detection are presented [37]; whereas the detection of sub-resolution defects is considered via measurement and simulation in Chapter 13. Finally, Chapter 14 discusses material characterization by SAM. In [39], $V(z)$ SAM measurements are utilized in order to obtain the Rayleigh wave velocity of a layered sample and a comparison to LUS results is made. Good agreement between SAM and LUS measurements as well as EFIT simulation outcome is found.

10 SCANNING ACOUSTIC MICROSCOPY (SAM) PRINCIPLE

The operating principle of a SAM can be found in the book by Briggs and Kolosov [14] for example. A short overview was given in *e.g.* [34]. The summary of the SAM principle presented in this chapter follows [34] closely.

The key element of a SAM is a piezoelectric transducer mounted on an x-y-z stage. The transducer emits ultrasonic waves that propagate through a lens towards the sample of interest, see Figure 38. The lenses are often fabricated out of sapphire and a thin anti-reflective coating (ARC) is applied in order to achieve maximal transmisson from the lens into the coupling liquid (mostly water). By moving the transducer in the z-direction, the sound field can be focused onto the surface of the sample. Decreasing the distance between lens and sample even further (de-focus), the sound field can be focused inside the sample, where additional wave modes are excited, if the opening angle of the lens is big enough, see Figure 38. At the interfaces, the acoustic sound wave is partially reflected

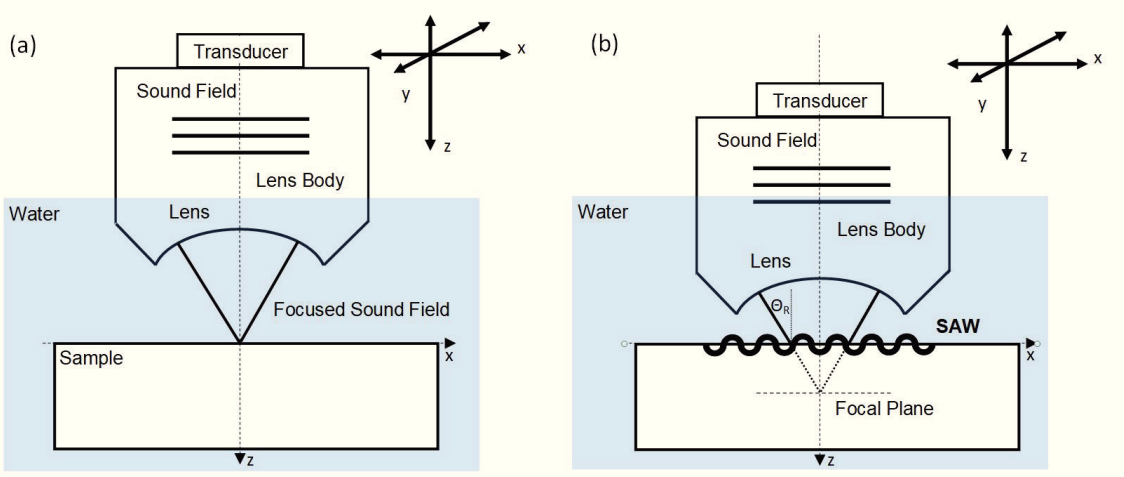

Figure 38: Schematic of SAM measurements. Measurement in-focus (a) and measurement de-focused (b), where surface acoustic waves are excited on the sample [64].

according to

$$R(90°) = \frac{-(Z_1 - Z_2)}{(Z_1 + Z_2)} \tag{26}$$

where perpendicular incidence of the sound waves is assumed. Z_1 denotes the acoustic impedance (product of sound velocity and mass density) of the medium 1, from which the sound field is transmitted into medium 2 (with acoustic impedance Z_2). The non-reflected remaining ultrasonic wave is transmitted into the sample where it undergoes further reflection as well as attenuation and scattering. The reflected parts of the acoustic waves travel back through the coupling liquid and the acoustic lens to the transducer. Here, they are spatially integrated by the piezoelectric element and "transduced" into a time-variant electrical signal. This signal is presented as a function of time in the

amplitude-scan mode, also called SAM **A-scan** mode.

As an example, Figure 39 shows the simulated sound field (EFIT simulation, see Section 10.2) transmission and reflection considering three contrasting samples: (a) a PMMA-epoxy sample, (b) a copper-epoxy sample and (c) an epoxy sample with an air inclusion, representing the case of a delamination in a material. Figure 40 shows the corresponding A-scans to Figure 39. In case (a), the sound field is transmitted through the water-PMMA interface and subsequently through the PMMA-epoxy interface with almost no reflection due to the similar acoustic impedances of water, PMMA and epoxy. In contrast, a high amount of reflection takes place at the water-copper interface, due to the impedance mismatch of water and copper. In the case of the epoxy layer with an air inclusion, almost no signal is reflected at the water-epoxy interface, whereas practically the entire remaining acoustic waves are reflected at the epoxy-air interface.

Considering the high reflection of sound waves at air in a material - and the resulting drastic change in the SAM A-scan (see Figure 40) - the SAM is predestined for the detection of delamination and cracks. In general, the SAM outperforms *e.g.* the otherwise powerful X-Ray analysis in this respect [34]. In Figure 40, the signal components arriving later in the SAM A-scan correspond to larger distances that the ultrasonic waves had to travel. If the longitudinal sound velocity in the concerned material of the sample is known, the time delay between two pulses can be converted to the physical distance between the two sources of the reflection (in the z-direction). The frequency components of the reflected ultrasonic wave can be obtained by Fourier transformation. The dominant frequency f of the acoustic wave determines the achievable lateral resolution W :

$$W = \frac{\lambda}{2NA}, \tag{27}$$

with the wavelength $\lambda = v/f$, and $NA = \sin(\theta)$; where θ is the semi-angle of the lens aperture and v is the velocity of the acoustic wave in the propagation medium. Therefore, an increase in frequency leads to smaller W, thus smaller structures can be resolved. However, an increase in frequency causes increased damping by the coupling liquid [164] and is inevitably connected to a decrease in penetration depth caused by attenuation effects in the analysed sample.
The resolution in z-direction is also of high relevance in SAM measurements. According to [87], the axial resolution of a SAM is

$$\delta_{axial,pulse} = \frac{c\delta t}{2}, \tag{28}$$

if two pulses need to be separated (δt denotes the temporal pulse width of the ultrasonic signal and c denotes the longitudinal wave velocity inside the sample). Axial surface extensions of the sample can be detected via SAM according to

$$\delta_{axial,water} = \frac{c_W}{2SR}, \tag{29}$$

where SR denotes the sampling rate of the acoustic microscope and c_W the velocity of sound in water.

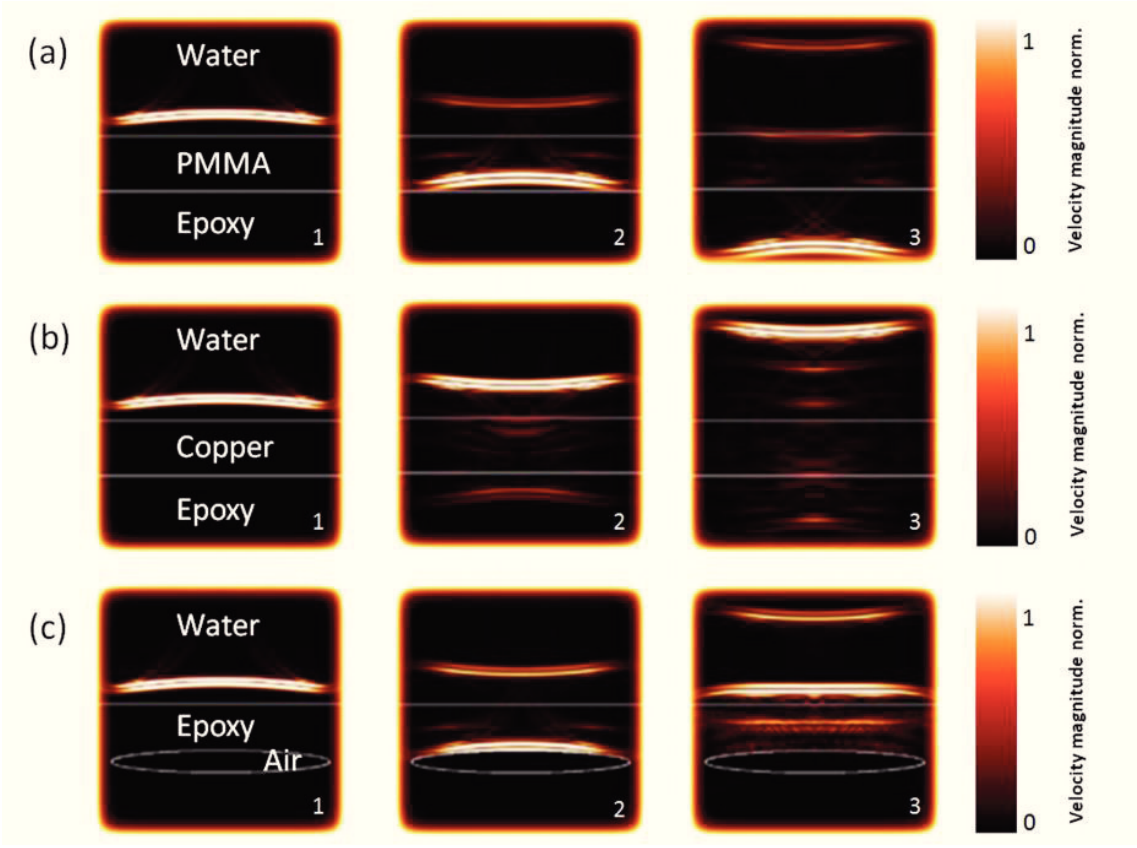

Figure 39: EFIT [27] simulation of SAM measurements in the case of the reflection at (a) a PMMA-epoxy sample, (b) a copper-epoxy sample and (c) an epoxy layer with an air bubble. All three samples are immersed in water. Time-steps 1 - 3 are shown [34].

The A-scan mode gives information about the sample along the z-axis at a single x-y location. By moving the transducer in the x-y plane (keeping the z distance fixed) and collecting the A-scan data at each point, 3D information of the sample can be obtained. Alternatively, 2D cross-sections at a certain time range in the A-scan (corresponding to a depth range in the sample) can be acquired and represented as so-called SAM **C-scan** images. In SAM C-scans, the maximum amplitude in a given time-interval (often referred to as "time gate" or simply "gate") of the A-scan is evaluated and depicted as gray value. Brighter pixels correspond to higher signal amplitudes and thus high reflection coefficients of the sample at this x-y position.

10.1 ACOUSTIC MATERIAL SIGNATURE $V(z)$

One outstanding attribute of SAM was investigated in [39]: The SAM offers the possibility to monitor the intensity V of the reflected sound field as a function of the defocus position z, see *e.g.* [14]. This section follows [39] almost at verbatim.
As already mentioned, Rayleigh waves can be excited on the surface of the sample (see Figure 38), if the opening angle of the lens includes the Rayleigh angle θ_R:

$$\theta_R = \sin^{-1}\left(\frac{v_0}{v_R}\right). \tag{30}$$

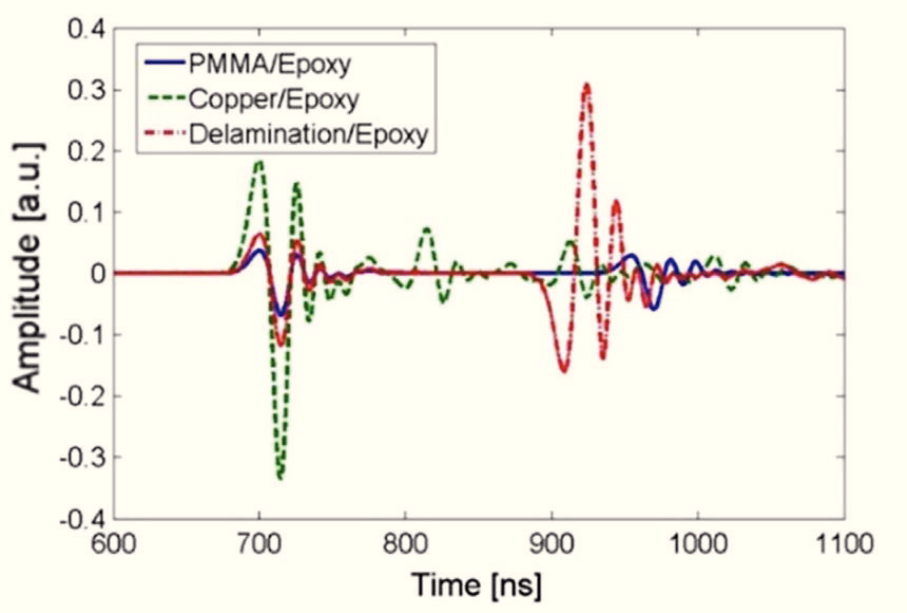

Figure 40: EFIT [27] simulation of the A-scan in the case of the reflection at a PMMA-epoxy sample (blue solid line), copper-epoxy sample (green broken line) and at an epoxy layer with an air bubble (red dotted line), corresponding to the case of delamination. All three samples are immersed in water [34].

Here, v_0 denotes the sound velocity in water and v_R the Rayleigh wave velocity of the sample. Once excited, the Rayleigh wave propagates along the surface of the sample and leaks energy back to the transducer. At the piezoelectric element of the transducer, the phase and amplitude of the longitudinal sound wave reflected from the sample and the leaky Rayleigh wave are summed up [14]. The two wave modes (Rayleigh wave and longitudinal wave) interfere alternating constructively and destructively, depending on the defocus position z of the transducer. According to [14], the periodicity Δz of the oscillation depends on the Rayleigh sound velocity v_R of the investigated sample via

$$\Delta z = \frac{\lambda_0}{2\,(1-\cos(\theta_R))} \tag{31}$$

where λ_0 denotes the wavelength of the acoustic wave in water.
The importance of $V(z)$ measurements relies on the possibility to measure the Rayleigh wave velocity in a broad frequency range (which is interesting for layered samples) at a very small spot (the focal spot of the lens) on the sample.

10.2 INTRODUCTION TO EFIT

The simulation of acoustic wave propagation via the elastodynamic finite integration technique (EFIT) was introduced in [27]. The EFIT simulations presented in this thesis are results of the cooperation with **René Hammer** (Materials Center Leoben, Simulation Department).
EFIT offers a good compromise in terms of accuracy taking into consideration its com-

putational cost. For the simulation, the basic equations for (1) the kinetics

$$\rho \frac{\partial \vec{v}}{\partial t} = \vec{\nabla} \times \sigma, \tag{32}$$

(2) the kinematics

$$\frac{d\epsilon}{dt} \approx \frac{1}{2}\left[\left(\vec{\nabla} \otimes \vec{v}\right) + \left(\vec{\nabla} \otimes \vec{v}\right)^{T}\right], \tag{33}$$

(3) and material law

$$\sigma \approx E \cdot \epsilon, \tag{34}$$

are put on a staggered grid and evolved in time via a leap frog scheme [27] (see also [39]). Here, $\vec{v}$ denotes the particle velocity, ρ the mass density, σ is the stress tensor and E and ϵ denote the stiffness tensor and the strain tensor, respectively.

10.3 SAM SETUP

In the presented research [34, 35, 39, 64, 66], a commercially available scanning acoustic microscope "SAM 400" (PVA TePla Analytical System GmbH, Westhausen, Germany) was operated in reflection mode, using various transducers with frequencies from 75 MHz to 400 MHz, equipped with lenses of small opening angles (about 8°) and wide opening (up to 120°) acoustic objectives (AO). The reflected signal was analysed by the inspection software "WinSAM5" (PVA TePla Analytical Systems GmbH, Westhausen, Germany) and by custom made programs in the case of the $V(z)$ measurements. The SAM was adapted in order to perform $V(z)$ measurements, where the SAM is usually operated in tone burst (TB) mode (PVA TePla Analytical Systems GmbH, Westhausen, Germany). In the TB mode, the longer excitation time of the pulses results in a very narrow signal in the frequency domain, allowing for precise frequency-dependent measurements (see *e.g.* [59]). The SAM was additionally equipped with a 7 GHz ADC card.

11

3D FAILURE CHARACTERIZATION OF PCBS VIA SAM

This chapter concerns the non-destructive failure analysis of printed circuit boards (PCBs), where an indirect delamination detection is proposed. Complementary simulation efforts and destructive sample analysis corroborate the obtained results. The results presented in this work are published in [34].

11.1 MOTIVATION

The ongoing miniaturization trends (considering MtM technologies, see also Section 1.1) have high impact on the design of PCBs. The multi-layered build ups - involving metals in combination with composite materials - render PCBs complex systems, as far as failure analysis and detection are concerned. Invasive analysis methods are not to be preferred due to the possibility of introducing new defects by the failure inspection itself. Moreover, the measurement cannot be repeated if the sample is (partly) destroyed. In non-destructive failure detection and analysis, also preferred methods like X-ray computed tomography have difficulties due to the high amount of copper in the analysed PCB samples [34]. One of the major failure modes in PCBs are delaminations which can be caused by manufacturing processes or thermo-mechanical exposure. In [34], the detection of delaminations in PCBs by SAM is described. It is shown that, even though the acoustic analysis is complicated because of the multi-layered, multi-material build-up (see also Chapter 10) of the investigated PCBs, delaminations can be detected within the PCB. To this purpose, the resulting curvatures of the layers were analysed and SAM 2D data in combination with novel 3D data was evaluated. In addition, EFIT simulations (see Section 10.2) were carried out. Complementary destructive physical cross-sectioning corroborates the obtained results.

11.2 MEASUREMENT AND DATA EVALUATION

The measurements were performed using SAM (Chapter 10), where the data analysis was supported via EFIT simulations (Section 10.2). In Table 16, the EFIT simulation parameters and settings for the analysis of acoustic wave interaction with PCBs presented in this chapter are summarized and Table 17 gives details about the used material properties.

MATERIAL	REFERENCE	$f[MHz]$	$\Theta[°]$	$Area$	ngp
Cu, Epoxy	[15, 95]	100	20	xz	25

Table 16: Summary of EFIT parameters and simulation settings. f denotes the frequency and Θ is the semi-angle of the lens aperture. $Area$ refers to the 2 dimensional simulation area, in this case the xz plane (the coordinates refer to Figure 38) and ngp denotes the grid points per wavelength.

MATERIAL	REFERENCE	$E[GPa]$	ν	$\rho[kg/m^3]$	$d[\mu m]$
Cu	[15]	117	0.34	8960	64
Epoxy	[95]	3.5	0.33	1540	200

Table 17: Summary of material parameters of PCBs for EFIT simulations, where the elastic modulus E, the Poisson ratio ν, the mass density ρ and the thickness of the layers are given.

11.2.1 *Scanning acoustic microscopy*

The "SAM 400" (PVA TePla Analytical System GmbH, Westhausen, Germany) was operated in reflection mode, using a transducer of 75MHz nominal center frequency. The reflected signal was analysed by the inspection software "WinSAM5" (PVA TePla Analytical Systems GmbH, Westhausen, Germany). See also Section 10.3 for details on the SAM measurement. In addition, the "Avizo Fire 8.0" software was utilized in order to obtain 3D representations of the analysed PCBs.

11.2.2 *Sample and complementary assessment*

A cross-section of the analysed PCB (48.5×82×1.2 mm^3) is shown in [34]. Via a thermal cycling process, delamination in the PCB was introduced. For the acoustic analysis, the multiple copper layers in the sample present a severe hindrance. According to Equation 26, R at an epoxy – copper interface is approximately 80 %. As a consequence, the copper layers embedded in the epoxy matrix render PCBs nearly impenetrable for acoustic analysis [13].

After the SAM analysis, the PCB was ground and imaged sequentially using optical microscopy. Using the Olympus Streamsoftware, the imaged sections were stitched into a single image of the PCB, where the delamination could be located. The cross-sectioning took place without considering the results obtained by the SAM analysis.

11.3 RESULTS

In this work, a two dimensional EFIT simulation [27] of the SAM measurement of delaminated PCBs was performed. Simulated equivalents of the SAM A-scan were obtained and compared to the A-scans from the SAM measurements, see Figure 41.

Altough the delamination could not be detected directly, the analysis of the 3D data and the comparison to the simulation enabled the detection of the delamination in the x-y plane and the delaminated layer could be identified. Figure 42 shows the comparison of the SAM data analysis (green) to the physical cross-sectioning results (red and blue lines).

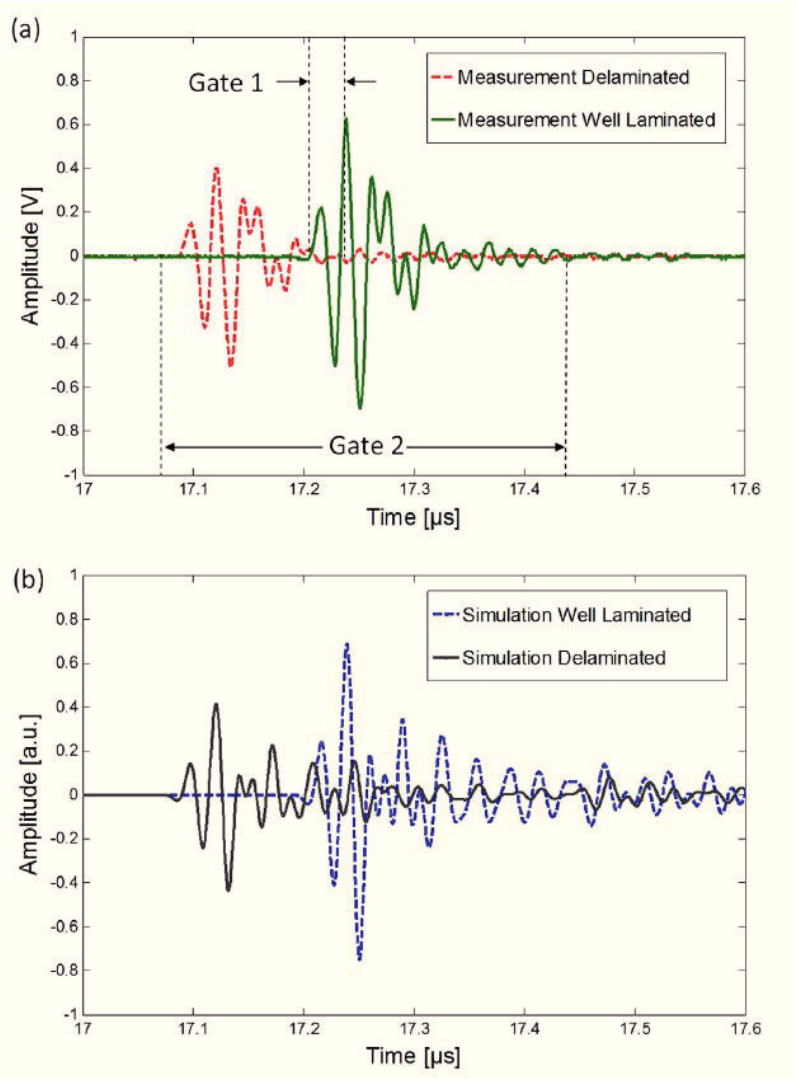

Figure 41: A-scan of well laminated and delaminated area of PCB (a) SAM measurement and (b) EFIT simulation result from [34].

11.4 DISCUSSION AND SUMMARY

Although the failure characterization of PCBs presents a highly relevant task in context of MtM technologies, state of the art methods show drawbacks in their characterization [34]. Also the SAM analysis is complicated because of the multi-layered material combination of copper and epoxy, which represents a severe hindrance for the otherwise powerful SAM failure detection in analysis.

Here, the indirect detection of delamination in PCBs is proposed and carried out via SAM measurements and advanced data analysis. EFIT simulations support the presented SAM analysis and good agreement was found. The indirect delamination detection shows the advantage of being applicable even if the delaminated area is filled with water or SAM through scans (see *e.g.* [164] for details on SAM through scans) are not feasible, as pointed out in [34].

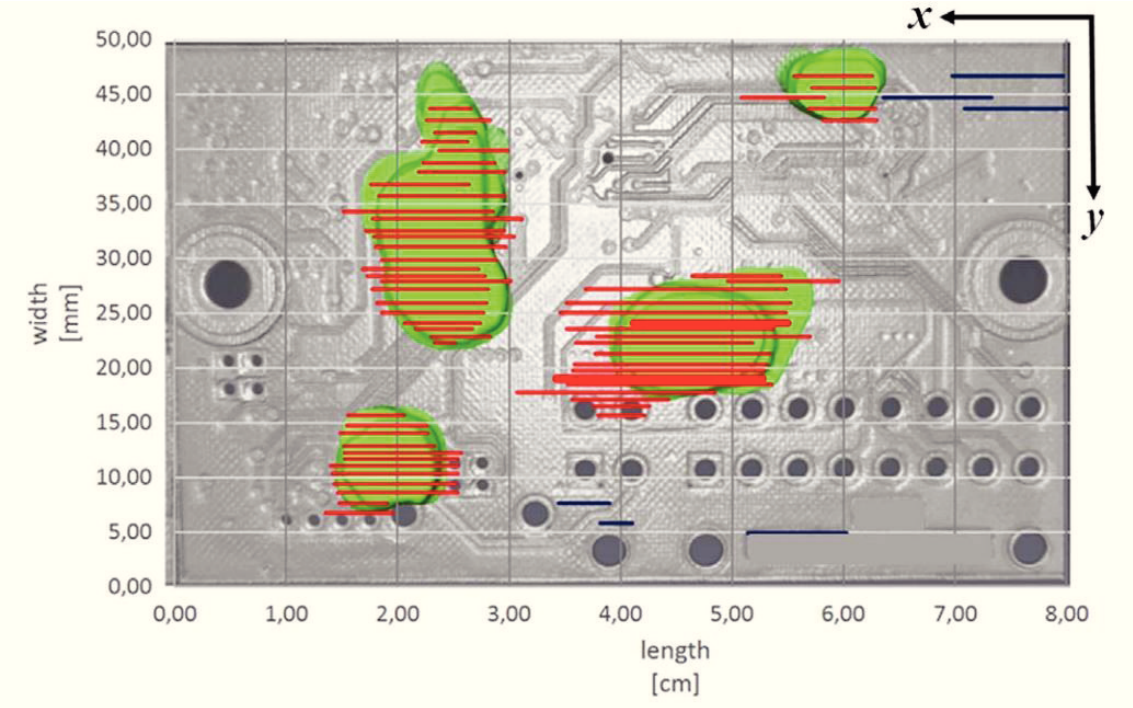

Figure 42: Comparison of SAM measurements (green) to mechanical cross-sectioning results (red and blue lines) of PCB [34].

12 SAM ANALYSIS OF TSVS: MEASUREMENT AND SIMULATION

Publications [35] and [37] consider the failure detection in through silicon vias (TSVs) for 3D integrated technologies by SAM. In the following, the results obtained in [35] are summarised briefly and [37] is put into context.

12.1 MOTIVATION

A promising way to realize More-than-Moore technologies (see also Section 1.1) is the 3D integration of devices [30]. Here, a key element is the vertical electrical interconnection between two or more layers of active electronic components. Such vertical interconnections are referred to as through silicon vias (TSVs) [74]. Although the TSV technology is a promising candidate in the ongoing trend of miniaturization, aiming for higher electrical performance, lighter weight and lower power consumption, the processing, material engineering and quality management of TSVs remains highly demanding [74].

A distinction between "open" and "filled" TSVs can be made. While the latter are completely filled with conducting materials - often copper - open TSVs have a metallized side wall for the electrical connection and remain hollow. In comparison to filled TSVs, open TSVs show advantages regarding stress relaxation [41] and are highly relevant for sensor applications - as pointed out in [67, 68]. Open TSVs are processed by etching holes into the silicon using deep reactive ion etching (Bosch process) [74]. During this process, the generated TSV structures are protected with a polymer coating that is removed in several cleaning steps before the metallization. In *e.g.* [41] it was pointed out that residual stresses in the metallization have direct impact on the defect formation in TSVs.

For an improved material engineering and quality management of TSVs, the detection and understanding of different failure modes is crucial. Especially the detection of polymer residues and defects in the metallization are a big challenge in terms of the characterization of the whole TSV (side-wall and bottom), and the necessary resolution down to the nm regime. In the defect detection and evaluation of open TSVs, non-destructive analysis methods are preferably applied. Non-destructive methods show the advantages of repeatable measurements, minimizing the potential introduction of additional failure modes by the testing itself and are attractive for industrial applications due to their potential for in-line or at-line inspection. However, several state of the art methods show drawbacks in the characterization of open TSVs. For example, SEM (see *e.g.* [119]) is a method that provides high resolution for the bottom and side wall inspection of TSVs. However, it demands special sample stages and preparation of the sample, is time consuming and costly (if the damaged TSVs are not pre-defined) due to the necessary step by step inspection of each TSV. Some other potential TSV characterization methods and their drawbacks are summarised in [64].

In [35], the possibility to detect metallization defects with extensions of about 50µm in an automatized way by SAM is discussed.

12.2 SAM MEASUREMENT, EFIT SIMULATION AND DATA ANALYSIS

In [35], the commercially available scanning acoustic microscope "SAM 400" (PVA TePla Analytical System GmbH, Westhausen, Germany) was operated in reflection mode, using an AO transducer of 100MHz nominal center frequency. The reflected signal was analysed by the inspection software "WinSAM5" (PVA TePla Analytical Systems GmbH, Westhausen, Germany), providing SAM C-scan images. Subsequently, the SAM C-scan images were analysed via a pattern recognition algorithm [85, 113].

In addition, the SAM measurement of a TSV showing a bottom defect was simulated via the EFIT [27] approach, see also Section 10.2. Here, the interaction of an acoustic wave with 100MHz center frequency with defect and intact TSVs was simulated, see Figure 43 for the simulation schematic.

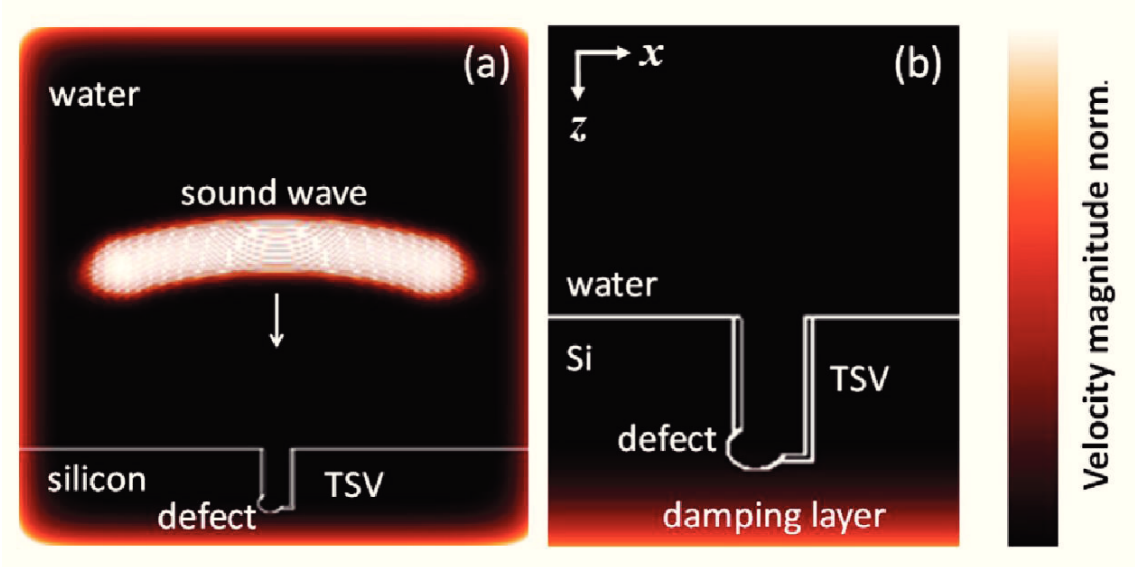

Figure 43: Principle of SAM measurement of TSVs (EFIT simulation): (a) a sound wave propagates from top to bottom and (b) close up [35].

In Figure 43, an acoustic wave propagates from the top through water to the silicon sample. The sound field is focused by excitation along a circular arc. In this manner, the angular aperture of 60° and the aperture diameter of approximately 1mm are realized. This represents the geometries of the AO lens applied in the SAM measurement. In Table 18, the EFIT simulation parameters and settings for the analysis of sound field interaction with TSVs presented in this chapter are summarized and Table 19 gives details about the used material properties.

The A-scan is detected at one point in our simulation in contrast to the detection in the measurement, where the lens is sensitive to the reflected acoustic field at its whole opening angle and therefore detects *e.g.* energy emitted by surface acoustic waves.

MATERIAL	REFERENCE	f[MHz]	Θ[°]	Area	ngp
Si, W	[15, 124]	100	30	xz	20

Table 18: Summary of EFIT parameters and simulation settings, where f denotes frequency and Θ is the semi-angle of the lens aperture. Area refers to the 2 dimensional simulation area, in this case the xz plane (the coordinates refer to Figure 38) and ngp denotes the grid points per wavelength.

MATERIAL	REFERENCE	E[GPa]	ν	ρ[kg/m^3]
Si	[49]	130	0.28	2330
W	[15]	405	0.28	18250

Table 19: Summary of material parameters of TSVs for EFIT simulations, where the elastic modulus E, the Poisson ratio ν and the mass density ρ are given.

In order to prevent back-reflections, a damping layer was implemented at the boundaries of the simulation area, see Figure 43 (r.h.s.) and the colour-scale displays the normalized velocity magnitude.

12.3 RESULT

In Figure 44 the EFIT simulation of the SAM measurement of a TSV with a metallization defect at the bottom is shown. Figure 44 depicts that the sound wave cannot be focused to TSV bottom, due to the geometries of the AO and the small diameter of the TSV. Therefore, positioning the transducer centered over the TSV, a first reflection from the surrounding silicon followed by a second reflection from the bottom of the TSV is observed. In Figure 44 time-step 2, the incident longitudinal sound wave excites additional wave modes in the silicon. In Figure 44 time-steps 3 and 4, the Rayleigh wave, which leaks energy back toward the transducer through the coupling liquid, can be observed. In Figure 44 time-step 4, parts of the sound waves have left the TSV and travel back through the coupling liquid towards the transducer. In [35] slight differences were found in the simulated A-scans for various failure modes.

Concerning the SAM measurement, a SAM C-scan is presented in Figure 45. Here, the TSVs showing no defect are marked with a blue circle via the circular Hough transform algorithm [85, 113]. In Figure 45 the scale bar is omitted in order to protect the manufacturers' expertise.

12.4 DISCUSSION AND SUMMARY

The SAM failure analysis of open TSVs with an AO lens proved to be very powerful in the detection of bottom defects with extension of about 50µm. The resolution of the SAM C-scan images was sufficient to successfully apply a pattern recognition algorithm in order to distinguish defect TSVs from TSVs where no failure mode was detected in the SAM analysis automatically. In addition, the SAM software was updated in order

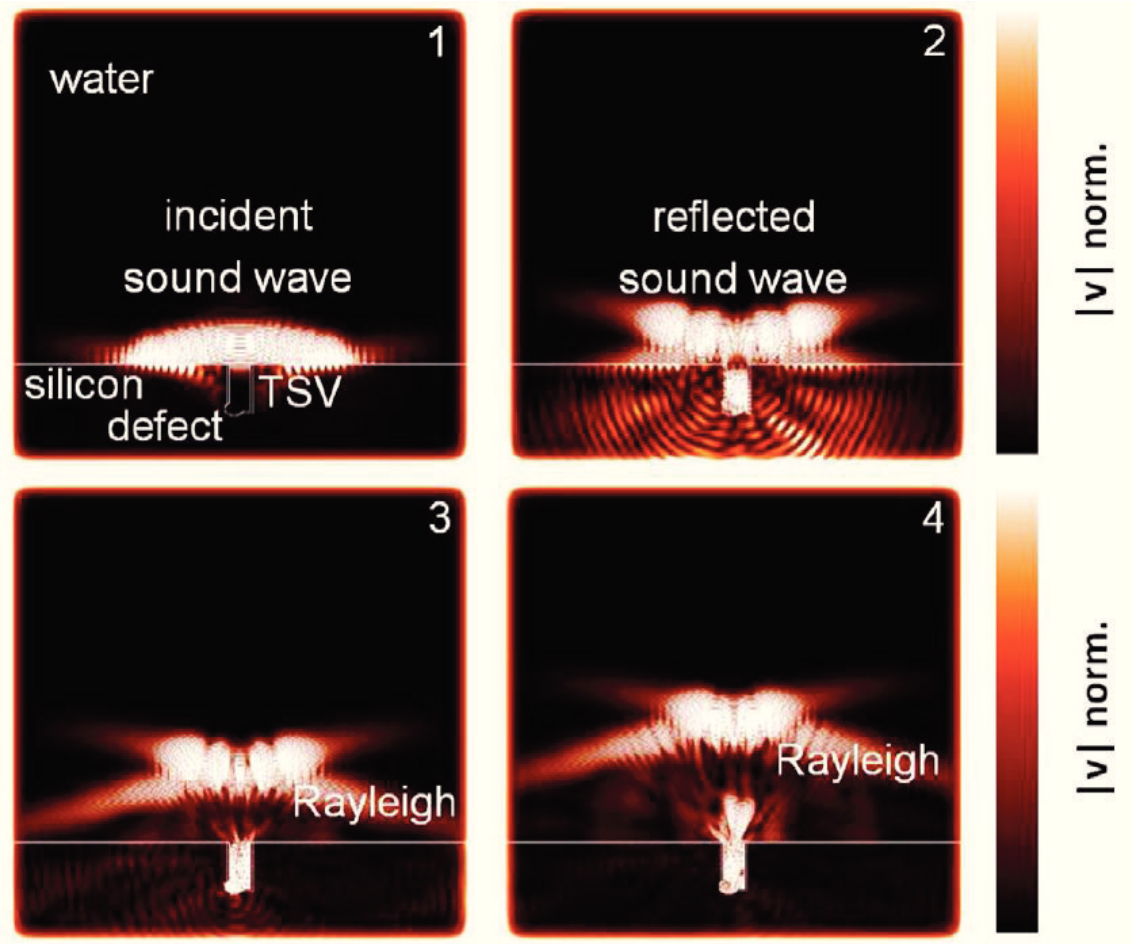

Figure 44: SAM measurement of defect TSV (EFIT simulation), time-steps 1 - 4.

to perform SAM C-scans at predefined de-focus positions automatically, enabling fast and reliable failure detection. The obtained EFIT simulation results support the SAM analysis.

12.4.1 *Enhanced accretion detection via SAM*

The work published in [35] discusses the possibility to detect TSV bottom defects with extension of about 50µm. In [35], the center frequency of the applied transducer was at 100MHz, which gives a wavelength in water of approximately 15µm. According to Equation 27, the resolution of the SAM is about half a wavelength, if the numerical aperture is close to one. A numerical aperture close to one can be achieved in some cases [164]. In *e.g.* the book by Briggs and Kolosov [14], the detection of surface cracks with openings below the resolution limit is discussed. The detection of sub-resolution surface defects considered in [14] relies on the excitation of SAWs, that interact with the surface defects. The defects are then detected via interference fringes.

In [37], similar effects in open TSVs are discussed, where additional wave modes can enhance the detection of accretions in TSVs. By EFIT simulation efforts, it is shown how acoustic waves are affected by accretions within TSVs, see Figure 46 and [37] for details.

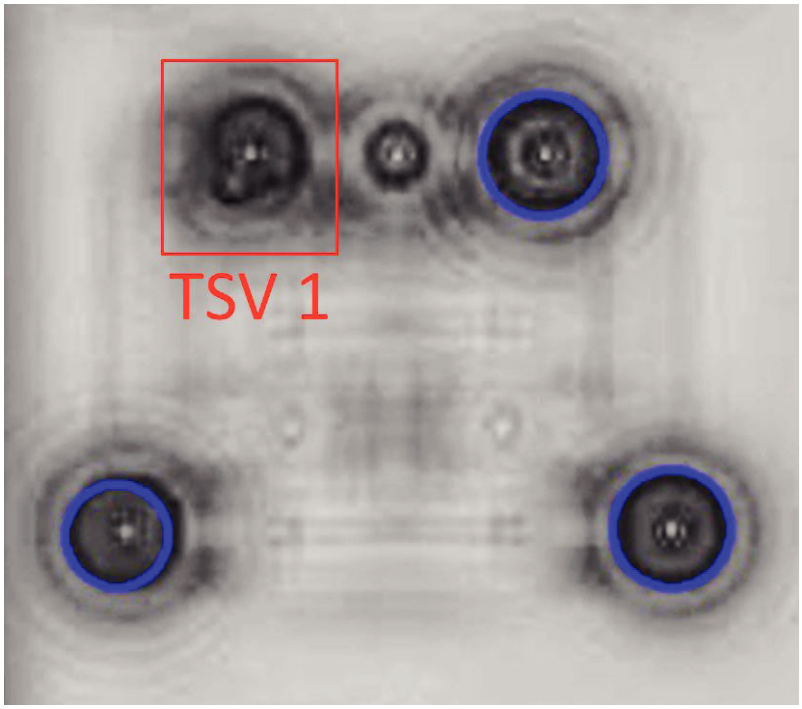

Figure 45: Pattern recognition algorithm (circular Hough transform [85, 113]) applied to SAM C-scan (xy-plane) in order to detect a bottom defect. Intact TSVs are marked with a blue circle, "TSV 1" shows a bottom defect.

In Table 20, the EFIT simulation parameters and settings for the analysis of the sound

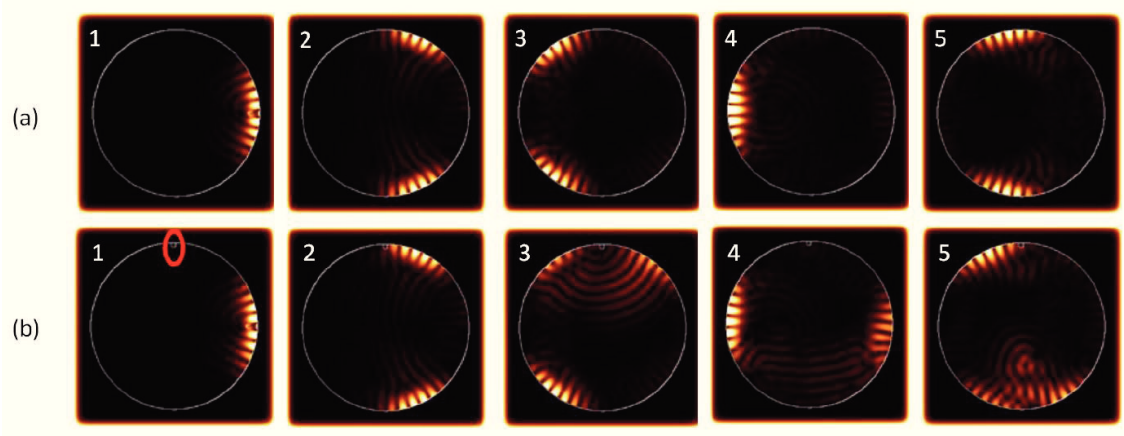

Figure 46: EFIT simulation of sound propagation along the rim of an open TSV, in the xy-plane: (a) shows the case of an intact TSV, in (b) a small accretion at the TSV coating disturbs the sound wave propagation. The TSV is filled with water and the colour-scale represents the normalized velocity magnitude.

propagation along the TSV rim are summarized.

In the next section, the detection of cracks with openings below the lateral and axial resolution limit is demonstrated (by SAM measurement and simulation) and it is shown how additional wave modes are indeed beneficial in this process.

MATERIAL	REFERENCE	f[MHz]	Area	ngp
Si	[15, 124]	100	xy	25

Table 20: Summary of EFIT parameters and simulation settings for the sound wave propagation along the TSV rim. Here, f denotes the frequency and Area refers to the 2 dimensional simulation area, in this case the xy plane (the coordinates refer to Figure 38) and ngp denotes the grid points per wavelength, the Si input values are listed in Table 19, according to [15].

13 SUB-RESOLUTION CRACK DETECTION IN MTM COMPONENTS

In the following chapter, the detection of artificially introduced cracks in open TSVs (see Section 12.1) by SAM is discussed. Notably, the cracks show openings below the lateral and axial resolution limit of the SAM and they run parallel as well as normal to the SAM axis. The experimental results and the theoretical evaluation are planned to be published in the near future in accompanying papers [64, 66].

13.1 MOTIVATION

The potential of SAM to detect surface cracks which show less than half a wavelength opening (compare to Equation 27) has attracted great attention in recent decades. One underlying principle is the excitation of SAWs on the sample via transducers equipped with AO lenses. Interference effects make the surface crack detection below the lateral resolution limit of half a wavelength possible [14]. In [1] the influences of subsurface cracks on SAW propagation are considered. More recently, a wide range of literature considering the ultrasonic detection of surface-breaking cracks (perpendicular to the sample surface) in single material samples via experiment and theoretical evaluations has been published [18, 45, 60, 81, 82, 92, 149, 165].

In [64], the measurement of cracks of less than one micron opening – corresponding to less than a tenth of the acoustic wavelength – by SAM is demonstrated. Notably, the evaluated samples in [64] are open TSV (see Section 12.1) test arrays, highly relevant for 3D integration technology in microelectronics. It is speculated that Rayleigh waves might be the driving force enabling the sub-resolution defect detection in [64].

In [66], the destructive analysis of pre-defined TSVs (showing a special characteristic in SAM measurements [64]) is presented. In this way, additional cracks along the TSV coating – normal to the sample surface – are found. These cracks are circumferential cracks along the TSV coating (see [64] , additional material). In [66] EFIT [27] simulations are carried out in order to determine if (1) Rayleigh waves are indeed the key element in the SAM analysis presented in [64] and (2) in order to investigate the influence on SAM A-scans of the cracks normal and parallel to the SAM axis separately.

13.2 MEASUREMENTS

In [64] the failure detection in open, tungsten coated TSVs is discussed in detail, where various failure modes are addressed. The outcome of the SAM analysis is corroborated by SEM and µXCT data evaluations. The failure mode considered in the following concerns cracks with openings of less than a tenth of the acoustic wavelength. These circumferential-cracks lead to reproducible intensity patterns - reminding of blossoms - in the SAM C-scans, see Figure 47, TSV "D6 β". However, the inspection of TSV "D6 β" by µXCT shows no failure mode, see Figure 48.

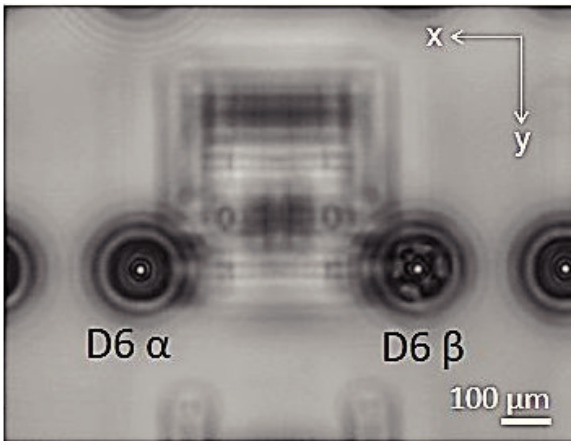

Figure 47: Blossom characteristic of defect TSV in SAM C-scan: SAM measurement of TSV without failure mode "D6 α" and defect TSV "D6 β" showing a blossom-like characteristic.

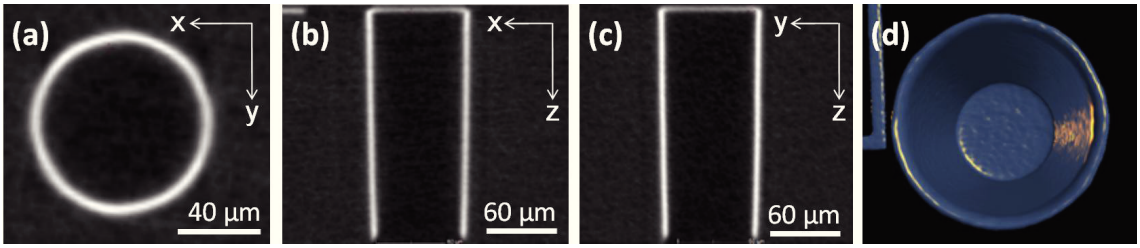

Figure 48: µXCT analysis of TSV "D6 β": (a) horizontal cross-section at the TSV bottom, (b) vertical cross-section 0°, (c) vertical cross-section 90° and (d) 3D representation of µXCT data, no failure mode is found. The coordinates refer to Figure 38.

13.3 EFIT SIMULATIONS

The numerical simulation of ultrasonic waves in isotropic linear elastic media is described in [27], where the elastodynamic finite integration technique (EFIT) is presented (see also Section 10.2). In Figure 49, the EFIT simulation [66] of the SAM measurement [64] is shown for the case of an intact TSV. A lens body and an ARC are included in the simulation in accordance with the SAM measurements. The analysed TSVs have a diameter of approximately 100µm, a height of approximately 200µm and a coating of about 1µm . The center frequency of the transducer is 100MHz and the opening angle of the lens is 60°. In Figure 49 the transducer excites an ultrasonic wave of 100MHz center frequency in timestep 1, which propagates through the lens body to the anti-reflective coating (ARC) and through the coupling liquid towards the sample in timestep 2, until it reaches the sample surface in timestep 3. SAWs are excited in timestep 3 and the wave modes in the silicon can be observed in timesep 4, when part of the acoustic signal travels back towards the transducer and part of the signal is still within the TSV, travelling towards the TSV bottom. In the EFIT simulations, the axial symmetry in the pseudo 3D simulations is implemented according to [134]. The pseudo 3D simulations make use of the axial symmetry of the acoustic lens, the TSVs and defects in the TSVs. In the EFIT simulation, the elongation in the z-direction was summed up along the width of the transducer, in accordance with the SAM measurements in order to obtain a simulated

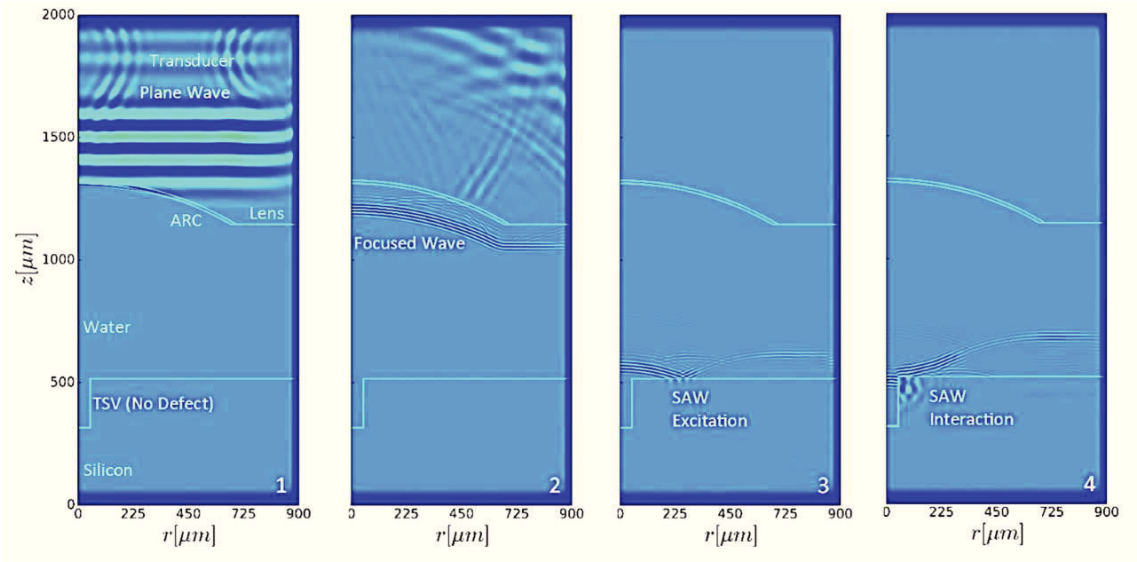

Figure 49: EFIT simulation of axial-symmetric SAM measurement: Sound interaction with intact TSV.

SAMPLE	LENS, COATING	f[MHz]	Θ[°]	AREA	ngp
Si, W	sapphire, SiO_2	100	30	axi	30

Table 21: Summary of EFIT parameters and simulation settings. f denotes frequency, Θ is the semi-angle of the lens aperture, Lens and ARC define the lens and the antireflective coating in the simulations. Area refers to axial symmetric (with respect to the z-axis) simulation area (the coordinates refer to Figure 38) and ngp denotes the grid points per wavelength. The material parameters for Si and W are listed in Table 19 according to [15, 49].

version of the SAM A-scan.

In Table 21, the EFIT simulation parameters and settings for the analysis of sound field interaction with TSVs presented in this chapter are summarized and Table 22 gives details about the used material properties.

13.4 RESULTS

In the following, the results from the SAM measurement, the data analysis and the simulation efforts are summarised. In this section, certain scale bars are omitted in order to protect the manufacturers' know-how. Figure 50 shows the SEM analysis of a pre-defined TSV (blossom-like characteristic in SAM C-scan). A circumferential crack is found, see Figure 50. Notably, the crack opening is approximatley 200nm. The crack has been imaged along the whole coating via SEM. To this purpose, the sample was mounted on a rotation and tilting stage, see the supplementary material of [64]. The SEM investigation of TSVs without the blossom-like characteristic in the SAM C-scan did not reveal circumferential cracks. In addition, the applicability of a geometry based

MATERIAL	REFERENCE	$E[GPa]$	ν	$\rho[kg/m^3]$
sapphire	[15]	345	0.29	3980
silicon dioxide	[124]	70	0.19	2200

Table 22: Summary of material parameters for EFIT simulations of TSVs SAM measurement, where the elastic modulus E, the Poisson ratio ν and the mass density ρ are given. The material parameters for Si and W are listed in Table 19 according to [15, 49].

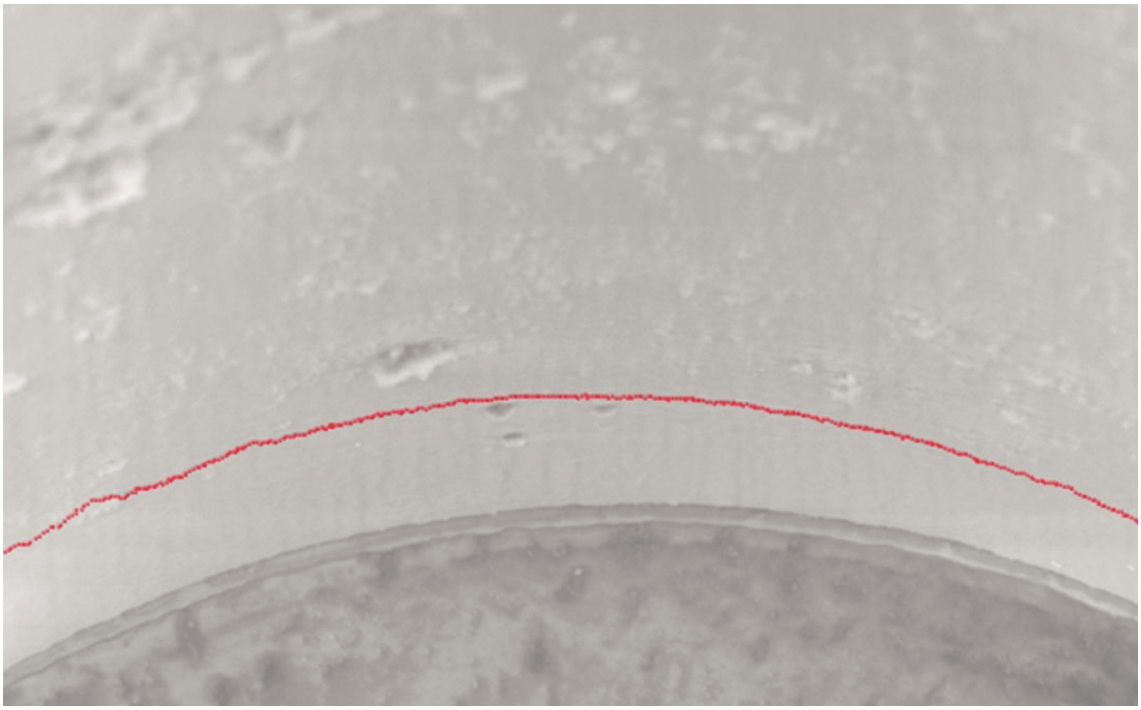

Figure 50: SEM image of pre-defined TSV: a circumferential crack is detected. The crack is coloured red to guide the eye.

pattern recognition algorithm [85, 113] to the blossom-like characteristics in the SAM C-scan was successfully tested, see Figure 51. Further destructive investigation (via ion slicing) revealed additional cracks at the TSV bottom and a delamination of the coating, see Figure 52. In Figure 52, the TSV was tilted for the slicing. The crack openings are below 200nm.

EFIT simulations were carried out in analogy to the SEM results presented in Figure 52: for the case of cracks parallel to the SAM axis, a delamination between silicon and coating and for the combination of both failure modes. See Figure 53 for a schematic representation of the failure modes within the TSV. The EFIT results for the different failure modes are compared to the case of sound interaction with an intact TSV. In Figure 54, the SAM A-scans are shown in direct comparison for the case of (a) a lens opening angle smaller than the critical Rayleigh angle and (b) a lens opening exceeding the critical Rayleigh angle. According to Equation 30, the critical Rayleigh angle is about 17°. Here, the Rayleigh wave velocity of silicon is assumed to be 5150m/s and the sound velocity of water is 1480m/s [124]. The results presented in Figure 54 show a clear sensitivity of the SAM to different failure modes, if the lens opening is sufficiently large.

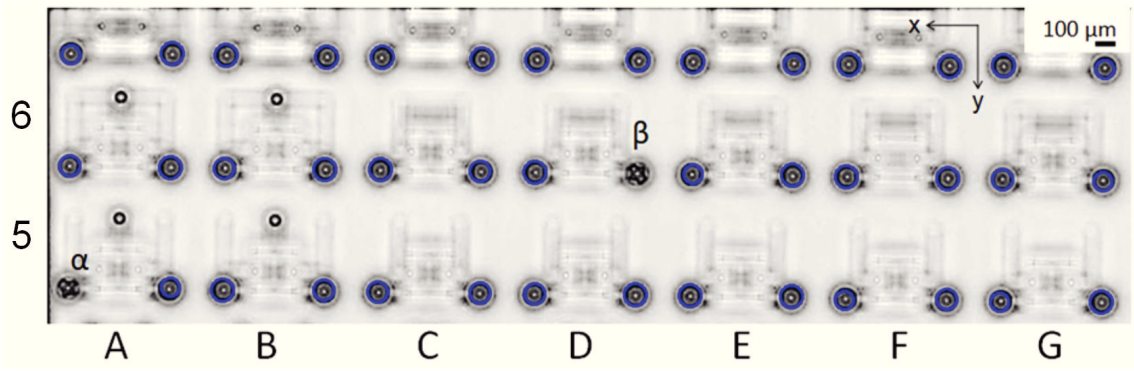

Figure 51: Indirect detection of circumferential cracks in TSVs via a pattern recognition algorithm: The TSVs showing no failure mode are detected via a geometry based pattern recognition algorithm. TSVs showing the blossom-like characteristic are not marked by the algorithm.

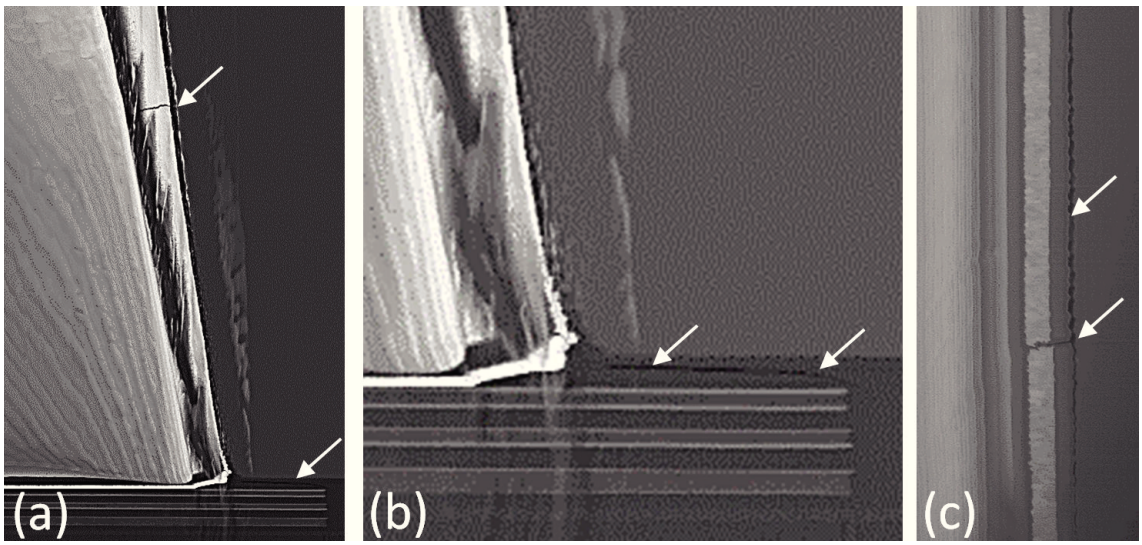

Figure 52: SEM image after ion slicing of the TSV. In addition to the circumfirential crack, also a crack at the TSV buttom and along the TSV coating are found. The crack openings are below 1µm.

13.5 DISCUSSION

In state of the art failure detection and characterization, the guiding principle seems to be "high frequency evaluation" when devices become smaller, *e.g.* [12, 108, 122]. However, an increase in frequency means also a decrease in penetration depth [164]. In [64] and [66] we demonstrate that the resolution limit of a SAM is not its detection limit via EFIT simulation and SAM measurements. It is shown, that via the excitation of additional wave modes, the SAM is capable of detecting cracks with openings of less than a tenth of the acoustic wavelength (compare also to Equation 27) in MtM relevant components. In many cases, especially for at-line or in-line inspection, it is sufficient to detect a failure mode. The detection (without high resolution images of the defect) gives the possiblity to dismiss the flawed sample or to inspect with other high resolution methods,

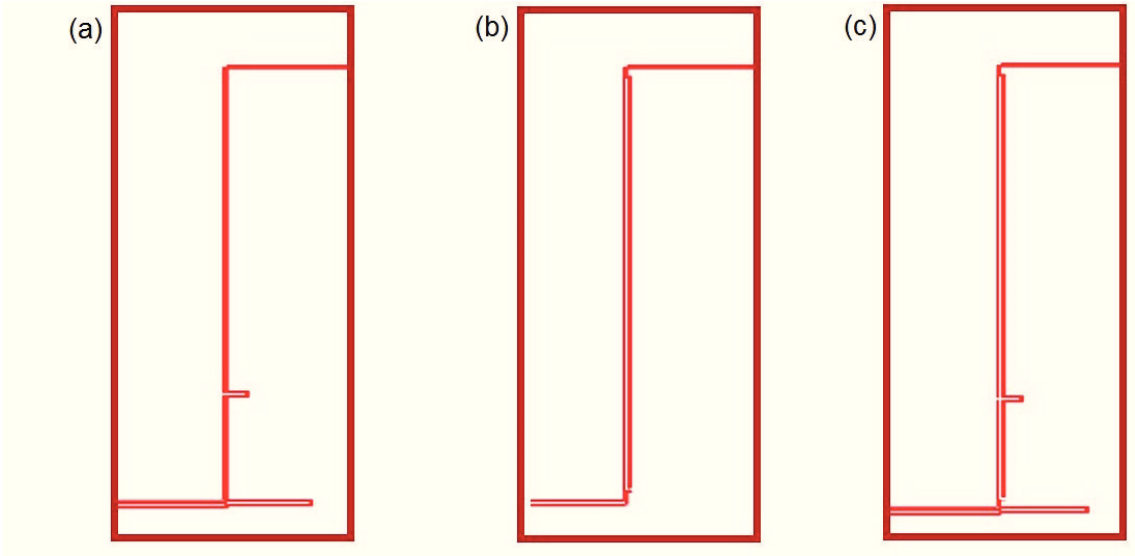

Figure 53: Schematic of the failure modes within the TSV: (a) TSV with cracks parallel to the surface, (b) cracks normal to the surface (delamination) and (c) the combined failure modes of cracks parallel to the SAM axis and delamination.

e.g. SEM or XCT.

It is also demonstrated in [64] that the XCT and SEM analysis are quite cumbersome, time consuming and therefore expensive without the prior knowledge from the time-efficient SAM analysis.

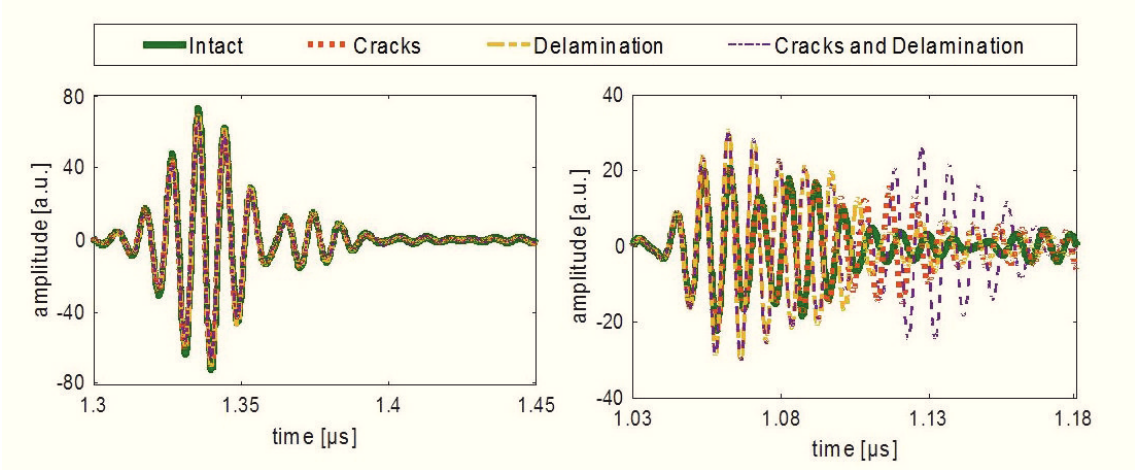

Figure 54: Simulated A-scans for the case of (a) a lens opening smaller than the critical Rayleigh angle and (b) for the case of an opening angle exceeding the critical Rayleigh angle. The cases of an intact TSV, a TSV with cracks parallel to the surface, cracks normal to the surface (delamination) and the combined failure modes of cracks parallel to the SAM axis and delamination.

One advantage (in terms of frequency) of a 100MHz transducer - in contrast to GHz acoustic microscopy [12, 108, 122] – is the longer working distance between lens and sample, allowing for simpler handling and easier automatization. Besides, the attenuation of the low frequency sound waves is smaller, leading to higher penetration depth.

In addition, transducers and SAM setups below the GHz regime are in general easier to access at lower costs [35]. In conclusion, it is not a priori advisable to increase the frequency in a SAM measurement when devices and structures become smaller; additional wave modes can be utilized in order to detect small defects even if they are not breaking the sample surface and concern multi-material devices.

13.6 ACKNOWLEDGEMENTS

The samples (with artificially introduced defects) were kindly provided by J. Siegert and F. Schrank (ams AG, Premstätten, Austria). The μXCT measurements were carried out by J. Rosc (MCL) and the SEM analyses by B. Sartory (MCL). The EFIT simulations were performed in cooperation with R. Hammer (MCL).

14

SIMULATION OF V(Z) CURVES AND COMPARISON TO EXPERIMENT

In the work reported in [39], intensity (V) – defocus (z) curves (Section 10.1) were simulated via EFIT (Section 10.2) and compared to experimental results. The simulations of the $V(z)$ measurements, obtained by SAM, were first carried out on an aluminium bulk sample, and secondly on a $1\mu m$ aluminium coating deposited on a silicon wafer. Aluminium on silicon layered systems are of high relevance for MtM applications [154]. The $V(z)$ curves were used to determine the Rayleigh wave velocity of the aluminium bulk sample and the aluminium coating. The results of the simulations with respect to the Rayleigh velocity were corroborated by non-destructive SAM and LUS measurements.

14.1 MOTIVATION

The $V(z)$ curve measurement by SAM enables the determination of the Rayleigh-velocity of a sample locally, in the focal spot of the acoustic lens. The Rayleigh wave velocity can be used directly for material characterization or material monitoring. Alternatively, *e.g.* elastic parameters can be determined. Thus, the $V(z)$ measurements are of high relevance in the fields of MtM technologies (Section 1.1). In the work presented in [39] the simulation of $V(z)$ curves - and therefore acoustic wave propagation in samples during the SAM measurement - was carried out. In the following, the content of [39] is briefly revised.

14.2 MATERIAL AND METHODS

14.2.1 *Samples*

For the calibration measurement, an aluminium block of $5x3x1cm^3$ was investigated. The aluminium coated sample was a $4x2cm^2$ segment of an aluminium-coated silicon wafer, crystallographic orientation (100). The aluminium was deposited on the silicon wafer by a physical vapor deposition procedure and a thickness of $1\mu m$ was determined via profilometry. The density of the aluminium thin film was determined by X-ray diffraction measurements that yielded a mass density of $2.709g/cm^3$.

14.2.2 *Scanning acoustic microscopy*

The results published in [39] were obtained by using the SAM 400 (PVA, Analytical Systems GmbH, Westhausen, Germany) in reflection mode. The SAM was equipped with a custom-built tone-burst setup in order to perform precise frequency-dependent measurements. For the calibration measurement on bulk aluminium, an AO with an opening angle of $120°$ was used, attached to a transducer of $400MHz$ nominal center frequency. The transducer was addressed at approximately $430MHz$, corresponding to

SAMPLE	LENS, COATING	f[MHz]	Θ[°]	AREA	ngp	D[Neper/mHz^2]
Si, Al	sapphire, SiO_2	430	30	axi	30	$3.7 \cdot 10^{-11}$
Si, Al	sapphire, SiO_2	400	60	axi	30	$3.7 \cdot 10^{-11}$

Table 23: Summary of EFIT parameters and simulation settings for the V(z) analysis, where f denotes the frequency, Θ is the semi-angle of the lens aperture, Lens and Coating define the lens and the antireflective coating in the simulations. Area refers to the axial symmetric (with respect to the z-axis) simulation area (the coordinates refer to Figure 38) and ngp denotes the grid points per wavelength. D denotes to the exponential damping factor implemented in the EFIT simulations, the material parameters can be found in [15, 124].

MATERIAL	REFERENCE	E[GPa]	ν	ρ[kg/m^3]
Si	[49]	130	0.28	2330
Al	[15]	70	0.35	2698
sapphire	[15]	345	0.29	3980
SiO_2	[124]	70	0.19	2200

Table 24: Summary of material parameters for V(z) EFIT simulations., where the elastic modulus E, the Poisson ratio ν and the mass density ρ are given.

the resonance frequency of the transducer. In the case of the aluminium thin film on the silicon substrate, an AO (60°) was applied. The transducer was addressed at about 400MHz. The Rayleigh wave velocities were extracted from the V(z) curves according to Equation 31.

14.2.3 *EFIT*

The simulation of V(z) curves was carried out for the aluminium block and the aluminium layer deposited on a silicon substrate (see Section 14.2.1). Isotropic, linear elastic material behaviour was assumed in the simulations. The assumption of isotropy is made for aluminium because its Zener anisotropy ratio is close to one [124]. Literature values for the longitudinal and transverse sound velocity and the density of aluminium were used as input values [15, 124]. The literature values for silicon were taken from [124].

In Table 23, the EFIT simulation parameters and settings for the V(z) analysis presented in this chapter are summarized and Table 24 gives details about the used material properties.

For more than 30 defocus positions an equivalent of the A-scan data obtained in SAM measuements was determined and the V(z) curves were evaluated, see [39] for details. The dominant frequency and the opening angle of the lens were implemented in the EFIT simulations in accordance with the SAM measurement. Also an ARC was consid-

ered in the simulations. Figure 55 shows the EFIT simulation of the SAM measurement at nine time-steps, where the ultrasonic field is presented by the normalized magnitude of the velocity fields z-component. In timestep 1 and 2, the sound wave is excited by the transducer and propagates through the lens body from top to bottom towards the surface of the sample in timestep 3 and 4. At time-step 5, the ultrasonic waves reach the surface of the sample. Here, part of the sound field is transmitted into the sample (see time-step 6). The reflected sound field travels back towards the lens (time-step 7 and 8) and reaches the transducer at time-step 9. In analogy to the SAM measurement, the simulated A-scan is obtained by summing up the z-component of the velocity field along the width of the transducer at the position of the transducer.

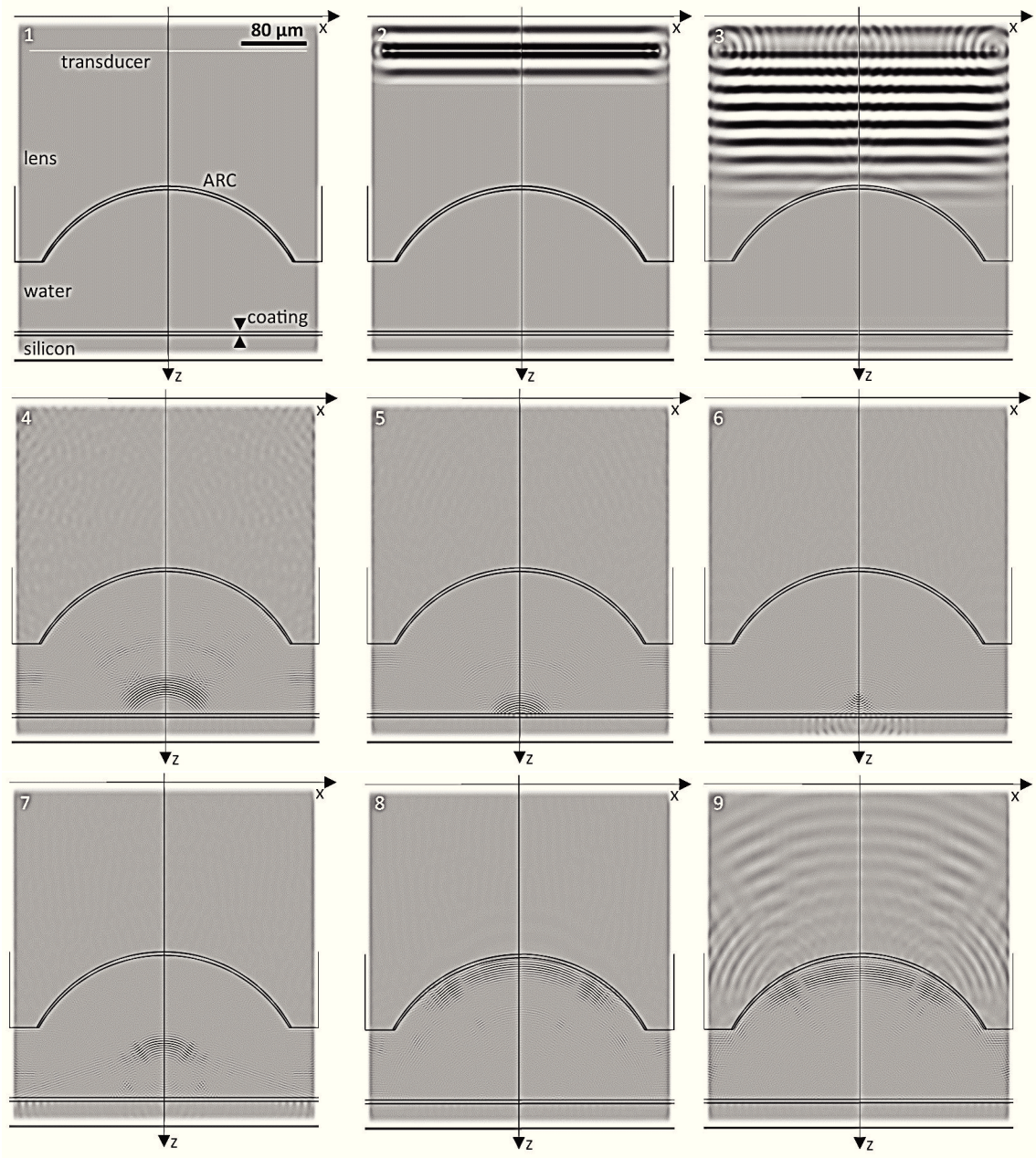

Figure 55: EFIT simulation of sound propagation in an aluminium thin film.

14.3 RESULTS

In the following, the results of [39] are briefly summarised.

Figure 56 shows the direct comparison of the $V(z)$ measurement to the EFIT simulation results for the calibration measurement of the aluminium bulk sample. Good agreement between measurement and simulation was found and the Rayleigh wave velocity of aluminium determined for the aluminium sample is comparable to literature values, see [39] for details.

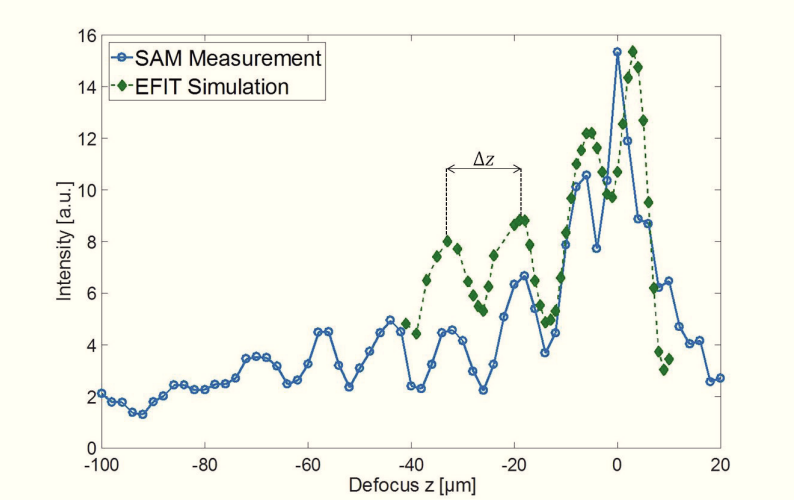

Figure 56: SAM measurement (open circles) and EFIT simulation (diamonds) of $V(z)$ curve for an aluminium sample.

In Figure 57 the $V(z)$ measurement and the EFIT simulations were carried out for a aluminium thin film of 1µm thickness on a silicon substrate. Again, good agreement between measurement and simulation was found. Because the Rayleigh wave velocity depends on frequency if the surface layer of the sample is thinner than about 1-2 wavelength, the frequency dependent Rayleigh wave velocity was determined and is shown in Figure 58, see [39] for details. The outcome is directly compared to LUS measurements in the frequency range up to 200MHz. At 400MHz, the SAM and EFIT results are shown in Figure 58, where good agreement was found.

14.4 DISCUSSION

The work reported in [39] shows good agreement between SAM and LUS measurements and EFIT simulation results. The performed measurements and simulations are of high relevance concerning the challenges in the SAM analysis of MtM technologies, namely (1) the accurate data interpretation, (2) the choice of the most suitable transducer or (3), the design of the most effective lens for a specific sample.

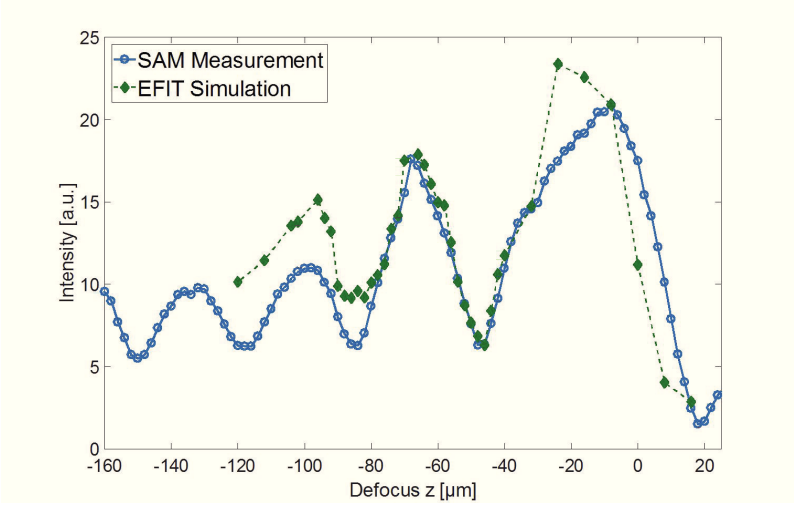

Figure 57: SAM measurement (open circles) and EFIT simulation (diamonds) of $V(z)$ curve for the 1µm aluminium thin film on a silicon substrate.

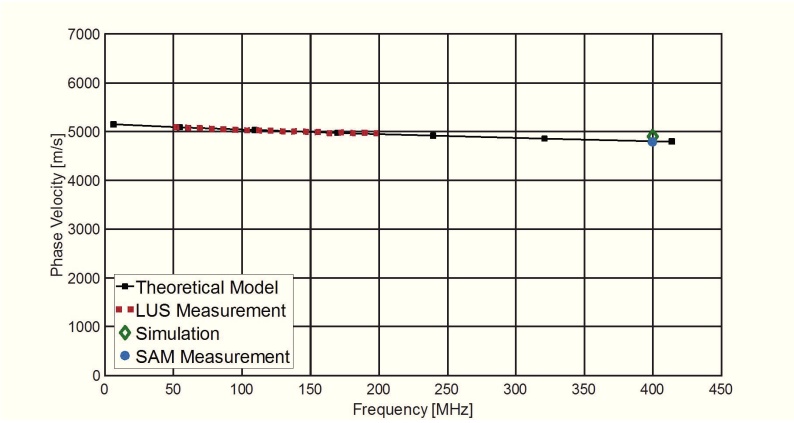

Figure 58: Rayleigh wave velocity as function of frequency for the 1 µm aluminium layer on a silicon substrate.

Part IV

EPILOGUE

15

CONCLUSION AND OUTLOOK

As stated in the preamble, the realization of MtM technologies demands the increased advanced failure and material characterization of devices, where methods with at-line or in-line potential are most valuable due to decreased qualification times. Especially the material characterization and failure detection concerning metallic and polymer coatings are of high relevance due to their vast application in microelectronic devices. However, many state of the art methods for the characterization of thin films and the failure detection in coatings are destructive or at least require the direct loading of the analysed sample.

The two utilized ultrasonic methods LUS and SAM proved to be tools of choice in the failure and material characterization regarding MtM technology relevant samples. The LUS method, applied to the characterization of metallic and polymer layers on silicon substrates also showed great potential for at-line or in-line inspection. The possibility to distinguish different deposition procedures via LUS and the sensitivity of surface acoustic waves to light exposure of polymer coatings was tested. Moreover, multiple-layer characterization was considered.

The SAM analysis was successfully applied to the delamination detection in multi-layered PCBs, where an indirect failure detection method was discussed. Moreover, TSV test arrays - highly relevant for the 3D integration of devices in MtM technologies – were characterized in detail. In this context, the SAM analysis of metal coated TSVs was performed via relatively low frequency evaluations, where the excitation of additional wave modes proved to be a powerful method in state of the art defect detection. The SAM and LUS results were compared in one publication, where good agreement was found [39].

The results presented in this work were corroborated via EFIT simulations and a variety of other state of the art characterization techniques, *e.g.* µXCT analysis, SEM images and nano-indentation results; they are published in [33–38].

The encouraging results presented in this thesis already enabled further ultrasonic evaluations in follow up projects. Concerning the LUS applications, the characterization of *e.g.* porous media and doped samples (see also Appendix A) via Lamb and bulk waves is already considered in succeeding projects. Concerning the SAM analyses, the failure detection of sub-resolution defects is a very interesting topic, probably applicable for a number of samples. The method is currently tested on filled TSVs with diameters of about 5 µm with ultrasonic frequencies up to 400 MHz. With respect to the simulation efforts, parallelized full 3D simulations of sound propagation in anisotropic media are planned.

Part V

PUBLICATIONS

In the following part, the publications [33–39] are attached.

Available online at www.sciencedirect.com

ScienceDirect

materialstoday: PROCEEDINGS

ELSEVIER

Materials Today: Proceedings 2 (2015) 4289 – 4294

nanoFIS 2014 - Functional Integrated nanoSystems

Young's Modulus and Poisson's Ratio Characterization of Tungsten Thin Films via Laser Ultrasound

E. Grünwald[a], R. Nuster[b], R. Treml[c], D. Kiener[c], G. Paltauf[b] and R. Brunner[a,*]

[a]*Materials Center Leoben Forschung GmbH (MCL), Leoben, Austria*
[b]*Karl-Franzens University, Graz, Austria*
[c]*Montanuniversität Leoben, Leoben, Austria*

Abstract

The non-destructive examination of microstructural properties of thin films is of consistent significance in microelectronic applications and simulations. Here, a laser ultrasonic (LUS) method is used to determine Young's modulus E and Poisson's ratio υ of thin films deposited on silicon substrates. In particular, we determine the longitudinal and transversal sound velocity of a surface acoustic wave (SAW) in a 695 nm tungsten layer on a silicon (100) substrate, from which E and υ are derived. The setup uses laser pulses to generate SAWs on the sample of interest. By detecting the SAWs with an optical beam deflection method, it is possible to determine the frequency-dependent phase velocity. Fitting a theoretical model to the experimentally evaluated dispersion curve, the longitudinal and transversal sound velocities of the thin film are derived.

Selection and peer-review under responsibility of Conference Committee of nanoFIS 2014 - Functional Integrated nanoSystems.

Keywords: Laser Ultrasound; Thin Films; Tungsten Layer; Mechanical Properties; Young's Modulus; Poisson's Ratio

1. Introduction

Latest developments in microelectronics and nanoelectronics aim for an increased density of components by further miniaturization, whilst simultaneously enhancing functionality and reducing the costs of electronic devices. Reducing the size and increasing the functionality – "More-than-Moore-technology" – often includes the need for thin films, *e.g.* in the realization of micro-electro-mechanical systems (MEMS) [1], 3D integration [2], nanosensors [3], or energy harvesting applications [4]. In the ongoing miniaturization and diversification processes, tungsten is a material that

* Corresponding author. Tel.: +43-3842-459-2248 ; fax: +43-3842-459-22500.
E-mail address: roland.brunner@mcl.at

Selection and peer-review under responsibility of Conference Committee of nanoFIS 2014 - Functional Integrated nanoSystems.
doi:10.1016/j.matpr.2015.09.015

can endure the increasing current densities that arise as microelectronic devices become smaller [5]. In 3D integration, tungsten is used as coating material in through silicon vias (TSVs) as alternative to copper fillings in TSVs [2]. Recently, the residual stresses in tungsten thin films have been studied experimentally and via simulation [1, 6] due to their relevance in the realization of MEMS. In order to assess the risk of component failure via material modelling, the mechanical properties of tungsten thin films have to be accurately determined. In this sense, the microstructural properties of tungsten thin films are of major importance in micro- and nanotechnologies and the corresponding material modeling [1, 6]. However, the mechanical properties of coatings may deviate significantly from their bulk counterparts, especially when multi-layer systems or constrained layers are considered. Many current testing techniques require direct loading of the thin film, *e.g.* nano-indentation, and additionally the influence of the substrate or supporting structures can obscure the film properties [7]. Laser ultrasonic (LUS) characterization presents a non-destructive analysis method and is presumed to be probably the most suitable technique to determine the acoustic wave related mechanical properties of thin films [7]. The LUS approach applied in this work uses laser pulses to generate broadband surface acoustic waves (SAWs) which propagate dispersively on the layer-substrate system [7-13]. The frequency dependent phase velocity can be evaluated from the measurement and additionally be determined numerically. Fitting the theoretically evaluated phase velocity to the measurement yields the mechanical properties of the thin film. The LUS method has been applied to several layer-substrate systems [7, 10-13] in the past. In the presented work, a contactless characterization of Young's modulus and Poisson's ratio of a tungsten layer deposited on a silicon (100) substrate was carried out. The determined mechanical properties are input values for current material simulations [1] where very similar substrate-layer systems are investigated. To this purpose, an optical SAW detection setup and a theoretical model were implemented and validated. The approach represents an analytical method with high potential for reliable and fast material characterization.

2. Experimental Setup and Measurement

The setup (Fig.1.) uses a nanosecond laser system (Nd:YAG laser) providing laser pulses with a pulse duration of 10 ns at a repetition rate of 10 Hz. To excite a broad-band surface acoustic wave (SAW) the laser beam is focused with a cylindrical lens onto the sample surface. To detect the SAWs a beam deflection technique is used. A continuous wave (cw) laser beam is focused onto the sample surface and the deflection of the back reflected light is detected by a balanced photodetector (BPD). The back reflected light is divided into two parts by placing a mirror with a sharp edge into the beam path. The two separated parts are detected with the two photodiodes working in differential mode of the BPD. Since the division ratio of the back reflected light power detected by the two laser diodes of the BPD is proportional to the deflection the recorded signal is proportional to the slope of the surface displacement.

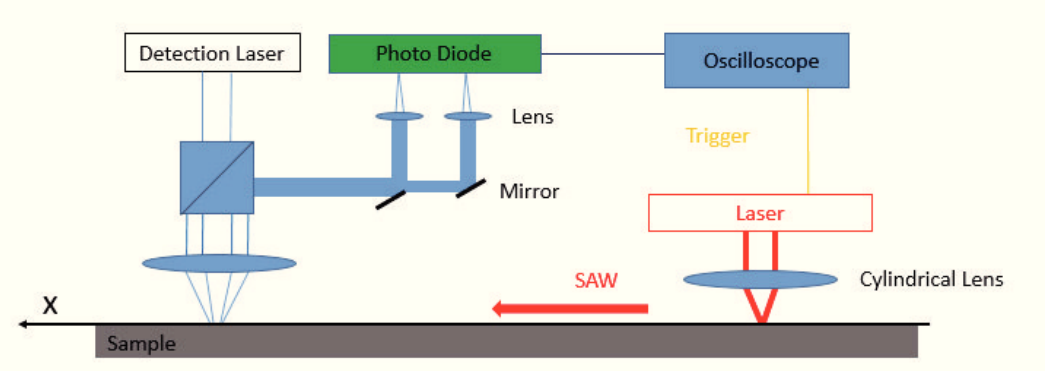

Fig. 1. Schematic of the experimental setup to excite and detect SAWs.

3. Theoretical Description of the Dispersion Relation

The frequency dependent phase velocity of a surface acoustic wave propagating on a coated solid can be evaluated numerically. To this purpose, a semi-infinite, linear elastic, substrate-layer system is considered. The layer and the substrate are assumed to be isotropic. This assumption has been made for the tungsten thin film because no pronounced texture was observed by using X-Ray diffraction (XRD) analysis. According to [8] the particle displacement vector $\boldsymbol{u}$ in the solid can be written as $\boldsymbol{u} = \boldsymbol{\nabla\phi} + \boldsymbol{\nabla} \times \boldsymbol{\psi}$, when $\boldsymbol{\phi}$ denotes the scalar potential of particle displacement and $\boldsymbol{\psi}$ denotes the vector potential of the particle displacement. Both potentials have to fulfill the wave equation,

$$\boldsymbol{\nabla}^2\phi - \frac{1}{v_L^2}\frac{\partial^2\phi}{\partial t^2} = 0, \tag{1}$$

$$\boldsymbol{\nabla}^2\boldsymbol{\psi} - \frac{1}{v_T^2}\frac{\partial^2\boldsymbol{\psi}}{\partial t^2} = 0, \tag{2}$$

where $\boldsymbol{v_L}$ denotes the longitudinal sound velocity and $\boldsymbol{v_T}$ denotes the transversal sound velocity. Equations (1) and (2) combined with the appropriate ansatz for $\boldsymbol{\phi}$ and $\boldsymbol{\psi}$ and the corresponding boundary conditions for displacement and traction at the surface and interface yield a system of six linear algebraic equations, which has non-trivial solutions at the zeros of its 6x6 coefficient determinant. According to [8], this 6x6 determinant can be rewritten as a 4x4 determinant, the roots of which can be found via numerical evaluation. We determined the frequency dependent phase velocity theoretically using MATLAB.

4. Data Analysis and Results

4.1. Data Analysis of Laser Ultra Sonic (LUS) Measurement of a Layered System

Surface acoustic waves on bulk materials propagate dispersion-free. However, if a thin film is deposited on the substrate, the lower frequency components of the SAWs propagate mainly in the substrate, whereas higher frequency parts of the wave propagate mostly in the thin film. Therefore, the coating causes the SAW to propagate dispersively on the layer-substrate system, meaning the phase velocity v depends on the frequency f.

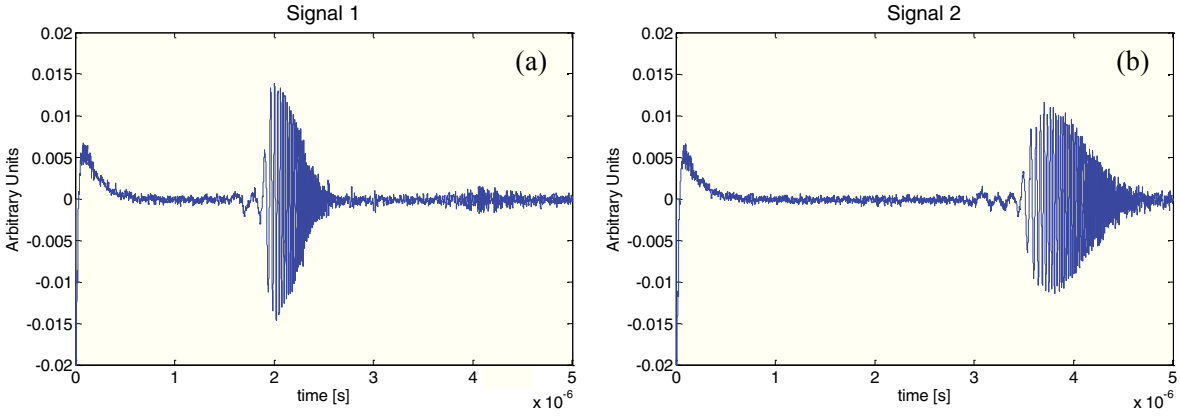

Fig. 2. (a) Laser induced signals $u_1(t)$ detected at position x_1; (b) laser induced signals $u_2(t)$ detected at position x_2.

By detecting the SAWs of *e.g.* a tungsten layer with an optical beam deflection method (Fig.1.), it is possible to determine the frequency-dependent phase velocity. To this purpose, the laser induced signals $u_i(t)$, detected at different distances x_i as shown in (Fig. 2.), are Fourier transformed to their complex spectral functions, denoted by $U_i(f)$. According to [10], the phase velocity $v\,(f)$ is then given by

$$v(f) = \frac{(x_2 - x_1)2\pi f}{\left[\Phi_2(f) - \Phi_1(f)\right]}, \tag{3}$$

where $\Phi_i(f)$ denote the phases of the frequency components $U_i(f)$.

4.2. Young's Modulus and Poisson's Ratio of a 695 nm Tungsten Film on a Si Substrate

In Fig.3. the analyzed system consisting of a Si substrate, a barrier coating of TiN and a 695 nm thick tungsten layer is shown. For the MATLAB evaluation, the longitudinal velocity $\boldsymbol{v_L^S}$ and transversal velocity $\boldsymbol{v_T^S}$ of Si, 8432 m/s and 5843 m/s respectively [14], were taken as input parameters as well as the density of the substrate ρ^S and the density of the tungsten layer ρ. Furthermore, the thickness of the tungsten layer had to be measured as input value for the MATLAB program. This was done using ImageJ [15] evaluation software for REM images (Fig.3.). The TiN as well as the W film were deposited via chemical vapor deposition (CVD). The influence of the thin TiN barrier coating was neglected in our analysis.

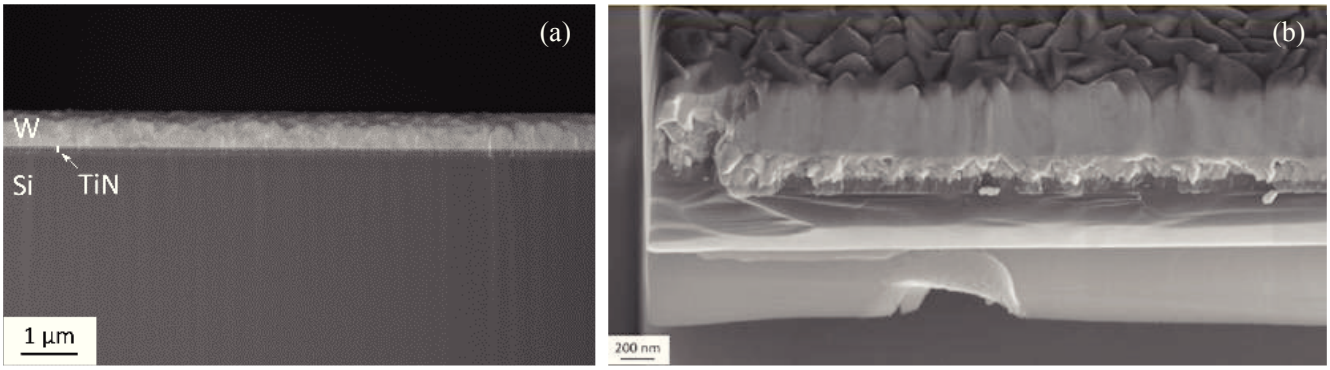

Fig. 3. (a) REM image of the analyzed system; (b) high resolved image detail for thickness measurement. Cross-section of investigated sample: 695 nm tungsten layer on Si substrate with a TiN barrier layer.

Fitting the theoretical curve to the experimentally evaluated frequency dependent phase velocity yields the longitudinal and transversal sound velocities $\boldsymbol{v_L}$ and $\boldsymbol{v_T}$ of the SAW in the thin tungsten film. To this purpose, the longitudinal and transversal velocities are altered until the theoretical model shows best agreement to the measurement.

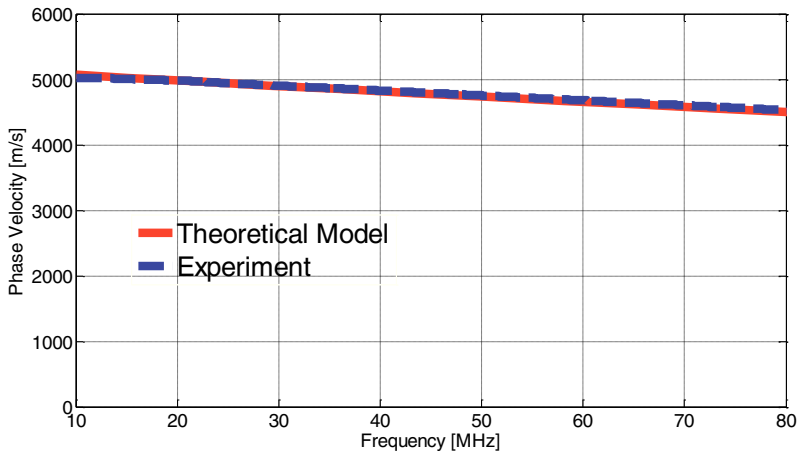

Fig. 4. Phase velocity c as a function of frequency f of a tungsten layer on a Si substrate from LUS measurement (blue) and a fitted theoretical curve (red) from simulation (MATLAB).

In Fig. 4. we show the result for the experimentally evaluated dispersion relation and the fitted theoretically determined frequency dependent phase velocity for the 695 nm tungsten film on a Si (100) substrate. Under the assumption of an isotropic, linear elastic solid, the elastic constants $c_{11} = v_L^2\rho$ and $c_{12} = c_{11} - v_T^2\rho$ are related to the Young's Modulus E and Poisson's ratio υ via

$$E = c_{11} - 2\left(\frac{c_{12}^2}{c_{11}+c_{12}}\right) \quad \text{and} \tag{4}$$

$$\upsilon = c_{12}/(c_{11} + c_{12}) .$$

The evaluation via fitting the theoretical curve to the experimentally evaluated data gives a Young's modulus E of 405 GPa and a Poisson's ratio ν of 0.28, which is in accordance with values reported in literature of 380 GPa – 420 GPa and 0.28 – 0.3 for Young's modulus E and Poisson's ratio ν, respectively [19]. The error in the measurement of the frequency dependent phase velocity can be estimated via [10]

$$\left|\frac{\Delta v}{v}\right| \leqq \left|\frac{2\Delta x}{x_2-x_1}\right| + \left|\frac{2\Delta t\omega}{(\phi_2-\phi_1)}\right| . \tag{5}$$

An oscilloscope of 2GSa/s was used and the accuracy of the positioning and translation stage was of $\Delta\, x \pm 1.2$ µm. The signals in Fig. 3. were measured with a distance of $x_2 - x_1 = 8$ mm. Applying equation (5), the error in the determined phase velocity is smaller than 3m/s in our measurement. From equation (5) it can be seen that by increasing the distance between the two measurements by a factor of 4, the accuracy increases by the same factor.

5. Conclusion and Outlook

In this work, we report on the determination of the Young's modulus **E** and the Poisson's ratio **ν** of a 695 nm thin tungsten film on a Si (100) substrate with laser-induced ultrasonic surface waves. The proposed method provides an analytical, non-destructive measurement of elastic constants for material and reliability inspection. The presented results are the basis for the further development of Young's modulus and Poisson's ratio characterization via LUS and ongoing projects concerning the comparison of material parameters determined via scanning acoustic microscopy or nanoindentation [16–18]. Moreover, future studies will be concerned with the characterization of the elastic properties of differently processed layers of tungsten and muli-layered systems.

Acknowledgements

This work is done as part of the project eRamp, which is co-funded by grants from ENIAC Joint Undertaking and from Austria, Germany, the Netherlands, Romania, Slovakia and the UK. Financial support by the Austrian Federal Government (in particular from Bundesministerium für Verkehr, Innovation und Technologie and Bundesministerium für Wissenschaft, Forschung und Wirtschaft) represented by Österreichische Forschungsförderungsgesellschaft mbH and the Styrian and the Tyrolean Provincial Government, represented by Steirische Wirtschaftsförderungsgesellschaft mbH and Standortagentur Tirol, within the framework of the COMET Funding Programme is gratefully acknowledged.

References

[1] Schöngrundner R., Treml R., Antretter T., Kozic D., Ecker W., Kiener D., Brunner R., *Thin Solid Films* 564 (2014) 321–330.
[2] Krauss C., Labat S., Escoubas C., Thomas O., Carniello S., Teva J., Schrank F., *Thin Solid Films* 530 (2013) 91–95.
[3] Ponzoni A., Comini E., Sberveglieri G., Zhou J., Deng S. Z., Xu N. S., Ding Y., Wang Z. L., *Appl. Phys. Lett.* 88 (2006) 203101.
[4] Yan J., Wang T., Wu G., Dai W., Guan N., Li L., Gong J., *Adv. Mater.* 26 (2014), 2514–2520.
[5] Plyushcheva S. V., Mikhailov G. M., Shabel'nikov L. G., Shapoval S. Y., *Neorganicheskie Materialy*, 45 (2009), 176–180.
[6] Kozic D., Treml R., Schöngrundner R., Brunner R., Kiener D., Antretter T., Gänser H.P., EuroSimE, Ghent, BE, April 2014.

Vogel D., Auerswald E., Auersperg J., Bayat P., Rodriguez R.D., Zahn D.R.T, Rzepka S., Michel B., *Microelectronics Reliability* 54 (2014) 1963–1968. Korsunsky A. M., Sebastiani M., Bemporad E., Materials Letters 63 (2009) 1961–1963.
[7] Zhang F., Krishnaswamy S., Fei D., Rebinsky D. A., Feng B., *Thin Solid Films* 503 (2006) 250–258.
[8] Tiersten H.F., *J. Appl. Phys.* 40, 2 (1969).
[9] Neubrand A., Hess P., *J. Appl. Phys.* 71 (1992) 227.
[10] Schneider D., Witke T., Schwarz T., Schöneich B., Schultrich B., *Surface and Coatings Technology* 126 (2000) 136–141.
[11] Schneider D., Schwarz T., Scheibe H. J., Panzer M., *Thin Solid Films* 295 (1997) 107–116.
[12] Schneider D., Schwarz T., *Surface and Coating Technologies* 91 (1997) 136–146.
[13] Hurley D. C., Tewary V. K., Richards A. J., *Meas. Sci. Technol.* 12 (2001) 1486–1494.
[14] Royer D. and Dieulesaint E., *Elastic Waves in Solids I*, Springer (1996).
[15] Rasband, W.S., ImageJ, U. S. National Institutes of Health, Bethesda, Maryland, USA, http://imagej.nih.gov/ij/, 1997-2014.
[16] Schöberl T., Sabirov I, Pippan R., *Zeitschrift für Metallkund* 96 (2005) 1056–1062.
[17] Cordill M.J., Moody N.R., Gerberich W.W., *International Journal of Plasticity* 25 (2009) 281–301.
[18] Chen S., Liu L., Wang T., *Surface & Coatings Technology* 191 (2005) 25–32.
[19] E. Harry, A. Rouzaud, M. Ignat, P. Juliet, *Thin Solid Films* 332 (1998) 195.
A. Rouzaud, E. Barbier, J. Ernoult, E. Quesnel, *Thin Solid Films* 270 (1995) 270.
H.L. Sun, Z.X. Song, D.G. Guo, F. Ma, K.W. Xu, *J. Mater. Sci. Technol.* 26 (2010) 8–7.

Characterization of Polyimid-Multi-Layer Thin Films Combining Laser Ultrasonic Measurements and Numerical Evaluations

E. Grünwald[1], R. Nuster[2], R. Hammer[1], H. Aßmann[3], G. Paltauf[2], R. Brunner[1]*
[1]Materials Center Leoben Forschung GmbH (MCL), Austria
[2]Karl-Franzens University of Graz, Austria
[3]Infineon Dresden GmbH, Germany
*roland.brunner@mcl.at, Tel.: +43 3842 45922 - 48, www.mcl.at

Abstract

Modern microelectronic devices frequently require the use of thin films and multi-layer systems [1]. Especially the application of advanced material models to simulate e.g. reliability issues for such components relies on the accurate determination of the layers' elastic properties [2]. Polyimides (PI) show many beneficial mechanical and chemical properties for applications in the field of micro-electronics, e.g. in the realization of MEMS packages [3]. In the work reported here, the combination of a laser ultrasonic measurement and a numerically solved theoretical model [4] is presented in order to determine the elastic properties of a multi-layer system. The multi-layer system consists of a polyimide layer of 11 µm thickness and an 800 nm silicon nitride film on a (100) silicon substrate. The theoretical model uses a partial wave ansatz and a global matrix method in order to determine the frequency dependent phase velocity [5]. For the measurement of the frequency dependent phase velocity, nanosecond laser pulses were focused to a line shape onto the sample surface. This line excitation generates plane broadband surface acoustic waves (SAWs). The phase velocity depends on the frequency as a consequence of the different sound velocities of substrate and layers. The low frequency SAWs propagate mainly in the substrate, whereas higher frequency waves propagate mostly in the thin layers. An optical beam deflection method was applied to detect the SAWs. The Young´s Modulus and the Poisson ratio of the polyimide layer were derived by fitting the theoretical curve to the experiment. The presented method provides the possibility to measure contactless on wafer level. It represents a valuable tool regarding the non-destructive evaluation of elastic properties of thin films in multi-layered systems. The Young´s modulus and the Poisson ratio can serve as essential input for various advanced measurement techniques and simulations [2].

1. Introduction

Current trends in the fields of micro- and nanoelectronics require the application of thin films, e.g. in the realization of micro-electro-mechanical systems (MEMS) [2], nanosensors [6], packaging and 3D integration [2], or in energy harvesting applications [7]. Polyimides show many beneficial mechanical and chemical properties for the application in micro-systems. In the realization of MEMS, polyimides are used as photoresists and as structural or buffer materials. Moreover, the properties of polyimide can be adapted to an outstanding extent. For example, piezoelectric properties can be introduced, leading to a new type of polyimides (PolyMEMS), which can be used in aerospace applications [3]. The modelling of the failure behaviour of micro- or nanoelectronic devices requires the precise measurement of the mechanical properties of the thin polyimide films. In addition, fabrication attendant characterization methods on wafer level are highly in demand. However, many current testing techniques are destructive, e.g. nano-indentation, and additionally the influence of the substrate can mask the actual mechanical properties of the thin films [8]. Suitable techniques to determine the acoustic wave speed related properties of thin films and thin film systems are laser ultrasound (LUS) methods [8]. The LUS approach applied in this work uses laser pulses to generate surface acoustic waves (SAWs) on the layer-substrate system [9]. The frequency dependent phase velocity can be evaluated from the LUS measurement and additionally be calculated numerically. Fitting the theoretically determined dispersion relation to the measurement of the frequency dependent phase velocity yields the mechanical properties of the thin film. In the past, the LUS method has been applied to several layer-substrate systems [9]. In the work reported here, the contactless characterization of a polyimide layer was carried out. The multi-layer system consists of a polyimide layer of 11 µm thickness and an 800 nm silicon nitride film on a (100) silicon substrate. The determined material properties can serve as input values for simulations [2].

2. Experimental set-up and Measurement

In the work reported here, surface acoustic waves (SAWs) are excited using a pulsed laser system (Nd:YAG laser) with a repetition rate of 10 Hz and a pulse length of 10 ns. The laser light is focused onto the sample with a cylindrical lens, generating a line focus, therefore 2 plane SAWs propagate in opposite direction on one distinct spatial axis of the system. As a consequence of the 10 ns pulse length, the SAWs show frequencies up to approximately 100 MHz. A beam deflection method is applied in order to detect one of the 2 propagating SAWs on the sample (Figure 1). To this purpose, a continuous wave (CW) laser beam is focused onto the sample surface and the reflected light is divided into two equivalent parts which are then detected by a balanced photodetector (BPD). When the SAW passes the focus spot of the CW laser, the two separated beams are altered and the division ratio of the back reflected light power, detected by the

978-1-5090-2106-2/16/$31.00 ©2016 IEEE

2016 17th International Conference on Thermal, Mechanical and Multi-Physics Simulation and Experiments in Microelectronics and Microsystems

two laser diodes of the BPD, is proportional to the slope of the surface displacement.

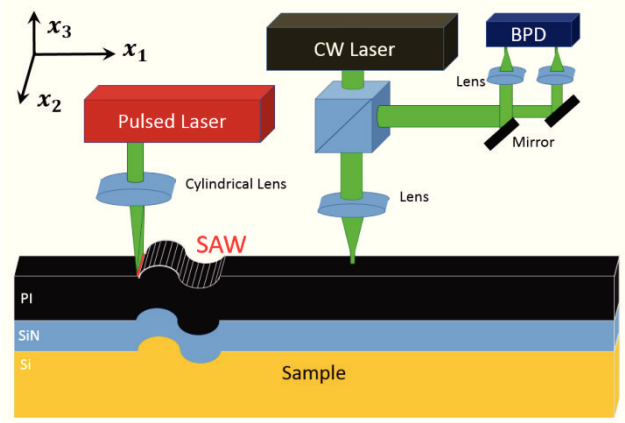

Figure 1: Schematic of experimental set-up.

3. Theoretical description of the dispersion relation

In the following, the frequency dependent phase velocities of the wave modes in a 2-layer on substrate system (Figure 2) are determined by using the partial wave technique.

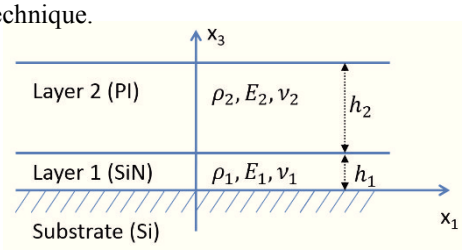

Figure 2: Schematic of the PI-SiN-Si-system.

According to [5], the partial wave technique can be extended to multiple layers on a half space. For the linear elastic, isotropic case, only four wave modes in each layer have to be considered, corresponding to up- and down-going longitudinal and transversal waves. In a linear elastic, isotropic substrate, only the down-going longitudinal and transversal waves have to be considered in the ansatz. When a sound wave travels through a medium, the particles of the medium are displaced from their equilibrium positon. For a wave propagating in the x_1-direction (Figure 1), the particle displacement u_1 in x_1-direction and u_3 in x_3-direction in the nth layer, where $n = 1,2,3, \ldots$, are given by [5]

$$u_1^{(n)} = \sum_{m=4n-3}^{4n} C_m e^{ik(x_1+\alpha_m x_3 - c_P t)},$$

$$u_3^{(n)} = \sum_{m=4n-3}^{4n} C_m U_{3m} e^{ik(x_1+\alpha_m x_3 - c_P t)}. \quad (1)$$

C_m are the coefficients of the polarization vector $\vec{U}$, k is the wave number, α_m denotes the x_3 component of the direction vector, c_P the phase velocity of the SAW and t denotes the time. From equation (1), the entries of the strain and stress tensors can be computed [5], where isotropic, linear elastic layers and substrate are assumed in the presented analysis. The boundary conditions concerning the stresses σ_{ij} and particle displacements u_i in the two layer system on Si (100) substrate are:

1. Stress free surface:
$$\sigma_{31}^2 = 0 \; @ \; x_3 = h_1 + h_2,$$
$$\sigma_{33}^2 = 0 \; @ \; x_3 = h_1 + h_2.$$
2. Continuity of particle displacement and stress tensor entries at the interfaces:
$$u_{31}^2 = u_{31}^1 \; @ \; x_3 = h_1,$$
$$u_{33}^2 = u_{33}^1 \; @ \; x_3 = h_1,$$
$$\sigma_{31}^2 = \sigma_{31}^1 \; @ \; x_3 = h_1,$$
$$\sigma_{33}^2 = \sigma_{33}^1 \; @ \; x_3 = h_1,$$
$$u_{31}^1 = u_{31}^{Substrate} \; @ \; x_3 = 0,$$
$$u_{33}^1 = u_{33}^{Substrate} \; @ \; x_3 = 0,$$
$$\sigma_{31}^1 = \sigma_{31}^{Substrate} \; @ \; x_3 = 0,$$
$$\sigma_{33}^1 = \sigma_{33}^{Substrate} \; @ \; x_3 = 0. \quad (2)$$

Considering the particle displacements u_i and the stresses σ_{ij} at the boundaries of the system yields a matrix equation. Only if the determinant of the 10x10 boundary matrix , in case of 2 layers on a substrate, is forced to zero by the right combination of frequency and phase velocity, a sound wave can propagate in the solid [5]. The dispersion relation for the allowed wave modes in an 11 µm polyimide (PI) on 800 nm silicon nitride on silicon system are shown in Figure 3.

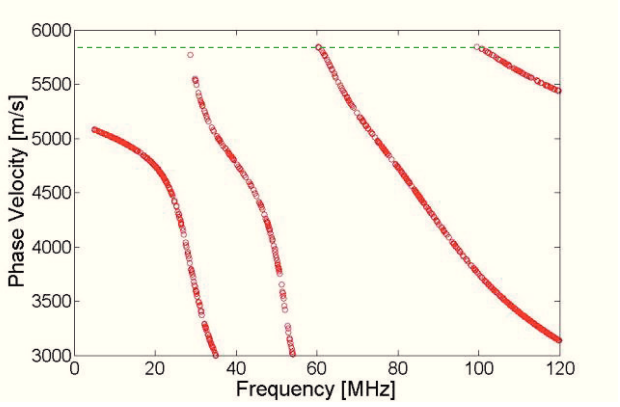

Figure 3: Theoretically determined dispersion relation of wave modes in a PI-SiN-Si-System.

In the frequency range up to 120 MHz, 4 wave modes are present in the considered phase velocity range (Figure 3).

The first wave mode (Rayleigh wave) starts at the Rayleigh wave velocity of the substrate (5150m/s) [12]. The additional wave modes start at the transversal sound velocity v_T of the substrate (5843m/s). The input parameters for the evaluation of Figure 3 are summarized in Table 1.

	ρ[kg/ m^3]	v_L[m/s]	v_T[m/s]
Polyimide	1464	2660	1160
SiN	3185	10607	6204
Si [100]	2329	8432	5843

Table 1: Density ρ, longitudinal (v_L) and transversal sound velocity (v_T), of polyimide [10], SiN [11] and Si [12].

4. Data-Analysis

SAWs propagate dispersively on the surface of the sample because higher frequency waves show lower penetration depth and propagate mainly in the layers, whereas lower frequencies with high penetration depth propagate mostly in the substrate. If the layers and the substrate have different sound propagation velocities, the phase velocity of the SAWs depends on frequency. Detecting the SAWs on the PI-SiN-Si-System (Figure 1) at two positions on the sample surface, the frequency dependent phase velocity of the surface acoustic wave can be determined. If the Fourier transformed laser induced signals, detected at different positions x_i, are denoted $U_i(f)$, then according to [4], the phase velocity $c(f)$ is given by

$$c(f) = \frac{(x_2 - x_1)2\,\pi f}{\Phi_2(f) - \Phi_1(f)}, \qquad (3)$$

where $\Phi_i(f)$ denote the phases of the frequency components $U_i(f)$. Figure 5 shows five laser induced signals detected at the surface of the PI-SiN-Si-System. The spatial distance between the detection points is 2mm.

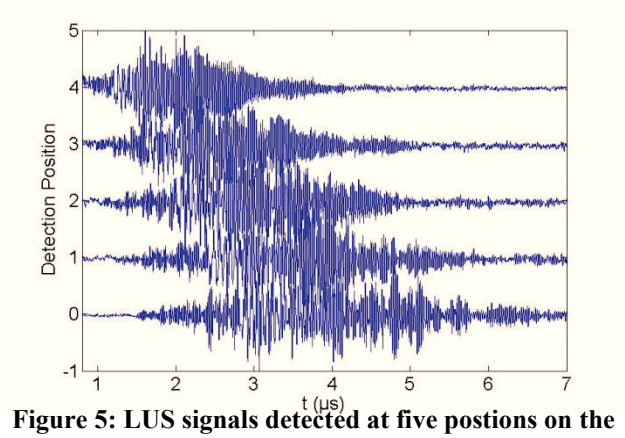

Figure 5: LUS signals detected at five postions on the PI-SiN-Si-System.

In Figure 5, the typical shape of the laser induced signals expected from e.g. [1] are not observed as a consequence of the multiple wave modes present in the frequency range up to 100 MHz, see Figure 3.

5. Results and Discussion

In Figure 6 we show the result for the experimentally evaluated dispersion relation for the 11 µm polyimide (PI) film on 800 nm SiN on a Si (100) substrate and the fitted theoretical curve. The considered frequency range for the fitting procedure is approximately up to 27 MHz (broken line), below which only one wave mode is present. In the frequency range where more than one wave mode are allowed, the measured phase velocity lies between the two present wave modes (Figure 6). The data evaluation uses the input parameters from literature which are summarized for SiN and Si in Table 1. Additionally, the thicknesses of the SiN layer and the PI layer are input for the theoretical model. Only the longitudinal and transversal sound velocity in the PI layer are altered in the fitting procedure.

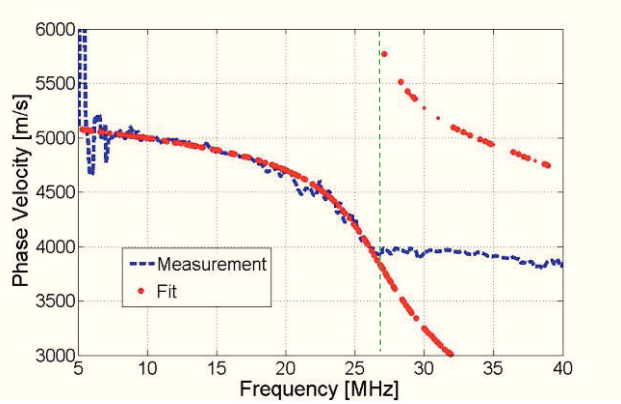

Figure 6: Dispersion relation of PI-SiN-Si-System. Theory (dots) fitted to experiment (broken line).

Since an isotropic substrate was assumed, in analogy to [4], the measurement was performed along the [100] direction of the silicon substrate for which the literature values, given in Table 1, can be used as input parameters. The evaluation via fitting the theoretical curve to the experimentally evaluated data gives a Young's modulus E of 4.92 GPa and a Poisson's ratio ν of 0.39, summarized in Table 2.

	ρ	v_L	v_T	E	ν
Fit	1464	2600	1100	**4.92**	**0.39**
Literature	1464	2660	1160	**5.44**	**0.38**

Table 2: Results compared to literature values [11]. Mass density ρ, sound velocities v_L and v_T, Young's modulus E and Poisson's ratio ν.

The signals in Figure 6 were measured with a distance of $x_2 - x_1 = 4\,mm$. This distance would be highly sufficient for most state of the art application in the manufacturing of semiconductor power devices.

The error in the measurement of the frequency dependent phase velocity can be estimated via [4]

$$\left|\frac{\Delta v}{v}\right| \leqq \left|\frac{2\Delta x}{x_2 - x_1}\right| + \left|\frac{2\Delta t\omega}{(\phi_2 - \phi_1)}\right|. \qquad (4)$$

The accuracy of the positioning and translation stage in the measurement was of $\Delta x \pm 1.2$ µm. An oscilloscope of 2GSa/s was used. The signals were measured with a distance of 4 mm. Applying equation (5), the error in the determined phase velocity is smaller than 10 m/s in our measurement.

In Figure 7, direct comparison of the wave modes in a PI-SiN-Si-system with the elastic constants from literature of Table 1 and the wave modes with the input parameters from the fitted theoretical dispersion relation, from Table 2, are shown.

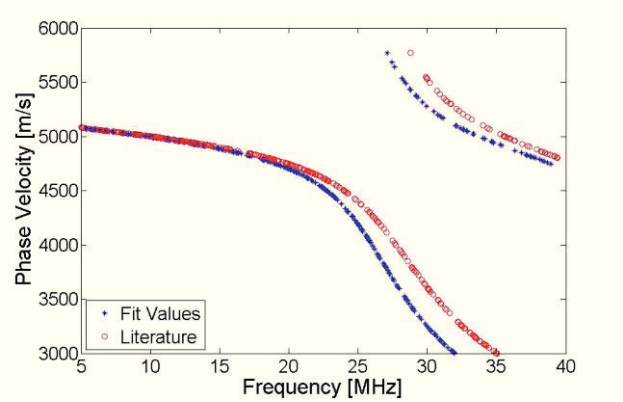

Figure 7: Dispersion relation of PI-SiN-Si-System from theoretical evaluations.

From Figure 7 it can be observed that small changes of the Young's modulus E and the Poisson's ratio ν change the dispersion relation of the Rayleigh wave to measureable extent in the considered frequency range. For higher wave modes, in the frequency range up to 120 MHz (Figure 8), the sensitivity to changes in the elastic properties of the polyimide layer continues to increase.

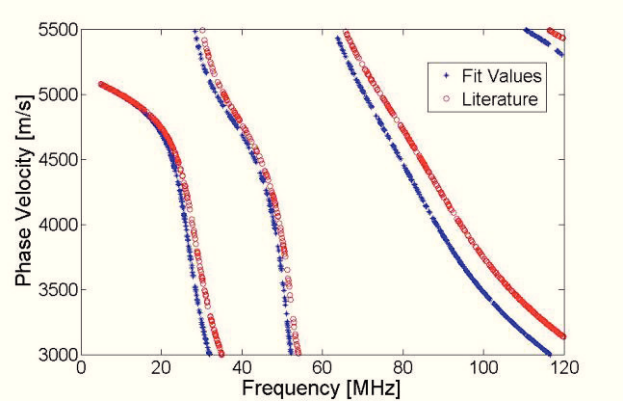

Figure 8: Dispersion relation of PI-SiN-Si-System from theoretical evaluations. Literature values as input (circles) compared to fitted values (crosses).

6. Conclusion

In this work, we report on the determination of the Young's modulus E and the Poisson's ratio ν of an 11 µm polyimide film, which is deposited on a silicon nitride (800 nm) coated silicon substrate (100). The analysis was performed by combining laser ultrasonic experiments and a numerically solved theoretical model. Additionally, the numerical model showed that especially the higher wave modes in the system are very sensitive to changes in the longitudinal and transversal sound velocities of the polyimide layer. The higher wave mode excitation and analysis in thin film systems is part of further studies. The laser ultrasonic method provides an efficient, non-destructive way to determine elastic constants of thin films on wafer level. Thus, the presented approach is a promising candidate for process-attendant characterization. The Young's modulus E and the Poisson's ratio ν can serve as valuable input for state-of the art measurement techniques and simulations [2].

Acknowledgments

This work is done as part of the project eRamp (P.No. 843740), which is co-funded by grants from ENIAC Joint Undertaking and from Austria, Germany, the Netherlands, Romania, Slovakia and the UK. Financial support by the Austrian Federal Government (in particular from Bundesministerium für Verkehr, Innovation und Technologie and Bundesministerium für Wissenschaft, Forschung und Wirtschaft) represented by Österreichische Forschungsförderungsgesellschaft mbH and the Styrian and the Tyrolean Provincial Government, represented by Steirische Wirtschaftsförderungsgesellschaft mbH and Standortagentur Tirol, within the framework of the COMET (P.No.837900) Funding Programme is gratefully acknowledged.

References

1. Grünwald, E. *et al*, "Young's Modulus and Poisson's Ratio Characterization of Tungsten Thin Films via Laser Ultrasound," *Materials Today: Proceedings 2* (2015), pp. 4289-4294.
2. Schöngrundner, R. *et al*, "Critical assessment of the determination of residual stress profiles in thin films by means of the ion beam layer removal method," *Thin Solid Films* 564 (2014) pp. 321-330.
   Treml R., *et al*, "High resolution determination of local residual stress gradients in single- and multilayer thin film systems," *Acta Materialia* 103 (2016) 616-623. Kozic D., *et al*, "Evaluation of the residual stress distribution in thin films by means of the ion beam layer removal method," *EuroSimE 2014*, BEL, April pp 1-5. Kozic D., *et al*, "Fracture mechanics of thin film systems on the sub- micron scale," *EuroSimE 2015*, HUN, April, pp 1-5.
3. Wilson W. C., "Review of Polyimides used in the Manufacturing of Micro Systems" Technical Memorandum, *NASA/TM-2007-214870* (2007).
4. Schneider D., *et al*, "Testing ultra-thin films by laser-acoustics" *Surface and Coatings Technology* 126 (2000) 136-141.
5. Rose J. L., Ultrasonic Waves in Solid Media, Cambridge University Press (New York 2014).
6. Ponzoni A., *et al*, "Ultrasensitive and highly selective gas sensors using three-dimensional tungsten oxide nanowire networks," *Appl. Phys. Lett.* 88 (2006).
7. Park K., *et al*, "Highly efficient, flexible piezoelectric PZT thin film nanogenerator on plastic substrates," Adv. Mater. 26 (2014), 2514–2520.
8. Zhang F., *et al*, "Ultrasonic characterizaion of mechanical properties of Cr- and W-doped diamond

like carbon hard coatings," *Thin Solid Films* 503 (2006) 250–258.
9. Tiersten H.F., "Elastic Surface Waves Guided by Thin Films," *J. Appl. Phys.* 40, 2 (1969).
Neubrand A., *et al,* "Laser generation and detection of surface acoustic waves: Elastic properties of surface layers," *J. Appl. Phys.* 71, (1992) 227.
Schneider D., *et al*, "Non-destructive evaluation of diamond and diamond-like carbon films by laser induced surface acoustic waves," *Thin Solid Films* 295 (1997) 107–116.
Schneider D., *et al*, "A photoacoustic method for characterising thin films," *Surface and Coating Technologies* 91 (1997) 136–146.
Hurley D. C., *et al*, "Surface acoustic wave methods to determine the anisotropic elastic properties of thin films," *Meas. Sci. Technol.* 12 (2001) 1486–1494.
10. Dhar L. *et al*, "Moduli determination in polyimid film bilayer systems," J. Appt. Phys., Vol. 77, No. 9, (1995) 4431-4444.
11. Briggs G. A. D. and Kolosov O.V., Acoustic Microscopy Oxford University Press (New York 2010)
12. Royer D. and Dieulesaint E., Elastic Waves in Solids I, Springer (1996).

Available online at www.sciencedirect.com

ScienceDirect

Materials Today: Proceedings 4 (2017) 7122–7127

materialstoday: PROCEEDINGS

www.materialstoday.com/proceedings

nanoFIS 2016

Laser Ultrasonic Thin Film Characterization of Si-Cu-Al-Cu Multi-Layered Stacks

Eva Grünwald[a], Robert Nuster[b], Günther Paltauf[b], Thomas Maier[c], Robert Wimmer-Teubenbacher[a], Ruth Konetschnik[d], Daniel Kiener[d], Verena Leitgeb[a], Anton Köck[a], Roland Brunner[a]*

[a]*Materials Center Leoben Forschung GmbH (MCL), Leoben, Austria*
[b]*Karl-Franzens University of Graz (KFU), Department of Experimental Physics, Graz, Austria*
[c]*Austrian Institute of Technology GmbH (AIT), Vienna, Austria*
[d]*Montanuniversität Leoben, Department of Material Physics, Leoben, Austria*

Abstract

In this work, the step-wise determination of elastic properties of a Si-Cu-Al-Cu stack via laser induced ultrasonic measurements is presented. The analysed Si-Cu-Al-Cu system consists of a silicon (100) substrate, two copper layers and an aluminium layer embedded between the copper layers, with a thickness of about 1 µm of each layer. The obtained results for the Young's moduli and Poisson's ratios of the multi-layered system are compared to literature values for bulk materials. The presented non-contact method shows high potential regarding the non-destructive evaluation of elastic properties of thin films in multi-layered systems.

Selection and/or Peer-review under responsibility of nanoFIS 2016 – Functional Integrated nano Systems.

Keywords: Thin Film Characterization; Laser Ultrasound; Multi-Layered Systems; Stack Charakterization

1. Introduction

The frequent application of coatings and thin film stacks in state of the art micro- and nano-electronic devices increases the interest in thin film stack characterization [1-6], especially since the mechanical properties of bulk

* Corresponding author. Tel.: +43-3842-459-2248; fax: +43-3842-459-22500.
E-mail address: roland.brunner@mcl.at

Selection and/or Peer-review under responsibility of nanoFIS 2016 – Functional Integrated nano Systems.

materials may differ from their thin film counterparts. However, at the same time, the use of various thin film materials at small scales makes the characterization of thin films and thin film stack configurations demanding. Many current testing techniques, *e.g.* nano-indentation measurements [7], require mechanical loading of the analysed thin film systems. In addition, the influence of the substrate can obscure the properties of the thin films [8]. Laser induced ultrasound (LUS) enables the contactless determination of acoustic wave related mechanical properties of thin films, *e.g.* [8-16]. In the presented work, the non-destructive, step-wise characterization of the Young's moduli and the Poisson's ratios of a Si-Cu-Al-Cu stack was carried out using laser induced ultrasonic measurements in combination with a theoretical model [17]. All layers have a thickness of 1 µm and were deposited via the same sputter process in order to keep the variation of the film properties to a minimum. Fitting the theoretical model to the experimentally evaluated data, only a limited number of parameters can be derived, *e.g.* the longitudinal and transversal sound velocities of one of the layers. The use of the step-wise approach enables the analysis of the whole Si-Cu-Al-Cu multi-layered stack. We characterize (i) a Si-Cu system, (ii) a Si-Cu-Al system and use the gained results for the characterization of (iii) a Si-Cu-Al-Cu stack. The results are a Young's modulus of 132 GPa and a Poisson ratio of 0.35 for the first copper layer, a Young's modulus of 70 GPa and a Poisson ratio of 0.33 for the intermediate aluminium layer and a Young's modulus of 112 GPa and a Poisson ratio of 0.35 for the Cu top layer.

2. Experimental Setup, Measurement and Data Analysis

2.1. Set-up

A schematic of the experimental set-up is shown in Figure 1. For the excitation of broadband surface acoustic waves (SAWs), nanosecond laser pulses were focused on the surface of the sample using a cylindrical lens. The Nd:YAG laser provided 10 ns light pulses of 532 nm wavelength at a repetition rate of 10 Hz. The line focus excitation generated SAWs propagating along the x_1-direction, see Figure 1, in a frequency range up to 100 MHz. For the contactless detection of the SAWs, a continuous wave (CW) laser beam was focused onto the sample surface. In the applied optical beam deflection approach, the light reflected back from the sample was divided into two equivalent parts by placing a sharp edged mirror in the beam path. The resulting two light beams were then detected via two photodiodes of a balanced photodetector (BPD) working in differential mode. A SAW propagating through the focus spot of the detection laser caused a deflection of the reflected light beam and therefore a change in the division ratio of the reflected light power detected at the two photo diodes of the BPD. Thus, the recorded signal was proportional to the slope of the surface displacement.

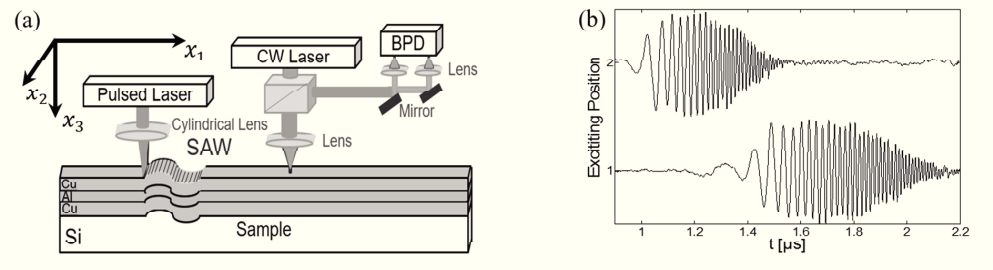

Fig. 1. (a) Schematic of experimental set-up and (b) laser induced SAWs excited at two different positions on the sample surface.

2.2. Measurement and data analysis

In accordance with literature [8-16], the surface displacement caused by the SAWs is detected for 2 excitation positions on each sample along the x_1-direction, while the detection position is kept constant, see Figure 1 (a). The excitation locations 1 and 2 in Figure 1 (b) are separated by a distance dx, which ranges from 6 mm to 8 mm in our measurements. Two detected SAW signals $u_1(t)$ and $u_2(t)$ are shown in Figure 1 (b). If $u_1(t)$ and $u_2(t)$ are Fourier transformed to their complex spectral functions, denoted by $U_i(f)$, the frequency dependent phase velocity $v\,(f)$ can be derived, *e.g.* [8-16]:

$$v(f) = \frac{2\,\pi f\,dx}{\Phi_2(f) - \Phi_1(f)}, \tag{1}$$

where $\Phi_i(f)$ denote the phases of the frequency components $U_i(f)$.

3. Theoretical Determination of the Frequency Dependent Surface Acoustic Wave Velocity

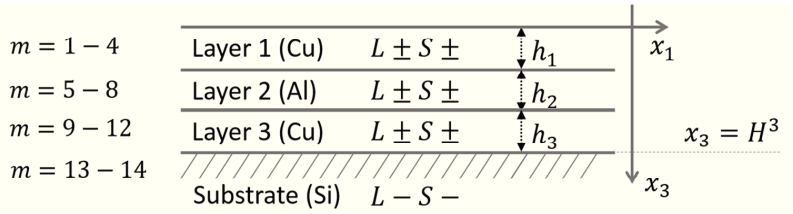

Fig. 2. Three layers (Cu-Al-Cu) on Silicon substrate [17].

Figure 2 shows a schematic of the analyzed Si-Cu-Al-Cu stack. In order to determine the frequency dependent phase velocity of a SAW propagating on a 3-layer on substrate system theoretically, a partial wave ansatz and a global matrix formalism were applied [17]. Each layer in Figure 2 has a height of h_i, where $H^i = \sum h_i$, i= 1,2,3. For the case of isotropic media and the assumption of linear elastic media, only four wave modes in each layer have to be considered. The four wave modes correspond to up- and down-propagating longitudinal and shear waves. In Figure 2, the longitudinal and shear waves are denoted by L and S, where + and – represent the up and down propagating wave modes and the index m counts the wave modes present in each layer. In a linear elastic, isotropic substrate, only the down-going longitudinal and shear waves have to be considered in the ansatz. Thus, a total of 14 wave modes are present in the three layer on substrate system. For an acoustic wave propagating in the x_1-direction (Figure 1), the particle displacement u_1 in x_1-direction and u_3 in x_3-direction in the nth layer, where $= 1,2,3, \ldots$, are given by [17]:

$$u_1^{(n)} = \sum_{m=4n-3}^{4n} C_m e^{ik(x_1 + \alpha_m x_3 - c_P t)},$$

$$u_3^{(n)} = \sum_{m=4n-3}^{4n} C_m U_{3m} e^{ik(x_1 + \alpha_m x_3 - c_P t)}. \tag{2}$$

In equation (2), the index m numbers the wave modes in the layers, C_m are the coefficients of the polarization vector $\vec{U}$, k is the wave number, α_m denotes the x_3 component of the direction vector, c_P the phase velocity of the SAW and t denotes the time. From equation (2), the entries of the strain and stress tensors can be computed [17]. The boundary conditions concerning the stresses σ_{ij} and particle displacements u_i in the three layer on substrate system are stress free interfaces:

$$\sigma_{31} = 0 \;@\; x_3 = 0 \text{ and } \sigma_{33} = 0 \;@\; x_3 = 0; \tag{3}$$

and the continuity of particle displacement and stresses at the interfaces:

$$u_{31}^n = u_{31}^{n-1};\; u_{33}^n = u_{33}^{n-1};\;\; \sigma_{31}^n = \sigma_{31}^{n-1} \text{ and } \sigma_{33}^n = \sigma_{33}^{n-1} \;@\; x_3 = H^{n-1}. \tag{4}$$

Considering the boundary conditions for the particle displacements u_i and the stresses σ_{ij} yields a matrix equation. Only if the determinant of the 14 x 14 boundary condition matrix, is forced to zero by the right combination of phase velocity and frequency, the condition for sound waves propagating in the solid is fulfilled [17].

4. Results

4.1. Thickness measurement of the multi-layered stacks

The thickness of each layer was measured from scanning electron microscopy (SEM) images - where secondary electrons (SE) were detected - using ImageJ evaluation software [18]. Figure 3 (a) shows a SEM image of the 1 µm Cu on Si System and Figure 3 (b) shows the Si-Cu-Al-Cu stack, consisting of a Si substrate, and three layers of approximately 1 µm thickness. The Cu as well as the Al films were deposited on the silicon wafers via DC magnetron sputtering.

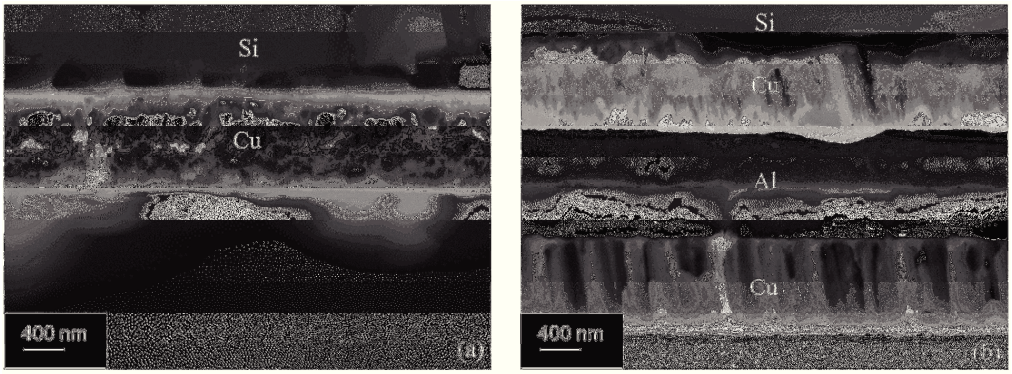

Fig. 3. SEM images of (a) Si-Cu system and (b) Si-Cu-Al-Cu stack measured with the (SE)-detector.

4.2. Young's moduli and Poisson's ratios of three stack configurations

The characterization of the Si-Cu-Al-Cu multi-layered system was realized via a step-wise procedure: As step (i) the copper layer of a Si-Cu system was analysed and the result of step (i) was used as input for step (ii), the characterization of the Al layer in a Si-Cu-Al system. The results for the Cu layer of step (i) and the Al layer of step (ii) were applied in order to determine the Young's moduli and the Poisson's ratios of the entire Si-Cu-Al-Cu stack as step (iii). In Figure 4 we show the results for the experimentally evaluated dispersion relations (solid lines) and the fitted theoretically determined frequency dependent phase velocities (dashed lines) for (i) the Si-Cu system (diamonds), (ii) the Si-Cu-Al system (circles) and (iii) the entire Si-Cu-Al-Cu stack (crosses).

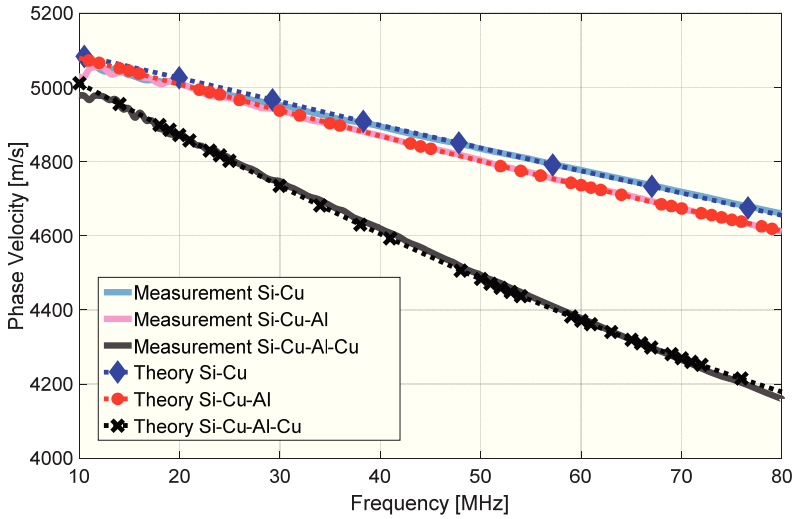

Fig. 4. Theoretically evaluated dispersion curve fitted to experimental results from LUS measurements.

For the theoretical evaluation, the longitudinal sound velocity and transversal sound velocity of Si, 8432 m/s and 5843 m/s, as well as the density of Si 2329 kg/m^3 were taken from literature [18,19] as input values. The densities of copper (8933 kg/m^3) and aluminium (2698 kg/m^3) were chosen according to [18,19]. Assuming isotropic, linear elastic layers and substrate, the elastic constants $c_{11} = v_L^2\rho$ and $c_{12} = c_{11} - v_T^2\rho$ are related to the Young's Modulus E and Poisson's ratio υ via

$$\mathrm{E} = \mathrm{c}_{11} - 2\left(\frac{\mathrm{c}_{12}^2}{\mathrm{c}_{11}+\mathrm{c}_{12}}\right) \text{ and } \upsilon = \mathrm{c}_{12}/(\mathrm{c}_{11} + \mathrm{c}_{12}), \tag{5}$$

where v_L denotes the longitudinal sound velocity, v_T the transversal sound velocity and ρ denotes the density. The evaluated Young's moduli E and Poisson's ratios ν are compared to literature values from [18-20] in Table 1.

Table 1. Comparison of LUS results to literature values

Analysed Layer	E (Result)	ν (Result)	E [18-20]	ν [18-20]
Cu Layer 1	132 GPa	0.35	110 – 130 GPa	0.33 – 0.36
Al Layer	70 GPa	0.33	70 GPa	0.33
Cu Layer 2 (top)	112 GPa	0.35	110 – 130 GPa	0.33 – 0.36

The error in the measurement of the frequency dependent phase velocity can be estimated via [11-13]

$$\left|\frac{\Delta v}{v}\right| \leqq \left|\frac{2\Delta x}{dx}\right| + \left|\frac{2\Delta t\omega}{(\phi_2-\phi_1)}\right|. \tag{6}$$

An oscilloscope of 2 GSa/s was used in our LUS measurements and the applied positioning and translation stage was of $\Delta\, x \pm 1.2$ µm accuracy. Equation (6), evaluated for the whole frequency range of LUS data, yields an error in the determined phase velocity which is smaller than ± 5 m/s in our measurements.

5. Discussion & Conclusion

A number of influences can alter thin film properties, *e.g.* microstructure differences due to various deposition procedures, residual stresses due to lattice mismatch of different materials and additional interfacial effects. From Table 1, it can be seen that the literature values [18-20] for copper can scatter significantly and the measurement of thin copper film properties might be essential, *e.g.* for state of the art material modelling. Many current testing techniques, *e.g.* nano-indentation, require the mechanical contact of sample and testing device and are therefore difficult to implement directly as in-line material testing and quality control tools. Additionally, substrate influences can conceal the coating properties. In this work, we propose the contactless, step-wise characterization of a Si-Cu-Al-Cu multi layered system via laser induced ultrasound. By characterizing a Si-Cu system as first step and a Si-Cu-Al system as second step, the whole Si-Cu-Al-Cu stack could be characterized. The outcome of our analysis is comparable to literature values for bulk media. The determined Young's modulus of 70 GPa and the Poisson ratio of 0.33 for aluminium agree with literature values for bulk aluminium. The evaluated differences in the Young's moduli of the first and second copper layer in the Si-Cu-Al-Cu stack (Table 1) might be a consequence of the microstructure, *e.g.* cracks and pores in the submicron scale and grain structure, see Fig. 3 (b). Complementary measurements of the film properties and advanced theoretical models, including *e.g.* residual stresses, are part of ongoing work. The presented contactless, step-wise characterization method shows high potential for fast determination of elastic properties of thin films and thin film stacks on wafer level.

Acknowledgements

This work is done as part of the project eRamp, which is co-funded by grants from ENIAC Joint Undertaking (P. No. 621270) and from Austria, Germany, the Netherlands, Romania, Slovakia and the UK (P. No. 843740). In addition financial support by the Austrian Federal Government (in particular from Bundesministerium für Verkehr, Innovation und Technologie and Bundesministerium für Wissenschaft, Forschung und Wirtschaft) represented by

Österreichische Forschungsförderungsgesellschaft mbH and the Styrian and the Tyrolean Provincial Government, represented by Steirische Wirtschaftsförderungsgesellschaft mbH and Standortagentur Tirol, within the framework of the COMET Funding Programme (P.No. 837900) is gratefully acknowledged.

References

[1] Schöngrundner R., et al., *Thin Solid Films* **564** (2014) 321–330.
[2] Chen S., Liu L., Wang T., *Surface & Coatings Technology* **191** (2005) 25–32.
[3] Kozic D., et al., EuroSimE 2015, April, *DOI: 10.1109/EuroSimE.2015.7103088.*
[4] Treml R., et al., *Acta Materialia* **103** (2016) 616–623.
[5] Treml R., et al., *Extreme Mechanics Letters*, in press, *DOI: 10.1016/j.eml.2016.01.004.*
[6] Kozic D., et al., *"Extracting flow curves from nano-sized metal layers in a thin film system" (submitted)*.
[7] Saha R. and Nix W.D., *Mater. Sci. Eng.,* **A319–321** (2001) 898–901.
[8] Zhang F., Krishnaswamy S., Fei D., Rebinsky D. A., Feng B., *Thin Solid Films* **503** (2006) 250–258.
[9] Tiersten H.F., *J. Appl. Phys.* **40** (1969).
[10] Neubrand A., Hess P., J. *Appl. Phys.* **71** (1992) 227.
[11] Schneider D., Witke T., Schwarz T., Schöneich B., Schultrich B., *Surface and Coatings Technology* **126** (2000) 136–141.
[12] Schneider D., Schwarz T., Scheibe H. J., Panzer M., *Thin Solid Films* **295** (1997) 107–116.
[13] Schneider D., Schwarz T., *Surface and Coating Technologies* **91** (1997) 136–146.
[14] Hurley D. C., Tewary V. K., Richards A. J., *Meas. Sci. Technol.* **12** (2001) 1486–1494.
[15] Grünwald E., et al., *Materials Today: Proceedings* **2** (2015) 4289-4294.
[16] Grünwald E., et al., EuroSimE 2016, April, *DOI: 10.1109/EuroSimE.2016.7463353.*
[17] Rose J. L., *Ultrasonic Waves in Solid Media*, Cambridge University Press (2014).
[18] Rasband, W.S., ImageJ, U. S. National Institutes of Health, Bethesda, Maryland, USA, *http://imagej.nih.gov/ij/*, 1997-2014.
[19] Briggs G. A. D and Kolosov O.V., *Acoustic Microscopy*, Oxford University Press (2010).
[20] Royer D. and Dieulesaint E., *Elastic Waves in Solids I*, Springer (1996).
[21] Punmia B.C., et al., *Mechanics of Materials*, Firewall Media (2002).
[22] Sanders P.G., Eastman J.A., Weertman J.R., *Acta Materialia*, **45** (1997) 4019–4025.

NDT&E International 84 (2016) 99–107

Contents lists available at ScienceDirect

NDT&E International

journal homepage: www.elsevier.com/locate/ndteint

Advanced 3D failure characterization in multi-layered PCBs

E. Grünwald[a], R. Hammer[a], J. Rosc[a], G.A. Maier[a], M. Bärnthaler[b], M.J. Cordill[b], S. Brand[c], R. Nuster[d], T. Krivec[e], R. Brunner[a,*]

[a] Materials Center Leoben Forschung GmbH (MCL), Leoben, Austria
[b] Erich Schmid Institute of Materials Science (ESI), Austrian Academy of Sciences and Department of Material Physics, Montanuniversität Leoben, Austria
[c] Fraunhofer Institute for Microstructure of Materials and Systems (IMWS), Halle, Germany
[d] Institute for Experimental Physics, Karl-Franzens University, Graz, Austria,
[e] Austria Technologie & Systemtechnik AG (AT&S), Leoben, Austria

ARTICLE INFO

Keywords:
Scanning acoustic microscopy
PCB reliability
Delamination
3D visualization

ABSTRACT

The non-destructive inspection of printed circuit boards (PCBs) represents an issue of constant importance in microelectronics. In this study, the detection of delaminations in modern PCBs by scanning acoustic microscopy (SAM) is described. It is shown that, even though the acoustic analysis is complicated due to the multi-layered build-up, delamination/delaminations can be located within the PCB by (1) utilizing the resulting curvatures of the layers for the detection, (2) analysing the generated SAM 2D data in combination with novel 3D data and (3) using Elastic Finite Integration Technique (EFIT) based simulations. Complementary destructive physical cross-sectioning corroborates the obtained results.

1. Introduction

Microelectronic devices in areas such as mobile communications, computing or networking are continuously pushed towards smaller scales, while their performance is simultaneously improved and their costs are reduced, More-than-Moore is the key approach in this context [1]. These ongoing efforts have impact on wafer level *e.g.* [2–4] but also on the design of printed circuit boards (PCBs). The need for multi-layered build ups, including conducting materials, such as copper, and composite materials makes state of the art PCBs complex systems [5] with respect to failure detection and analysis. Major failure modes in PCBs are delaminations which can be caused by manufacturing processes or thermo-mechanical influences [5].

In the fields of metrology, one distinguishes between invasive and non-destructive methods. Invasive analysis methods require mechanical preparation and may partially destroy the sample during inspection. In the latter the introduction of additional failures cannot be excluded. Non-destructive reliability analysis on the other hand exhibits many immanent advantages, such as the ability to repeat measurements offering the potential for in-line inspection. Therefore, especially the application of non-destructive inspection techniques of failure modes in PCBs is pursued in the field of metrology.

However, state of the art non-destructive analysis methods show inefficiencies in the analysis of PCBs. X-ray computed tomography (XCT), for instance, does not represent an ideal candidate for PCB failure analysis in general. High X-ray attenuating metals, like inherent copper layers lead to a considerable amount of scattered radiation [6]. The delaminations in PCBs are often extremely thin, resulting in a wide extension in *x-y* dimensions but only a very small extension in the *z*-direction. This presents a severe hindrance for the otherwise powerful XCT analysis: the necessary resolution (in *z*-direction) can only be obtained after destructive sample preparation, since the specimen has to be placed as close as possible to the X-ray tube but still allowing for rotation [6].

Scanning acoustic microscopy (SAM) shows high potential for rapid in-line inspection. It provides sufficient axial and lateral resolution to identify and localize defects in microelectronic devices [7–10]. However, the multiple copper layers embedded in an epoxy matrix render PCBs nearly impenetrable for acoustic waves [11]. Therefore, common delamination detection techniques by SAM, based on reflection- or through transmission, are highly challenging.

The current work describes the application of advanced SAM methods for the detection and visualization of delaminations in modern PCBs. To that purpose (1) the sensitivity of the SAM to local surface and sub-surface irregularities and its ability to penetrate opaque media is exploited, (2) sophisticated data analysis, SAMnalysis (IMWS) toolbox for SAM 3D data sets, and the 3D analysis software “Avizo Fire 8.0”, was used to create 3D visualizations of the PCBs. In addition (3) the analyses were supported by “EFIT” [12] simulations (MCL). Complementary destructive inspection of one PCB-sample corroborates the SAM results, identifying SAM as tool of choice for non-destructive PCB characterization.

* Corresponding author.

http://dx.doi.org/10.1016/j.ndteint.2016.08.003
Received 19 May 2016; Accepted 16 August 2016
Available online 24 August 2016

2. Material and methods

2.1. Scanning acoustic microscopy (SAM)

A scanning acoustic microscope (SAM) operated in reflection mode uses a piezoelectric transducer to generate acoustic waves which are then focused on the surface of the investigated sample [13,14]. Since the acoustic waves need a medium to couple to the specimen of interest, the sample is immersed in water acting as coupling fluid. The sound field can be focused below the specimen surface by decreasing the distance between the acoustic lens and the sample (z-axis). At the water-sample interface, the incident acoustic wave is partially reflected according to

$$R(90°) = -(Z_1-Z_2)/(Z_1+Z_2), \quad (1)$$

where perpendicular incidence of the sound waves is assumed. Z_1 denotes the acoustic impedance of water (product of sound velocity and mass density) and Z_2 denotes the acoustic impedance of the sample. The remaining ultrasonic wave is transmitted into the sample where it undergoes attenuation, scattering and reflection. The reflected acoustic waves travel back through the coupling liquid through the acoustic lens where they are spatially integrated by the piezoelectric element and converted into a time-variant electrical signal. This signal is commonly presented in time domain and referred to as "A-scan" (amplitude scan). The Fourier-transformation transfers the A-scan into the spectral domain giving access to the frequency components of the reflected ultrasonic wave. The dominant frequency f of the sound wave largely influences the achievable lateral resolution W:

$$W=\frac{\lambda}{2NA} \quad (2)$$

with the wavelength $\lambda = v/f$, and $NA = \sin(\theta_0)$; where θ_0 is the semi-angle of the lens aperture and v is the velocity of the acoustic wave in the propagation medium [13]. However, an increase in frequency (corresponding to higher resolution) is inevitably connected to a decrease in penetration depth caused by attenuation effects. According to [15], the axial resolution of a SAM is

$$\delta_{\text{Axial,Pulse}}=\frac{c}{2}\delta_t, \quad (3)$$

if two pulses need to be separated, δ_t denotes the temporal pulse width of the ultrasonic signal and c denotes the longitudinal wave velocity inside the sample. Axial surface extensions of the sample can be detected via SAM according to

$$\delta_{\text{Axial,Water}}=\frac{c_W}{2SR}, \quad (4)$$

where SR denotes the sampling rate of the acoustic microscope and c_W the velocity of sound in water.

2.1.1. Data acquisition in the SAM measurement

The A-scan signal contains 1-D information (along the z-direction) about the sample at a single location in the x-y plane. Signal components arriving at larger time delays in the A-scan correspond to larger distances the ultrasonic wave travelled. Provided the longitudinal sound velocity in the concerned material is known, the time delays between two pulses can be converted to the physical distance between the two sources in axial-direction. By moving the transducer in the x-y plane (at a fixed z distance) and collecting the A-scan data at each point, 3D information about the sample can be derived. The application of sophisticated analysis tools to the 3D data, allows the 3D visualization of the specimen and its interior. Alternatively, 2D cross-sections at a certain time range ("gate") in the A-scan (corresponding to the depth range) can be acquired and represented in C-scans (Fig. 1). In Fig. 1, the maximum amplitude in a given time-interval of the A-scan ("gate") is evaluated and depicted in grey values. Brighter pixels correspond to higher signal amplitudes and thus high reflection coefficients of the sample.

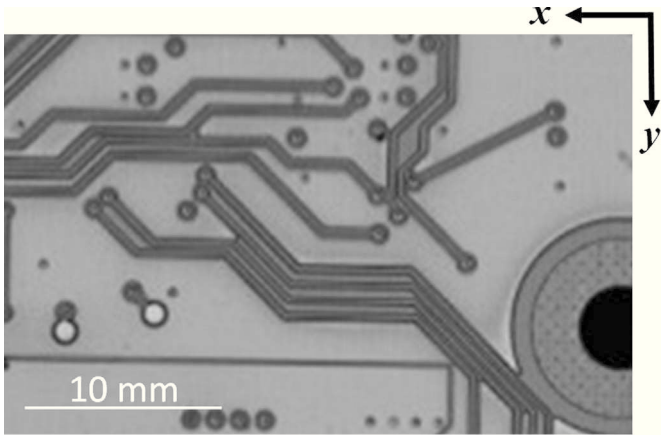

Fig. 1. SAM C-scan at the surface of the PCB, ("WinSAM5", PVA TePla).

In the work reported here, a commercially available scanning acoustic microscope "SAM 400" (PVA TePla Analytical System GmbH, Westhausen, Germany) was operated in reflection mode, using a 75 MHz focused transducer of 12.7 mm focal length. The A-scan acquired with this transducer at a well laminated part of the analysed PBC and its Fourier-transformed are shown in Fig. 2. The spectrum represents the frequency components reflected from the sample, in contrast to the nominal frequency of the transducer which is 75 MHz. The spectral maximum occurs at approximately 40 MHz. The sample and part of the transducer were immersed in water at room temperature that served as the coupling medium. The reflected signal, which was recollected by the same transducer, was analysed by the inspection software "WinSAM5" (PVA TePla Analytical Systems GmbH, Westhausen, Germany).

Additionally, the 3D data of the PCB were extracted using the advanced software package "SAMnalysis" (IMWS). 3D representations of the PCB were obtained using "Avizo Fire 8.0" based on the "SAMnalysis" data analysis results.

2.1.2. EFIT simulation of the SAM measurements

The discretization of the governing equations of ultrasonic wave motion in isotropic, linear elastic materials based on the Finite Integration Technique (EFIT) is described elsewhere [12].

In the analysis shown here, a two dimensional simulation (in the x-z-plane) of the SAM measurement was performed. Specifically, the reflection and scattering of sound waves at a model of the PCB and at relevant interfaces, *e.g.* copper-epoxy interfaces, were simulated. For the model of the multi-layered PCB, the longitudinal and transverse sound wave velocities as well as the mass density and thickness of the PCBs layers were input values. Here isotropic materials were assumed. The glass fibres, which cause attenuation and scattering of the acoustic waves in the measurement, as well as the frequency dependent attenuation were not included in the simulation. The focusing of the sound waves was simulated by a sound field emitted following a circular arc, corresponding to a semi-angle of the lens aperture of 20°.

Parts of the propagating sound waves are reflected at the interfaces of the PCB. Various detection points can be implemented in the simulations, yielding *e.g.* the back reflected signal from the sample as function of time which can be compared to the measurement. The mesh size within the EFIT simulation has been chosen to meet the necessary accuracy.

2.1.3. Optimized transmission trough copper layers

In contrast to the reflection at a single interface which is given by

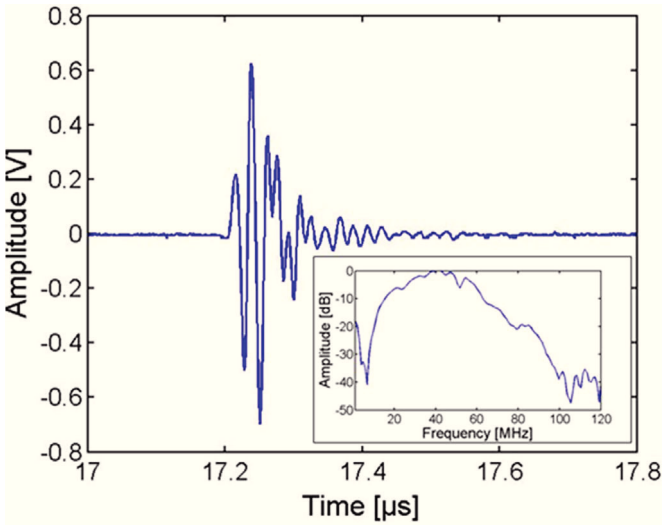

Fig. 2. A-scan of the reflected signal at well laminated area of the PCB and its spectrum ("SAMnalysis", (IMWS)).

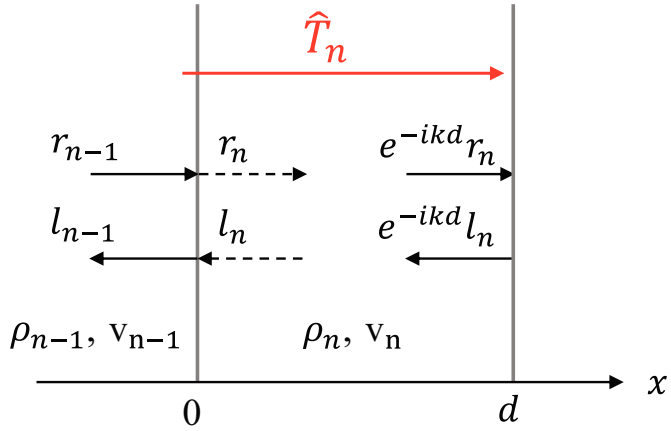

Fig. 3. Schematic of sound transmission through a copper layer of thickness d embedded in epoxy.

Eq. (1), the transmission through copper layers embedded in epoxy is frequency dependent, see *e.g.* [16]. The frequency dependence is caused by resonator effects and can be described by destructive interference of incoming and reflected waves. For perpendicular incidence, the frequency with maximal transmission correspond to $n\lambda/2 = d$ (the half wavelength in the copper layer has to be a multiple of the layer thickness) with n=1,2,3,... This can be exploited for an optimized choice of the transducer frequency. The mathematical description of the frequency dependent transmission through the copper layer is revealed by the transfer matrix technique.

In each layer an approach for right and left-going plane waves is used (see Fig. 3)

$$u_n = r_n e^{i(\omega t - k_n x)} + l_n e^{i(\omega t + k_n x)},$$

where ω denotes the angular frequency, t the time and k the wave vector component. The first constraint at the interface requires the displacement u to be continuous

$$r_{n-1} + l_{n-1} = r_n + l_n.$$

The second constraint imposes the stress $\sigma = (\lambda + 2\mu)\frac{\partial u}{\partial x}$ to be continuous across the boundary which leads to

$$Z_{n-1}(r_{n-1} - l_{n-1}) = Z_n(r_n - l_n)$$

where $Z_n = \rho_n v_n$ and $k_n = \omega/v_n$. The right-going wave picks up the phase $e^{-ik_n d}$ by traversing the layer and the left-going $e^{ik_n d}$, respectively. Normalizing by $\frac{1}{2Z_n}$ provides the transfer matrix

$$\begin{pmatrix} r_n \\ l_n \end{pmatrix} = \frac{1}{2Z_n} \begin{pmatrix} (Z_n + Z_{n-1})e^{i2\pi f d_n/v_n} & (Z_n - Z_{n-1})e^{-i2\pi f d_n/v_n} \\ (Z_n - Z_{n-1})e^{i2\pi f d_n/v_n} & (Z_n + Z_{n-1})e^{-i2\pi f d_n/v_n} \end{pmatrix} \begin{pmatrix} r_{n-1} \\ l_{n-1} \end{pmatrix}.$$

The transfer matrix propagates the wave from material $n-1$ into material n to the end of material n. For the transfer from epoxy through copper and into epoxy again one has to apply the transfer matrix $\hat{T}_n$ and then $\hat{T}_{n+1}$ (with d_{n+1}=0). Setting the incoming wave as r_{n-1} =1, r_{n-1}=0 and evaluating r_{n+1} leads to the formula for the amplitude transmission coefficient

$$T_{\mathrm{Epoxy-Cu-Epoxy}} = \frac{4Z_{\mathrm{Cu}}Z_{\mathrm{Epoxy}}e^{-\frac{i2\pi f d_{\mathrm{Cu}}}{v_{\mathrm{Cu}}}}}{(Z_{\mathrm{Cu}} + Z_{\mathrm{Epoxy}})^2 e^{-\frac{i4\pi f d_{\mathrm{Cu}}}{v_{\mathrm{Cu}}}} - (Z_{\mathrm{Cu}} - Z_{\mathrm{Epoxy}})^2}$$

Obviously, $|T|$=1 for $-\frac{4\pi f d_{\mathrm{Cu}}}{v_{\mathrm{Cu}}} = 2\pi n$ (n=0,1,2,3,...), leads to the resonance frequencies $\rightarrow f = \frac{v}{2d}n$ (this corresponds to half of the wavelength condition $\frac{n\lambda_{\mathrm{Cu}}}{2} = d_{\mathrm{Cu}}$). For a 64 µm copper layer with a longitudinal sound velocity in copper of 4600 m/s one gets the (T=1) frequencies at 0 MHz, 35.9 MHz, 71.9 MHz, 107.8 MHz, 143.8 MHz, ... The transmission spectrum is shown in Fig. 4.

2.2. Sample

A cross-section of the analysed PCB (48.5×82×1.2 mm³) is shown in Fig. 5. The PCB was thermally cycled using the reflow test. As a consequence of the thermal cycling process, failures like delaminations and a bending over the PCBs entire lateral extension were induced.

For acoustic analysis, the copper layers in the sample present a severe hindrance: According to Eq. (1), the reflection coefficient R at a epoxy – copper interface is approximately 79% for Z_{epoxy}=5. 15MRayl and Z_{Copper}=42. 64MRayl. Multiple copper layers embedded in an epoxy matrix render PCBs nearly impenetrable for acoustic analysis [11].

2.3. Complementary assessment

After the SAM analysis, the PCB was sequentially ground and imaged using optical microscopy along the y-direction (48.5 mm). Each grinding step was performed with 400 grit SiC paper and removed approximately 0.8 ± 0.2 mm of the PCB at each pass. In total, 54 steps were required to cross-section the entire PCB. After each step, the entire width of the PCB was imaged using 12–15 images at a low magnification and stitched together into one image (Olympus Streamsoftware). Areas of delamination were imaged a second time at a higher magnification also employing the stitching technique (Fig. 6). For each identified delamination, the x-position and length were measured. It should be noted that the mechanical cross-sectioning took place without considering the results obtained by the SAM analysis.

3. Results

3.1. EFIT results: reflection at various interface configurations

Fig. 7 shows the simulated reflection of acoustic waves at various epoxy interfaces. The ultrasonic waves travel from top to bottom until they are reflected. In Fig. 7(a), the acoustic wave penetrates the epoxy layer underneath the PMMA layer as a consequence of the similar elastic properties of water, PMMA and epoxy. In contrast, the majority of the signal is reflected at the water-copper interface shown in Fig. 7(b). At an air-filled delamination, practically the whole signal is reflected since the acoustic impedance of air is close to zero, Fig. 7(c).

In Fig. 8, the simulated A-scans corresponding to Fig. 7 are shown. The A-scan of a PMMA-layer on epoxy (solid line) shows one reflection

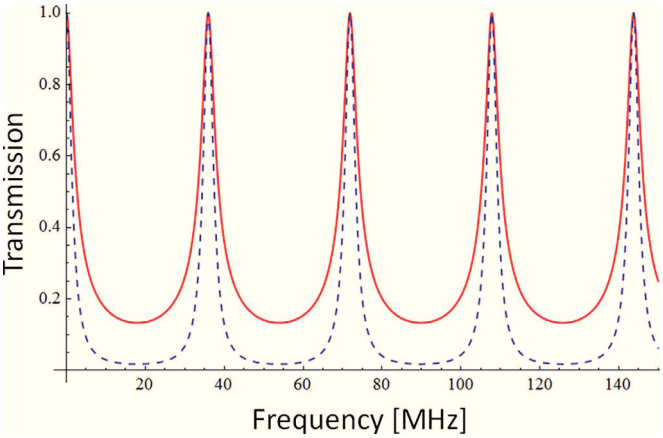

Fig. 4. The transmission spectrum *versus* acoustic frequency, shown for amplitude transmission (solid red line) and intensity transmission (dashed blue line). (For interpretation of the references to color in this figure legend, the reader is referred to the web version of this article.)

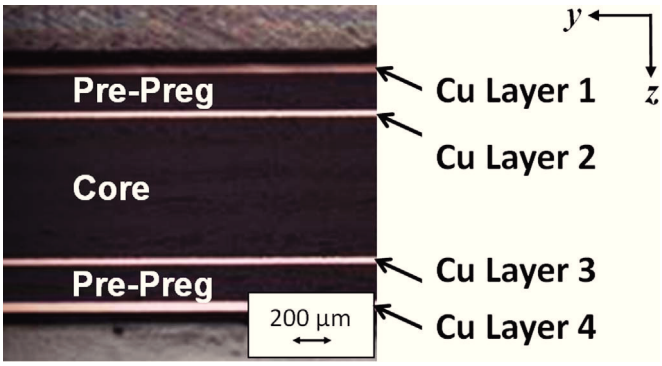

Fig. 5. Cross-section of the multi-layered PCB that was inspected by SAM. The core, the pre-preg (epoxy glass fibre composite) and the copper layers are visible.

at the water-PMMA interface and a second, similar in amplitude at the PMMA-epoxy interface. The copper-epoxy A-scan (broken line) shows high amplitude at the first water-copper interface and multiple reflections ("ringing") caused by the epoxy-copper or the water-copper interface, respectively. In the case of a delamination in an epoxy layer (dotted line), the reflected signal shows highest amplitude and a change in phase at the delamination. The presented simulations (Figs. 7 and 8) are in accordance with Eq. (1): the smaller the impedance mismatch of the adjacent media, the lower is the reflection coefficient.

3.2. Penetration depth analysis via "SAMnalysis" (IMWS)

Fig. 9 shows images computed by the software package "SAMnalysis" (IMWS). The highly reflecting first layer of copper is shown in Fig. 9(a), only a small amount of the signal is left in the underlying layer shown in Fig. 9(b). Fig. 9 was obtained by applying the sliding window analysis (SWA) to time domain SAM data in combination with the tilt compensation of the "SAMnalysis" (IMWS) software toolbox. The SWA uses the SAM signal in the whole time range (A-scan) and divides it into overlapping time-windows from which acoustic C-scans are computed using the backscatter amplitude integral (BAI) signal parameter. In this manner, very fine z-steps can be obtained. Applying one of the multiple options for tilt-compensation implemented in the "SAMnalysis", IMWS, the interior of the sample can be represented accurately. The tilt compensation used here detects the threshold crossing of the signal of the surface in a defined time range in the A-scan and places the surface signals at equal times or *z*-positions, respectively. In this manner, the bent surface of the PCBs was synthetically "flattened" and the appropriate penetration depth was estimated. It has to be mentioned, that the tilt compensation smoothed the delaminations and the surface. Therefore, the application of the filter with respect to delaminated areas needs to be well considered. Only a very slight contrast variation (circled in Fig. 9) can be seen at the delaminated areas of the PCBs. These small variations cannot be classified as delaminations directly.

3.3. Indirect failure detection

According to Eq. (1) and Fig. 8, the direct detection of a delamination would lead to an increase of the amplitude in the A-scan corresponding to a high reflectivity, caused by the large impedance mismatch at the delamination. Therefore, detecting a delamination directly would lead to largely increased brightness in the acoustic micrograph. Additionally, the reflection at a delamination would lead to a phase reversal of the signal, as illustrated in Fig. 8. In the analysis reported here, the delaminations could not be detected directly. More precisely, the delamination has neither been detected by an increase in amplitude nor by a phase reversal as shown in Fig. 8. Since the acoustic waves have been attenuated to a large extent on the way to the delaminations and/or at the way back to the material composition and the various copper-epoxy interfaces, the interface to the delamination vanished. However, delaminations were detected indirectly, exploiting the below explained effects.

3.3.1. Time shifted A-scans due to delaminations

The first effect is the depiction of delaminations as dark spots in the acoustic micrographs as shown in Fig. 10.

The dark delaminated areas result from so called "gating-effects". The *x*-*y* scan was computed from a fixed *z*-position, resulting in the sound wave reflected at the delamination arriving earlier at the transducer; compare timestep 4 in Fig. 11.

Fig. 11(a) shows the simulated reflection of an ultrasonic wave at a well laminated area of the PCB. In comparison, the reflection and scattering at a local curvature caused by a delamination is shown in Fig. 11(b). In Fig. 11, the top layer represents the PCB coating, underneath is the first copper layer on the pre-preg (the glass-fibres are not included in the model) followed by the second copper layer. The ultrasonic waves travel from top to bottom and the colour-scale in Fig. 11 represents the normalized velocity magnitude. In accordance with the experiment, all simulations in Fig. 11 were performed at a frequency of 40 MHz and a pulse width of 20 ns.

The shorter way the ultrasonic wave has to travel, in the case of reflection at a delaminated area, leads to time-shifted A-scans shown in Fig. 12. Here, the experimental results are confirmed by the simulations. Setting the gate to *e.g.* the surface of the sample at a well laminated area results in a gate below the surface at the delaminated area, see Fig. 12(a), "Gate 1". In Fig. 10, the positions where the A-scans shown in Fig. 12(a) were acquired are marked by a black "X"

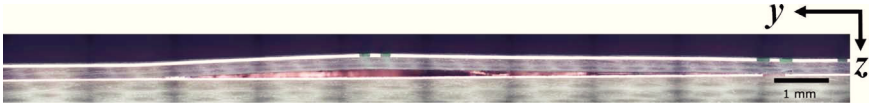

Fig. 6. An example of a delamination found in the PCB. The cross-section was imaged with optical light microscopy using a "stitching" technique.

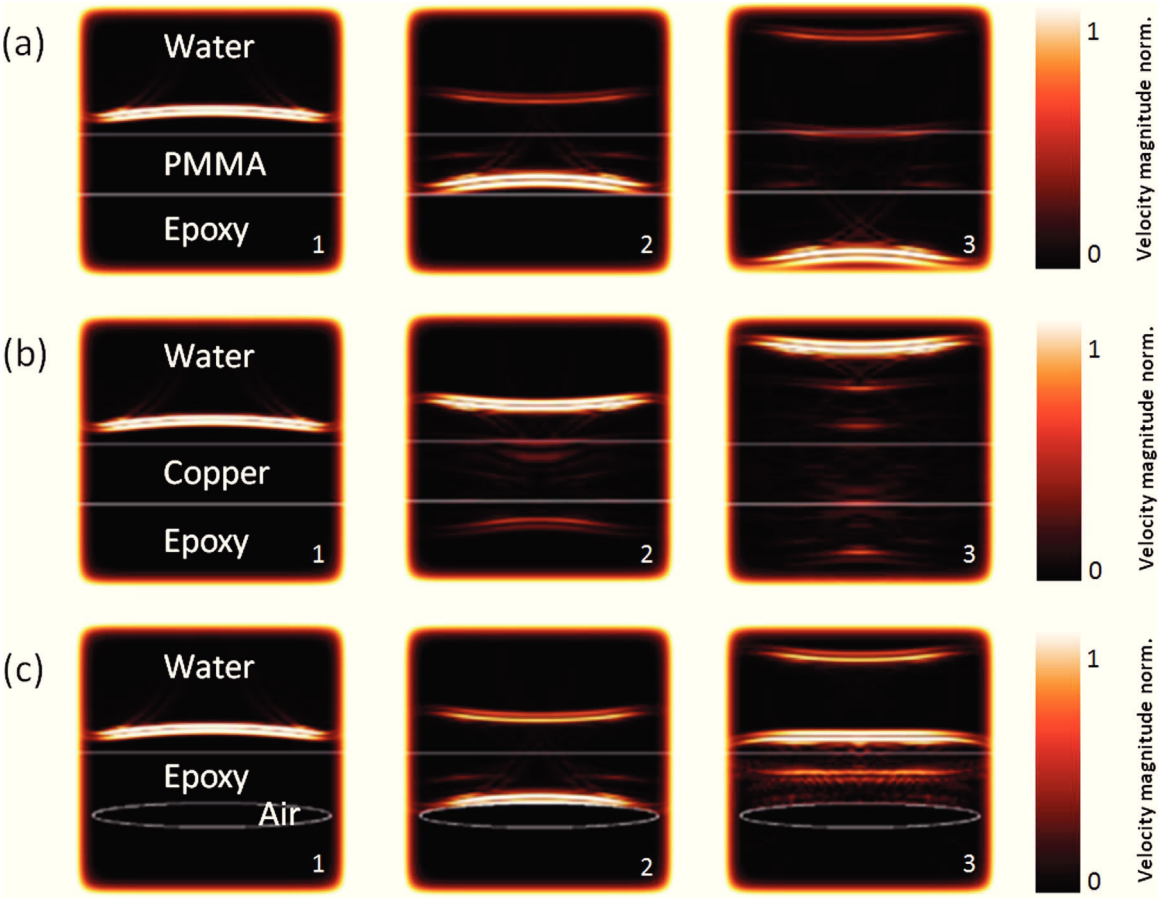

Fig. 7. Reflection of acoustic waves at a water-PMMA-epoxy interfaces (a), a water-copper-epoxy interfaces (b) and on a delamination in an epoxy layer (c), timesteps 1–3, ("EFIT", MCL).

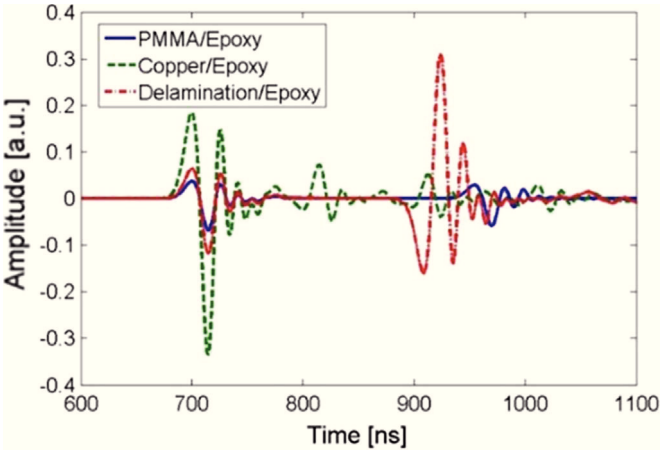

Fig. 8. Simulated A-scans in a water-PMMA-epoxy system (solid line), water-copper-epoxy system (broken line) and a delamination in epoxy (dotted line), ("EFIT", MCL).

(well laminated) and a white "X" (local curvature).

In Fig. 12, the A-scans of the SAM measurement (a) and the simulation (b) are compared. The amplitude-ratios (of "delaminated A-scan" compared to "well laminated A-scan") and the time-shift as well as the general wave form are in good agreement for measurement and simulation. Especially the first reflection at the PCB coating and the high amplitude in the A-scan resulting from the first copper layer coincide in the case of simulation and measurement. The exact wave form is very sensitive to the layer thickness. The values of the sound velocity of the analysed materials were taken from [11,17]. The attenuation is not implemented in the simulation. In the measurement, Fig. 12(a), the signal is not immune to attenuation effects, caused mainly by the glass-fibres in the pre-peg layer. This leads to decreasing amplitudes in the measured A-scan.

3.3.2. Decrease in the amplitude of the reflected signal due to delaminations

The second effect exploited in this work for indirectly detecting delaminations is the decrease in amplitude in the A-scan at a delaminated area of the PCB, which is corroborated by simulation and measurement in Fig. 12. As a result of the locally bent surface (Fig. 11), the acoustic waves are partially scattered at different angles and cannot contribute to the transducer signal.

Setting the gate to a wide time range in the A-scan, "Gate 2" in Fig. 12(a), and performing a SAM C-scan, the delaminated area shows a decrease in amplitude (see Fig. 13) compared to the well-laminated area.

3.4. Visualization of PCB delaminations in 3D image

Due to the bent specimen surface neither the number nor the full extent of the delaminations can be evaluated from a single 2D image in reflection mode acoustic microscopy. To visualize all delaminations in the PCB in a single image, without any loss of information, a 3D representation of the PCBs was obtained (Fig. 14).

To this purpose, all time-domain data aquired by "WinSAM5" (PVA TePla) and analysed using the SWA in "SAMnalysis" (IMWS) was combined into a 3D visualization using "Avizo Fire 8.0". In the 3D image, the *x-y* extension of the delaminations can be measured (Fig. 12). According to Eq. (4), surface extensions of approximately

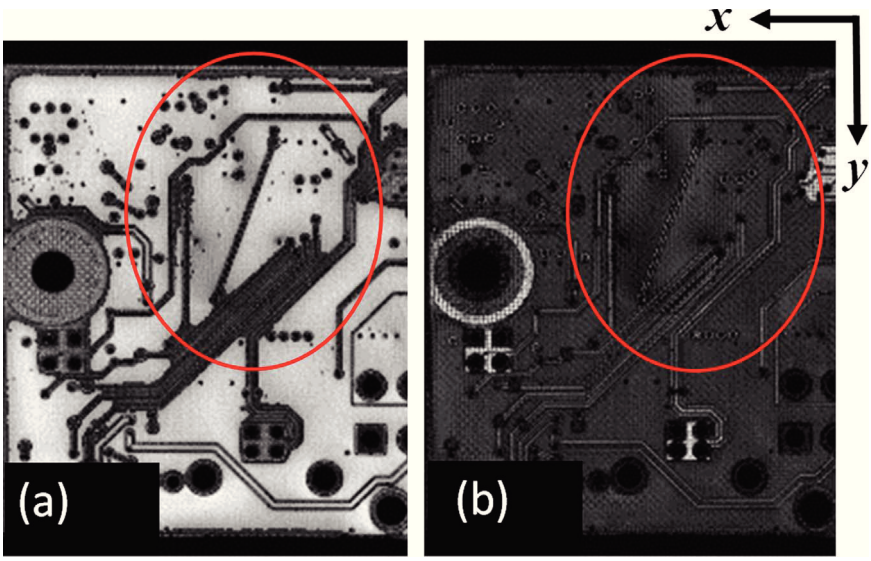

Fig. 9. (a) Scan at the first copper layer showing a signal with rather high amplitudes and (b) inside the first layer of pre-preg with rather small amplitudes due to the strong reflection at the first copper layer ("SAMnalysis", IMWS).

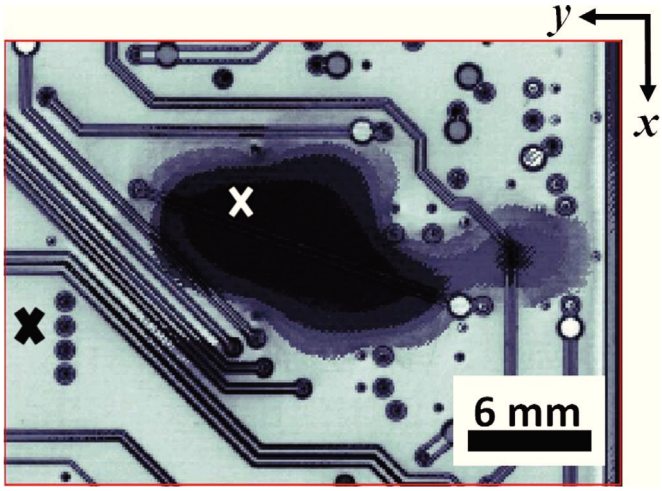

Fig. 10. Section of SAM C-scan of delaminated PCB ("SAMnalysis", IMWS).

750 nm are detectable by SAM since its ADC board has a sampling rate of 1 GHz.

Since the acoustic signal could be detected in the first layer of pre-preg without an increase in amplitude in the A-scan and without a phase reversal, as expected from Eq. (1) or Fig. 8, at a delamination, the poorly laminated areas must have occurred at the second copper layer (Fig. 5). It is noteworthy, that the PCB has been acoustically analysed from both sides. The analysis from the opposite side showed no indication of a delamination.

3.5. Comparison of SAM 3D visualization and physical cross-sectioning

The 3D representation of a PCB obtained from SAM data is shown in Fig. 15, in direct comparison to the results obtained by mechanical cross-sectioning.

The delaminated areas identified by SAM are marked green in the 3D visualization of the PCB. By mechanical cross-sectioning the entire PCB, four large delaminated areas were found at the same positions observed by SAM (Fig. 15).

4. Discussion

The major problems in analysing PCBs by conventional SAM methods are the highly reflecting copper-epoxy interfaces and the attenuation effects due to *e.g.* the glass fibres embedded in the PCBs. The strong attenuation and scattering effects in the PCB cause a continuous decrease in the A-scan amplitude shown in Fig. 12(a). In contrast, the amplitude in the A-scan decreases less in the simulation, where the glass fibres and the frequency dependent attenuation of acoustic waves are not implemented, see Fig. 12(b) for comparison.

For practical applications, the frequency of the transducer should be as low as possible to overcome attenuation effects and to increase transmissivity at low frequencies (Fig. 4). On the other hand, the applied frequency should be as high as possible to obtain maximal lateral resolution, according to Eq. (2). In addition, the transmission maxima shown in Fig. 4 for the underlying structure should be taken into account.

Therefore, the most promising technique would employ a custom made transducer for each analysed sample. In this way, even SAM through scans might be possible where not the reflected but the transmitted signal is recorded and analysed.

The presented indirect failure detection bypasses the challenging requirements, caused by the highly attenuating glass fibres, the strongly reflecting copper-epoxy interfaces and other scattering effects in the PCBs and without the need for customized transducer build-ups.

In the work reported here, four large delaminated areas detected in the PCB by SAM indirectly were complementary corroborated by mechanical cross-sectioning (Fig. 15). Moreover, the isolation of possible delaminated interfaces by SAM was confirmed since all delaminations were found to occur at the pre-preg to "copper layer 2" interface (see Fig. 5) in the physical cross-sectioning analysis. Additional small delaminations, marked by blue lines in Fig. 15, were observed in the mechanical cross-section analysis. These small delaminations are likely caused by the mechanical polishing procedure and may not be representative. The placement and irregularity supports this hypothesis. Benefits of the non-destructive SAM analysis are therefore the exclusion of introducing additional failure modes as preparation artefacts, as well as the opportunity to examine the PCB invasively for verification. One delamination shown in Fig. 15 (at 4–5 cm length) shows a very fine extension which was not fully observed by SAM or may be explained by inaccuracies in measuring the distance and length of the delamination in the optical micrographs.

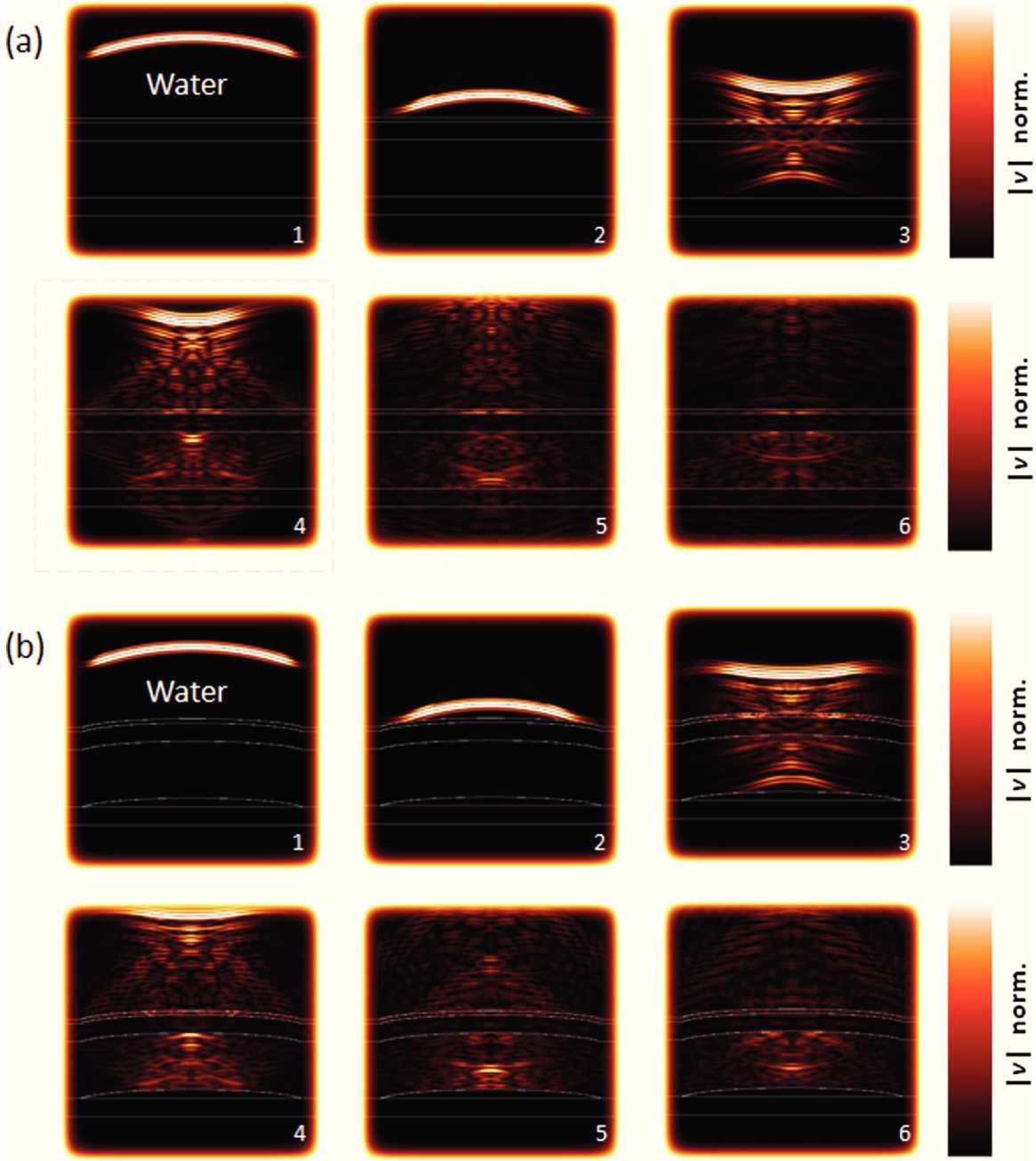

Fig. 11. (a) Reflected and scattered ultrasonic waves at well laminated area of the PCB and (b) at a local curvature caused by a delamination (b) at 40 MHz, timesteps 1–6 ("EFIT", MCL).

It should be mentioned that the SAM measurement was performed in less than about 30 min, whereas the mechanical cross-sectioning of the entire PCB took approximately 30 h.

5. Conclusion

The current work presents the indirect detection and 3D visualization of delaminations in multi-layered PCBs using scanning acoustic microscopy. The proposed method of indirect failure detection is applicable even if the optimal transducer for a specific sample is not available, through scans cannot be conducted, or the delamination is filled with water.

The lateral extensions of the delaminations were determined and the delaminated layer was identified by SAM. This represents a major advantage compared to other analysis methods which are sensitive to the surface topography but cannot penetrate opaque media. Another significant advantage of the SAM-based analysis presented in this work is the option to compute 3D visualizations of the delaminated areas and their height profile. For comparison, the SAM measurements conducted here were simulated and showed good agreements between simulation and the experimental results. The accordance of the acoustic analysis with the mechanical cross-sectioning technique corroborates SAM as a suitable, time-efficient and non-destructive tool in detecting and visualizing delaminations in PCBs, especially when combined with state of the art analysis software and simulations. Thus, the indirect failure detection by SAM presented in this work should be considered as an alternative analysis tool for PCB quality assessment.

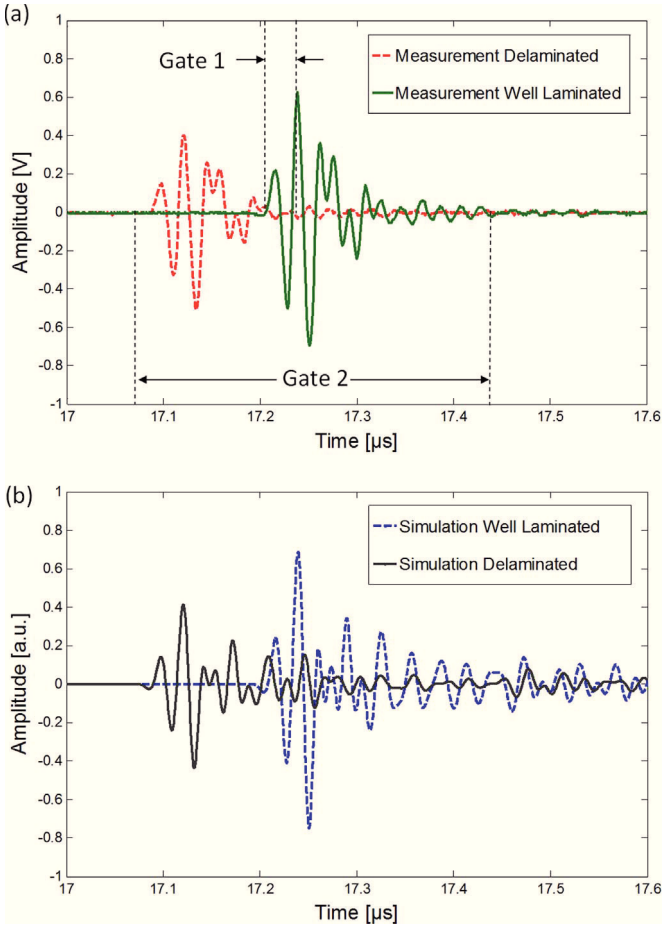

Fig. 12. A-scan of delaminated and well laminated area (a) SAM measurement, compared to (b) ("EFIT", MCL).

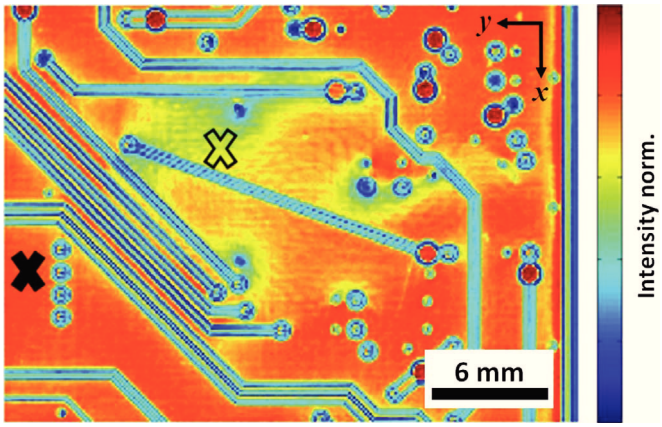

Fig. 13. SAM C-scan section of delaminated (dashed line) PCB ("SAMnalysis", IMWS).

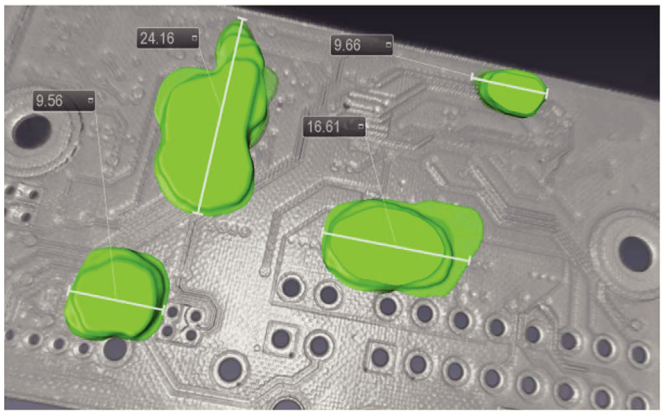

Fig. 14. 3D visualization and measurement of delaminations in PCBs according to SAM data ("WinSAM5", PVA TePla, "SAMnalysis", IMWS and "Avizo Fire 8.0").

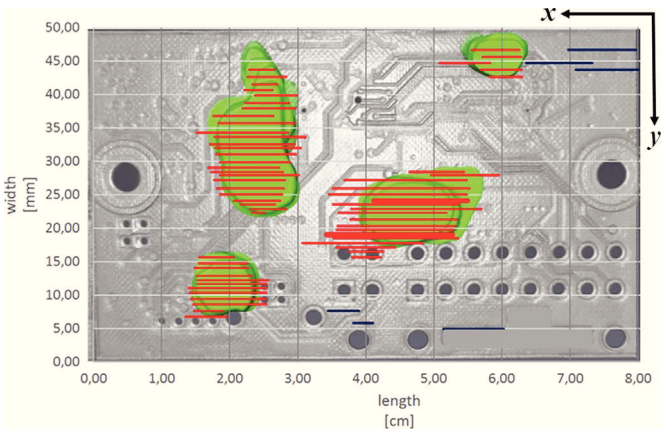

Fig. 15. Comparison of delamination detection by SAM based data analysis (green) and mechanical cross-sectioning results (red and blue lines) ("WinSAM5", PVA TePla, "SAMnalysis", IMWS and "Avizo Fire 8.0"). (For interpretation of the references to color in this figure legend, the reader is referred to the web version of this article.)

Acknowledgements

The authors would like to thank Peter Westenberger (FEI), Peter Czurratis (PVA TePla) and Peter Hoffrogge (PVA TePla) for helpful discussion. This work is done as part of the project eRamp, which is co-funded by grants from ENIAC Joint Undertaking (P.No. 621270) and from Austria, Germany, the Netherlands, Romania, Slovakia and the UK (P.No 843740). Financial support by the Austrian Federal Government (in particular from Bundesministerium für Verkehr, Innovation und Technologie and Bundesministerium für Wissenschaft, Forschung und Wirtschaft) represented by Österreichische Forschungsförderungsgesellschaft mbH and the Styrian and the Tyrolean Provincial Government, represented by Steirische Wirtschaftsförderungsgesellschaft mbH and Standortagentur Tirol, within the framework of the COMET Funding Programme (P.No. 837900) is gratefully acknowledged.

References

[1] Garrou P, et al. Handbook of 3D integration: vols. 1 and 2. Germany: Wiley-VCH Verlag & Co.; 2012.
[2] Schöngrundner R, Treml R, Antretter T, Kozic D, Ecker W, Kiener D, et al. Thin Solid Films 2014;564:321–30.
[3] Treml R, Kozic D, Zechner J, Maeder X, Sartory B, Gänser H-P, et al. Acta Mater 2016;103:616–23.
[4] Grünwald E, Nuster R, Treml R, Kiener D, Paltauf G, Brunner R. Mater Today: Proc 2015;2:4289–94.
[5] Hu G, et al. Microelectron Reliab 2;2011:416–24; Geniy K, et al. EPJ web of conferences; 2015. p. 82.
[6] Flisch A, et al. iCT; 2008. p. 109–15. ISBN: 978-3-8322–9418-2.
[7] Brand S, et al. Microelectron Reliab 2012;50:1469–73.
[8] Rajamand P, et al. Microelectron Reliab 2003;43:1815–20.
[9] Gilmore RS. Industrial ultrasonic imaging/microscopy. Physical acoustics, vol. 24. New York: Academic Press; 1999. p. 275–346.
[10] Zinin PV, et al. Ultrasonic and electromagnetic NDE for structure and material characterization: engineering and biomedical applications. In: Kundu Tribikram, editor. . CRC Press; 2012. p. 611–87.

[11] Briggs A, Arnold W. Advances in acoustic microscopy, vol. II. New York: Plenum Press; 1996.
[12] Fellinger P, et al. Wave Motion 1995;21.
[13] Briggs A. Acoustic microscopy, 2nd ed.. New York: Plenum Press; 1995.
[14] Yu Z, Boseck S. Scanning acoustic microscopy and its applications to material characterization. Rev Mod Phys 1995. http://dx.doi.org/10.1103/RevModPhys.67.863.
[15] Maev RG. Advances in acoustic microscopy and high resolution imaging. Germany: Wiley-VCH Verlag & Co.; 2013.
[16] Rose JL. Ultrasonic waves in solid media. New York: Cambridge University Press; 2014.
[17] Dowling N. Mechanical behavior of materials, 4th ed.. USA: Prentice Hall; 2012.

Microelectronics Reliability 64 (2016) 370–374

Contents lists available at ScienceDirect

Microelectronics Reliability

journal homepage: www.elsevier.com/locate/microrel

Automatized failure analysis of tungsten coated TSVs via scanning acoustic microscopy

E. Grünwald [a], J. Rosc [a], R. Hammer [a], P. Czurratis [b], M. Koch [b], J. Kraft [c], F. Schrank [c], R. Brunner [a,*]

[a] Materials Center Leoben Forschung GmbH (MCL), Leoben, Austria
[b] PVA TePla Analytical System AG (PVA TePla), Aalen, Germany
[c] ams AG, Unterpremstätten, Austria

ARTICLE INFO

Article history:
Received 1 July 2016
Accepted 8 July 2016
Available online 18 September 2016

Keywords:
Microelectronics
Ultrasound
EFIT simulations
TSVs

ABSTRACT

In 3D integrated microelectronics, the failure analysis of through silicon vias (TSVs) represents a highly demanding task. In this study, defects in tungsten coated TSVs were analysed using scanning acoustic microscopy (SAM). Here, the focus lay on the realization of an automatized failure detection method towards rapid learning. We showed that by using a transducer of 100 MHz center frequency, established with an acoustical objective (AO), it is possible to detect defects within the TSVs. In order to interpret our analysis, we performed acoustic wave propagation simulations based on the elastodynamic finite integration technique (EFIT). In addition, high resolution X-ray computed tomography (XCT) was performed which corroborated the SAM analysis. In order to go towards automatized defect detection, firstly the commercially available software "WinSAM8" was enhanced to perform scans at defined working distances automatically. Secondly, a pattern recognition algorithm was successfully applied using "Python" to the SAM scans in order to distinguish damaged TSVs from defect-free TSVs. Besides the potential for automatized failure detection in TSVs, the SAM approach exhibits the advantages of fast and non-destructive failure detection, without the need for special preparation of the sample.

1. Introduction

In the fields of micro- and nanoelectronics, More-than-Moore technologies push towards improved integration density, higher performance and increased functionality of devices [1–9]. In these ongoing efforts, 3D integration is considered a most promising technique [10]: two or more layers of active electronic components are vertically interconnected [11] using through silicon vias (TSVs), e.g. [12,13]. Advantages of the key-enabling TSV technology are higher electrical performance, lower power consumption, higher density and lighter weight [11].

However, 3D integration technologies are faced with many challenges concerning the processing, design and performance of microelectronic devices. Especially the failure analysis and defect detection in TSVs present highly demanding tasks and are in focus of latest advanced reliability studies, e.g. [13,14]. Considering the demand for rapid in-line inspection, non-destructive analysis methods are pursued.

Scanning acoustic microscopy (SAM) shows high potential for failure characterization on wafer level. With frequencies ranging up to the GHz regime, SAM provides sufficient axial and lateral resolution to identify and localize defects in many microelectronic devices [14].

In the work reported here, we used scanning acoustic microscopy to detect defects in tungsten coated TSVs in an automatized way. This approach is highly interesting for process attendant failure analysis. The outcome of the SAM analysis was corroborated by high resolution X-ray computed tomography (XCT) scans. The advantages of SAM, in comparison to the XCT analysis, are the potential for automatized measurement and data analysis without the need for special sample preparation, resulting in fast, non-destructive and efficient failure analyses. In order to interpret our results, the SAM measurement has been simulated. Good agreement between measurement and simulations was found. The detection via lower frequencies, 100 MHz in our case, includes the advantages of accessible acoustic objectives (AOs) at lower costs and larger working distances between lens and sample compared to GHz lenses and set-ups. The possibility to scan e.g. a whole wafer in a single measurement allows for uncomplicated analyses, which can be easier to automatized. Considering the increasing demand for rapid process attendant inspection, the commercially available control software "WinSAM 8" has been upgraded in order to perform scans at arbitrary equidistant z-positions automatically. Finally, the applicability of a pattern recognition algorithms using "Python" [15,16], to distinguish damaged from defect-free TSVs, is presented in this work.

* Corresponding author.
E-mail address: roland.brunner@mcl.at (R. Brunner).

http://dx.doi.org/10.1016/j.microrel.2016.07.075
0026-2714/

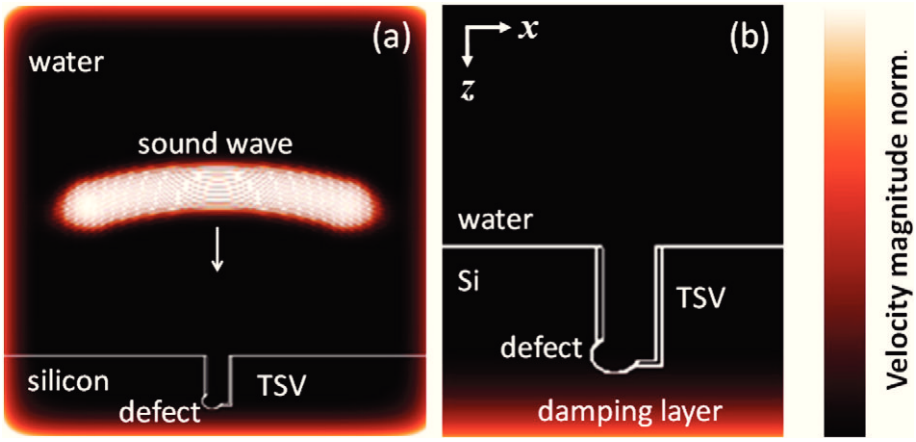

Fig. 1. (a) EFIT simulation of the SAM measurement. (b) Zoom into a tungsten coated damaged TSV.

2. Materials and methods

2.1. Scanning acoustic microscopy (SAM)

A scanning acoustic microscope (SAM) uses a piezoelectric transducer to generate ultrasonic sound waves which can be focused onto the surface of the investigated sample via an acoustic lens or an acoustic objective (AO). The frequency f of the sound wave is related to the lateral resolution L:

$$L = \frac{\lambda}{2NA} \tag{1}$$

via the wave-length $\lambda = v/f$, where $NA = \sin(\theta_0)$ and θ_0 is the semi-angle of the lens aperture and v is the velocity of the acoustic wave in an arbitrary medium [17]. Due to attenuation effects, an increase in frequency (corresponding to higher resolution) involves a decrease in penetration depth.

Decreasing the distance between lens and sample (z-direction), the sound waves can be focused into the specimen. In reflection mode, a SAM detects the reflected acoustic field of the sample. The reflected ultrasonic wave is presented as a function of time in the so-called A-scan. The A-scan gives information about the analysed samples in z-direction. 2D images can be obtained, by scanning in the x-y plane, keeping the lens-sample distance constant.

Choosing a certain time range in the A-scan, 2D cross-sections at certain z-position in the x-y plane can be acquired, so-called SAM C-scans.

Additional wave modes can be excited in the investigated sample at negative defocus, when the distance between lens and sample becomes smaller than the focal length, and the angle of the lens aperture is sufficiently large. If the additional excited wave modes leak energy back to the transducer through the coupling liquid, the piezoelectric element sums up both their amplitude and phase and interference effects can be observed [17].

2.2. Elastodynamic finite integration technique (EFIT)

The simulation of ultrasonic wave propagation in isotropic, linear elastic materials, discretized via the finite integration technique (FIT), has been described elsewhere, e.g. [18]. In the work reported here, the propagation of sound waves, their reflection and scattering at defect and non-damaged TSVs, was simulated in two space dimensions using EFIT.

In Fig. 1(a), an ultrasonic wave propagates from top to bottom through water to the sample, where the colour-scale displays the normalized velocity magnitude. The focusing of the sound waves was simulated by a sound field emitted following a circular arc. In this manner, the angular aperture of 60° was realized as well as the aperture diameter of approximately 1 mm. This represents the geometries of the AO applied in the SAM measurement. In accordance with the SAM

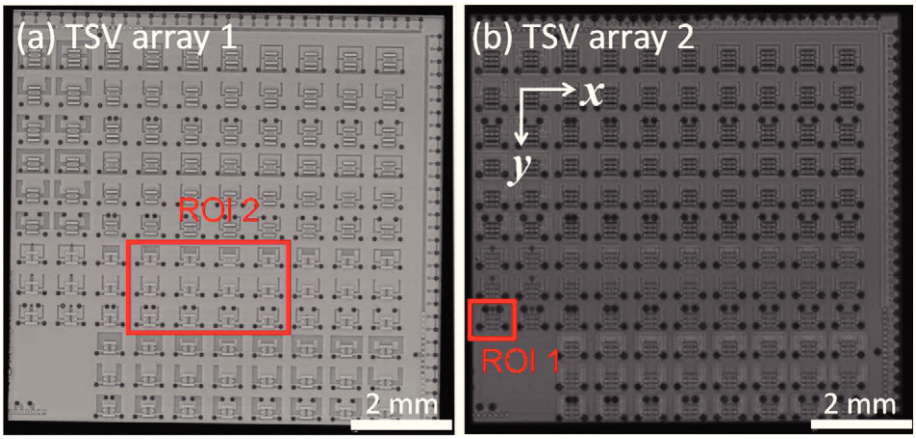

Fig. 2. SAM C-scans of TSV test arrays. Region of interest (ROI) of regions 1 and 2 are highlighted. (a) "TSV array 1" scanned at focus position and (b) "TSV array 2" scanned at negative defocus.

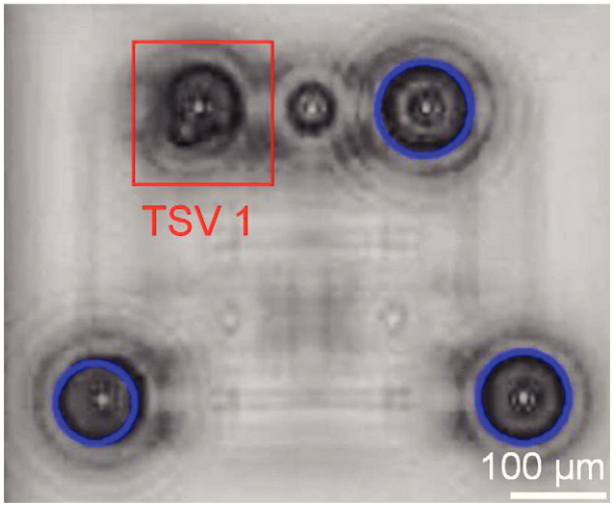

Fig. 3. Defocused SAM C-scan (ROI 1) for TSV array 2. Three defect-free TSVs are marked by pattern recognition algorithm (circles), one TSV is damaged (rectangle).

measurement, the distance between lens and sample was slightly smaller than the focal length.

In order to prevent back-reflections, a damping layer was implemented at the boundaries of the simulation area, see Fig. 1(b). The frequency dependent damping of ultrasonic waves was not implemented in the EFIT simulation.

2.3. Sample

The experimental characterization via SAM was performed on two test arrays of TSV structures (Fig. 2). Both test arrays were exposed to electrical loading to induce failure modes within the TSV. The analysis via SAM was performed without the prior knowledge of the failure positions on the TSV arrays.

Fig. 2(a) was obtained keeping the acoustic lens at the focus position, Fig. 2(b) at slight negative defocusing of the lens. As a consequence, Fig. 2(b) shows smaller contrast. According to the SAM C-scans the TSVs have an approximate diameter of about 100 µm and a height of 200 µm. The TSVs are tungsten coated and not filled with any additional material. In Fig. 2, two regions of interest (ROIs) under discussion are marked with red rectangles.

3. Results and discussion

3.1. SAM analysis

In Fig. 3, a negative defocused SAM scan of ROI 1, marked in Fig. 2(b), is shown. The brightness and contrast has been increased for better visibility in Fig. 3. "TSV 1", marked with a red rectangle, shows an irregular structure compared to the other presented TSVs. It is presumed that "TSV 1" is damaged. The potential defect is apparently extended to half of the TSV's diameter. Additionally, distinctive fringes around some of the TSVs are shown in Fig. 3, see also [19].

3.2. High resolution XCT analysis of "TSV 1"

In order to represent the presumably damaged "TSV 1" in 3D, a high resolution XCT was performed. Due to the conical shape of the X-ray beam of this type of X-ray system, the analysed structure has to be placed very close to the X-ray tube and has to be rotatable to certain extent [20].

In the case of the TSV arrays shown in Fig. 2, only TSVs located close to the edge of the sample, e.g. ROI 1 in TSV array 2, can be analysed without further destructive sample preparation. In Fig. 5, in a 3 dimensional XCT representation, the damaged "TSV 1" from ROI 1 is visualized. The XCT analysis in Fig. 5 confirms the SAM defect detection. Moreover, the shape of the defect observed in the SAM C-scan (Fig. 3), extending to half of the TSV's diameter, is confirmed in Fig. 4. From the XCT measurements, the dimensions of the defect in "TSV 1" from ROI 1 could be estimated and were used as input for the subsequent EFIT simulations. The height of the defect is estimated from Fig. 4(a) to be approximately 20 µm. The lateral extension of the defect is approximately 50 µm, according to Fig. 4(b).

3.3. EFIT simulation of SAM measurement

The EFIT simulations were carried out for the case of a defect-free TSV, a TSV with a bottom defect (Fig. 5) and for a TSV with a 10 µm open crack of 30 µm length near to the silicon surface. It was assumed that the empty TSVs fill with water in the simulation.

3.3.1. TSV with bottom defect (EFIT simulation)

From XCT measurements (Fig. 5), the dimensions of the defect in "TSV 1" from ROI 1 could be estimated and were used as input for the EFIT simulations. In Fig. 5 at time step (1), the sound wave incident on the TSV array surface is shown. In Fig. 5 at time step (2), additional

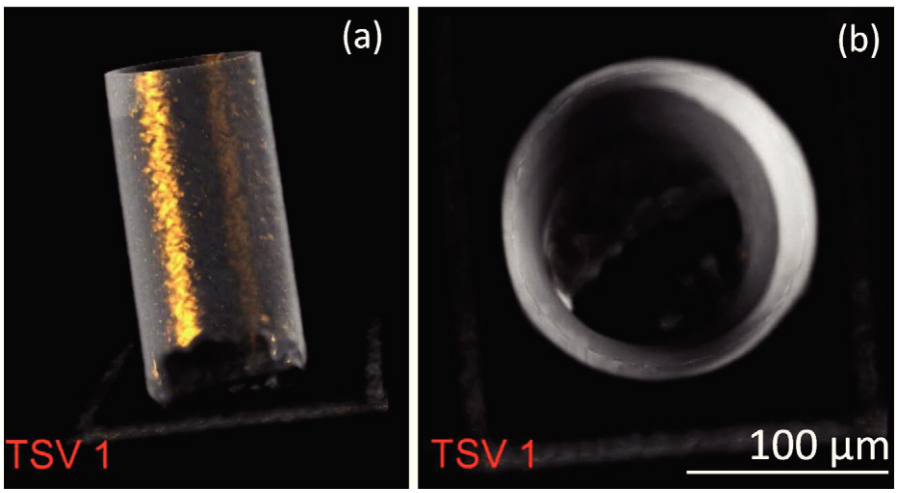

Fig. 4. High resolution 3D XCT image of "TSV 1" (ROI 1), (a) side view and (b) top view with defect.

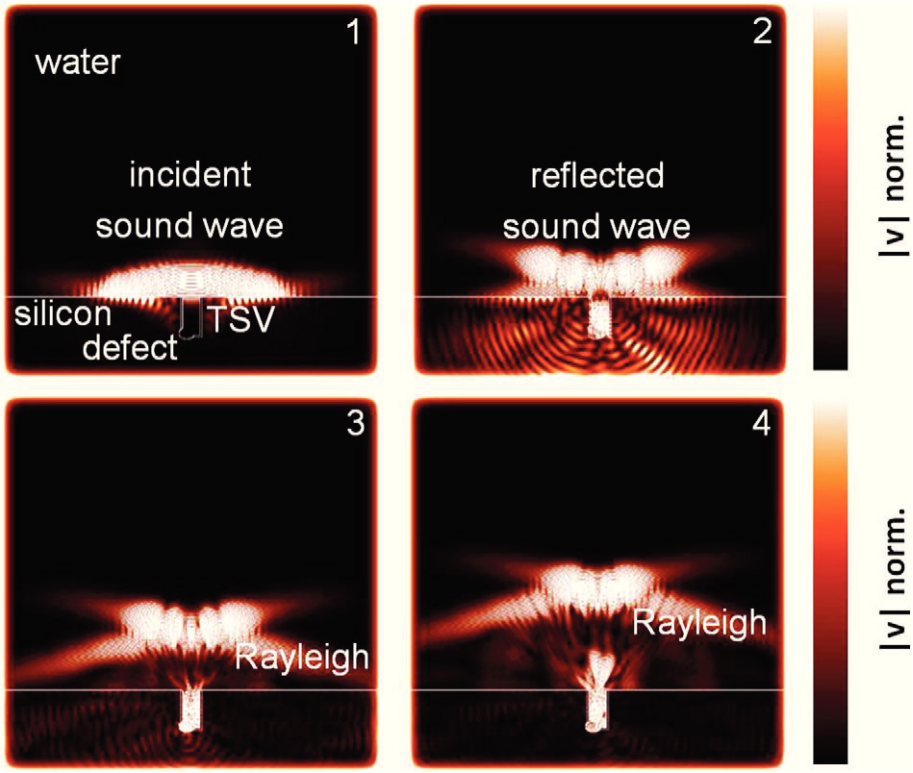

Fig. 5. EFIT simulation. Scattering of a sound wave at a defect TSV (bottom defect), timesteps 1–4.

wave modes have formed in the silicon and the incident longitudinal wave travels through the water to the bottom of the TSV.

In Fig. 5 at time step (3), the sound wave reached the defect through the water. In Fig. 5 (4), the leaky Rayleigh wave can be observed as well as the sound waves which are still present in the defect TSV.

3.3.2. Comparison of damaged and defect-free TSVs

For the defect-free TSV, a TSV with a bottom defect (Fig. 6) and for a TSV with a crack near to the surface, a detection point at the center of the simulated area was implemented in the simulation. This allows for an estimation of the reflected acoustic field from the sample, see Fig. 6. Fig. 6 corresponds to the simulated A-scans of the SAM measurement. Here, the first reflected signal from the surface as well as the reflected signal from the bottom of the TSV can be seen.

A third signal, marked as "TSV", most pronounced (highest amplitude) in the case of the defect-free TSV, is also present, resulting from the acoustic field which is reflected inside the TSV before it travels back to the transducer.

Fig. 7 shows a zoom-in of the "surface signal". A defect, which extends to a sufficient amount towards the surface of the TSV array, can affect the "surface" signal. The sound velocity in silicon of 8430 m/s is more than 5 times faster than the sound velocity in water, 1495 m/s. The first incident waves which travel directly through the "faster" silicon to the defect on the bottom have time to go back to the surface and influence the reflected ultrasonic waves going back to the transducer. A crack closer to the surface of the TSV should affect the surface signal earlier which is confirmed in Fig. 7.

Also the "TSV bottom" signal and the "TSV" signal, marked in Fig. 6, change due to defects.

3.3.3. Additional wave modes, Rayleigh waves

In Fig. 5 the simulations show clearly the excitation of additional wave modes in the silicon wafer.

The excited surface acoustic waves, or Rayleigh waves, propagate at the surface of the TSV array and can form interference fringes when reflected at obstacles, e.g. cracks [17]. These fringes can be disturbed at irregular structures, such as defects in TSVs, see Fig. 3. The corroboration of additional wave modes in the simulation accounts at least partly for the presence of interference fringes observed in the SAM C-scan shown in Fig. 3, see also [19]. However, one major difference between the measurement and the simulation is, that due to just one detection point in the EFIT simulation, the leaky Rayleigh wave is hardly detected in contrast to the experiment. In the measurement, the Rayleigh wave leaks energy back at the angle at which it was excited and is therefore detected to a major extent by the lens. The detailed modelling of the transducer – lens system is subject of ongoing work.

3.4. Automatization

3.4.1. Automatization of the scanning approach

The optimal defocus position, for detecting defects in TSVs, can be found from SAM C-scans. To that purpose, SAM C-scans at increasing negative defocus positions have to be performed.

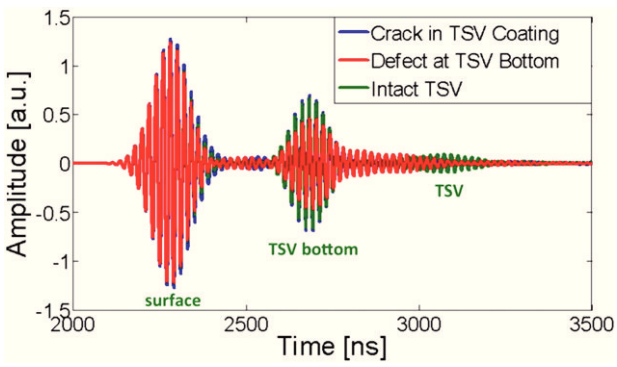

Fig. 6. Simulated signals for damaged and undamaged TSV models, EFIT.

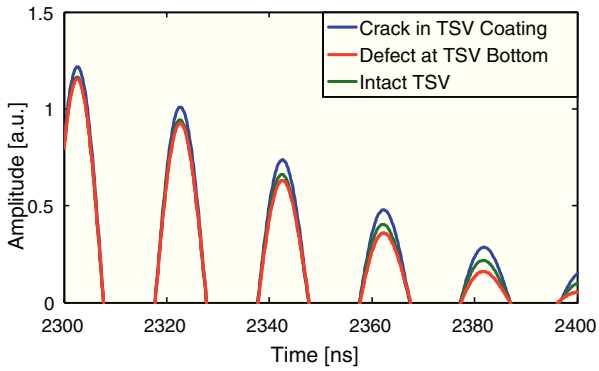

Fig. 7. Part of simulated surface signals for damaged and undamaged TSV models, EFIT.

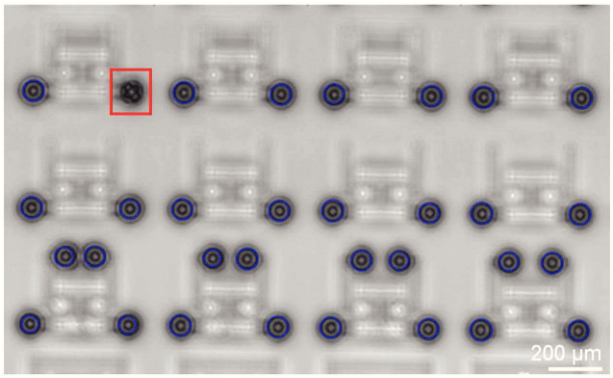

Fig. 8. SAM C-Scan of ROI 2 for TSV array 1, defect-free TSVs spotted via pattern recognition (circles), one damaged TSV is manually marked (rectangle).

In order to automatize this procedure for unknown samples, the commercially available control software "WinSAM 8" was enhanced to perform C-scans at a sequence of equidistant defocus positions automatically.

3.4.2. Pattern recognition (ROI 1 & ROI 2)

In the negative defocused SAM C-scan of ROI 1, shown in Fig. 3, the defect-free TSVs are spotted by the circular Hough transform algorithm [15,16] and are automatically marked with blue circles, defining "TSV 1", marked red in Fig. 3 manually, to be damaged. "TSV 1" was corroborated to be defect via XCT analysis, see Fig. 4. The brightness of Fig. 3 was increased for better visibility after the circular Hough algorithm was applied.

In order to test the pattern recognition algorithm for a larger scan field, the circular Hough transform algorithm was also applied to a negative defocus SAM C-scan of ROI 2 shown in Fig. 8. In ROI 2, 31 TSVs are automatically marked with blue circles. One damaged TSV does not show a distinguishable circular boundary. It is therefore not detected by the algorithm and manually marked with a red rectangle in Fig. 8. The brightness of Fig. 8 was increased for better visibility after the circular Hough algorithm was applied.

The algorithm employed in Figs. 3 and 8 can in principle be applied to a whole wafer with TSV structures.

In this study, the detected failure modes are of approximately 20 µm–50 µm extensions.

4. Conclusion

In this work, we report on the detection and visualization of defects in TSV arrays using scanning acoustic microscopy (SAM), where the focus lays on the potential for automatized, fast and cost efficient failure inspection for rapid learning applications. The interpretation of the measurement was supported by EFIT simulations. They are conclusive with the SAM measurements.

Moreover, the automatization potential of the SAM measurement and data analysis has been shown in this study. A pattern recognition algorithm [15,16] was successfully applied to the SAM C-scans in order to spot defect TSVs automatically. The pattern recognition algorithm used in this work can in principle be employed to examine whole wafers, further improving the potential of SAM concerning time- and cost-efficient failure detection and analysis.

Acknowledgements

This work is done as part of the project eRamp, which is co-funded by grants from ENIAC Joint Undertaking (P. No. 621270) and from Austria, Germany, the Netherlands, Romania, Slovakia and the UK (P. No. 843740) and by the FFG project ACINTECH (Active Interposer Technology). In addition financial support by the Austrian Federal Government (in particular from Bundesministerium für Verkehr, Innovation und Technologie and Bundesministerium für Wissenschaft, Forschung und Wirtschaft) represented by Österreichische Forschungsförderungsgesellschaft mbH and the Styrian and the Tyrolean Provincial Government, represented by Steirische Wirtschaftsförderungsgesellschaft mbH and Standortagentur Tirol, within the framework of the COMET Funding Programme (P.No. 837900) is gratefully acknowledged.

References

[1] W. Arden, et al., 'More-than-Moore' White Paper," International Technical Roadmap for Semiconductors, 2010.
[2] G.Q. Zhang, More than Moore: Creating High Value Micro/Nanoelectronics Systems, Springer Verlag, Berlin, 2009.
[3] X. Chen, et al., Sensors Actuators B Chem. 177 (2013) 178–195.
[4] G. Mutinati, et al., Prod. Eng. 47 (2012) 490–493.
[5] R. Schongrundner, et al., Thin Solid Films 564 (2015) 321–330.
[6] R. Treml, et al., Acta Mater. 103 (2016) 616–623.
[7] D. Kozic, et al., EuroSimE 2014, BEL (April 2014) 1–5.
[8] D. Kozic, et al., EuroSimE 2015, HUN (April 2015).
[9] E. Grünwald, et al., Materials Today: Proceedings, 2 (2015) 4289–4294.
[10] P. Garrou, C. Bower, P. Ramm, Handbook of 3D Integration: Volumes 1 and 2, Wiley-VCH, Germany, 2012.
[11] J.H. Lau, Through Silicon Vias for 3D Integration, McGraw-Hill Education, 2012.
[12] M.J. Wolf, et al., 58th Electronic Components and Technology Conference, Lake Buena Vista, FL, 2008, 2008 563–570.
[13] J. Kraft, et al., Reliability Physics Symposium (IRPS), 2012 IEEE International, Anaheim, CA (2012) PI.2.1.–PI.2.5.
[14] S. Brand, et al., Microelectron. Reliab. 50 (2012) 1469–1473.
[15] Python Software Foundation, Python Language Reference, Version 2.7(Available at http://www.python.org, Bradski G., opencv_library, Dr. Dobb's Journal of Software Tools) 2000.
[16] D. Luo, Pattern Recognition and Image Processing, Woodhead Publishing, 1998.
[17] G.A.D. Briggs, O.V. Kolosov, Acoustic Microscopy, Oxford University Press, New York, 2010.
[18] P. Fellinger, et al., Wave Motion 21 (1995) 47–66.
[19] I. De Wolf, et al., Proc. 41st Intern. Symp. For Testing and Failure Analysis (ISTFA2015) (2015) 119–125.
[20] J. Rosc, et al., Electronics System-Integration Technology Conference (ESTC), Helsinki (2014) 1–6.

1466
doi:10.1017/S1431927617007991
Microsc. Microanal. 23 (Suppl 1), 2017

Accretion Detection via Scanning Acoustic Microscopy in Microelectronic Components - Considering Symmetry Breaking Effects

Eva Grünwald[1], René Hammer[1], Jördis Rosc[1], Bernhard Sartory[1] and Roland Brunner[1]

[1.] Materials Center Leoben Forschung GmbH, Leoben, Austria.

Currently, micro – and nano-electronic devices are pushed towards higher performance, increased functionality and higher integration density. A promising technique to achieve „More than Moore devices“ is 3D integration. Here, layers of active electronic components are connected vertically via so-called through silicon vias (TSVs). These TSVs are practically cylindrical holes with diameters in the range from 5 – 200 µm in silicon which are filled or coated with conducting materials. The processing, design and the performance of TSVs faces many challenges and especially the defect detection, failure characterization and reliability analysis are in the focus of state of the art reliability studies [1, 2].

In this work, we consider scanning acoustic microscopy (SAM) as a tool of choice in the characterization of TSVs. With frequencies ranging up to the GHz regime, SAM provides sufficient lateral resolution and with fast sampling rates of state of the art ADC boards down to ps, SAM provides high axial resolution in the analysis of microelectronic samples. The non-destructive nature of the SAM analysis allows for subsequent analyses with other methods and minimizes the possibility of introducing new failure modes by the analysis itself. Moreover, SAM shows high potential with respect to rapid learning towards rapid in-line inspection of 3D integrated samples. Recently, the high potential for the automatization of SAM measurements concerning defects in tungsten coated TSVs was shown [2].

In the work reported here, the SAM analysis of metal coated TSVs of approximately 100 µm diameter was carried out. The analyzed sample was an array of TSV test structures, where different kinds of failure modes were artificially introduced in order to test the ability of SAM concerning their detection.

In the SAM measurement, an acoustic objective with a center frequency of 100 MHz and an opening angle of the lens with about 60° was used. The SAM analysis showed high sensitivity to accretions. Figure 1 (a) shows a SAM C-scan image of a TSV labeled with “TSV 1”, where an irregularity in the TSV can be observed on the left hand side. In Figure 1 (b), the X-ray computed tomography (XCT) result for “TSV 1” is shown. The XCT shows only an indication of a possible failure. Therefore, no reliable measurement can be performed in Figure 1 (b). The SEM analysis of “TSV 1” shown in Figure 1 (c) shows an accretion and allows an estimation of the extension. The accretion shows an extension of approximately 30 times 10 microns parallel to the coating but only a very small extension reaching towards the center of the TSV.

In order to interpret the SAM results, elastodynamic finite integration (EFIT) simulations [3] of sound wave propagation in TSVs in two space dimensions were carried out, see Figure 2. The time-steps in the simulation are numbered from 1 to 5. The sound wave starts in time-step 1 from the right hand side of the TSV and propagates along the wall of the TSV. Figure 2 (a) shows a sound wave propagating on the wall of an intact TSV, whereas Figure 2 (b) shows the case of a sound wave propagating on the wall of a TSV with a small accretion. The accretion is marked red in time-step 1 in Figure 2 (b). From Figure 2, it can be seen, that the sound field in the symmetric intact TSV, Figure 2 (a) is disturbed by the presence

of the accretion Figure 2 (b), especially in time-step 3 directly at the accretion. In the later time-step 5, the effect of the accretion on the wall is visible in the middle of the TSV.

Here, the sensitivity of SAM to accretions in metal coated TSVs was demonstrated, Figure 1 (a). The results were corroborated by high resolution X-ray computed tomography (Figure 1 (b)) and via SEM (Figure 1 (c)). In order to interpret the SAM results, EFIT simulations were carried out. From the simulations, it seems that a combination of the longitudinal sound waves, the Rayleigh waves and other wave modes in the TSVs can increase the sensitivity of SAM concerning the detection of accretions [4].

References:
[1] E. Grünwald *et al*, Microelectron. Reliab. **64** (2016), p. 370.
[2] S. Brand, *et al,* Microelectron. Reliab. **50** (2012), p. 1469.
[3] P. Fellinger, *et al,* Wave Motion **21** (1995), p. 47.
[4] The ams AG is acknowledged for their support. This work has received funding from ENIAC Joint undertaking under FP7 research (No.:621270) and FFG (No.:843740) and partly from the EU, H2020 (No.: 688225). Financial support by the Austrian Federal Government (in particular from Bundesministerium für Verkehr, Innovation und Technologie and Bundesministerium für Wissenschaft, Forschung und Wirtschaft) represented by Österreichische Forschungsförderungsgesellschaft mbH and the Styrian and the Tyrolean Provincial Government, represented by Steirische Wirtschaftsförderungsgesellschaft mbH and Standortagentur Tirol, within the framework of the COMET Funding Programme (No. 837900) is also gratefully acknowledged.

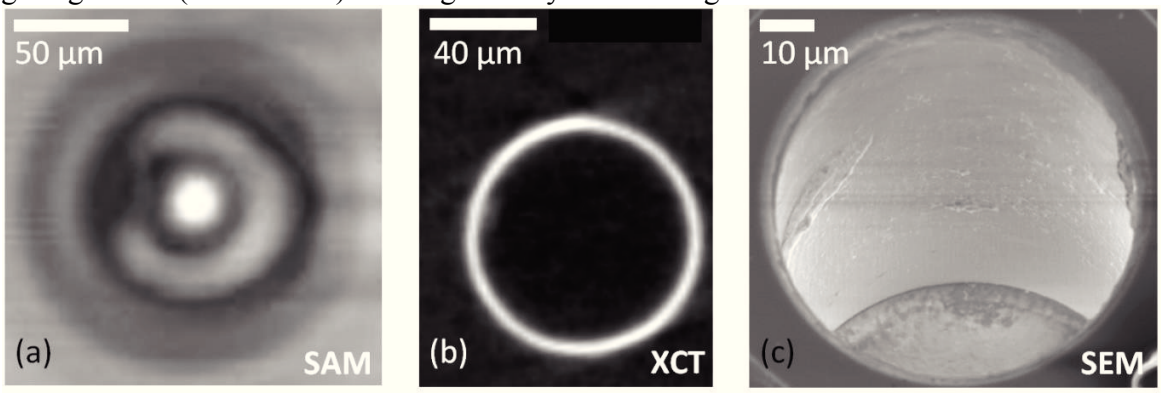

Figure 1. Accretion in "TSV 1", (a) SAM C-Scan, (b), XCT result and (c) SEM image.

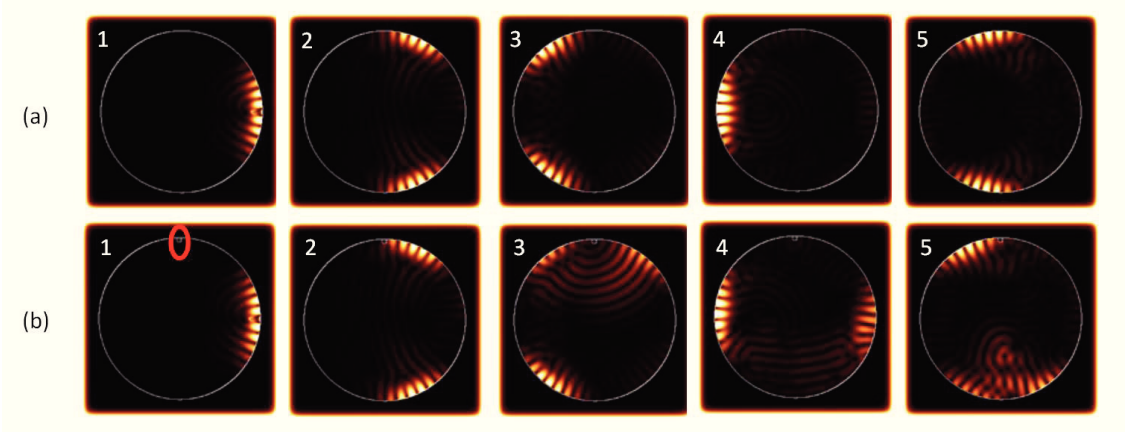

Figure 2. EFIT simulation of (a) sound wave propagation in intact TSV and (b) sound wave propagation in TSV with accretion.

https://doi.org/10.1017/S1431927617007991

coatings

MDPI

Article

Simulation of Acoustic Wave Propagation in Aluminium Coatings for Material Characterization

Eva Grünwald [1], René Hammer [1], Robert Nuster [2], Philipp Aldo Wieser [1], Martin Hinderer [3], Ingo Wiesler [3], Rudolf Zelsacher [4], Michael Ehmann [4] and Roland Brunner [1,*]

1 Materials Center Leoben Forschung GmbH (MCL), Leoben 8700, Austria; eva.gruenwald@mcl.at (E.G.); Rene.Hammer@mcl.at (R.H.); Philipp.Wieser@mcl.at (P.A.W.)
2 Institute of Physics, Karl-Franzens University of Graz (KFU), Graz 8010, Austria; ro.nuster@uni-graz.at
3 PVA TePla Analytical Systems GmbH (PVA AS), 73463 Westhausen, Germany; martin.hinderer@pvatepla.com (M.H.); Ingo.Wiesler@pvatepla.com (I.W.)
4 Infineon Technologies Austria AG (IFAT), Villach 9500, Austria; Rudolf.Zelsacher2@infineon.com (R.Z.); Michael.Ehmann@infineon.com (M.E.)
* Correspondence: Roland.Brunner@mcl.at; Tel.: +43-3842-459-48

Academic Editors: Timon Rabczuk, Michael Nolan and Alessandro Lavacchi
Received: 28 September 2017; Accepted: 4 December 2017; Published: 14 December 2017

Abstract: Aluminium coatings and their characterization are of great interest in many fields of application, ranging from aircraft industries to microelectronics. Here, we present the simulation of acoustic wave propagation in aluminium coatings via the elastodynamic finite integration technique (EFIT) in comparison to experimental results. The simulations of intensity (I)–defocus (z) curves, obtained by scanning acoustic microscopy (SAM), were first carried out on an aluminium bulk sample, and secondly on a 1 µm aluminium coating deposited on a silicon substrate. The $I(z)$ curves were used to determine the Rayleigh wave velocity of the aluminium bulk sample and the aluminium coating. The results of the simulations with respect to the Rayleigh velocity were corroborated by non-destructive SAM measurements and laser ultrasonic measurements (LUS).

Keywords: aluminium coatings; acoustic simulation; scanning acoustic microscopy; $V(z)$; acoustic material signature; Rayleigh wave velocity, integrated computational material engineering

1. Introduction

Aluminium coatings offer a variety of favourable properties, including high reflectivity, high conductivity, high corrosion resistance, and low costs. The benefits of aluminium coatings render them attractive candidates for large-scale applications in aircraft industries, and also for implementation in small-scale devices, concerning micro- and nano-electronics [1].

The frequent use of aluminium coatings increases the demand for their precise characterization. However, some state-of-the-art methods show drawbacks concerning thin film characterization; e.g., they require the direct loading of the sample [2]. Alternatively, ultrasonic waves can be used in order to determine thin film properties; e.g., via laser-induced ultrasound (LUS) [3–6] or via scanning acoustic microscopy (SAM) [7,8].

SAM represents a well-established tool in state-of-the-art failure and material characterization, providing high potential regarding automation [9], allowing fast and accurate failure detection. With commercially available SAM set-ups, the challenge lies mainly in (1) the necessary specific hardware for the measurement (e.g., emitter/sensor), high time resolution (ps), and accurate movement of emitter/sensor over the sample, and (2) in the interpretation of the SAM data—which can be quite cumbersome due to the presence of various wave modes in thin films.

One outstanding attribute of acoustic microscopy is the possibility to monitor the intensity I of the reflected sound waves as a function of the defocus position z—also called $V(z)$ curves or acoustic material signatures (AMS) [7,8]—from which the Rayleigh wave velocity of the analysed material can be obtained.

The $I(z)$ measurement relies on the excitation of Rayleigh waves that propagate on the sample surface and leak back to the piezoelectric transducer. Decreasing the distance between lens and sample, the Rayleigh contribution interferes with the acoustic field reflected from the sample—alternating destructively and constructively, resulting in an oscillation of the measured intensity I as function of the defocus position z.

The Rayleigh wave velocity can be used directly for material characterization or material monitoring [10,11], or alternatively, material properties can be extracted [3–8]. In layered media, the Rayleigh velocity depends on frequency if the analysed coatings are thinner than approximately 1–2 wavelengths [12,13]. Considering a broad-band Rayleigh wave, the lower frequency part of the wave propagates more in the substrate, whereas higher frequency components travel mainly in the coating due to their lower penetration depth. Consequently, the Rayleigh wave velocity becomes dispersive (i.e., depends on frequency); this effect has been extensively studied in the past (e.g., [13–15]). The dispersion of the Rayleigh wave can be used to extract elastic mechanical parameters like the Young´s modulus, because the Rayleigh wave velocity depends on the density as well as the elastic constants. In this sense, the determination of the Rayleigh wave velocities is of high interest for the characterization of materials—especially of coatings—and was studied via LUS in, e.g., [3–6] and via SAM in, e.g., [8,16–19]. In the past, $I(z)$ measurements have been investigated analytically via ray theory [7,20,21] and via wave theory approaches [7,22].

For general numerical elastic wave propagation, finite element [23–25], spectral element [26,27], pseudospectral [28,29], finite volume methods [30], finite difference [31–34], and the elastodynamic finite integration technique (EFIT) [35,36] can be found in the literature. It is a common feature of all real-space numerical schemes for elastic wave propagation in higher dimensions that the linear dispersion relation of the wave equation is not reproduced exactly, but numerical dispersion errors are introduced. Severe dispersive errors and even spurious solutions force standard finite element methods (FEMs) with low-degree ansatz functions to use excessively high mesh densities [23–25]. In this work, to access the $I(z)$ curves we use EFIT for the full elastic wave propagation, because of its good compromise in terms of accuracy relative to its computational cost. The field variables, velocity and stress, are placed in a staggered manner onto the computational grid, which greatly improves the dispersion relation of the scheme. Interestingly, this property is also exploited in electrodynamics, where the finite difference time domain (FDTD) scheme is unsurpassed for inhomogeneous domains [37], and recently also for the relativistic wave equation [38]. The elastic wave discretization using a staggered grid and the EFIT are related, with the difference being that the material properties are placed differently on the grid, allowing the EFIT to more accurately describe material inhomogeneities [35].

We simulated the $I(z)$ curve for an aluminium bulk sample for calibration, because bulk values for aluminium can be found in the literature (e.g., [7]). In addition, the Rayleigh wave velocity can be measured very accurately via LUS [3–6]. After this calibration step, the $I(z)$ curve of an aluminium-coated silicon sample was simulated and directly compared to results obtained from SAM measurements. The Rayleigh wave velocity—as a material parameter—was obtained from the EFIT simulation and from the SAM measurement, using a 400 MHz acoustic lens. The SAM and the LUS measurements corroborated the EFIT simulation results regarding the Rayleigh wave velocity of the aluminium sample and the aluminium coating. The use of full wave simulation as tested here on aluminium bulk and coated samples allows for arbitrarily varying real thickness and material property distribution up to complex geometrical structures like microelectronics components.

Although ray theory approaches outperform the EFIT simulation of $I(z)$ curves with respect to time-efficiency in general, the EFIT simulation provides more possibilities with respect to: (a) depicting

the sound field propagation for various time-steps in the measurement, (b) creating an A-scan equivalent, (c) analysing the influence of, e.g., anti-reflective coating (ARC) or damping of the coupling liquid, and (d) most notably, complex multi-layered structures—relevant for, e.g., micro- and nanoelectronic devices—can be conveniently analysed via state-of-the-art EFIT simulations.

2. Materials and Methods

2.1. Sample

The analysed sample was a 4×2 cm^2 segment of an aluminium-coated silicon wafer with (100) crystallographic orientation. The aluminium layer was deposited via physical vapour deposition, and its thickness was determined via profilometry. In addition, the density of 2.709 g/cm^3 of the aluminium thin film was determined via X-ray diffraction (XRD) using a D8 Discover system (Bruker, Billerica, MA, USA).

2.2. Scanning Acoustic Microscopy (SAM)

In scanning acoustic microscope measurements, piezoelectric transducers (emitter/sensor) are used to generate ultrasonic waves (see Figure 1), e.g., [7]. The sound waves are focused onto or below the surface of the investigated sample via an acoustic lens. At the sample–water interface, part of the acoustic field is reflected and propagates back to the transducer. At the transducer, the reflected acoustic field is converted into a time-variant electric signal which is presented in time domain and commonly referred to as A-scan (see e.g., [39]).

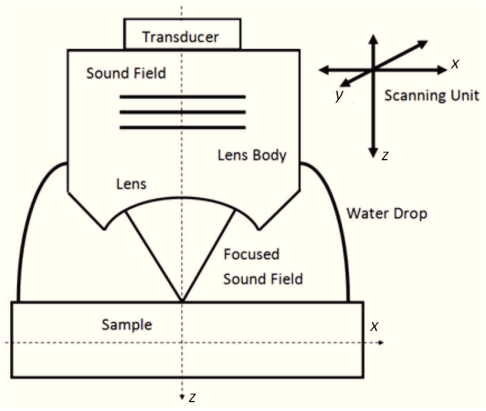

Figure 1. Schematic of scanning acoustic microscopy (SAM) principle.

If the opening angle of the lens exceeds the critical Rayleigh angle θ_R,

$$\theta_R = \sin^{-1}\left(\frac{v_0}{v_R}\right) \quad (1)$$

Rayleigh waves can be excited at the surface of the sample (Equation (1)). Here, ν_0 denotes the sound velocity in water, which is approximately 1500 m/s at room temperature. Once excited, the Rayleigh wave propagates along the surface and leaks energy back to the lens and subsequently to the transducer. At the piezoelectric element of the transducer, the phase and amplitude of the longitudinal sound wave reflected from the sample and the leaky Rayleigh wave are summed up [7]. The two wave modes (Rayleigh and longitudinal wave) interfere alternating constructively and destructively, depending on the defocus position of the transducer. According to [7], the periodicity Δz of the oscillation depends on the Rayleigh sound velocity ν_R of the investigated sample via

$$\Delta z = \frac{\lambda_0}{2 \times (1 - \cos\theta_R)} \quad (2)$$

where λ_0 denotes the wavelength of the sound wave in water, see Equation (2).

A SAM can be operated in either pulsed or tone-burst mode [22]. The generally longer excitation time in tone burst mode results in signals which are very narrow in the frequency domain, allowing precise frequency-dependent measurements.

In the work reported here, a commercially available SAM 400 (PVA, Analytical Systems GmbH, Westhausen, Germany) was operated in reflection mode, equipped with a custom-built tone-burst set-up, to perform precise frequency-dependent measurements. For the calibration measurement on bulk aluminium, an acoustic objective (AO) was used with a transducer of 400 MHz nominal centre frequency and an opening angle of 120° (PVA, Analytical Systems GmbH, Westhausen, Germany). The resonance frequency of the transducer was found at approximately 430 MHz. In the case of the aluminium coating, an acoustic objective with an opening angle of 60° was applied (PVA, Analytical Systems GmbH, Westhausen, Germany). Operated in tone-burst mode, the transducer was addressed at approximately 400 MHz, at the resonance frequency of the transducer. The $I(z)$ curve was monitored with a step size of 2 µm in the case of the calibration measurement and in the case of the coating measurement. From the periodicity Δz of the $I(z)$ curves, the Rayleigh wave velocities were extracted.

2.3. Elastodynamic Finite Integration Technique (EFIT)

The description of ultrasonic sound field propagation simulation in isotropic linear elastic materials, discretized via the elastodynamic finite integration technique, can be found in [35].

The underlying set of differential equations is given by the kinetics

$$\rho \frac{\partial \vec{v}}{\partial t} = \vec{\nabla} \times \sigma$$

the kinematics

$$\frac{d\epsilon}{dt} \approx \frac{1}{2}[(\vec{\nabla} \otimes \vec{v}) + (\vec{\nabla} \otimes \vec{v})^T]$$

and the constitutive (or material) law relating them by $\sigma \approx E \cdot \epsilon$

ρ is the mass density, $\vec{v}$ is the particle velocity field (being the first derivative of the displacement field $\vec{u}$ with respect to time), ϵ is the (second rank) strain tensor, σ is the (second rank) stress tensor, and E is the (forth rank) stiffness tensor. As shown in Figure 2, the velocities and stress field variables are discretized in a staggered manner on the spatial grid together with a leap-frog updating procedure in time (c.f. Figure 2) [35]. It is shown in [35] that the scheme can be written for arbitrary anisotropy and inhomogeneity of the elastic material behaviour.

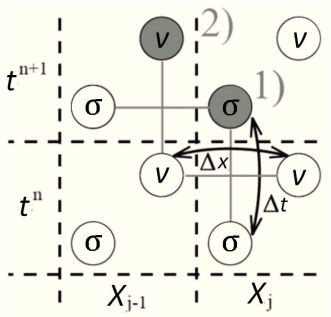

Figure 2. The staggered discretization of field variables velocity v and stress σ in the elastodynamic finite integration technique (EFIT).

Figure 3 shows EFIT results for the SAM measurement of a coated sample at nine time-steps. In accordance with the SAM measurement, an anti-reflective coating (ARC) on the lens was implemented. The ultrasonic field is depicted by the normalized magnitude of the z-component of the velocity field in Figure 3. The sound wave is excited by the transducer in Figure 3, time-steps 1

and 2, and propagates from top to bottom through the lens body (time-step 3) towards the surface of the sample (time-step 4). At the surface (time-step 5), part of the sound field is transmitted into the sample (time-step 6). The remaining sound field is reflected and travels back to the lens at time-steps 7 and 8. At time-step 9, the reflected sound waves reach the transducer. The artificial A-scan is obtained by summing up the z-component of the velocity field along the width of the transducer at the position of the transducer.

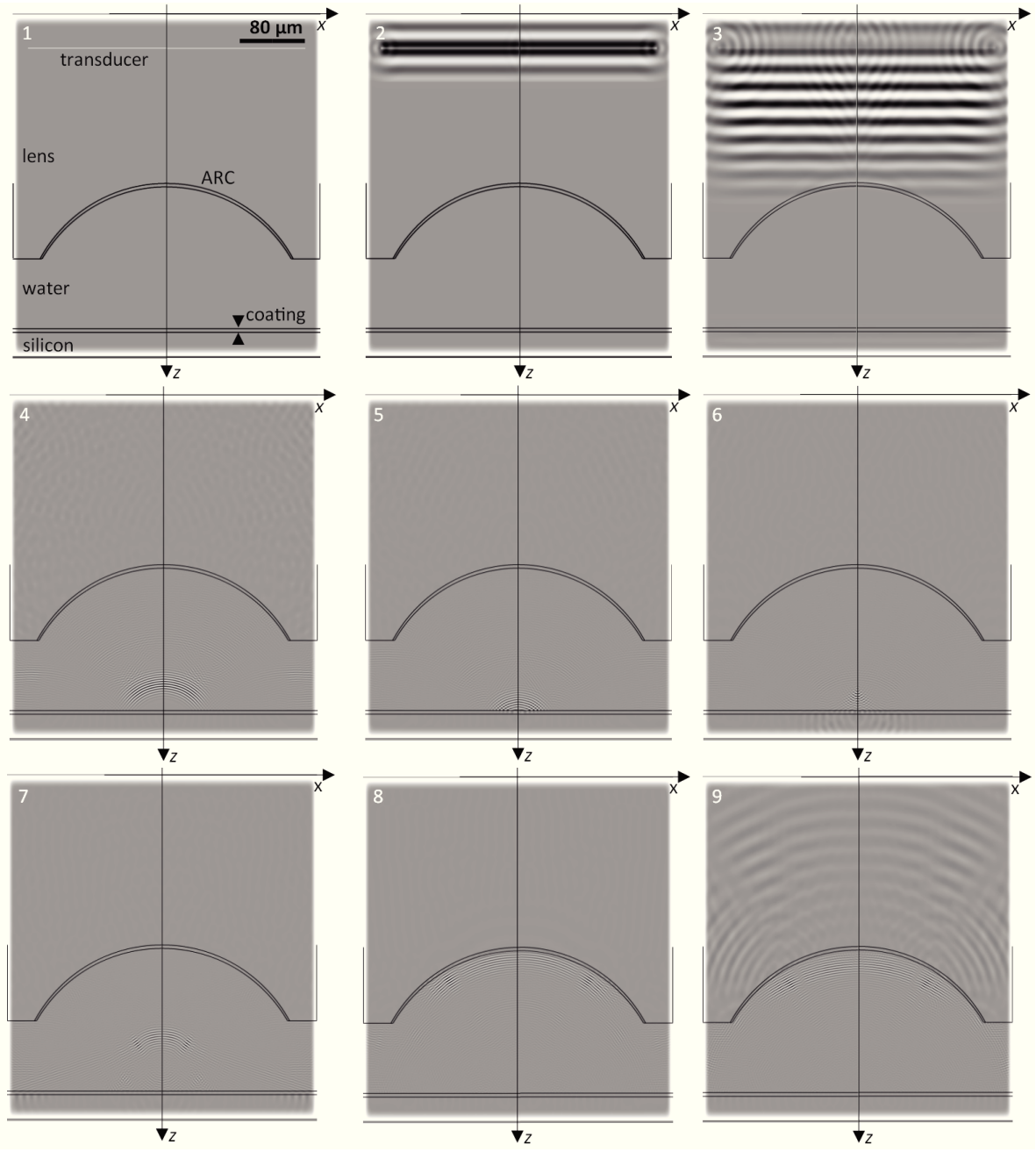

Figure 3. EFIT simulation of SAM measurement, time steps 1–9.

The $I(z)$ measurement, carried out via SAM, was simulated for the case of (1) an aluminium block of approximately 40 × 50 × 3 mm^3, referred to as bulk aluminium, and (2) an aluminium coating of approximately 1 µm thickness, deposited on a silicon wafer (100). In accordance with the SAM measurement, we implemented a transducer of approximately 430 MHz centre frequency and a lens-opening angle of 120° in the simulation for case (1). For the simulation, isotropic linear

elastic material behaviour was assumed, in accordance with [13]. The assumption of isotropy is made for aluminium because its Zener anisotropy ratio is close to one [40]. Literature values for the longitudinal and transversal sound velocity and the density of aluminium were used as input values [7,40]. The simulation was carried out for more than 30 defocus positions, and the A-scan data was assembled for each of them. From the A-scan data, the relevant time window was identified, and the intensity was computed and integrated over the identified time interval. For case (2), the aluminium coating on a silicon substrate, literature values for the longitudinal and transversal sound velocity and the density of aluminium as well as silicon were used as input values, taken from [7,40]. The simulation was carried out for a transducer of 400 MHz centre frequency and a lens-opening angle of 60°. For more than 30 defocus positions, the A-scan data were computed and the intensity of the acoustic signal as a function of the defocus position z was computed. The frequency-dependent damping of the coupling liquid was implemented via an exponential damping factor in the simulation, and due to the spherical focus of the lens used in the SAM measurement, an axial symmetric simulation along the z-axis was performed [36].

2.4. Laser Ultrasound (LUS)

The laser ultrasonic measurement is described in [3–6]. Here, a pulsed laser is focused via a cylindrical lens on the sample surface, exciting a Rayleigh wave. A second, continuous wave laser is used in order to detect the Rayleigh wave, using a beam deflection approach. A schematic of the set-up is shown in Figure 4. From the measurement at two detection points, the phase velocity of the Rayleigh wave v_R as function of frequency f (Equation 3) can be determined via [3–6]:

$$v_R(f) = \frac{(x_2 - x_1)\, 2\, \pi f}{\Phi_2(f) - \Phi_1(f)} \tag{3}$$

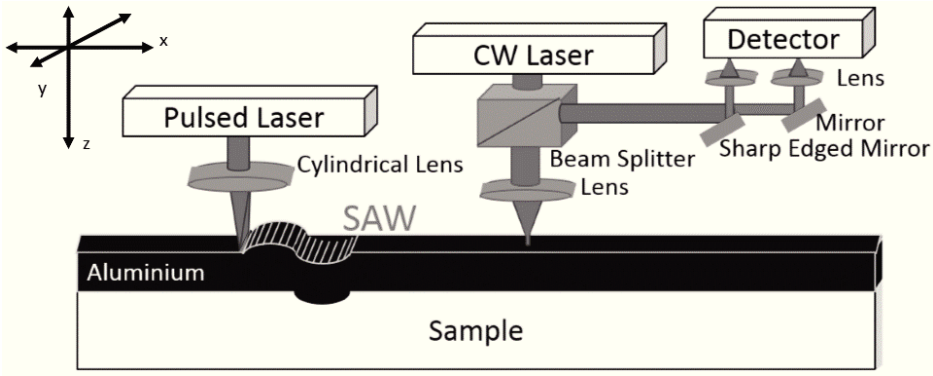

Figure 4. Schematic of laser-induced ultrasound (LUS) set-up; CW laser denotes a continuous wave laser, SAW denotes a surface acoustic wave.

In Equation (3), $x_2 - x_1$ is the distance between the detection points and Φ denotes the phases of the Fourier-transformed laser-induced signals.

In the case of (1), the calibration measurement on bulk aluminium, Rayleigh waves were excited via a pulsed laser at 11 positions. The applied Nd:YAG laser has a pulse width of approximately 2 ns, a repetition rate of 10 Hz, and a wavelength of 532 nm. For the 11 cases, the excited Rayleigh waves were detected via a second continuous wave laser. The time at which the Rayleigh waves passed the detection point are plotted as function of the distance the waves travelled in Figure 5.

For the aluminium coating, the pulsed laser from the calibration measurement was used in order to excite broadband Rayleigh waves on the sample. The measurement was performed in the frequency range up to 200 MHz. The Rayleigh wave velocity was obtained from the measurement at two detection points via Equation (3). Since the Rayleigh wave velocity depends on frequency

in the case of a coated sample, a theoretical model for the evaluation of the dispersion curve was considered [13]. In the theoretical model, isotropic material behaviour is assumed. This assumption is valid if the measurement is carried out along a symmetry axis of the silicon [3–6]. Our measurements were performed along the [110] symmetry axis of the silicon sample.

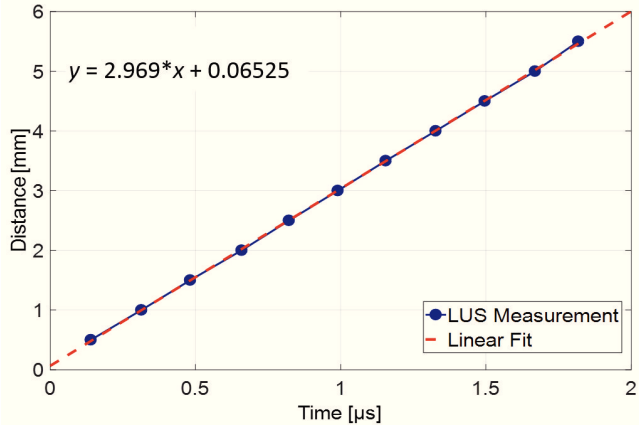

Figure 5. LUS measurement on bulk aluminium. Comparison of EFIT result to LUS measurement.

3. Results

3.1. Aluminium Bulk Sample for Calibration

In the case of the aluminium sample, the simulated intensity I as function of the defocus positions z is shown in Figure 6, in direct comparison to the SAM measurement. From Figure 6, the periodicity of the $I(z)$ oscillation Δz was determined and used to calculate the Rayleigh wave velocity v_R via $v_R \cong \sqrt{f v_0 \Delta z}$, according to [22]. In [22], the important property of the $I(z)$ curves in the evaluation of Rayleigh wave velocities is appointed to be Δz, not the amplitude. However, differences in the amplitudes of the $I(z)$ curves in Figure 6 might stem from actual higher damping coefficients (e.g., for water we used literature values for the damping coefficient; the damping in the sapphire lens body is not included in our simulations). Concerning the LUS measurement, the slope of the linear fit in Figure 5 was used to determine the Rayleigh wave velocity. The EFIT, SAM, and LUS results are listed in Table 1, in comparison to a literature value for the Rayleigh wave velocity in bulk aluminium [7].

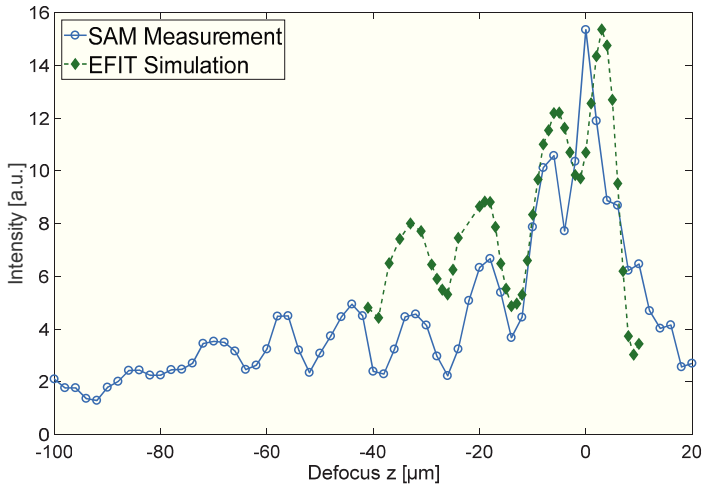

Figure 6. EFIT simulation (diamonds) and SAM measurement (circles) of $I(z)$ for the aluminium bulk sample at 430 MHz.

Table 1. Rayleigh wave velocity results for an aluminium sample.

Method	Δz (µm)	v_R (m/s)
EFIT	13	2896
SAM	13	2896
LUS	–	2969
Literature [7]	–	2906

3.2. Aluminium Thin Film on Silicon Substrate

Here, the simulation of $I(z)$ on an aluminium coating with a thickness of approximately 1 µm on a silicon substrate (100) was performed. The simulated results are directly compared to the SAM measurement in Figure 7.

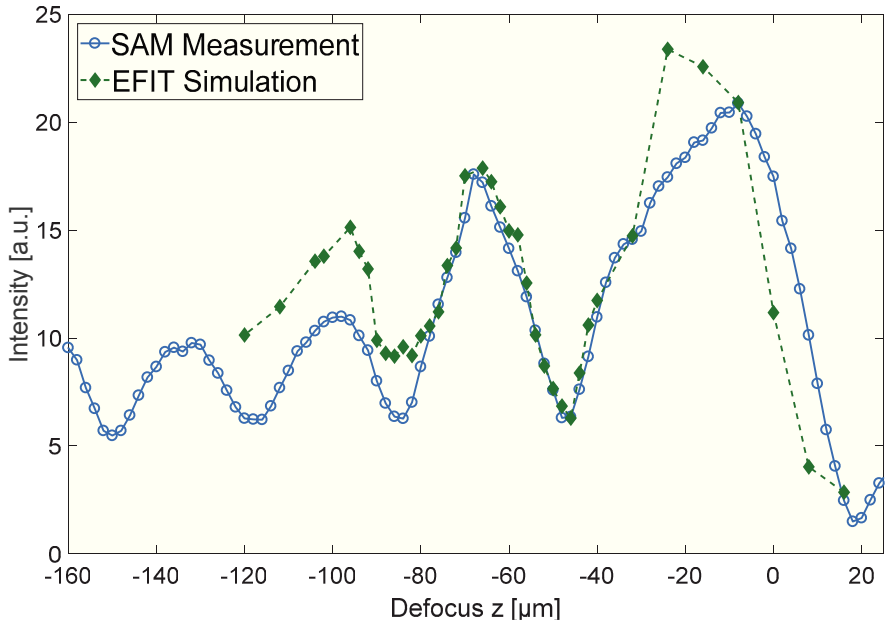

Figure 7. EFIT simulation (diamonds) and SAM measurement (circles) of $I(z)$ for an aluminium coating on silicon sample at 400 MHz.

Figure 8 shows the Rayleigh phase velocity v_R as function of frequency. The solid line corresponds to the theoretical model, predicting the Rayleigh dispersion curve of a 1 µm aluminium coating on a silicon substrate. The dotted line in the frequency range from 50 to 200 MHz was obtained by laser ultrasonic measurements, where good agreement was found. The empty diamond corresponds to the EFIT simulation result, and the full circle corresponds to the SAM measurement.

There is only one data point obtained from the SAM measurement and SAM simulation data because the measurement and simulation were performed in tone burst mode in order to obtain signals which are very narrow in the frequency domain (in our case at 400 MHz). The LUS measurement uses broadband acoustic surface waves in a frequency range from about 50 MHz to 200 MHz.

The wavelengths considered in this work are on the order of 10 µm. This means that they do penetrate the coating and their propagation is influenced by the substrate. However, the aluminium coating has a measurable influence on the phase velocity of the Rayleigh wave (see Figure 8).

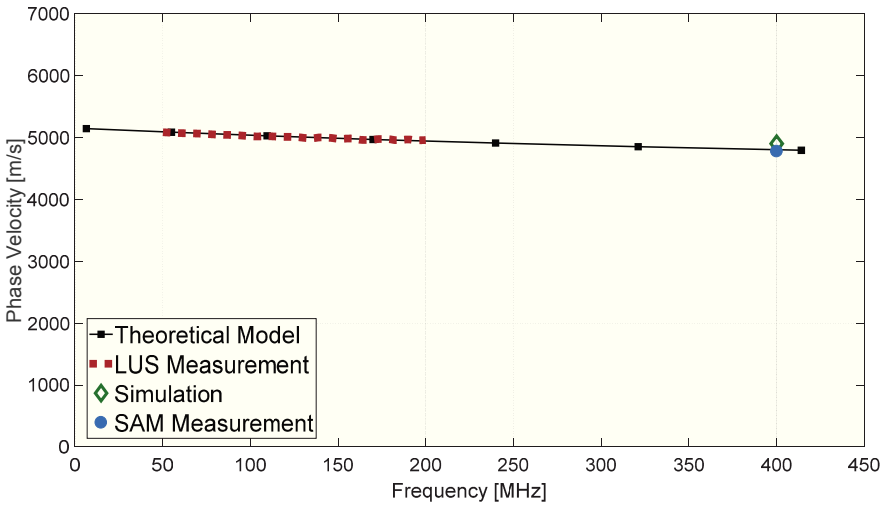

Figure 8. Rayleigh wave velocity as function of frequency for a 1 µm aluminium coating on silicon.

4. Discussion and Conclusions

In this work, SAM $I(z)$ measurements were simulated via EFIT, where (1) an aluminium bulk sample for calibration and (2) an aluminium-coated silicon wafer were analysed. From the $I(z)$ curves, the Rayleigh wave velocity of samples (1) and (2) were determined. The simulated results were corroborated via non-destructive SAM and LUS measurements. The obtained results demonstrate that the presented approach is highly useful for the material characterization of coatings.

The results summarized in Tables 1 and 2 give integer values for the $I(z)$ periodicity Δz, because the SAM measurement is limited by the number of oscillations and the 2 µm steps of defocus positions. Moreover, the number of evaluable A-scans is restricted due to multi-reflected signals in the measurement and in the simulation. Nevertheless, the Rayleigh wave velocities evaluated via EFIT simulations and SAM measurements are corroborated via the LUS method. The error in the determined Rayleigh velocity of the LUS measurements lies in the range of ± 10 m/s.

Table 2. Rayleigh wave velocity results at 400 MHz for 1 µm aluminium coating on silicon.

Method	Δz (µm)	v_R (m/s)
EFIT	38	4775
SAM	40	4899
Theoretical Model	–	4819

The advantages of the performed EFIT simulation tackle the challenges of state-of-the-art SAM measurements—namely, accurate data interpretation and the choice of the most suitable transducer. In addition, the most effective lens for a specific sample can be designed via EFIT simulation support.

Acknowledgments: The authors thank Jördis Rosc (MCL) for valuable discussions and Manfred Wießner (MCL) for the XRD measurements. PVA TePla Analytical Systems GmbH, (Westhausen, Germany) is gratefully acknowledged, especially Peter Czurratis, Peter Hoffrogge and Tatjana Djuric-Rissner for their contribution regarding the SAM equipment. This work has received funding from ENIAC Joint undertaking under FP7 research (No. 621270) and FFG (No. 843740) and partly from the EU, H2020 (No. 688225). Financial support by the Austrian Federal Government (in particular from Bundesministerium für Verkehr, Innovation und Technologie and Bundesministerium für Wissenschaft, Forschung und Wirtschaft) represented by Österreichische Forschungsförderungsgesellschaft mbH and the Styrian and the Tyrolean Provincial Government, represented by Steirische Wirtschaftsförderungsgesellschaft mbH and Standortagentur Tirol, within the framework of the COMET Funding Programme (No. 837900) is also gratefully acknowledged.

Author Contributions: Roland Brunner conceived and designed the experiments; Eva Grünwald (LUS&SAM), Philipp Aldo Wieser (SAM) and Robert Nuster (LUS) performed experimental work; René Hammer and

Eva Grünwald performed simulations for the experimental work; Rudolf Zelsacher and Michael Ehmann manufactured the samples; Martin Hinderer and Ingo Wiesler developed the tone burst device for the SAM. Eva Grünwald and Roland Brunner wrote the paper.

Conflicts of Interest: The authors declare no conflict of interest.

References

1. Grovenor, C.R.M. *Microelectronic Materials*; Plenum Press: New York, NY, USA, 1989.
2. Zhang, F.; Kirshnaswamy, S.; Fei, D.; Rebinsky, D.A.; Feng, B. Ultrasonic characterization of mechanical properties of Cr- and W-doped diamond-like carbon hard coatings. *Thin Solid Films* **2006**, *503*, 250–258. [CrossRef]
3. Neubrand, A.; Hess, P. Laser generation and detection of surface acoustic waves: Elastic properties of surface layers. *J. Appl. Phys.* **1992**, *71*, 227–238. [CrossRef]
4. Schneider, D.; Witke, T.; Schwarz, T.; Schöneich, B.; Schultrich, B. Testing ultra-thin films by laser-acoustics. *Surf. Coat. Technol.* **2000**, *126*, 136–141. [CrossRef]
5. Schneider, D.; Schwarz, T. A photoacoustic method for characterizing thin films. *Surf. Coat. Technol.* **1997**, *91*, 136–146. [CrossRef]
6. Hurley, D.C.; Tewary, V.K.; Richards, A.J. Surface acoustic wave methods to determine the anisotropic elastic properties of thin films. *Meas. Sci. Technol.* **2001**, *12*, 1486–1494. [CrossRef]
7. Briggs, G.A.D. *Advances in Acoustic Microscopy*, 2nd ed.; Plenum Press: New York, NY, USA, 1995.
8. Yu, Z.; Boseck, S. Scanning acoustic microscopy and its applications to material characterization. *Rev. Mod. Phys.* **1995**, *67*, 863. [CrossRef]
9. Grünwald, E.; Rosc, J.; Hammer, R.; Czurratis, P.; Koch, M.; Kraft, J.; Schrank, F.; Brunner, R. Automatized failure analysis of tungsten coated TSVs via scanning acoustic microscopy. *Microelectron. Reliab.* **2016**, *64*, 370–374. [CrossRef]
10. Shin, S.W.; Yun, C.B.; Popovics, J.S.; Kim, J.H. Improved rayleigh wave velocity measurement for nondestructive early-age concrete monitoring. *Res. Nondestruct. Eval.* **2017**, *18*, 45–68. [CrossRef]
11. Debboub, S.; Boumaïza, Y.; Boudour, A.; Tahraoui, T. Attenuation of Rayleigh surface waves in a porous material. *Chin. Phys. Lett.* **2012**, *29*, 044301. [CrossRef]
12. Levy, M.; Bass, H.E.; Stern, R. *Modern Acoustical Techniques for the Measurement of Mechanical Properties*; Academic Press: San Diego, CA, USA, 2001.
13. Tiersten, H.F. Elastic surface waves guided by thin films. *J. Appl. Phys.* **1969**, *40*, 770–789. [CrossRef]
14. Farnell, G.W.; Adler, E.L. Elastic wave propagation in thin layers. *Phys. Acoust.* **1972**, *9*, 35–127. [CrossRef]
15. Chimenti, D.E.; Nayfeh, A.H.; Butler, D.L. Leaky Rayleigh waves on a layered halfspace. *J. Appl. Phys.* **1982**, *53*, 170–176. [CrossRef]
16. Liang, K.K.; Kino, G.S.; Khuri-Yakub, B.T. Material characterization by the inversion of $V(z)$. *IEEE Trans. Sonics Ultrason.* **1985**, *32*, 213–224. [CrossRef]
17. Ghosh, T.; Maslov, K.I.; Kundu, T. A new method for measuring surface acoustic wave speeds by acoustic microscopes and its application in characterizing laterally inhomogeneous materials. *Ultrasonics* **1997**, *35*, 357–366. [CrossRef]
18. Bamber, M.J.; Cooke, K.E.; Man, A.B.; Derby, B. Accurate determination of Young's modulus and Poisson's ratio of thin films by a combination of acoustic microscopy and nanoindentation. *Thin Solid Films* **2001**, *398*, 299–305. [CrossRef]
19. Comte, C.; Von Stebut, J. Microprobe-type measurement of Young's modulus and Poisson coefficient by means of depth sensing indentation and acoustic microscopy. *Surf. Coat. Technol.* **2002**, *154*, 42–48. [CrossRef]
20. Weglein, R.D. A model for predicting acoustic material signatures. *Appl. Phys. Lett.* **1979**, *34*, 179–181. [CrossRef]
21. Henry, L.B. Ray-optical evaluation of $V(z)$ in the reflection acoustic microscope. *IEEE Trans. Sonics Ultrason.* **1984**, *31*, 105–116.
22. Kim, J.N. Multilayer Transfer Matrix Characterization of Complex Materials with Scanning Acoustic Microscopy. Master's Thesis, The Pennsylvania State University, Pennsylvania, PA, USA, 2013.
23. Guddati, M.N.; Yue, B. Modified integration rules for reducing dispersion error in finite element methods. *Comput. Methods Appl. Mech. Eng.* **2004**, *193*, 275–287. [CrossRef]

24. Willberg, C.; Duczek, S.; Perez, J.M.V.; Schmicker, D.; Gabbert, U. Comparison of different higher order finite element schemes for the simulation of Lamp waves. *Comput. Methods Appl. Mech. Eng.* **2012**, *241*, 246–261. [CrossRef]
25. Ham, S.; Bathe, K.J. A finite element method enriched for wave propagation problems. *Comput. Struct.* **2012**, *94*, 1–12. [CrossRef]
26. Komatitsch, D.; Vilotte, J.-P. The spectral element method, an efficient tool to simulate seismic response. *Bull. Seismol. Soc. Am.* **1998**, *88*, 368–392.
27. Zampieri, E.; Pavarino, L.F. Approximation of acoustic waves by explicit Newmark's schemes and spectral element methods. *J. Comput. Appl. Math.* **2006**, *185*, 308–325. [CrossRef]
28. Fornberg, B. The pseudospectral method comparisons with finite differences for the elastic wave equation. *Geophysics* **1987**, *52*, 483–501. [CrossRef]
29. Zhao, Z.; Xu, J.; Horiuchi, S. Differentiation operation in the wave equation for the pseudospectral method with a staggered mesh. *Earth Planets Space* **2001**, *53*, 327–332. [CrossRef]
30. LeVeque, R.J. Wave propagation algorithms for multidimensional hyperbolic systems. *J. Comput. Phys.* **1997**, *113*, 327–353. [CrossRef]
31. Virieux, J. SH-wave propagation in heterogeneous media: Velocity-stress finite-difference method. *Geophysics* **1984**, *49*, 1933–1942. [CrossRef]
32. Graves, R.W. Simulating seismic wave propagation in 3D elastic media using staggered-grid. *Bull. Seismol. Soc. Am.* **1996**, *86*, 1091–1106.
33. Pitarka, A. 3D elastic finite-difference modeling of seismic motion using staggered grids with nonuniform spacing. *Bull. Seismol. Soc. Am.* **1999**, *89*, 54–68.
34. Saenger, E.H.; Gold, N.; Shapiro, S.A. Modeling the propagation of elastic waves using a modified finite-difference grid. *Wave Motion* **2000**, *31*, 77–92. [CrossRef]
35. Fellinger, P.; Marklein, R.; Langenberg, K.J.; Klaholz, S. Numerical modeling of elastic wave propagation and scattering with EFIT–elastodynamic finite integration technique. *Wave Motion* **1995**, *21*, 47–66. [CrossRef]
36. Schubert, F.; Köhler, B. Time domain modelling of axisymmetric wave propagation in isotropic elastic media with CEFIT–cylindrical elastodynamic finite integration technique. *J. Comput. Acoust.* **2001**, *9*, 1127–1146.
37. Taflove, A.; Hagness, S.C. *Computational Electrodynamics: The Finite-Difference Time-Domain Method*; Artech House: Boston, MA, USA, 2005.
38. Hammer, R.; Pötz, W.; Arnold, A. Single-cone real-space finite difference scheme for the time-dependent Dirac equation. *J. Comput. Phys.* **2014**, *265*, 50–70. [CrossRef]
39. Grünwald, E.; Hammer, R.; Rosc, J.; Maier, G.A.; Bärnthaler, M.; Cordill, M.J.; Brand, S.; Nuster, R.; Krivec, T.; Brunner, R. Advanced 3D failure characterization in multi-layered PCBs. *NDT E Int.* **2016**, *84*, 99–107. [CrossRef]
40. Royer, D.; Dieulesaint, E. *Elastic Waves in Solids. I. Free and Guided Propagation*; Springer: Berlin, Germany, 2000.

Part VI

APPENDIX

A

APPENDIX

The calculations of the elastic wave propagation on isotropic and anisotropic substrates and multi-layered systems is presented in this part and follows [121] closely. Details on the theory of elasticity can be found in *e.g.* [73, 147].

A.1 LINEAR ELASTICITY

The starting point for the evaluation of the phase velocity in an anisotropic material is Hooke's Law. This equation relates stress acting on an elastic solid body to strain.

$$\vec{F} = \kappa \vec{u}$$

$\vec{F}$ is an applied force, $\vec{u}$ denotes the deformation and κ is the material spring constant. If the state of stress in the solid is described by the stress tensor

$$\sigma_{ij} = \begin{pmatrix} \sigma_{11} & \sigma_{12} & \sigma_{13} \\ \sigma_{21} & \sigma_{22} & \sigma_{23} \\ \sigma_{31} & \sigma_{32} & \sigma_{33} \end{pmatrix}$$

and the strain at a certain point in the solid is described by the strain tensor

$$\epsilon_{ij} = \begin{pmatrix} \epsilon_{11} & \epsilon_{12} & \epsilon_{13} \\ \epsilon_{21} & \epsilon_{22} & \epsilon_{23} \\ \epsilon_{31} & \epsilon_{32} & \epsilon_{33} \end{pmatrix}$$

then Hooke's Law for the 3 dimensional elastic body reads

$$\sigma_{ij} = C_{ijkl}\epsilon_{kl}.$$

C_{ijkl} is the elastic stiffness tensor of order four and has 81 entries in general $(i, j, k, l ... 1, 2, 3 \rightarrow 3 \times 3 \times 3 \times 3)$. However, stress and strain are symmetric and additional energy considerations lead to 21 independent stiffness constants at most. The number of independent components can further be reduced invoking symmetry arguments. For example, there are only 3 independent components in the stiffness tensor of a material with cubic symmetry:

$$C_{ijkl}^{cubic} = \begin{matrix} c_{11} & c_{12} & c_{12} & 0 & 0 & 0 \\ & c_{11} & c_{12} & 0 & 0 & 0 \\ & & c_{11} & 0 & 0 & 0 \\ & & & c_{44} & 0 & 0 \\ & & & & c_{44} & 0 \\ & & & & & c_{44} \end{matrix}. \tag{35}$$

Newton's second law of motion relates the stress acting on a point in a solid to the motion of the particles in the solid:

$$\rho\ddot{u}_i = \sigma_{ij,i}$$

where u_i is the displacement of a particle in the body in the ith direction. It follows that

$$\rho\ddot{u}_i = C_{ijkl}\epsilon_{kl,j},$$

with the definition of elastic strain:

$$\epsilon_{kl} = \frac{1}{2}\left(u_{k,l} + u_{l,k}\right)$$

this yields

$$\rho\ddot{u}_i = \frac{1}{2}C_{ijkl}\left(u_{k,l} + u_{l,k}\right) = C_{ijkl}u_{k,jl}.$$

With the ansatz

$$\vec{u} = A\vec{p}\exp\left\{i(\vec{k}\vec{x} - \omega t)\right\}$$

the derivatives are given by

$$\ddot{u}_i = -\omega^2 u_i$$

and

$$u_{k,jl} = -k_j k_l u_k.$$

It follows, that

$$\rho\omega^2 u_i = C_{ijkl}k_j k_l u_k = C_{ijkl}k^2 d_j d_l u_k$$

and

$$\rho c^2 u_i = C_{ijkl}d_j d_l u_k.$$

The Christoffel equation for anisotropic solids reads

$$\left[\rho c^2\delta_{ik} - C_{ijkl}d_j d_l\right]\left[u_k\right] = 0 \tag{36}$$

and the Christoffel matrix for an anisotropic solids is given by

$$\begin{bmatrix} \lambda_{11} - \rho c^2 & \lambda_{12} & \lambda_{13} \\ \lambda_{12} & \lambda_{22} - \rho c^2 & \lambda_{23} \\ \lambda 13 & \lambda_{23} & \lambda_{33} - \rho c^2 \end{bmatrix} \tag{37}$$

with the following entries (see also [124]):

$$\lambda_{11} = d_1^2 C_{11} + d_2^2 C_{66} + d_3^2 C_{55} + 2d_2 d_3 C_{56} + 2d_3 d_1 C_{15} + 2d_2 d_1 C_{16},$$

$$\lambda_{22} = d_1^2 C_{66} + d_2^2 C_{22} + d_3^2 C_{44} + 2d_2 d_3 C_{24} + 2d_3 d_1 C_{15} + 2d_2 d_1 C_{26},$$

$$\lambda_{33} = d_1^2 C_{55} + d_2^2 C_{44} + d_3^2 C_{33} + 2d_2 d_3 C_{34} + 2d_3 d_1 C_{35} + 2d_2 d_1 C_{46},$$

$$\lambda_{12} = d_1^2 C_{16} + d_2^2 C_{26} + d_3^2 C_{45} + d_2 d_3 (C_{46} + C_{25}) + d_3 d_1 (C_{14} + C_{56}) + d_2 d_1 (C_{12} + C_{66}),$$

$$\lambda_{13} = d_1^2 C_{15} + d_2^2 C_{46} + d_3^2 C_{35} + d_2 d_3 (C_{45} + C_{36}) + d_3 d_1 (C_{13} + C_{55}) + d_2 d_1 (C_{14} + C_{56}),$$

$$\lambda_{23} = d_1^2 C_{56} + d_2^2 C_{24} + d_3^2 C_{34} + d_2 d_3 (C_{44} + C_{23}) + d_3 d_1 (C_{36} + C_{45}) + d_2 d_1 (C_{25} + C_{46}).$$

A.2 ACOUSTIC WAVE MODES IN ISOTROPIC PLATES - PARTIAL WAVE ANSATZ

A technique which can be applied also to anisotropic plates is the partial wave method. The particle displacement in the partial wave ansatz reads:

$$\vec{u} = A\vec{p} \exp\left\{ i(\vec{k}\vec{x} - \omega t) \right\} \tag{38}$$

where $\vec{p}$ is the polarization vector, $\vec{k} = \vec{d}k$ is the wave vector and $\vec{d}$ is the propagation vector.

$$u_1 = A p_1 \exp\{-i\omega t\} \exp\{ik(d_1 x_1 + d_2 x_2 + d_3 x_3)\}$$

$$u_2 = A p_2 \exp\{-i\omega t\} \exp\{ik(d_1 x_1 + d_2 x_2 + d_3 x_3)\}$$

$$u_3 = A p_3 \exp\{-i\omega t\} \exp\{ik(d_1 x_1 + d_2 x_2 + d_3 x_3)\}$$

For pure longitudinal modes, $p \parallel d \rightarrow p_i = d_i$ and for pure transverse modes $p \perp d \rightarrow p_i d_i = 0 \rightarrow p_1 d_1 + p_2 d_2 + p_3 d_3 = 0$. $d_1 = \cos(\phi)$, $d_2 = \sin(\phi)$ and $d_3 \equiv \alpha_z$, where ϕ denotes the angle to the x_1 axis. For $\phi = 0$ $p_1 = 1$ and $p_2 = 0 \rightarrow p_3 = -1/d_3$.
In the notation of [121], for the six wave modes which can travel in an isotropic plate, the partial wave ansatz in x_1-direction reads:

$$u_j^{(n)} = \sum_{n=1}^{6} C_n U_j^{(n)} \exp\left[ik\left(x_1 + \alpha^{(n)} x_3 \right) \right].$$

Inserting 35 into 36 leads to the Christoffel equation for a solid with cubic symmetry

$$\begin{bmatrix} c_{11} + c_{44} - \rho c^2 & 0 & (c_{12} + c_{44})\alpha \\ 0 & c_{11} + c_{44} - \rho c^2 & 0 \\ (c_{12} + c_{44})\alpha & 0 & c_{44} + c_{11} - \rho c^2 \end{bmatrix} \begin{bmatrix} U_1 \\ U_2 \\ U_3 \end{bmatrix} = 0. \tag{39}$$

Here, the shear horizontal waves decouple. The equation for the SH waves is $c_{44} + c_{44}\alpha^2 - \rho c^2 = 0$, from which two $\alpha^{(n)}$ for these wave modes follow. For an isotropic solid $c_{11} = \lambda + 2\mu$, $c_{12} = \lambda$ and $c_{44} = \mu = \frac{1}{2}(c_{11} - c_{12})$, the Christoffel equation for isotropic media therefore reads:

$$\begin{bmatrix} a & b \\ b & c \end{bmatrix} \begin{bmatrix} U_1 \\ U_2 \end{bmatrix} = 0 \tag{40}$$

where

$$a = (\lambda + 2\mu) + \mu\alpha^2 - \rho c_P^2,$$

$$b = (\lambda + \mu)\alpha$$

and

$$c = (\lambda + 2\mu)\alpha^2 + \mu - \rho c_P^2.$$

Due to the decoupling of the SH wave modes, only 4 wave modes (up and downgoing longitudinal and transverse modes) are to be considered:

$$u_j = \sum_{n=1}^{4} C_n U_j^{(n)} \exp\left[ik\left(x_1 + \alpha^{(n)} x_3\right)\right].$$

Since the propagation of wave modes is conditioned by the Christoffel equation, the eigenvalues $\alpha^{(n)}$ and the eigenvectors $U_j^{(n)}$ of 40 have to be found. To this purpose, the determinant of the Christoffel matrix in 40 has to go to zero, which leads to a 4th order polynomial equation for the α^n. Having all eigenvalues $\alpha^{(n)}$ and the corresponding $U_j^{(n)}$, the displacement vectors and stress tensor components

$$u_1 = \sum_{1}^{4} B_m \exp\{ik(x_1 + \alpha_m x_3 - c_P t)\},$$

$$u_3 = \sum_{1}^{4} B_m U_{3m} \exp\{ik(x_1 + \alpha_m x_3 - c_P t)\},$$

$$\sigma_{31} = \sum_{1}^{4} B_m [\alpha_m + U_{3m}]\, \mu(ik) \exp\{ik(x_1 + \alpha_m x_3 - c_P t)\},$$

$$\sigma_{33} = \sum_{1}^{4} B_m [\lambda + (\lambda + 2\mu)\alpha_m U_{3m}]\, (ik) \exp\{ik(x_1 + \alpha_m x_3 - c_P t)\}$$

can be inserted into the boundary conditions

$$\sigma_{31} = \sigma_{33} = 0 \quad @ \quad x_3 = d, \quad x_3 = 0$$

leading to the 4×4 matrix D, where

$$D_{1m} = (\lambda + (\lambda + 2\mu)\alpha_{(m)} U_{3m})(ik),$$

$$D_{2m} = (\alpha_m + U_{3m})\mu(ik),$$

$$D_{1m} = (\lambda + (\lambda + 2\mu)\alpha_{(m)} U_{3m})(ik)\exp(ik\alpha_m d),$$

$$D_{4m} = (\alpha_m + U_{3m})\mu(ik)\exp(ik\alpha_m d).$$

Varying the frequency and the phase velocity until the determinant of the matrix D goes to zero, the allowed wave modes can be found.

A.3 ELASTIC WAVES IN MULTI-LAYERED ISOTROPIC SYSTEMS

The elastice wave propagation in isotropic multi-layered systems is discussed in Section 4.2.3. The process of calculating the allowed wave modes in a system with an isotropic substrate and an in principle arbitrary number of isotropic layers (up to nine layers were tested) is summarized in Listing 1.

A.4 ELASTIC WAVES ON AN ISOTROPIC LAYER-ANISOTROPIC SUBSTRATE SYSTEM

In the case of an isotropic layer on an substrate with cubic symmetry, four wave modes of the layer and two wave modes of the substrate have to be considered if the wave propagates along the x_1 direction. The six conditions for the boundary condition matrix are

$$\sigma_{31}^{(L)} = 0 \quad @ \quad x = 0,$$

$$\sigma_{33}^{(L)} = 0 \quad @ \quad x = 0,$$

$$\sigma_{31}^{(L)} = \sigma_{31}^{(S)} \quad @ \quad x = -h,$$

$$\sigma_{33}^{(L)} = \sigma_{33}^{(S} \quad @ \quad x = -h,$$

$$u_{31}^{(L)} = u_{31}^{(S)} \quad @ \quad x = -h,$$

$$u_{33}^{(L)} = u_{33}^{(S} \quad @ \quad x = -h,$$

where h is the layer thickness and the superscripts L and S denote the layer and the substrate respectively. The requirement of a vanishing boundary condition matrix for the right combination of c_P and k leads to the dispersion relation of the system.

In Listing 2 the steps for the determination of the frequency dependent phase velocity of SAWs on an isotropic layer on an anisotropic cubic system along the x_1 axis are summarized.

A.5 ELASTIC WAVES ON ANISOTROPIC CUBIC SUBSTRATE

For the consideration of the angular dependent wave propagation on an anisotropic substrate, either ϕ in the determination of Equation 38 in the propagation vector $\vec{d}$ can be changed, or the stiffness tensor C is rotated to C'.

In [141], the determination of elastic constants from angular dependent measurements on (100) silicon is presented, where the rotation of $C_{i,j,k,l}$ to $C'_{m,n,p,q}$ is achieved via

$$c'_{mnpq} = \beta_{mi}\beta_{nj}\beta_{pk}\beta_{ql}c_{ijkl},$$

$\beta_{i,j}$ (denoting the rotation matrix) is given by

$$\beta_{ij} = \begin{bmatrix} \cos(\phi) & \sin(\phi) & 0 \\ -\sin(\phi) & \cos(\phi) & 0 \\ 0 & 0 & 1 \end{bmatrix}$$

The entries of the Christoffel matrix Equation 37 are then evaluated for the rotated system in order to obtain the eigenvalues and eigenvectors of the equation. With the condition of vanishing stresses at the surface $\sigma_{3i} = 0 \quad @ \quad x_3 = 0$, the boundary condition matrix D can be found. By the right combination of phase velocity and angle, the roots of D are determined.

Figure 59 shows the angular dependent Rayleigh wave velocity for seven LUS measurements and the theoretical evaluation described in Listing 3. In Figure 59 the samples "HD" are silicon samples with higher doping concentration, whereas the samples "ND" show doping of lower concentration. The theoretical model was evaluated with the literature values reported by [9] of $c_{11} = 166\text{GPa}$, $c_{12} = 64\text{GPa}$, $c_{44} = 80\text{GPa}$ and a mass density of 2329kg/m^3. No fitting routine was applied in Figure 59, but in principle the elastic constants of the substrate can be characterized via similar measurements accompanied by a fitting procedure [141]. The change in phase velocity due to the doping of silicon is expected from the literature [142]. Further investigations of doped silicon samples via bulk waves can be found in [109].

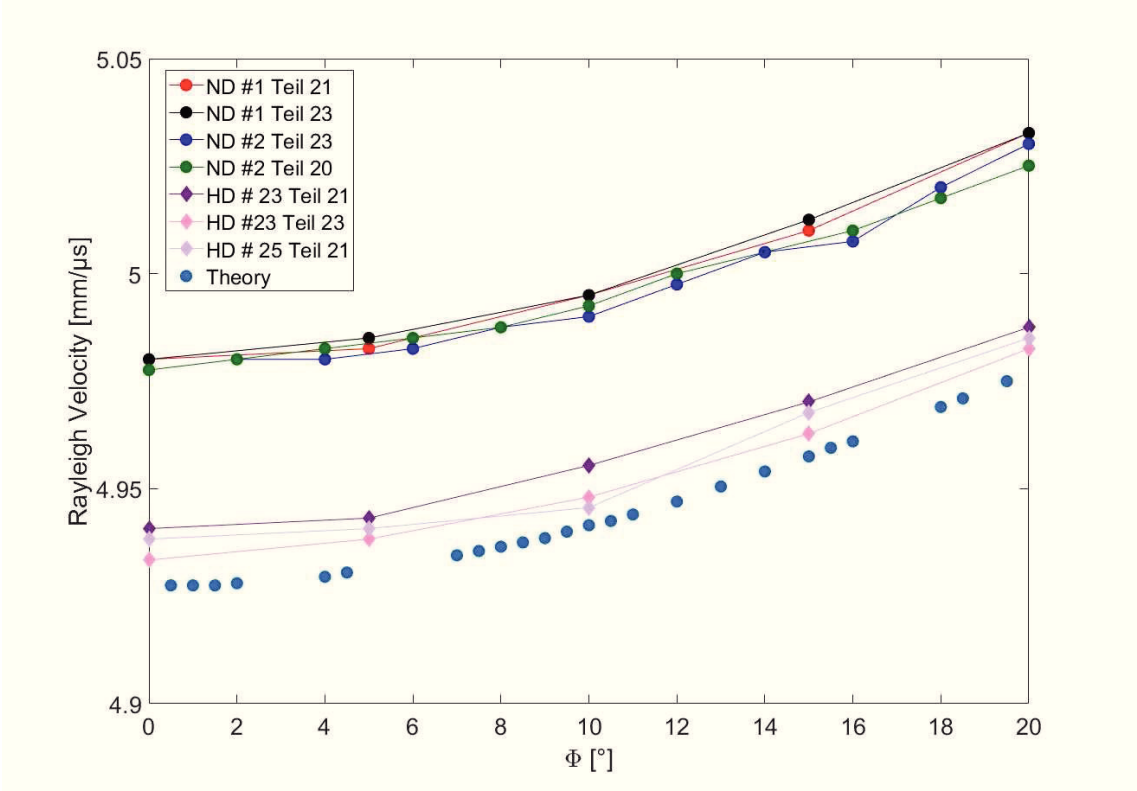

Figure 59: Angular dependent Rayleigh wave velocity on silicon (100), comparison of measurement and theory, where 0° corresponds to [100]. LUS measurements of highly doped Si samples "HD" (circles and solid lines) are compared to LUS measurements of samples with lower doping concentration "ND" (diamonds, solid line) and to theoretical evaluations (circles no line).

Listing 1: Global Matrix Method for Multi-Layered (Isotropic) System [121]

```
#Define ParamterMatrix
NumLayer= #Number of Layers
ParameterPerLayer=4; #rho, lambda, mu, h (Isotropic Materials)
ParameterMatrix=zeros(NumLayer,ParameterPerLayer);
Fill ParameterMatrix
#Create BoundaryConditionMatrix D
D=zeros(NumLayer*4,NumLayer+4);
#Find Frequency
for f = [fstart:fstep:fstop]
        omega=2*pi*f;
        #Find Phase Velocity
        for c = [cstart:cstep:cstop]
        k=omega/c;
                #Calculate Eigenvectors alphas, Eigenvectors U3s
                        alphas Layers
                        alphas Substrate
                        U3s Layers
        alphas  Substrate
        U3s Substrate
        Fill BoundaryConditionMatrix D
        # The boundary condition matrix, shows regularities allowing automatized
            filling the eigenvalues alpha, the eigenvalues U, the layer parameters
            must be known
        Find boundary matrix D zeros
        end
end
```

Listing 2: Isotropic Layer on Anisotropic Cubic Substrate [121]

```
#Determination Eigenvalues alpha, Eigenvectors U Cubic Symmetric Material
#Christoffel Equation:
l11=c11+c44*alpha^2-rho*c^2;
l22=(c44 + c11*alpha^2 - rho*c^2);
l12=(c12+c44)*alpha;
L=[l11 l12; l12 l22];
#--> Find Eigenvalues, Eigenvectors alpha5, alpha6, U35, U36
# Define Layer Properties
VL=# long. sound velocity
VT=# trans. sound velocity
rho=# density
h=# thickness
# Define parameters cubic symmetric substrate
c11= ;
c12= ;
c44= ;
rho2= ;
#Find frequency
for f = [fstart:fsteps:fstop]*10^6
    omega = 2*pi*f;
                #Find phase velocity
                for c = cstart:cstep:cstop
                k=omega/c;
                define alphas
                define Us
                define substrate alphas from Christoffel equation
                define substrate Us from Christoffel equation
                Fill boundary matrix D
                end
Find boundary matrix D zeros
end
```

Listing 3: Anisotropic Cubic Substrate [121]

```
Define Stiffnesstensor
#Define Rotation angle
for kk=0:0.5:20;
        theta = kk*pi/180;
        #Rotation matrix
        beta=[[cos(theta) sin(theta) 0];[-sin(theta) cos(theta) 0];[0 0 1];];
        Rotate stiffness tensor
        Determine eigenvalues alphas
        Determine eigenvectors Us
        #Determine phase velocity
                for cphase = cstart:cstep:cstop
                        Evaluate alphas
                        Evaluate Us
                        Fill D matrix
                end
        Find boundary matrix D zeros
end
```

BIBLIOGRAPHY

[1] J. D. Achenbach and R. J. Brind. "Scattering of surface waves by a sub-surface crack." In: *Journal of Sound and Vibration* 76.1 (1981), pp. 43–56. ISSN: 10958568. DOI: 10.1016/0022-460X(81)90289-3.

[2] Riaz Akhtar, J. Kennedy Cruickshank, Xuegen Zhao, Brian Derby, and Thomas Weber. "A pilot study of scanning acoustic microscopy as a tool for measuring arterial stiffness in aortic biopsies." In: *Artery Research* 13 (2016), pp. 1–5. ISSN: 18764401. DOI: 10.1016/j.artres.2015.11.001.

[3] I. Ames, F.M. D'Heurle, and R.E. Horstmann. "Reduction of Electromigration in Aluminum Films by Copper Doping." In: *IBM Journal of Research and Development* 14.4 (1970), pp. 461–463. ISSN: 0018-8646. DOI: 10.1147/rd.144.0461.

[4] I. Arias and J.D. Achenbach. "Thermoelastic Surface Waves Generated by Irradiation with a Line-Focused Laser Pulse." In: *Int. J. Sol. Struct.* 25.40 (2003), pp. 6917–6935.

[5] M. Arrigoni, Q. Hu, M. Boustie, L. Berthe, and J. P. Monchalin. "B-scan Simulations with Abaqus for Laser Ultrasonic Inspection of Structures." In: *1st International Symposium on Laser Ultrasonics: Science, Technology and Applications* Montreal, Canada (2018).

[6] Semiconductor Industry Association. "International Technology Roadmap for Semiconductors." In: *Itrpv* (2016), pp. 1–37. ISSN: 0018-9162. DOI: http://www.itrs.net/Links/2013ITRS/2013Chapters/2013Litho.pdf.

[7] Abdullah Atalar. "An angular-spectrum approach to contrast in reflection acoustic microscopy." In: *Journal of Applied Physics* 49.10 (1978), pp. 5130–5139. ISSN: 00218979. DOI: 10.1063/1.324460.

[8] Abdullah Atalar. "Penetration Depth of the Scanning Acoustic Microscope." In: *IEEE Transactions on Sonics and Ultrasonics* 32.2 (1985), pp. 164–167. ISSN: 00189537. DOI: 10.1109/T-SU.1985.31583.

[9] B.A.Auld. *Acoustic fields and waves in solids, volume II*. 1975, p. 397. ISBN: 0894644904. DOI: 10.1016/0003-682X(75)90008-0. arXiv: arXiv:1011.1669v3.

[10] Matthew D. Becton and Xianqiao Wang. "Grain-size Dependence of Mechanical Properties in Polycrystalline Boron-Nitride: A Computational Study." In: *Physical Chemistry Chemical Physics* 17 (2015), pp. 21894–21901. ISSN: 1463-9084. DOI: 10.1039/C5CP03460D.

[11] A. G. Bell. "On the Production and Reproduction of Sound by Light." In: *American Journal of Sciences* XX.118 (Oct. 1880), pp. 305–324.

[12] Sebastian Brand, Adriana Lapadatu, Tatjana Djuric, Peter Czurratis, Jan Schischka, and Matthias Petzold. "Scanning acoustic gigahertz microscopy for metrology applications in three-dimensional integration technologies." In: *Journal of Micro/Nanolithography, MEMS, and MOEMS* 13.1 (2014), p. 011207. ISSN: 1932-5150. DOI: 10.1117/1.JMM.13.1.011207.

[13] A. Briggs. *Advances in Acoustic Microscopy*. Advances in Acoustic Microscopy Bd. 1. Springer US, 2013. ISBN: 9781461518730.

[14] A Briggs and O Kolosov. *Acoustic Microscopy*. 2009, p. 384. ISBN: 978-019-923273-4.

[15] A. Briggs and O. Kolosov. *Acoustic Microscopy: Second Edition*. Monographs on the Physics and Chemistry of Materials. OUP Oxford, 2010. ISBN: 9780199232734.

[16] G. A. D. Briggs, J. Wang, and R. Gundle. "Quantitative acoustic microscopy of individual living human cells." In: *Journal of Microscopy* 172.1 (1993), pp. 3–12. ISSN: 13652818. DOI: 10.1111/j.1365-2818.1993.tb03387.x.

[17] J.F. Bussière, J.P. Monchalin, C.O. Ruud, and R.E. Green. *Nondestructive Characterization of Materials II*. Springer US, 2013. ISBN: 9781468453386.

[18] D. A. Cook and Y. H. Berthelot. "Detection of small surface-breaking fatigue cracks in steel using scattering of Rayleigh waves." In: *NDT and E International* 34.7 (2001), pp. 483–492. ISSN: 09638695. DOI: 10.1016/S0963-8695(00)00080-3.

[19] Kevin D. Costa, Steven H. Kleinstein, and Uri Hershberg. "Biomedical model fitting and error analysis." In: *Science Signaling* 4.192 (2011). ISSN: 19450877. DOI: 10.1126/scisignal.2001983. arXiv: NIHMS150003.

[20] Jacques Currie and Pierre Currie. "Développement, par pression, de l'électricité polaire dans les cristaux hémièdres à faces inclinées." In: *Comptes rendus de l ' Académie des sciences* 91 (1880), pp. 294–295.

[21] S J Davies, C Edwards, G S Taylor, and S B Palmer. "Laser-generated ultrasound: its properties, mechanisms and multifarious applications." In: *Journal of Physics D: Applied Physics* 26.3 (1993), pp. 329–348. ISSN: 0022-3727. DOI: 10.1088/0022-3727/26/3/001.

[22] L A Denisova, R G Maev, I Ya Poyurovskaya, T V Grineva, A F Denisov, E Yu Maeva, and E Yu Bakulin. "The use of acoustic microscopy to study the mechanical properties of glass-ionomer cement." In: *Dent Mater* 20.4 (2004), pp. 358–363. ISSN: 0109-5641. DOI: 10.1016/S0109-5641(03)00129-5.

[23] Lisa Dhar, John A. Rogers, Keith A. Nelson, and Fred Trusell. "Moduli determination in polyimide film bilayer systems: Prospects for depth profiling using impulsive stimulated thermal scattering." In: *Journal of Applied Physics* 77.9 (1995), pp. 4431–4444. ISSN: 00218979. DOI: 10.1063/1.359471.

[24] D. Ensminger. *Ultrasonics: Fundamentals, Technology, Applications, Second Edition, Revised and Expanded*. Dekker Mechanical Engineering. Taylor & Francis, 1988. ISBN: 9780824776596.

[25] A. G. Every. "Measurement of the near-surface elastic properties of solids and thin supported films." In: *Measurement Science and Technology* 13.5 (2002), pp. 21–39. ISSN: 0957-0233. DOI: 10.1088/0957-0233/13/5/201.

[26] A. G. Every and M. Deschamps. "Principal surface wave velocities in the point focus acoustic materials signature V(z) of an anisotropic solid." In: *Ultrasonics* 41.7 (2003), pp. 581–591. ISSN: 0041624X. DOI: 10.1016/S0041-624X(03)00155-0.

[27] P. Fellinger, R. Marklein, K. J. Langenberg, and S. Klaholz. "Numerical modeling of elastic wave propagation and scattering with EFIT - elastodynamic finite integration technique." In: *Wave Motion* 21.1 (1995), pp. 47–66. ISSN: 01652125. DOI: 10.1016/0165-2125(94)00040-C.

[28] Anthony C. Fischer-Cripps. *Nanoindentation*. 2011, p. 279. ISBN: 978-1-4419-9871-2. DOI: 10.1007/978-1-4419-9872-9.

[29] Pavel A. Fomitchov, Yeong K. Kim, Alexei K. Kromine, and Sridhar Krishnaswamy. "Laser Ultrasonic Array System for Real-Time Cure Monitoring of Polymer-Matrix Composites." In: *Journal of Composite Materials* 36.15 (2002), pp. 1889–1901. ISSN: 0021-9983. DOI: 10.1106/002199802026245.

[30] P. Garrou, C. Bower, and P. Ramm. *Handbook of 3D Integration: Volume 1 - Technology and Applications of 3D Integrated Circuits*. Wiley, 2011. ISBN: 9783527623068.

[31] V. G. Glebovsky, V. Yu Yaschak, V. V. Baranov, and E. L. Sackovich. "Properties of titanium-tungsten thin films obtained by magnetron sputtering of composite cast targets." In: *Thin Solid Films* 257.1 (1995), pp. 1–6. ISSN: 00406090. DOI: 10.1016/0040-6090(94)06326-5.

[32] Karl F. Graff. "Ultrasonics: Historical Aspects." In: *Ultrasonics Symposium* (1977), pp. 1–10. DOI: 10.1109/ULTSYM.1977.196782.

[33] E. Grünwald, R. Nuster, R. Treml, D. Kiener, G. Paltauf, and R. Brunner. "Young's Modulus and Poisson's Ratio Characterization of Tungsten Thin Films Via Laser Ultrasound." In: *Materials Today: Proceedings* 2.8 (2015). nanoFIS 2014 - Functional Integrated nanoSystems, pp. 4289 –4294. ISSN: 2214-7853. DOI: http://dx.doi.org/10.1016/j.matpr.2015.09.015.

[34] E. Grünwald, R. Hammer, J. Rosc, G.A. Maier, M. Bärnthaler, M.J. Cordill, S. Brand, R. Nuster, T. Krivec, and R. Brunner. "Advanced 3D failure characterization in multi-layered PCBs." In: *NDT & E International* 84 (2016), pp. 99 –107. ISSN: 0963-8695. DOI: http://dx.doi.org/10.1016/j.ndteint.2016.08.003.

[35] E. Grünwald, J. Rosc, R. Hammer, P. Czurratis, M. Koch, J. Kraft, F. Schrank, and R. Brunner. "Automatized failure analysis of tungsten coated TSVs via scanning acoustic microscopy." In: *Microelectronics Reliability* 64 (2016). Proceedings of the 27th European Symposium on Reliability of Electron Devices, Failure Physics and Analysis, pp. 370 –374. ISSN: 0026-2714. DOI: http://dx.doi.org/10.1016/j.microrel.2016.07.075.

[36] E. Grünwald, R. Nuster, R. Hammer, H. Aßmann, R. Brunner, and G. Paltauf. "Characterization of polyimid-multi-layer thin films combining laser ultrasonic measurements and numerical evaluations." In: *2016 17th International Conference on Thermal, Mechanical and Multi-Physics Simulation and Experiments in Microelectronics and Microsystems, EuroSimE 2016*. 2016. ISBN: 9781509021062. DOI: DOI:10.1109/EuroSimE.2016.7463353.

[37] E. Grünwald, R. Hammer, J. Rosc, B. Sartory, and R. Brunner. "Accretion Detection via Scanning Acoustic Microscopy in Microelectronic Components - Considering Symmetry Breaking Effects." In: *Microscopy and Microanalysis* 23.S1 (2017), 1466–1467. DOI: 10.1017/S1431927617007991.

[38] E. Grünwald, R. Nuster, G. Paltauf, T. Maier, R. Wimmer-Teubenbacher, R. Treml, D. Kiener, V. Leitgeb, A. Köck, and R. Brunner. "Laser Ultrasonic Thin Film Characterization of Si-Cu-Al-Cu Multi-Layered Stacks." In: 4.7 (2017), pp. 7122–7127. ISSN: 22147853. DOI: 10.1016/j.matpr.2017.08.006.

[39] E. Grünwald, R. Hammer, R. Nuster, P. Wieser, M. Hinderer, I. Wiesler, R. Zelsacher, M. Ehmann, and R. Brunner. "Simulation of Acoustic Wave Propagation in Aluminium Coatings for Material Characterization." In: *Coatings* 7.12 (2017), p. 230. ISSN: 2079-6412. DOI: 10.3390/coatings7120230.

[40] G. Guisbiers, E. Herth, L. Buchaillot, and T. Pardoen. "Fracture toughness, hardness, and Young's modulus of tantalum nanocrystalline films." In: *Applied Physics Letters* 97.14 (2010). ISSN: 00036951. DOI: 10.1063/1.3496000.

[41] René Hammer, Juraj Todt, Jozef Keckes, Bernhard Sartory, Georg Parteder, Jochen Kraft, and Stefan Defregger. "High resolution residual stress gradient characterization in W/TiN-stack on Si(100): Correlating in-plane stress and grain size distributions in W sublayer." In: *Materials Design* 132.Supplement C (2017), pp. 72 –78. ISSN: 0264-1275. DOI: https://doi.org/10.1016/j.matdes.2017.06.052.

[42] P.C. Hansen, V. Pereyra, and G. Scherer. *Least Squares Data Fitting with Applications*. Book collections on Project MUSE. ISBN: 9781421407869.

[43] Emmanuelle Harry, a Rouzaud, Michel Ignat, and Pierre Juliet. "Mechanical properties of W and W (C) thin films: Young's modulus, fracture toughness and adhesion." In: *Thin Solid Films* 332 (1998), pp. 195–201. ISSN: 0040-6090. DOI: 10.1016/S0040-6090(98)01056-6.

[44] K. Hasegawa, C. H. Turner, R. R. Recker, E. Wu, and D. B. Burr. "Elastic properties of osteoporotic bone measured by scanning acoustic microscopy." In: *Bone* 16.1 (1995), pp. 85–90. ISSN: 87563282. DOI: 10.1016/8756-3282(95)80016-J.

[45] Shiuh-Chuan Her and Sheng-Tung Lin. "Non-Destructive Evaluation of Depth of Surface Cracks Using Ultrasonic Frequency Analysis." In: *Sensors* 14.9 (2014), pp. 17146–17158. ISSN: 1424-8220. DOI: 10.3390/s140917146. URL: http://www.mdpi.com/1424-8220/14/9/17146/.

[46] Carmen M. Hernandez, Todd W. Murray, and Sridhar Krishnaswamy. "Photoacoustic characterization of the mechanical properties of thin films." In: *Applied Physics Letters* 80.4 (2002), pp. 691–693. ISSN: 00036951.

[47] P Hess. *Surface acoustic waves in materials science*. 2002. DOI: 10.1063/1.1472393.

[48] J a Hildebrand, D Rugar, R N Johnston, and C F Quate. "Acoustic microscopy of living cells." In: *Proceedings of the National Academy of Sciences of the United States of America* 78.3 (1981), pp. 1656–1660. ISSN: 0027-8424.

[49] Matthew A. Hopcroft, William D. Nix, and Thomas W. Kenny. "What is the Young's modulus of silicon?" In: *Journal of Microelectromechanical Systems* 19.2 (2010), pp. 229–238. ISSN: 10577157. DOI: 10.1109/JMEMS.2009.2039697.

[50] Martin Hoppe and Jurgen Bereiter-Hahn. "Applications of Scanning Acoustic Microscopy—Survey and New Aspects." In: *IEEE Transactions on Sonics and Ultrasonics* 32.2 (1985), pp. 289–301. ISSN: 00189537. DOI: 10.1109/T-SU.1985.31595.

[51] D C Hurley, V K Tewary, and A J Richards. "Surface acoustic wave methods to determine the anisotropic elastic properties of thin films." In: *Measurement Science & Technology* 12 (2001), pp. 1486–1494.

[52] D H Hurley. "Probing acoustic nonlinearity by mixing surface acoustic waves." In: *Review of Progress In Quantitative Nondestructive Evaluation, Vols 20a and 20b* 557 (2001), pp. 1236–1241.

[53] D H Hurley, Oliver B Wright, Osamu Matsuda, T Suzuki, Shin-ichiro Tamura, and Yoshihiro Sugawara. "Time-resolved surface acoustic wave propagation across a single grain boundary." In: *Physical Review B* 73.12 (2006), pp. 1–6. ISSN: 1098-0121. DOI: 10.1103/PhysRevB.73.125403. URL: http://link.aps.org/doi/10.1103/PhysRevB.73.125403.

[54] D. A. Hutchins. "Ultrasonic Generation by Pulsed Lasers." In: *Physical Acoustics* 18.C (1988), pp. 21–123. ISSN: 0893388X. DOI: 10.1016/B978-0-12-477918-1.50008-4.

[55] Chi Won In, Jin Yeon Kim, Kimberly E. Kurtis, and Laurence J. Jacobs. "Characterization of ultrasonic Rayleigh surface waves in asphaltic concrete." In: *NDT and E International* 42.7 (2009), pp. 610–617. ISSN: 09638695. DOI: 10.1016/j.ndteint.2009.04.007.

[56] M. Issouckis. "Imaging cells with acoustic microscopy." In: *Nature* 322.91 (1986). DOI: 10.1038/322091a0.

[57] R N Johnston, a Atalar, J Heiserman, V Jipson, and C F Quate. "Acoustic microscopy: resolution of subcellular detail." In: *Proceedings of the National Academy of Sciences of the United States of America* 76.7 (1979), pp. 3325–3329. ISSN: 0027-8424. DOI: 10.1073/pnas.76.7.3325.

[58] B.T. Khuri-Yakub. "Scanning acoustic microscopy." In: *Ultrasonics* 31.5 (1993), pp. 361–372. ISSN: 0041624X. DOI: 10.1016/0041-624X(93)90070-G.

[59] J.N. Kim, R. Tutwiler, D.R. Kwak, I. Park, and C. Miyasaka. "Multilayer transfer matrix characterization of complex materials with scanning acoustic microscopy." In: *Proceedings of SPIE - The International Society for Optical Engineering*. Vol. 8694. 2013. ISBN: 9780819494771. DOI: 10.1117/12.2012255.

[60] K. Kimoto, S. Ueno, and S. Hirose. "Image-based sizing of surface-breaking cracks by SH-wave array ultrasonic testing." In: *Ultrasonics* 45.1-4 (2006), pp. 152–164. ISSN: 0041624X. DOI: 10.1016/j.ultras.2006.08.006.

[61] Matthias Knapp, Alexey M Lomonosov, Paul Warkentin, Philipp M Jäger, Werner Ruile, Hans-Peter Kirschner, Matthias Honal, Ingo Bleyl, Andreas P Mayer, and Leonhard M Reindl. "Accurate characterization of SiO2 thin films using surface acoustic waves." In: *IEEE transactions on ultrasonics, ferroelectrics, and frequency control* 62.4 (2015), pp. 736–43. ISSN: 1525-8955. DOI: 10.1109/TUFFC.2014.006921. URL: http://www.ncbi.nlm.nih.gov/pubmed/25881351.

[62] D. B. Knorr and K. P. Rodbell. "The role of texture in the electromigration behavior of pure aluminum lines." In: *Journal of Applied Physics* 79.5 (1996), pp. 2409–2417. ISSN: 00218979. DOI: 10.1063/1.361168.

[63] D. Kozic, V. Maier-Kiener, R. Treml, H. P. Gänser, T. Antretter, R. Brunner, and D. Kiener. "Extracting flow curves from nano-sized metal layers in thin film systems." In: *Scripta Materialia* 130 (2017), pp. 143–147. ISSN: 13596462. DOI: 10.1016/j.scriptamat.2016.11.008.

[64] E. Kozic, J. Rosc, B. Sartory, J. Siegert, F. Schrank, and R. Brunner. "Novel Approach for Acoustic Microscopy Enabling nm-Sized Failure Detection in Open TSVs." In: *TBA* (2018).

[65] E. Kozic, R. Nuster, V. Razumovskiy, J. Zechner, B. Sartory, H. Katz, U. Kleb, R. Zelsacher, M. Ehmann, and R. Brunner. "TBA." In: *TBA* (2018).

[66] E. Kozic, J. Rosc, B. Sartory, J. Siegert, F. Schrank, and R. Brunner. "Wave Mode Enhanced Failure Detection via Scanning Acoustic Microscopy." In: *TBA* (2018).

[67] J. Kraft et al. "3D Sensor application with open through silicon via technology." In: *Proceedings - Electronic Components and Technology Conference*. 2011, pp. 560–566. ISBN: 9781612844978. DOI: 10.1109/ECTC.2011.5898567.

[68] M. Krause, F. Altmann, C. Schmidt, M. Petzold, D. Malta, and D. Temple. "Characterization and failure analysis of TSV interconnects: From non-destructive defect localization to material analysis with nanometer resolution." In: *Proceedings - Electronic Components and Technology Conference*. 2011, pp. 1452–1458. ISBN: 9781612844978. DOI: 10.1109/ECTC.2011.5898702.

[69] C. Krauss, S. Labat, S. Escoubas, O. Thomas, S. Carniello, J. Teva, and F. Schrank. "Stress measurements in tungsten coated through silicon vias for 3D integration." In: *Thin Solid Films*. Vol. 530. 2013, pp. 91–95. DOI: 10.1016/j.tsf.2012.05.091.

[70] Sridhar Krishnaswamy. *Theory and applications of laser-ultrasonic techniques*. 2003, pp. 435–494. ISBN: 0849314623. DOI: doi:10.1201/9780203501962.ch7.

[71] S E Kruger, a Moreau, C Bescond, and J Monchalin. "S. E. Kruger, A. Moreau, C. Bescond and J.-P. Monchalin." In: *Time* (2004).

[72] T. Kundu, J. Bereiter-Hahn, and K. Hillmann. "Measuring elastic properties of cells by evaluation of scanning acoustic microscopy V(z) values using simplex algorithm." In: *Biophysical Journal* 59.6 (1991), pp. 1194–1207. ISSN: 00063495. DOI: 10.1016/S0006-3495(91)82335-9.

[73] Lev D Landau, E M Lifshitz, J B Sykes, W H Reid, and Ellis H Dill. *Theory of Elasticity: Vol. 7 of Course of Theoretical Physics*. 1960. DOI: 10.1063/1.3057037.

[74] J.H. Lau. *Through-Silicon Vias for 3D Integration*. McGraw-Hill Education, 2012. ISBN: 9780071785150.

[75] Pascal Laugier, Amena Saïed, Mathilde Granke, and Kay Raum. "Quantitative Scanning Acoustic Microscopy of Bone." In: *Advances in Acoustic Microscopy and High Resolution Imaging: From Principles to Applications*. 2013, pp. 207–230. ISBN: 9783527410569. DOI: 10.1002/9783527655304.ch9.

[76] R. E. Lee and R. M. White. "Excitation of surface elastic waves by transient surface heating." In: *Applied Physics Letters* 12.1 (1968), pp. 12–14. ISSN: 00036951. DOI: 10.1063/1.1651832.

[77] Yung-Chun Lee, Jin O. Kim, and Jan D. Achenbach. "V(z) curves of layered anisotropic materials for the line-focus acoustic microscope." In: *The Journal of the Acoustical Society of America* 94.2 (1993), pp. 923–930. ISSN: NA 00014966. DOI: 10.1121/1.408194.

[78] R. A. Lemons and C. F. Quate. "Acoustic microscope—scanning version." In: *Applied Physics Letters* 24.4 (1974), p. 163. ISSN: 00036951. DOI: 10.1063/1.1655136.

[79] Qing Li, Kathleen Hoogeboom-Pot, Damiano Nardi, Chris Deeb, Sean King, Marie Tripp, Erik Anderson, Margaret M. Murnane, and Henry C. Kapteyn. "Characterization of ultrathin films by laser-induced sub-picosecond photoacoustics with coherent extreme ultraviolet detection." In: *Proc. of SPIE*. Vol. 8324. 2012, 83241P–83241P–8. ISBN: 0277-786X 978-0-8194-8980-7. DOI: 10.1117/12.916866.

[80] Der Jang Liaw, Kung Li Wang, Ying Chi Huang, Kueir Rarn Lee, Juin Yih Lai, and Chang Sik Ha. "Advanced polyimide materials: Syntheses, physical properties and applications." In: *Progress in Polymer Science* 37.7 (2012), pp. 907–974. ISSN: 00796700. DOI: 10.1016/j.progpolymsci.2012.02.005.

[81] Alexey M. Lomonosov, Peter V. Grigoriev, and Peter Hess. "Sizing of partially closed surface-breaking microcracks with broadband Rayleigh waves." In: *Journal of Applied Physics* 105.8 (2009). ISSN: 00218979. DOI: 10.1063/1.3110885.

[82] Roberto Longo, Steve Vanlanduit, Joris Vanherzeele, and Patrick Guillaume. "A method for crack sizing using Laser Doppler Vibrometer measurements of Surface Acoustic Waves." In: *Ultrasonics* 50.1 (2010), pp. 76–80. ISSN: 0041624X. DOI: 10.1016/j.ultras.2009.08.001.

[83] W. S. Lord Rayleigh. "Theory of Sound." In: *Theory of Sound*. Vol. 1. 1895, p. 235. ISBN: 1-152-06023-6.

[84] Kritsakorn Luangvilai. "Attenuation of Ultrasonic Lamb Waves with Applications to Material Characterization and Condition Monitoring." In: *PhD thesis* August (2007), p. 283.

[85] D. Luo. *Pattern Recognition and Image Processing*. Woodhead Publishing Series in Electronic and Optical Materials. Elsevier Science, 1998. ISBN: 9780857099761.

[86] R. G. Maev, J. H. Sokolowski, H. T. Lee, E. Y. Maeva, and A. A. Denissov. "Bulk and subsurface structure analysis of the 319 aluminum casting using acoustic microscopy methods." In: *Materials Characterization* 46.4 (2001), pp. 263–269. ISSN: 10445803. DOI: 10.1016/S1044-5803(00)00096-6.

[87] R.G. Maev. *Acoustic Microscopy: Fundamentals and Applications*. Wiley, 2008. ISBN: 9783527407446.

[88] T. H. Maiman. "Stimulated Optical Radiation in Ruby." In: *Nature* (1960). DOI: 10.1038/187493a0.

[89] P. A. Mante, J. F. Robillard, and A. Devos. "Complete thin film mechanical characterization using picosecond ultrasonics and nanostructured transducers: Experimental demonstration on SiO2." In: *Applied Physics Letters* 93.7 (2008). ISSN: 00036951. DOI: 10.1063/1.2975171.

[90] T. J. Marrow, G. A.D. Briggs, and S. G. Roberts. "In-situ scanning acoustic microscopy of crack bridging in alumina." In: *Journal of the European Ceramic Society* 14.2 (1994), pp. 111–116. ISSN: 09552219. DOI: 10.1016/0955-2219(94)90098-1.

[91] K. I. Maslov, P. V. Zinin, O. I. Lobkis, and T. Kundu. "V(z) curve formation of solid spherical microparticles in scanning acoustic microscopy." In: *Journal of Microscopy* 178.2 (1995), pp. 125–133. ISSN: 13652818. DOI: 10.1111/j.1365-2818.1995.tb03588.x.

[92] Bernard Masserey and Edoardo Mazza. "Ultrasonic sizing of short surface cracks." In: *Ultrasonics* 46.3 (2007), pp. 195–204. ISSN: 0041624X. DOI: 10.1016/j.ultras.2007.02.001.

[93] Bernard Masserey, Christian Raemy, and Paul Fromme. "High-frequency guided ultrasonic waves for hidden defect detection in multi-layered aircraft structures." In: *Ultrasonics*. Vol. 54. 7. 2014, pp. 1720–1728. ISBN: 9780735410138. DOI: 10.1016/j.ultras.2014.04.023.

[94] Osamu Matsuda, Maria Cristina Larciprete, Roberto Li Voti, and Oliver B. Wright. "Fundamentals of picosecond laser ultrasonics." In: *Ultrasonics* 56 (2015), pp. 3–20. ISSN: 0041624X. DOI: 10.1016/j.ultras.2014.06.005.

[95] Department of Materials Science Michigan Tech and John Pilling Engineering. *Properties of Seleced Matrices*. 2017. URL: http://www.mse.mtu.edu/~drjohn/my4150/props.html (visited on 03/30/2018).

[96] K.L. Mittal. *Polyimides: Synthesis, Characterization, and Applications*. Bd. 1. Springer US, 2013. ISBN: 9781461576372.

[97] Katsutoshi Miura and Seiji Yamamoto. "Pulmonary imaging with a scanning acoustic microscope discriminates speed-of-sound and shows structural characteristics of disease." In: *Laboratory Investigation* 92.12 (2012), pp. 1760–1765. ISSN: 0023-6837. DOI: 10.1038/labinvest.2012.135.

[98] Katsutoshi Miura and Seiji Yamamoto. "A scanning acoustic microscope discriminates cancer cells in fluid." In: *Scientific Reports* 5.1 (2015), p. 15243. ISSN: 2045-2322. DOI: 10.1038/srep15243. URL: http://www.nature.com/articles/srep15243.

[99] T Miwa. "Polyimides in microelectronics applications." In: *Journal of Photopolymer Science and Technology* 14.1 (2001), pp. 29–32. ISSN: 09149244 (ISSN). DOI: 10.2494/photopolymer.14.29.

[100] Jean-Pierre Monchalin. "Laser-Ultrasonics: From the Laboratory to Industry." In: *AIP Conference Proceedings*. Vol. 700. 2004, pp. 3–31. ISBN: 073540173X. DOI: 10.1063/1.1711602. URL: http://aip.scitation.org/doi/abs/10.1063/1.1711602.

[101] Gordon E. Moore. "Cramming more components onto integrated circuits, Reprinted from Electronics, volume 38, number 8, April 19, 1965, pp.114 ff." In: *IEEE Solid-State Circuits Newsletter* 20.3 (2006), pp. 33–35. ISSN: 1098-4232. DOI: 10.1109/N-SSC.2006.4785860. URL: http://ieeexplore.ieee.org/document/4785860/.

[102] Hideshi Nakano, Katsumi Naito, Shoko Suzuki, Keiko Naito, Kazuto Kobayashi, and Seiji Yamamoto. "Scanning acoustic microscopy imaging of tongue squamous cell carcinomas discriminates speed-of-sound between lesions and healthy regions in the mucous epithelium." In: *Journal of Oral and Maxillofacial Surgery, Medicine, and Pathology* 27.1 (2013), pp. 16–19. ISSN: 22125558. DOI: 10.1016/j.ajoms.2013.07.004.

[103] A. Neubrand and P. Hess. "Laser generation and detection of surface acoustic waves: Elastic properties of surface layers." In: *Journal of Applied Physics* 71.1 (1992), pp. 227–238. ISSN: 00218979. DOI: 10.1063/1.350747.

[104] W.K. Nowacki. *Progress in Thermoelasticity*. Applied mechanics series. Państw. Wyd. nauk., 1969.

[105] R. Nuster. "Berührungslose Ultraschalldiagnostik basierend auf der interferometrischen Registrierung von lasergenerierten, optoakustischen Wellen." In: *Diplomarbeit* (2004).

[106] R. Nuster. "Entwicklung und Anwendung breitbandiger optischer Sensoren zur Messung laserinduzierten Ultraschalls." In: *Dissertation* (2007).

[107] B. Perrin, B. Bonello, J. C. Jeannet, and E. Romatet. "Picosecond ultrasonics study of metallic multilayers." In: *Physica B: Condensed Matter* 219-220.1-4 (1996), pp. 681–683. ISSN: 09214526. DOI: 10.1016/0921-4526(95)00852-7.

[108] Alain Phommahaxay et al. "High frequency scanning acoustic microscopy applied to 3D integrated process: Void detection in Through Silicon Vias." In: *Proceedings - Electronic Components and Technology Conference*. 2013, pp. 227–231. ISBN: 9781479902330. DOI: 10.1109/ECTC.2013.6575576.

[109] T. Planko. "Bestimmung von Materialparametern mittels Laserultraschall." In: *Master Thesis* (2018).

[110] S. V. Plyushcheva, G. M. Mikhailov, L. G. Shabel'nikov, and S. Yu. Shapoval. "Tungsten thin-film deposition on a silicon wafer: The formation of silicides at W-Si interface." In: *Inorganic Materials* 45.2 (2009), pp. 140–144. ISSN: 0020-1685. DOI: 10.1134/S002016850902006X.

[111] D. M. Profunser. "Laserbased ultrasound for characterization of thin films and microstructures and resulting applications." In: *PhD thesis* September (2004), p. 154.

[112] B.C. Punmia. *Mechanics of Materials*. Laxmi Publications Pvt Limited, 2002. ISBN: 9788170082156.

[113] Python Software Foundation. *Python Language Reference, version 2.7*. 2013. DOI: https://www.python.org/. URL: http://www.python.org.

[114] T. Q. Qiu and C. L. Tien. "Femtosecond laser heating of multi-layer metals-I. Analysis." In: *International Journal of Heat and Mass Transfer* 37.17 (1994), pp. 2789–2797. ISSN: 00179310. DOI: 10.1016/0017-9310(94)90396-4.

[115] Changzi Qu, Junsong Hu, Xing Liu, Zheng Li, and Yanhuai Ding. "Morphology and mechanical properties of polyimide films: The effects of UV irradiation on microscale surface." In: *Materials* 10.11 (2017). ISSN: 19961944. DOI: 10.3390/ma10111329.

[116] Calvin F. Quate, Abdullah Atalar, and H. K. Wickramasinghe. "Acoustic microscopy with mechanical scanning—a review." In: *Proceedings of the IEEE* 67.8 (1979), pp. 1092–1114. ISSN: 15582256. DOI: 10.1109/PROC.1979.11406.

[117] WS Rasband. "ImageJ." In: *U. S. National Institutes of Health, Bethesda, Maryland, USA* (2012), //imagej.nih.gov/ij/.

[118] Sherief Reda. "3D integration advances computing." In: *Nature* 547 (2017). URL: http://dx.doi.org/10.1038/547038a.

[119] L. Reimer. *Scanning Electron Microscopy: Physics of Image Formation and Microanalysis*. Springer Series in Optical Sciences. Springer, 1998. ISBN: 9783540639763.

[120] A. Riley. *High Performance Polymers - Polyimides Based - from Chemistry to Applications*. Scitus Academics LLC, 2016. ISBN: 9781681174693.

[121] Joseph L Rose. *Ultrasonic Waves in Solid Media*. Vol. 107. 2004, p. 1807. ISBN: 9780521548892. DOI: 10.1121/1.428552.

[122] G. Ross, V. Vuorinen, M. Petzold, M. Paulasto-Kröckel, and S. Brand. "Gigahertz scanning acoustic microscopy analysis of voids in Cu-Sn micro-connects." In: *Applied Physics Letters* 110.5 (2017). ISSN: 00036951. DOI: 10.1063/1.4975305.

[123] André Rouzaud, E. Barbier, J. Ernoult, and E. Quesnel. "A method for elastic modulus measurements of magnetron sputtered thin films dedicated to mechanical applications." In: *Thin Solid Films* 270.1-2 (1995), pp. 270–274. ISSN: 00406090. DOI: 10.1016/0040-6090(95)06921-6.

[124] Daniel Royer and Eugene Dieulesaint. *Elastic waves in solids*. 2000, p. 474. ISBN: 3540659323. DOI: 10.1115/1.3167197.

[125] Yoshifumi Saijo, Motonao Tanaka, Hiroaki Okawai, and Floyd Dunn. "The ultrasonic properties of gastric cancer tissues obtained with a scanning acoustic microscope system." In: *Ultrasound in Medicine and Biology* 17.7 (1991), pp. 709–714. ISSN: 03015629. DOI: 10.1016/0301-5629(91)90103-4.

[126] P. G. Sanders, J. A. Eastman, and J. R. Weertman. "Elastic and tensile behavior of nanocrystalline copper and palladium." In: *Acta Materialia* 45.10 (1997), pp. 4019–4025. ISSN: 13596454. DOI: 10.1016/S1359-6454(97)00092-X.

[127] Selma Schenkl, Eike C. Weiss, Frank Stracke, Daniel Sauer, Martin Stark, Iris Riemann, Robert M. Lemor, and Karsten König. "In-vivo observation of cells with a combined high-resolution multiphoton-acoustic scanning microscope." In: *Microscopy Research and Technique*. Vol. 70. 5. 2007, pp. 476–480. ISBN: 1059-910X. DOI: 10.1002/jemt.20429.

[128] D. Schneider, H. Ollendorf, and T. Schwarz. "Non-destructive evaluation of the mechanical behaviour of TiN-coated steels by laser-induced ultrasonic surface waves." In: *Applied Physics A Materials Science & Processing* 61.3 (1995), pp. 277–284. ISSN: 09478396. DOI: 10.1007/BF01538193.

[129] D. Schneider and M. D. Tucker. "Non-destructive characterization and evaluation of thin films by laser-induced ultrasonic surface waves." In: *Thin Solid Films* 290-291 (1996), pp. 305–311. ISSN: 00406090. DOI: 10.1016/S0040-6090(96)09029-3.

[130] D Schneider, T Schwarz, H J Scheibe, and M Panzner. "Non-destructive evaluation of diamond and diamond-like carbon films by laser induced surface acoustic waves." In: *Thin Solid Films* 295 (1997), pp. 107–116. ISSN: 00406090. DOI: 10.1016/S0040-6090(96)09163-8.

[131] D. Schneider, B. Schultrich, H.-J. Scheibe, H. Ziegele, and M. Griepentrog. "A laser-acoustic method for testing and classifying hard surface layers." In: *Thin Solid Films* 332.1-2 (1998), pp. 157–163. ISSN: 00406090. DOI: 10.1016/S0040-6090(98)00988-2.

[132] D. Schneider, T. Witke, T. Schwarz, B. Schoöneich, and B. Schultrich. "Testing ultra-thin films by laser-acoustics." In: *Surface and Coatings Technology* 126.2-3 (2000), pp. 136–141. ISSN: 02578972. DOI: 10.1016/S0257-8972(99)00672-6.

[133] Dieter Schneider and Thomas Schwarz. "A photoacoustic method for characterising thin films." In: *Surface and Coatings Technology* 91.1-2 (1997), pp. 136–146. ISSN: 02578972. DOI: 10.1016/S0257-8972(96)03147-7.

[134] Frank Schubert, Bernd Koehler, and Alexander Peiffer. "Time Domain Modeling of Axisymmetric Wave Propagation in Isotropic Elastic Media with CEFIT — Cylindrical Elastodynamic Finite Integration Technique." In: *Journal of Computational Acoustics* 09.03 (2001), pp. 1127–1146. DOI: 10.1142/S0218396X0100098X.

[135] C.B. Scruby and L.E. Drain. *Laser Ultrasonics Techniques and Applications*. Taylor & Francis, 1990. ISBN: 9780750300506.

[136] Zhonghua Shen, Baiqiang Xu, Xiaowu Ni, and Jian Lu. "Numerical simulation of laser-generated ultrasonic waves in layered plates." In: *Journal of Physics D: Applied Physics* 37.17 (2004), pp. 2364–2370. ISSN: 0022-3727. DOI: 10.1088/0022-3727/37/17/004.

[137] C. J R Sheppard and T. Wilson. "Effects of high angles of convergence on V(z) in the scanning acoustic microscope." In: *Applied Physics Letters* 38.11 (1981), pp. 858–859. ISSN: 00036951. DOI: 10.1063/1.92198.

[138] David S Sholl and Janice A Steckel. *Density Functional Theory: A Practical Introduction*. Vol. 68. 1. 2009, p. 69. ISBN: 0470373172. DOI: 10.1119/1.19375.

[139] S. Smith. *Digital Signal Processing: A Practical Guide for Engineers and Scientists*. Demystifying technology series. Elsevier Science, 2013. ISBN: 97800080477329.

[140] X.Y Sokolov. "Ultrasonic methods of detecting internal flaws in metal articles." In: *Zavodskaya Laoratoriya* 4.4 (1935), pp. 1468–1473. DOI: 10.1016/j.ndteint.2009.04.007.

[141] Guorong Song, Guangfu Hong, Yan Lu, Yuyang Xu, Dengqian Qin, Bin Wu, and Cunfu He. "Inversion of Elastic Constants of Anisotropic (100) Silicon Based on Surface Wave Velocity by Acoustic Microscopy Using Particle Swarm-Based-Simulated Annealing Optimization." In: *Journal of Nondestructive Evaluation* 34.4 (2015), pp. 1–10. ISSN: 15734862. DOI: 10.1007/s10921-015-0316-6.

[142] A.K. Sood and M. Cardona. "Rayleigh surface waves in ultraheavily doped n-Si." In: *Solid State Communications* 60.8 (1986), pp. 629 –631. ISSN: 0038-1098. DOI: https://doi.org/10.1016/0038-1098(86)90256-5.

[143] R. Splinter. *Illustrated Encyclopedia of Applied and Engineering Physics, Three-Volume Set*. CRC Press, 2017. ISBN: 9781351625630.

[144] H.L. Sun, Z.X. Song, D.G. Guo, F. Ma, and K.W. Xu. "Microstructure and Mechanical Properties of Nanocrystalline Tungsten Thin Films." In: *Journal of Materials Science & Technology* 26.1 (2010), pp. 87–92. ISSN: 10050302. DOI: 10.1016/S1005-0302(10)60014-X.

[145] H. F. Tiersten. "Elastic Surface Waves Guided by Thin Films." In: *Journal of Applied Physics* 40.2 (1969), pp. 770–789. DOI: 10.1063/1.1657463. eprint: https://doi.org/10.1063/1.1657463.

[146] H. F. Tiersten. "Elastic surface waves guided by thin films." In: *Journal of Applied Physics* 40.2 (1969), pp. 770–789. ISSN: 00218979. DOI: 10.1063/1.1657463.

[147] S Timoshenko and J N Goodier. *Theory of Elasticity*. 1986. DOI: 10.1007/BF00046464.

[148] A Tourlog, W Li, and J D Achenbach. "Line-focus acoustic microscopy measurements of elastic constants for materials with high acoustic velocities." In: *Applied Physics Letters* 69.24 (1996), pp. 3680–3682. ISSN: 00036951.

[149] Benjamin Steven Vien, Louis Raymond Francis Rose, and Wing Kong Chiu. "Experimental and computational studies on the scattering of an edge-guidedwave by a hidden crack on a racecourse shaped hole." In: *Materials* 10.7 (2017). ISSN: 19961944. DOI: 10.3390/ma10070732.

[150] Thomas K. Vogt. "Determination of material properties using guided waves." In: *Ultrasonics* 42.1-9 (2004), pp. 641–6. ISSN: 0041-624X. DOI: 10.1016/j.ultras.2004.01.049. URL: http://www.ncbi.nlm.nih.gov/pubmed/21040919.

[151] M. Mitchell Waldrop. "The chips are down for Moore's law." In: *Nature* 530.7589 (2016), pp. 144–147. ISSN: 0028-0836. DOI: 10.1038/530144a. arXiv: Nature,2016,530(7589):144.. URL: http://www.nature.com/doifinder/10.1038/530144a.

[152] Y. Waseda, E. Matsubara, and K. Shinoda. *X-Ray Diffraction Crystallography: Introduction, Examples and Solved Problems*. Springer Berlin Heidelberg, 2011. ISBN: 9783642166358.

[153] M.J. Weber. *Handbook of Optical Materials*. Laser & Optical Science & Technology. Taylor & Francis, 2002. ISBN: 9780849335129.

[154] K. Wetzig and C.M. Schneider. *Metal Based Thin Films for Electronics*. Wiley, 2006. ISBN: 9783527606474.

[155] R. M. White. "Generation of elastic waves by transient surface heating." In: *Journal of Applied Physics* 34.12 (1963), pp. 3559–3567. ISSN: 00218979. DOI: 10.1063/1.1729258.

[156] H. K. Wickramasinghe. "Scanning acoustic microscopy: a review." In: *Journal of Microscopy* 129.1 (1983), pp. 63–73. ISSN: 13652818. DOI: 10.1111/j.1365-2818.1983.tb04161.x.

[157] R. G. Wilson and R. D. Weglein. "Acoustic microscopy of materials and surface layers." In: *Journal of Applied Physics* 55.9 (1984), pp. 3261–3275. ISSN: 00218979. DOI: 10.1063/1.333384.

[158] O. B. Wright. "Thickness and sound velocity measurement in thin transparent films with laser picosecond acoustics." In: *Journal of Applied Physics* 71.4 (1992), pp. 1617–1629. ISSN: 00218979. DOI: 10.1063/1.351218.

[159] O. B. Wright, B. Perrin, O. Matsuda, and V. E. Gusev. "Ultrafast carrier diffusion in gallium arsenide probed with picosecond acoustic pulses." In: *Physical Review B* 64.8 (2001), p. 081202. ISSN: 0163-1829. DOI: 10.1103/PhysRevB.64.081202. URL: https://link.aps.org/doi/10.1103/PhysRevB.64.081202.

[160] Stefan Wurster, Christian Motz, Monika Jenko, and Reinhard Pippan. "Micrometer Sized Specimen Preparation Based on Ion Slicing Technique." In: *Advanced Engineering Materials* 12.12 (), pp. 61–64. DOI: 10.1002/adem.200900263.

[161] T. Yamashita. *Photosensitive Polyimides: Fundamentals and Applications*. Taylor & Francis, 1995. ISBN: 9781566762977.

[162] J. Yoo, C. H. Lim, and S. H. Baik. "Thermoelastic Surface WAves Generated by Irradiation with a Line-Focused Laser Pulse." In: *Journal of the Korean Physical Society* 48.1 (2005), pp. 61–66.

[163] Z Yu and S Boseck. “Inversion of V(z) Data in the Scanning Acoustic Microscope to Determine Material Properties of a Layered Solid.” In: *Optik* 88.2 (1991), pp. 73–79.

[164] Zuliang Yu and Siegfried Boseck. “Scanning acoustic microscopy and its applications to material characterization.” In: *Reviews of Modern Physics* 67.4 (1995), pp. 863–891. ISSN: 00346861. DOI: 10.1103/RevModPhys.67.863.

[165] A. Zerwer, M. A. Polak, and J. C. Santamarina. “Rayleigh wave propagation for the detection of near surface discontinuities: Finite element modeling.” In: *Journal of Nondestructive Evaluation* 22.2 (2003), pp. 39–52. ISSN: 01959298. DOI: 10.1023/A:1026307909788.

[166] G. Q. Zhang, Mart Graef, and Fred Van Roosmalen. “The rationale and paradigm of "More than Moore".” In: *Proceedings - Electronic Components and Technology Conference*. Vol. 2006. 2006, pp. 151–157. ISBN: 1424401526. DOI: 10.1109/ECTC.2006.1645639.

[167] G.Q. Zhang, W.D. van Driel, and X.J. Fan. *Mechanics of Microelectronics*. Solid Mechanics and Its Applications. Springer Netherlands, 2006. ISBN: 9781402049354.

[168] Y. Zhou, S. Van Petegem, D. Segers, U. Erb, K. T. Aust, and G. Palumbo. “On Young’s modulus and the interfacial free volume in nanostructured Ni-P.” In: *Materials Science and Engineering A* 512.1-2 (2009), pp. 39–44. ISSN: 09215093. DOI: 10.1016/j.msea.2009.01.020.